THE MEASUREMENT OF AXIAL TURBINE TIP CLEARANCE FLOW PHENOMENA IN A MOVING WALL ANNULAR CASCADE AND IN A LINEAR CASCADE

GEORGE MORPHIS

Thesis Submitted in Partial Fulfillment of the Requirements for the Degree of Master of Science in the Department of Mechanical Engineering

University of Natal

Durban

October 1989

PREFACE

The author hereby states that this whole thesis, unless specifically indicated otherwise, is his own original work, and that no part of this thesis has been submitted to any other University .

SUMMARY

On unshrouded axial flow turbine rotors, the tip clearance, required for thermal expansion and manufacturing limitations, allows fluid to leak from the pressure side to the suction side of the blade. This flow across the blade tip causes a large proportion of the overall rotor loss. In this work, the flow was visualized, microscopic static pressures taken and flow field measurements were done in the blade tip region to investigate the complex nature of tip clearance flows.

An annular turbine cascade with a rotating outer casing was used to simulate the relative motion at the tip of an axial rotor. It was found that relative motion did not have a significant effect on the basic structure of the micro-flow, even though it reduced the leakage mass flow rate which is important as far as mixing loss formation is concerned. The existence of a narrow, very low pressure depression, caused by the flow remaining attached around the sharp pressure corner edge, was confirmed. The width and pressure of the separation bubble were found to be strongly dependent on gap size but the relationship was not linear. The point at which the separation bubble reattaches was seen to coincide with a slight rise in static pressure.

The separation bubble which caused the majority of the internal gap loss, and which was thought to contribute to the mixing loss, was shown to disappear when the pressure corner was given a radius of 2,5 gap widths.

A linear cascade was used to evaluate the performance of two blade tip shapes that substantially reduced internal gap loss and to compare them to a standard sharp or flat tip blade. A method whereby linear cascade data was analyzed as if it were a rotor with work transfer, was used to evaluate the performance of the various blade tip geometries. It was found that both modified tips increased the mixing loss due to the extra leakage mass flow rate. The first tip with the radiused pressure corner was seen to have a lower efficiency than the flat tip blade. A second tip that was contoured to shed flow in a radial direction and thus decrease the leakage mass flow rate through the gap was seen to significantly increase the overall efficiency.

ACKNOWLEDGEMENTS

The Author wishes to thank :

The Workshop staff of Department of Mechanical Engineering for their help in construction and modifications of apparatus.

Mr "Paddy" Padayachee for the photography.

Rick G Allsopp for his friendship and for proof reading the Thesis.

Doug and Sharon Davis for their friendship and CAD drawings.

Dr Graham D J Smith for his ideas and encouragement.

NIAST and DAST for financial support and funding of the project.

His parents, Andreas and Ourania Morphis for their endless support and encouragement.

Finally a special thanks to Professor J P Bindon for his original and fresh ideas, for his unending assistance, enthusiasm and encouragement, for his effort in integrating and analyzing the simulated rotor results and for his supervision of the work.

NOMENCLATURE

C_L Loss coefficient = $\frac{P_{01} - P_{02}}{\frac{1}{2}\rho V_1^2}$

C_p Static pressure coefficient = $\frac{P_1 - P_2}{\frac{1}{2}\rho V_1^2}$

C_v Velocity coefficient = $\frac{P_{02} - P_2}{\frac{1}{2}\rho V_1^2}$

C_ω Work transfer coefficient

C_{lm} Mixing loss coefficient

C_{lg} Internal gap loss coefficient

C_{lgi} Gap inlet loss coefficient

C_{lge} Gap exit loss coefficient

C_f Gap mass flow coefficient

C_d Gap discharge coefficient

C_L'	1D gap loss coefficient at given chord position
P	Pressure
P_{00}	Inlet total pressure
P_{s0}	Inlet static pressure
P_1	Probe center tube pressure
P_2, P_3	Probe yaw tube pressures
P_4, P_5	Probe pitch tube pressures
U	Hypothetical rotor velocity
V	Absolute velocity
W	Free stream inlet velocity, (with subscripts this refers to the varying relative velocities in the inlet and outlet flow fields).
z	Spanwise flow integration height
S	Pitch
s	Pitchwise distance
q	Dynamic pressure
ω	Specific work

ρ	Density
ψ	Yaw angle
θ	Pitch angle
η	Efficiency
$K\psi_2$	Yaw angle calibration coefficient
Ki	Dynamic pressure fraction coefficient
Δp_0	Total pressure loss

SUBSCRIPT NOTATION

o, t	total quantity
s	static
1	cascade inlet
2	cascade exit or any measurement point
is	isentropic
id	ideal
x	axial
tt	total to total
ts	total to static
θ	swirl

CONTENTS

CHAPTER 1

INTRODUCTION

The aerodynamic losses generated by the rotor stage of an axial turbine may be split into the following loss categories:

1) Profile loss which is caused by skin friction or shear flow over the blade surface.
2) Annulus loss due to skin friction or shear flow on the inner and outer annulus.
3) Tip clearance loss found on both shrouded and unshrouded rotors due to the clearance required for thermal expansion and manufacturing limitations.
4) Secondary flow loss resulting from all shear flows other than in 1, 2, 3 and is mainly due to the blade to blade pressure gradient turning the boundary layers and wrapping them into a vortex.

This thesis focuses on the **tip clearance loss** of unshrouded rotors, in which the fluid leaks from the concave (pressure) side to the convex (suction) side of the blade at the blade tip. The fluid emerging at the suction side rolls up into a vortex that rotates in the opposite direction to that of the secondary flow. (see Figure 1.1)

The losses generated by the tip clearance are due to shear flow (friction or entropy generation) and the failure of the rotor to deflect (i.e. extract work from) the flow. Figure 1.2 shows the reduction of work due to velocity vector reduction and due to reduced deflection.

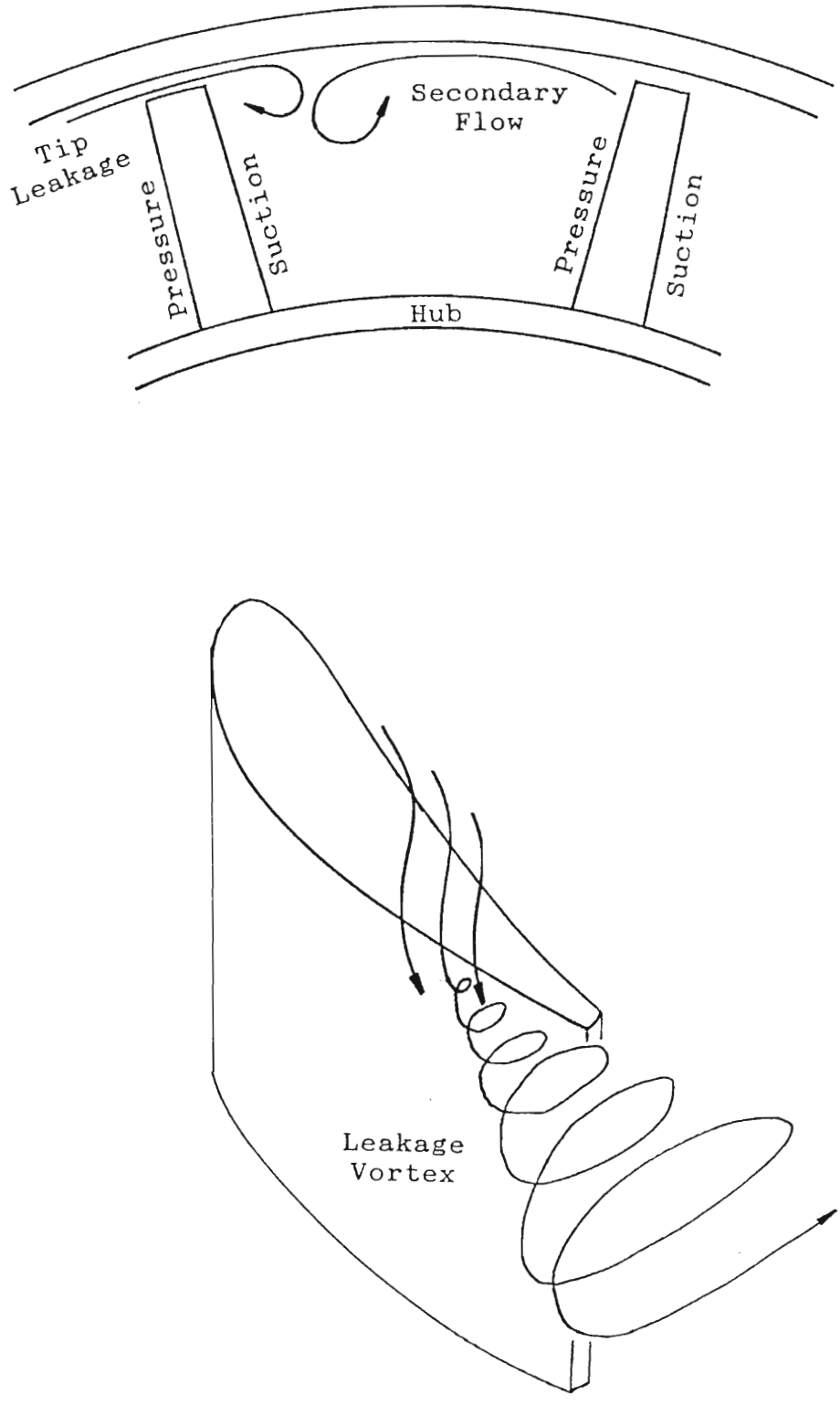

FIGURE 1.1 TIP CLEARANCE LEAKAGE FLOW

As illustrated in Figure 1.3, many different blade tip geometries and casing treatments have been developed to control or minimize tip clearance loss. The main strategy has been one of decreasing the amount of leakage flow or discharge coefficient. This approach has the inherent disadvantage in that the only way to block the leakage path is to form low velocity fluid which constitutes a loss or entropy generation. The ability of the blade tip to deflect the fluid (or extract work from the fluid) has in the main been ignored. A method was required to evaluate blade tip efficiency and thereby, through experimental means, develop blade geometries whereby entropy generation is minimized and deflection of the fluid is taken into account and so maximize blade tip efficiency. A suitable method which does this was applied in this thesis.

The study of tip clearance flows was for many years limited to an overall loss measurement where only the inlet and outlet flow fields were examined or where a rotor was tested for overall performance. This approach revealed nothing of the flow structure both in the mainstream leakage vortex region and in the microscopic gap between the blade and the casing.

More recently, relatively simple measurements and flow visualization in a low speed cascade have revealed a number of phenomena and posed some interesting questions regarding the tip clearance flows. It is with respect to these findings that this thesis is mainly addressed.

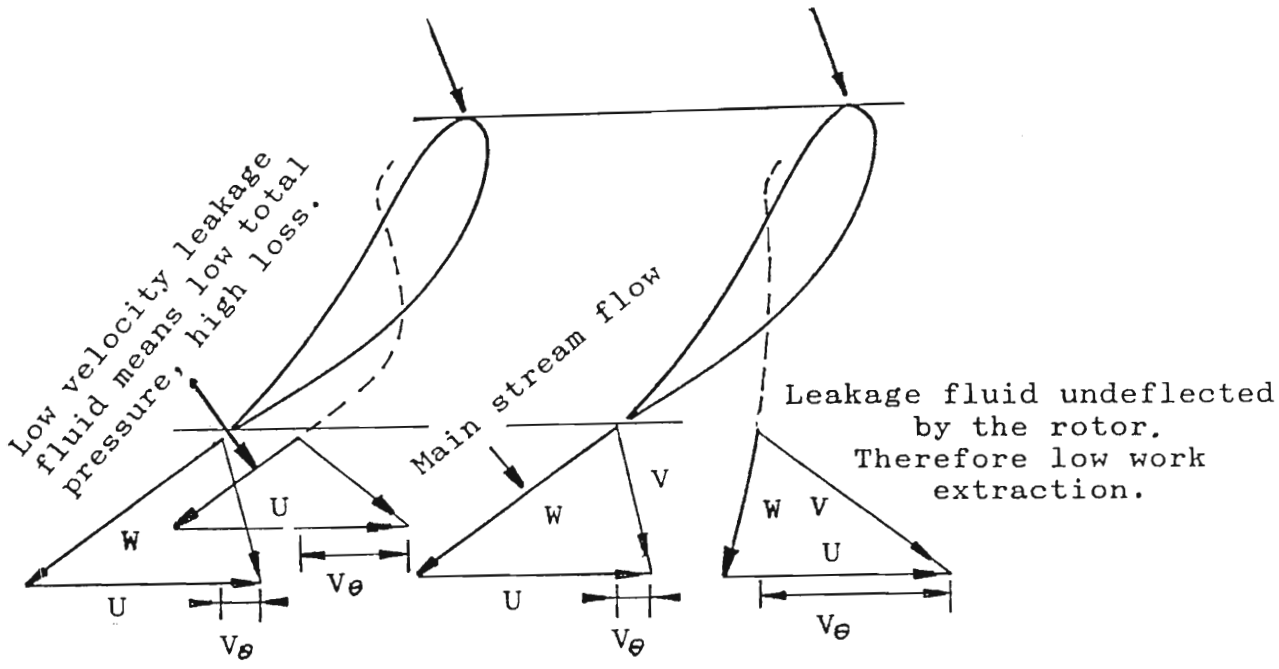

FIGURE 1.2 LEAKAGE FLUID LOSSES

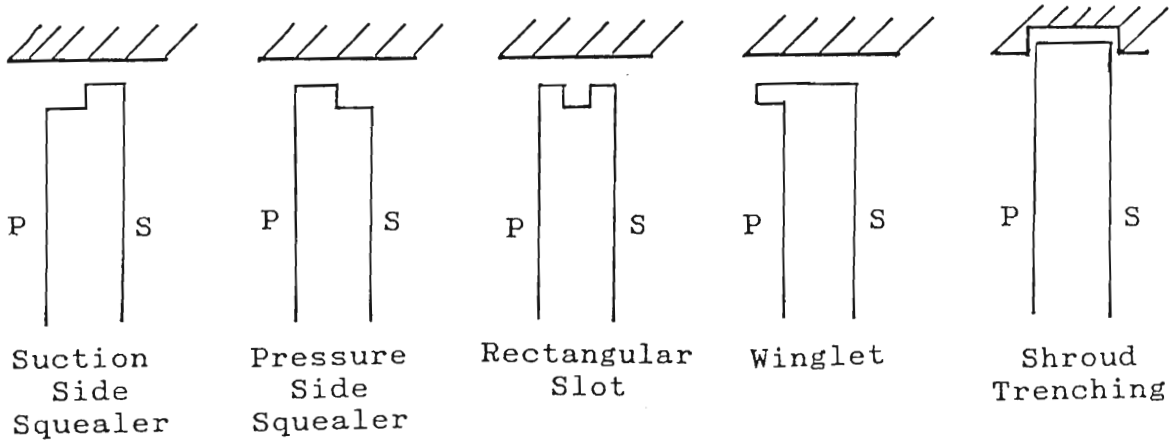

FIGURE 1.3 VARIOUS BLADE TIP GEOMETRIES

Two dominant features are evident in the microscopic flow field existing in the clearance gap; the separation bubble and the pressure distribution. As shown in Figure 1.4 the flow separates on the pressure corner of the tip to form a separation bubble. This separation bubble forms a blockage (or vena-contracta effect) which causes the static pressure to drop substantially below even the suction surface pressure and to stay low until the flow reattaches to the blade tip. This thesis provides flow visualization and detailed static pressure measurements to clarify the data regarding this bubble.

Smoke flow visualization experiments and oil surface flow studies have shown that the width of the separation bubble became wider with increased tip clearance. However static pressure distributions seem to indicate that the bubble width is independent of gap size. In this thesis the effect of gap size on the separation bubble was clarified.

An important aspect of the gap flow appears to be that as the fluid turns to enter the gap, the lowest static pressure is found at the edge of the blade in the form of a narrow extremely low pressure trough. This low pressure trough is thought to occur due to the flow remaining attached around the corner as shown in Figure 1.5. This low pressure trough was previously revealed by using a microscopic static tapping technique, but because of the small size of this zone only one measurement had been obtained. In this thesis the micro tapping technique was improved to obtain a higher resolution, to define the shape, and confirm the existence of this low pressure trough.

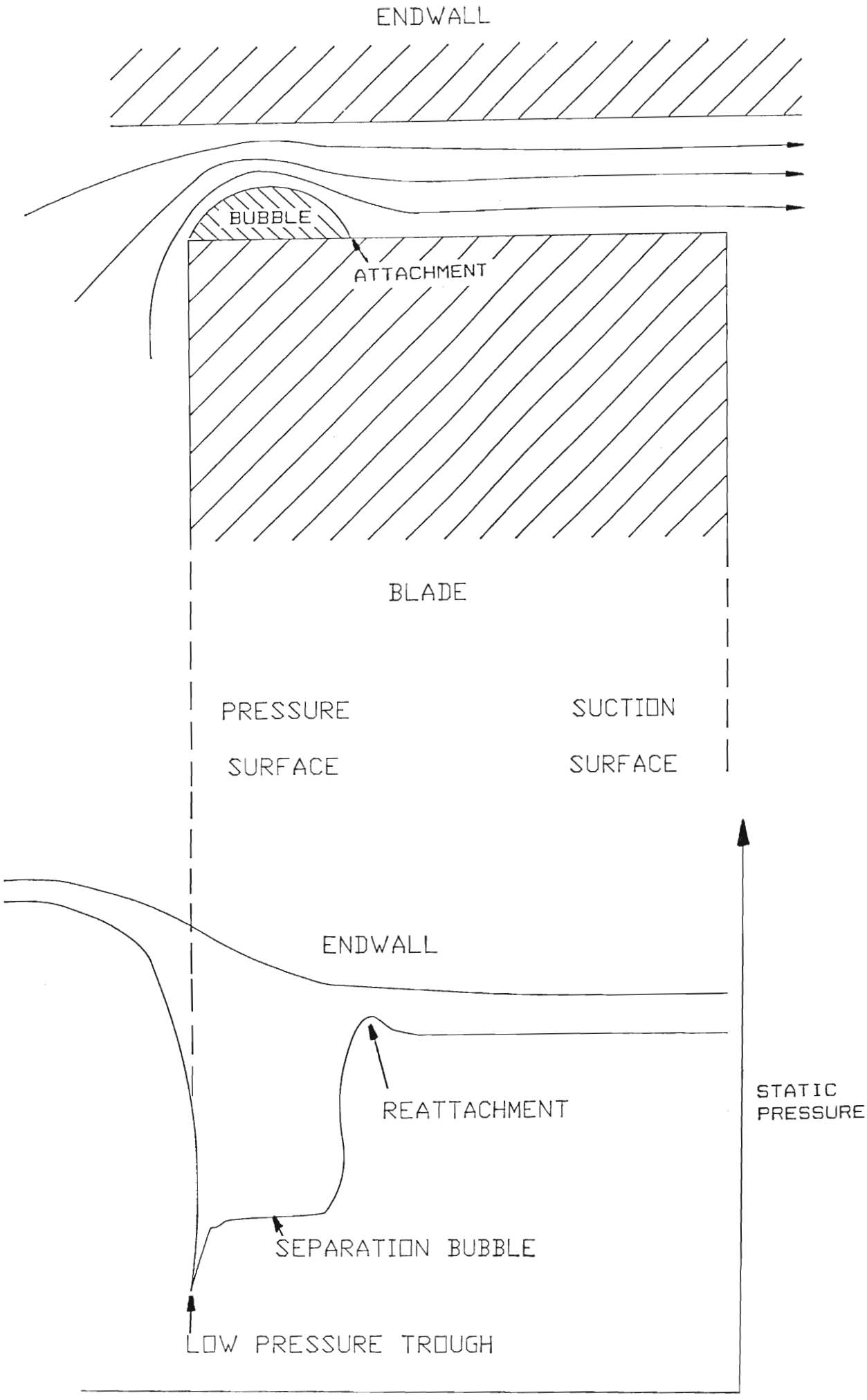

FIGURE 1.4 MERIDIONAL VIEW OF SEPARATION BUBBLE AND GAP PRESSURE DISTRIBUTION

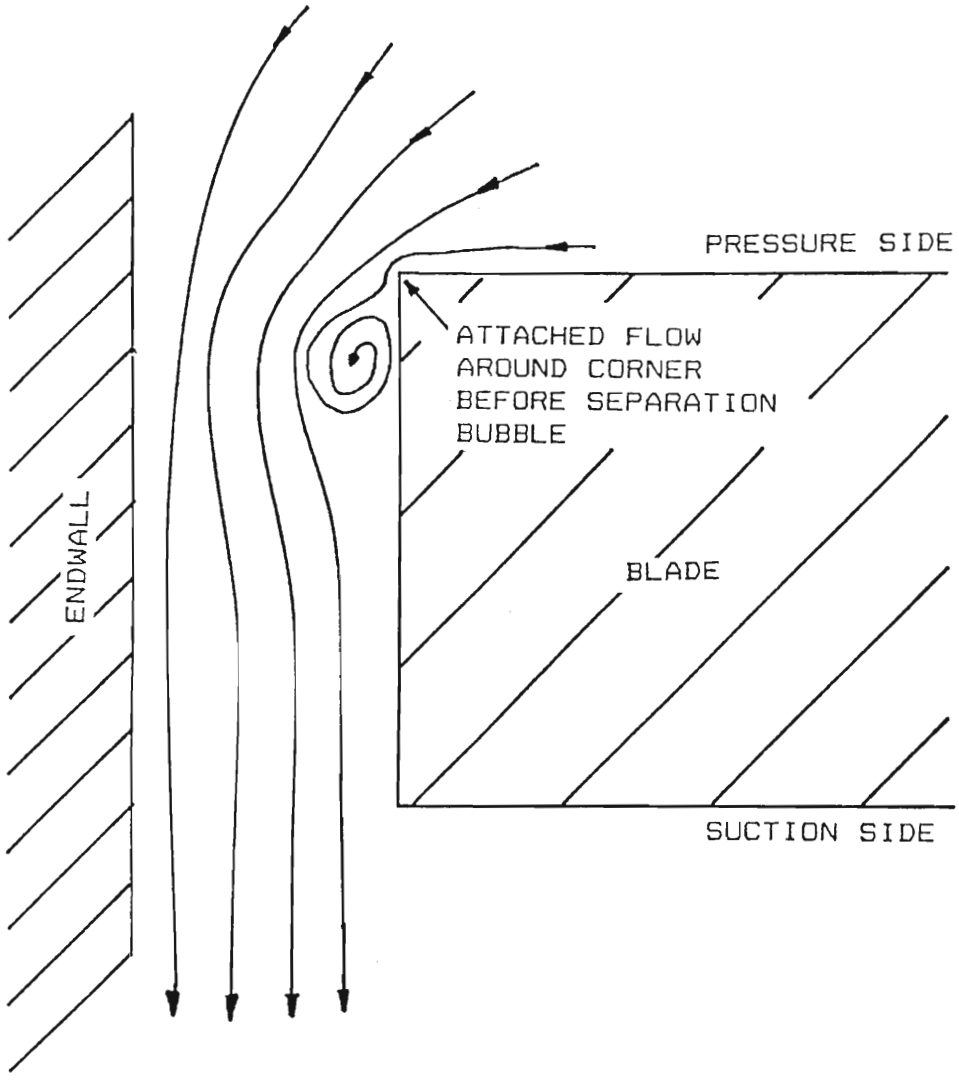

FIGURE 1.5 ATTACHED FLOW ARROUND PRESSURE CORNER

Traverses of the flow leaving the clearance gap revealed that the majority of the loss generated within the gap was present in the fluid leaving the gap over the latter half of the blade (i.e. from midchord to the trailing edge) (see Figure 1.6).

As shown in Figure 1.7, the overall loss in the blade tip region was broken down into the following components.

1) Secondary and endwall loss.
2) Loss generated within the gap.
3) Loss due to leakage flow mixing with mainstream flow.

It was seen that the loss generated within the clearance gap (mainly due to the separation bubble) was about 40% of the total endwall loss.

From Figure 1.7 it could be seen that the mixing loss only started occurring near the blade exit plane. The start of this mixing loss coincided with the area where the majority of the internal gap loss (due to separation bubble) left the gap. This suggested some relationship between mixing loss and internal gap loss caused by the separation bubble. It was thus thought that it could be illuminating to see how the mixing loss developed for a streamlined tip blade which would have no separation bubble. In this thesis the loss development was examined for two streamlined blade tip geometries and compared to a flat tip. All loss and channel flow measurements were done in a linear cascade.

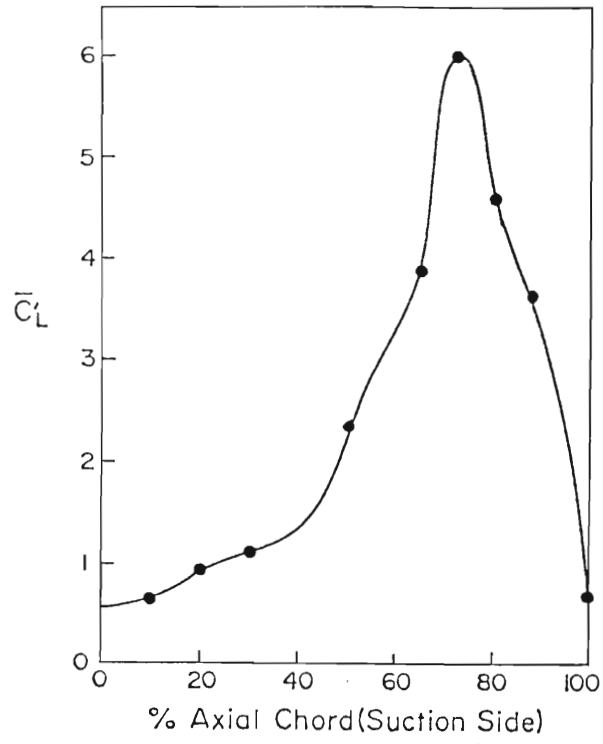

FIGURE 1.6 LOSS DISTRIBUTION OF FLOW LEAVING CLEARANCE GAP (BINDON 1988a)

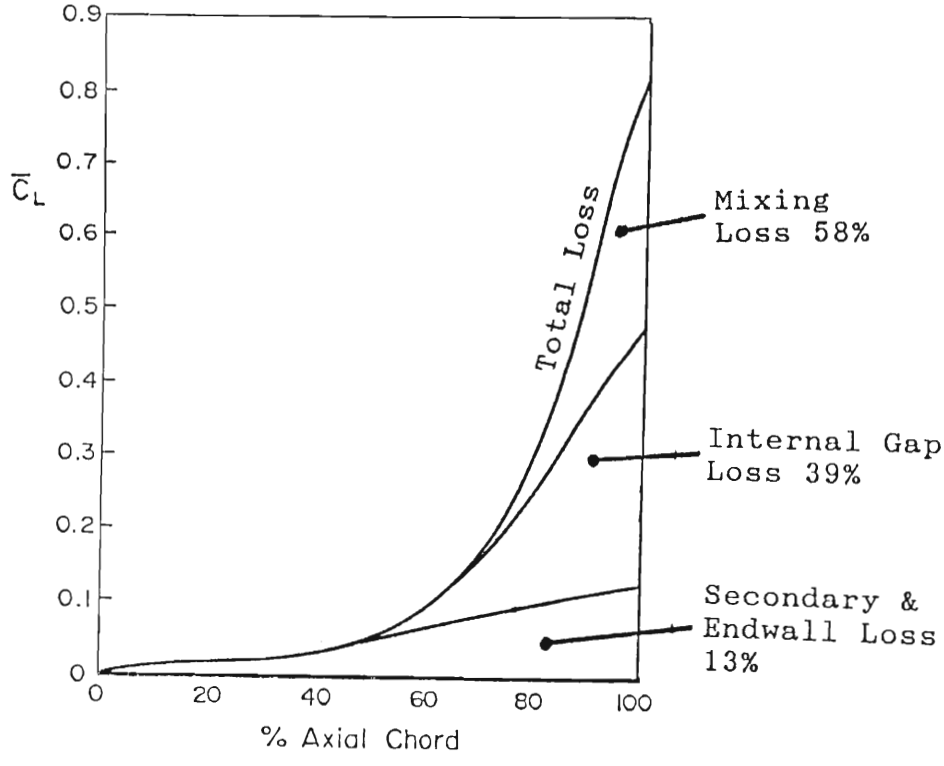

FIGURE 1.7 TOTAL ENDWALL LOSS DEVELOPMENT (BINDON 1988a)

In axial turbines the relative motion of the casing is in the opposite direction to the leakage flow, causing intense viscous shear on the gap endwall. The effect of relative motion on the flow and separation bubble within the clearance gap was thus examined in this thesis.

It is difficult to study the flow in a true rotating rotor. Relative motion between the blade tip and the endwall has previously been generated by using a moving belt in a stationary linear cascade. In the present study, an annular cascade/turbine combination was available which provided the opportunity to rotate the outer casing while keeping the stator blade stationary (see Figure 1.8).

Figure 1.9 is a schematic, illustrating the method used to create relative motion between the stator row (stationary annular cascade) and the rotating casing. The stationary test blade row was supported by the inlet section above it, which in turn was supported by four brackets which were bolted to the bottom fixed section of the casing. The casing surrounding the stator and rotor was attached to the rotor blades, which were driven by the main stream flow after it was given swirl by the test blades.

To summarize, the main objectives of this thesis were to study the effect of gap size and the effect of relative motion on the microscopic flow within the tip clearance gap. Streamlined blade tip geometry was introduced to control the separation bubble in the gap. The effect of this on the flow structure and the losses incurred were investigated to provide a greater understanding of

the mechanisms giving rise to tip clearance loss and possibly also to point the way towards more efficient blade shapes in the tip region.

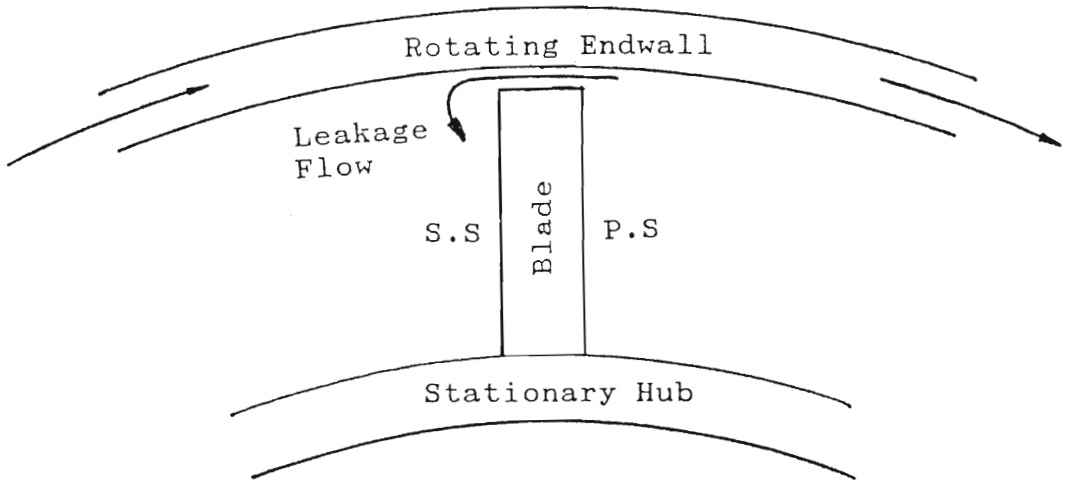

FIGURE 1.8 ROTATING CASING FOR RELATIVE MOTION

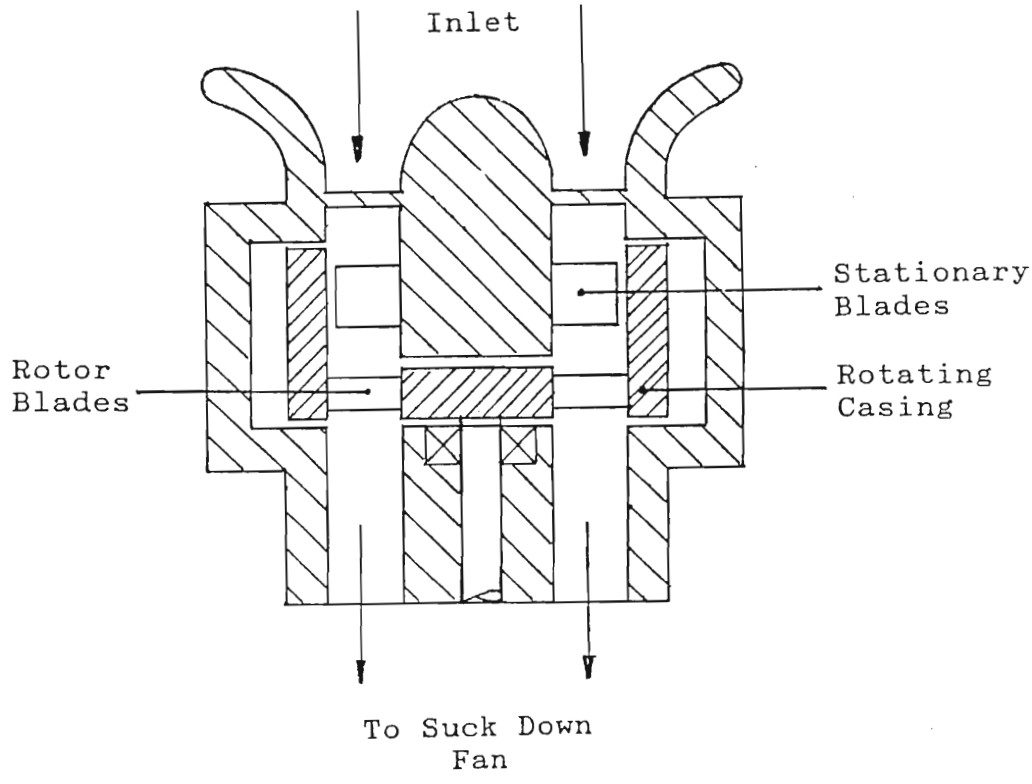

FIGURE 1.9 ROTATING CASING TURBINE RIG SCHEMATIC

CHAPTER 2

LITERATURE REVIEW

The earliest efforts at improving the efficiency of the blade tip region in turbines and compressors were based on reducing the tip clearance and thus decreasing the amount of leakage fluid. A physical limit of how small the clearance gap could be made was soon reached due to clearance required for thermal expansion, creep, manufacturing tolerances and thermal distortion of the casing.

Rains (1954) introduced colored oil droplets into the flow of an axial water pump with blading similar to a compressor, to study the generalized movement of tip fluid. The data gained here was used as a basis from which he developed two loss calculation flow models. The first was an idealized flow model applying Bernoulli`s equation at gap entry and exit, and ignored viscous effects. In a second more correct model he included the separation bubble (found at the entry to the gap), reattachment and flow mixing.

Many different blade tip geometries and casing treatments have been studied in the past, but the majority of this work has concentrated on quantifying and predicting the losses and the clearance gap discharge coefficient. Booth et al (1982) conducted a series of experiments on three water flow rigs in which leakage quantities were measured over simulated blade tips. As shown in Figure 2.1 the first two experimental rigs had a wall with a rectangular slot at the base. The flow was parallel to the wall

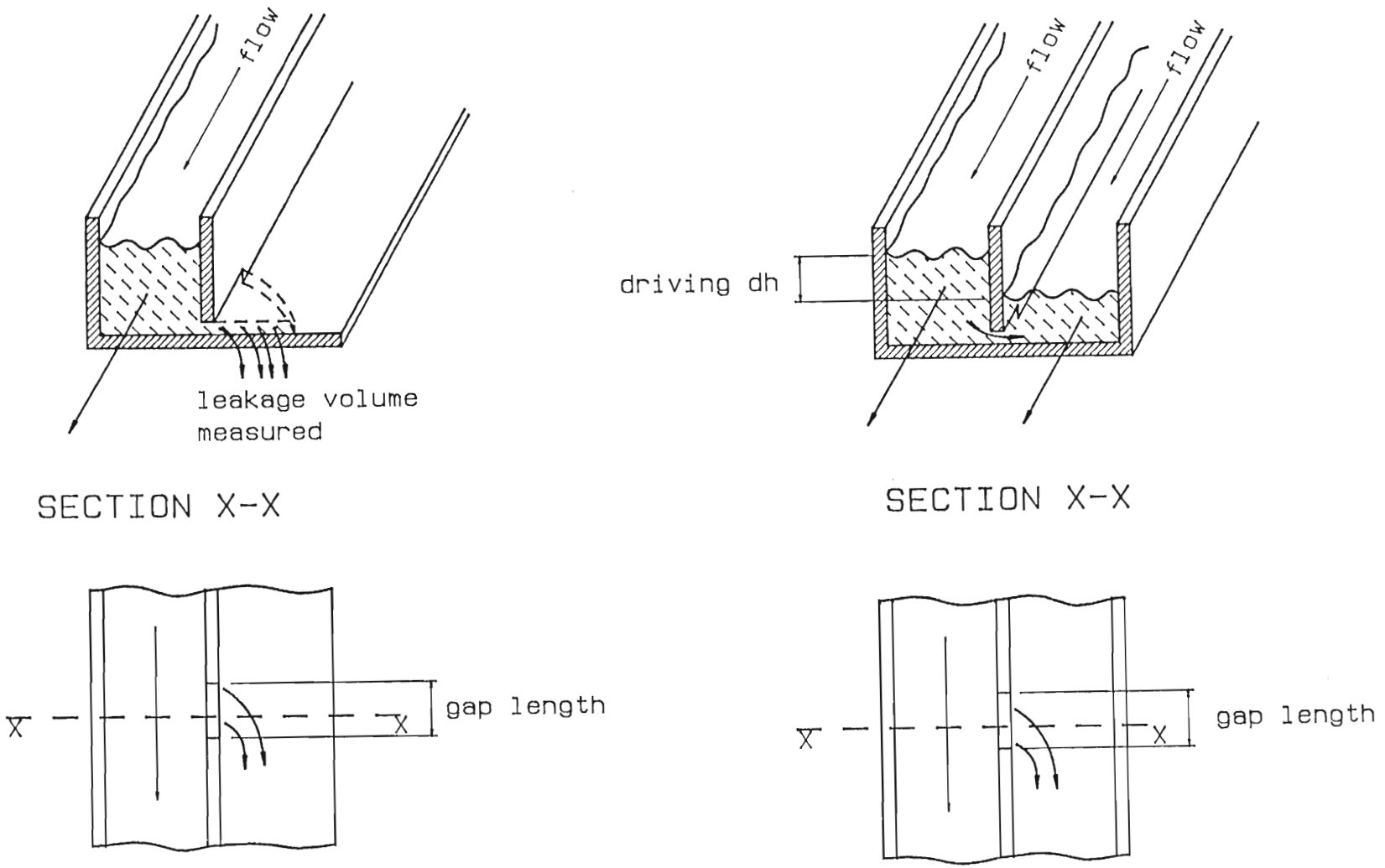

FIGURE 2.1 SINGLE AND DOUBLE SIDED DISCHARGE RIGS

and leaked through the slot to simulate flow through a clearance gap. The gap pressure ratio and transverse velocity were adjustable through columns of water upstream and downstream of the transverse flow. The first rig was very simple in that it only had water flow on the high pressure side of the gap and thus the leakage flow was not affected by flow on the low pressure side of the gap. The second rig was an improvement of the first and included transverse flow on the suction side of the gap so that the static pressure could be adjusted on both sides of the gap. The gap leakage flow was measured by recording the time needed to accumulate a quantity of water leaking through the gap. The third rig was a horizontal water table cascade with tip clearance in which the water height of the free surface could be measured on the pressure and suction sides of the blade to determine the static pressure distribution. Dye was injected into the flow and a high speed camera used to photograph the movement of the dye clusters to determine the velocity and direction of the leakage flow. Data obtained in these rigs was used to develop a model following Rains' (1954) theory to describe the leakage flow. Seventeen different blade configurations that represented variants of flat tips, squealers, grooves and winglets were tested. Winglets were shown to be the best tip configuration. A rotor with winglets was tested and compared against a rotor with flat tip blades and found to be more efficient.

Wadia and Booth (1982) used time dependent finite difference equations and assumed laminar incompressible flow to calculate the discharge coefficient for five basic tip geometries. Streamlines were calculated for the various tips but their

predictions failed to show the separation bubble at the entry to the gap.

Offenberg et al (1987) surveyed 12 casing treatments to study the effect of a trench in the casing on axial turbine performance. The casing treatments and tip clearance geometries were variations of the ones illustrated in Figure 2.2. Here it was found that at the nominal tip clearance (1.5% of blade height), an untrenched casing produced the least losses. As the tip clearance was increased to 3% of blade height it was found that shroud trenching returned less of a loss penalty than the solid wall.

The static pressure on the pressure surface and suction surface of the blade and thus the blade loading, deteriorate near the blade tip. Moore and Tilton (1987) took static pressure measurements on the blade pressure surface and on the endwall in a linear cascade with clearance. The data obtained was used to model the unloading along the pressure surface and the endwall static pressure distribution up to the separation bubble. Sjolander and Amrud (1986) used static pressure measurements in a linear cascade to evaluate the effect of tip leakage on the blade loading for various tip clearances. As shown in Figure 2.3 multiple rows of pressure tappings on the pressure and suction surface showed the unloading of the blade at the tip. Flow visualization was also used to examine the leakage flow and it was shown that the starting point of the leakage vortex moved rearward with increasing clearance.

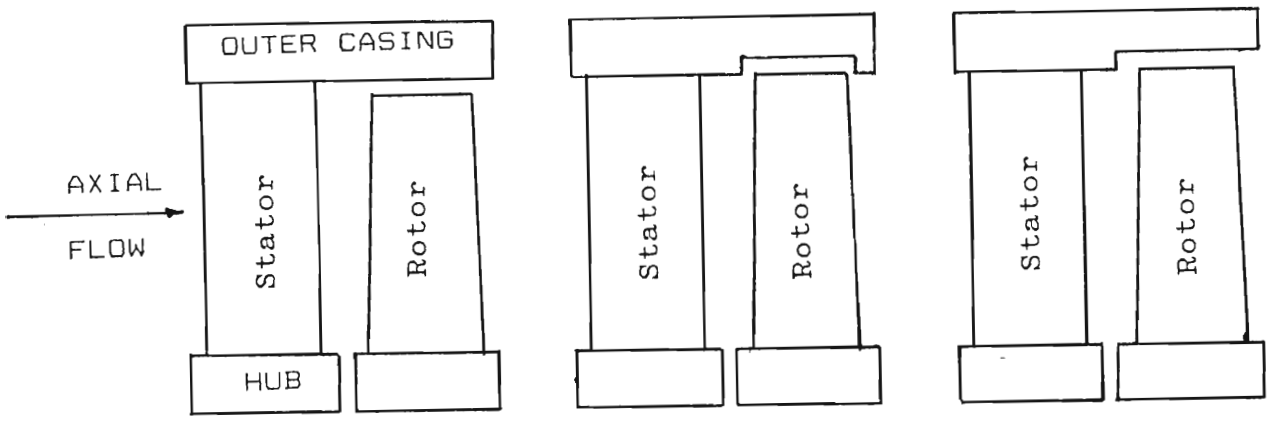

FIGURE 2.2 SHROUD TRENCHING CONFIGURATIONS

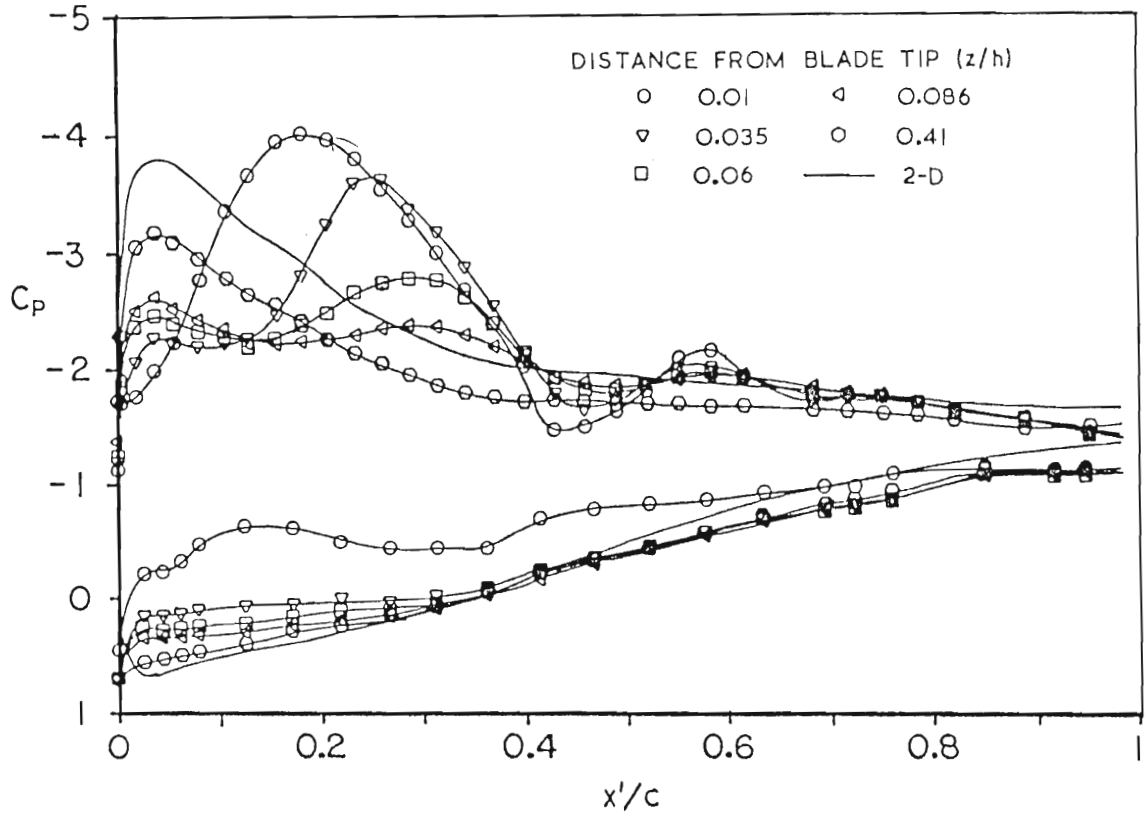

FIGURE 2.3 PRESSURE DISTRIBUTIONS FOR BLADE WITH CLEARANCE SHOWING EFFECT OF TIP CLEARANCE ON BLADE LOADING (SJOLANDER AND AMRUD 1986).

Until recently the complex and microscopic nature of the flow within the tip gap had been neglected. During experiments to investigate the causes of tip burn out, Bindon (1986 a, b) unravelled some of the basic mechanisms of the flow in the clearance gap. A static pressure survey in a linear cascade was done on the endwall and on the blade tip using a relatively simple but effective micro pressure tapping technique. As shown in Figure 2.4, it was revealed that as the flow turns to enter the gap, the pressure drops to the lowest value in the form of a narrow extremely low trough. This was believed to be due to the flow remaining attached around the corner. The flow then decelerates sharply and separates to form the bubble which causes the static pressure to remain relatively low as the main leakage flow accelerates over the blockage caused by the separation bubble. The static pressure then recovers to approximately suction surface pressure as the flow reattaches.

A chordwise pressure gradient was also found within the separation bubble, with the lowest pressure at midchord. As shown in Figure 2.5 Bindon (1988 a) suggested that the separated flow within the bubble moved in a chordwise direction towards midchord where it stagnated and then mixed with the leakage flow to be ejected at the suction side of the blade. When this high loss leakage wake enters the diffusing flow at the suction surface, it may separate to create the majority of the mixing loss. This would explain the sudden increase in loss found in the latter part of the blade. Since mixing loss appears to be linked to the flow within the separation bubble, it was hypothesized that the mixing loss could be reduced by using special tip geometries to

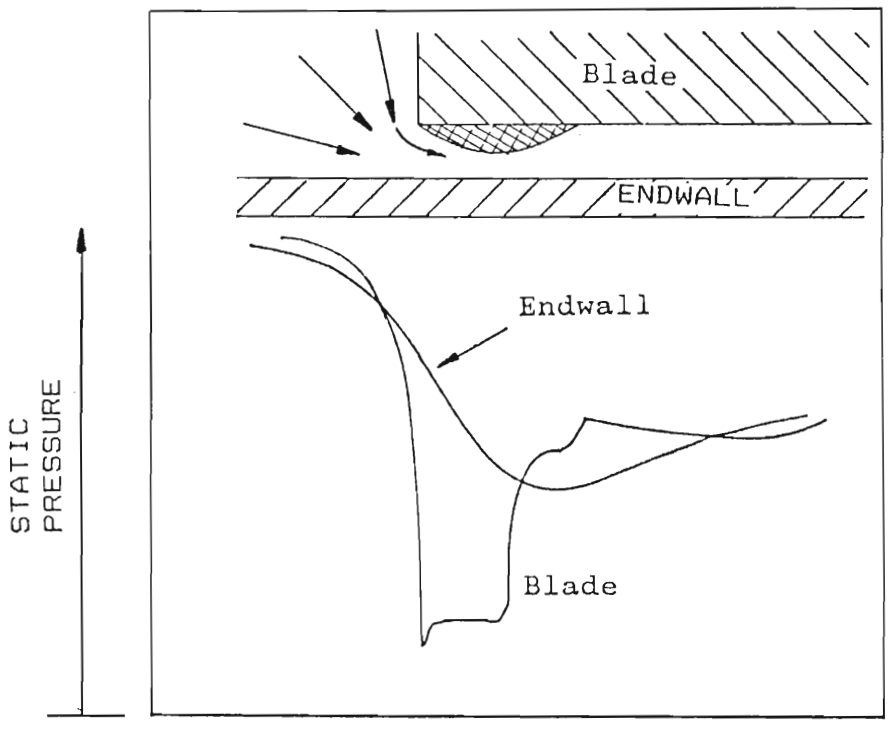

FIGURE 2.4 BLADE TIP AND ENDWALL STATIC PRESSURE DISTRIBUTION

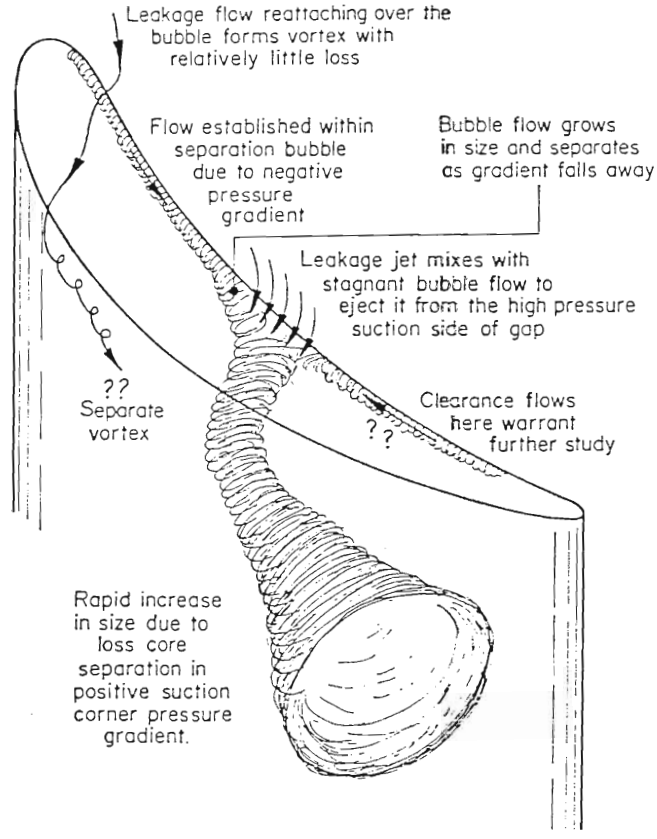

FIGURE 2.5 SUGGESTED HISTORY AND EFFECT OF CLEARANCE GAP SEPARATION BUBBLE (Bindon 1988a)

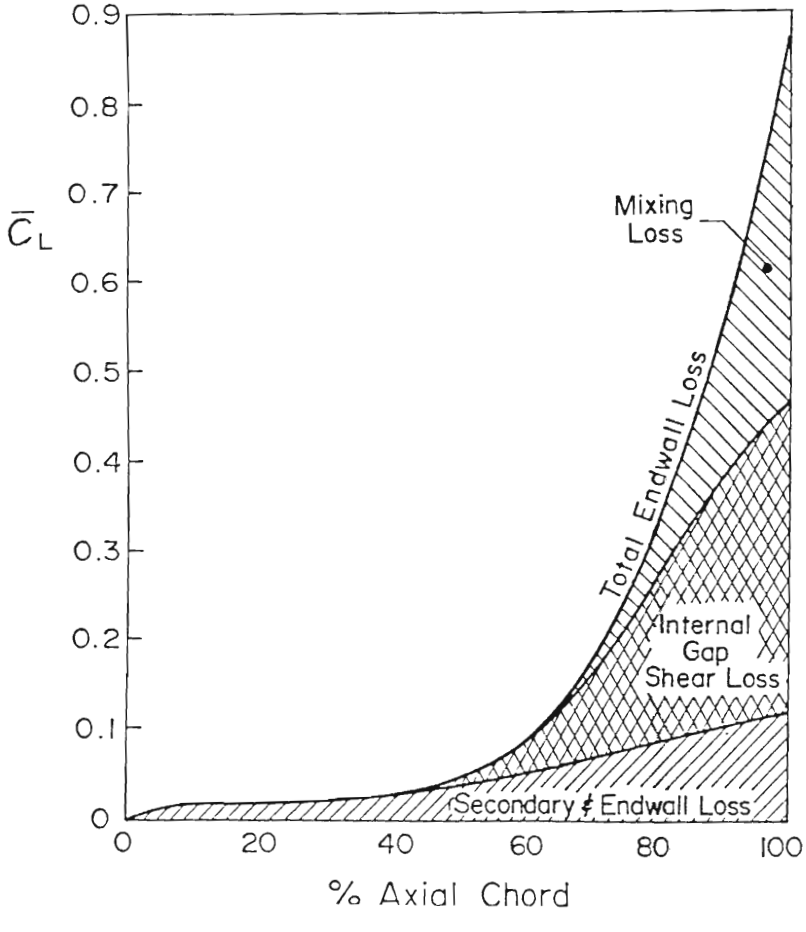

FIGURE 2.6 TOTAL ENDWALL LOSS DEVELOPMENT (Bindon 1988a)

eliminate the separation bubble.

Bindon (1988 a) measured the detailed development of tip clearance loss from the leading to the trailing edge of a linear turbine cascade within the clearance gap and on the endwall. These measurements were used to identify, separate and quantify for the first time the contributions made by mixing, by internal gap shear flow and by endwall/secondary flow. It was revealed that only 13% of the overall endwall loss is due to endwall/secondary flow and of the remainder, 39% loss was generated within the gap and about 48% was due to mixing (see Figure 2.6). Here it was further reasoned that the conventional method of decreasing the discharge coefficient actually introduced loss or increased entropy within the gap. It was also suggested that performance improvements may result from streamlined tip geometries designed to avoid the formation of separation bubble and which optimize the trade-off between entropy production and flow deflection.

Bindon (1986 a, 1987 a) investigated the effect of increasing the radius of the pressure corner on the static pressure distribution. As shown in Figure 2.7 the magnitude of the pressure depression on the edge of the blade was decreased by increasing the radius of the pressure corner. However only a single pressure reading was recorded at each chordwise station and more information was needed regarding the effect of blade edge radius on the clearance gap flow and loss formation.

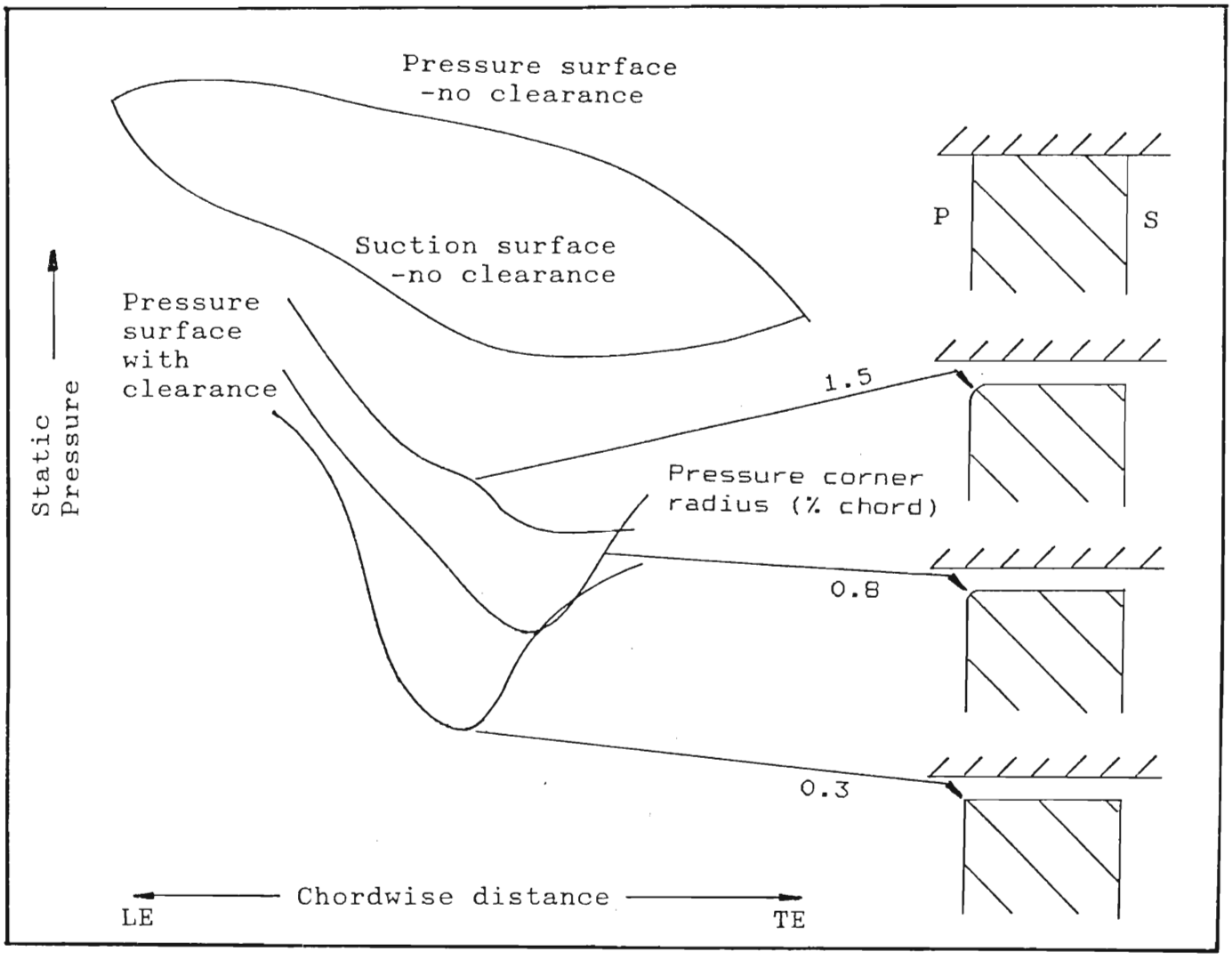

FIGURE 2.7 EFFECT OF PRESSURE SURFACE CORNER RADIUS ON THE BLADE TIP PRESSURE DISTRIBUTION (Bindon 1986a)

Yaras et al (1988) used a 3 hole pressure probe to measure the flow along the blade mean line in the clearance gap. These measurements were used to calculate the mass flow rate through the gap and showed that most of the leakage occurs towards the endwall. In work mentioned above, Bindon (1988 a) presented the loss profiles (between the blade and endwall) of the fluid leaving the gap and showed that the boundary layer on the blade tip was much larger than that on the endwall.

Most of the existing knowledge of tip clearance flow was obtained in simple linear cascades without relative motion between the blade tips and the endwall. Gearhart (1964) investigated the effect of relative motion by using an endless belt that moved in the direction of the leakage flow. His work was primarily aimed at water pumps and he found that relative motion increased the leakage mass flow rate through the clearance gap, due to the direction of motion being in sympathy with the leakage flow. Graham (1985), in a water flow cascade with a moving belt endwall, found that relative motion had the effect of reducing the mass flow rate through the gap and also the vortex strength. At small clearances he showed that the leakage flow could be cut off by increasing the speed of the belt. A drop in discharge coefficient was also shown by the model developed by Wadia and Booth (1982). Mayle and Metzger (1982) used a spinning disc and rectangular surface to show that the heat transfer coefficient of the tip was independent of relative motion. This, they argued, was because the gap radial length was too short for the two boundary layers to meet and interact viscously.

The effect of increased clearance gap on the separation bubble within the gap has been examined in the past. Smoke flow visualization experiments of Bindon (1986 b, 1987 b) showed an increase in bubble width with increased clearance. However static pressure distributions of Bindon (1986 a) suggested that the bubble pressure was independent of clearance. Moore and Moore (1986) calculated the velocity profile within the gap and found the separation bubble to be proportional to clearance height (bubble width = 2 x gap). In an oil surface flow study, Moore (1987) also claimed that the bubble width increased with clearance.

CHAPTER 3

ANNULAR CASCADE AND APPARATUS

3.1 ROTATING CASING TURBINE RIG

To assess the effect of relative motion on the flow within the gap, to measure the effect of gap size on the separation bubble width and to confirm the existence of the low blade edge pressures, a low speed vertical axis research turbine was used. the turbine had been modified during a previous project to have a rotating casing and a stationary row of test blades. The modification was carried out to simulate the relative motion at the tip of an axial rotor (Morphis 1986). The diameters of the outer annulus and hub were 406 mm and 284 mm respectively and the inlet axial velocity was 25 ms^{-1}.

The rig consisted of a stator row of blades (test blades) supported by the inlet section, followed by a row of rotor blades which were used to drive and support the rotating casing (Figure 3.1). A fan downstream of the blade rows was used to generate the axial flow through the turbine rig. The rotor and thus the rotating casing were driven by the flow exiting the first stator row (or annular cascade). In order to perform low speed flow visualization experiments a section of the rotating casing could be replaced by a segment made in a transparent material.

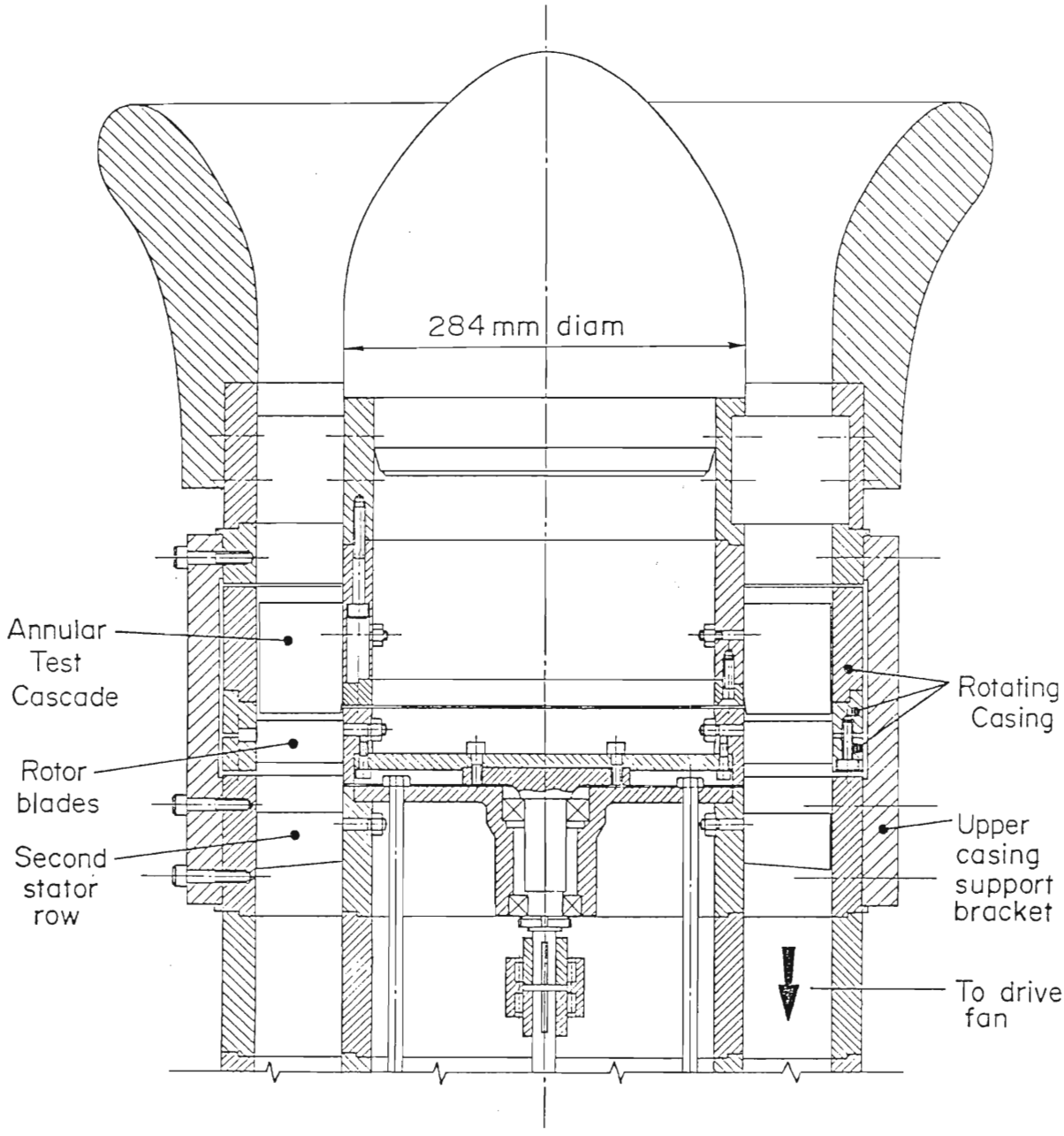

FIGURE 3.1 ONE AND A HALF STAGE LOW SPEED RESEARCH TURBINE WITH ROTATING CASING TO SIMULATE RELATIVE MOTION BETWEEN BLADE TIPS AND ENDWALL

The angular velocity (rotational velocity) of the rotating casing was adjusted so that the correct ratio of axial velocity to tangential velocity (of the rotating casing) could be obtained. The angular velocity of the rotating wall was dependent on the axial flow velocity (or Reynolds number) and the stagger angle of the rotor blades. The speed of the suck down fan and hence the axial velocity of the air flow could be adjusted at the rig.

As mentioned above, the function of the rotor was to drive and support the rotating casing. Thus the rotor had to extract the amount of work (or energy) from the flow equal to the loss generated by the rotating casing, the rotor, its bearings and dormant hydraulic pump, at the required rotational velocity. Applying the Euler equation and referring to Figure 3.2 ,the work extracted by the rotor is $W = U(V_{\theta 3} - V_{\theta 2})$. For a given rotor blade stagger angle and deviation, the direction of the outlet relative velocity W_3 is set. At a given axial flow velocity the rotor speed U will increase until the vector V_3 (absolute outlet velocity) gives a $V_{\theta 3}$ such that the work extracted by the rotor $U(V_{\theta 3} - V_{\theta 2})$ equals the losses.

The stagger angle of the rotor blades was adjusted to -20 degrees which set the Vx / Ucasing ratio to approximately 0.7 at the operating Reynolds number. Figure 3.3 shows the variation of Vx / Ucasing with Reynolds number. A summary of cascade and test data is presented in Table 3.1.

TABLE 3.1 : CASCADE AND TEST DATA

Chord	115 mm
Span	61 mm
Annulus Tip diameter	406 mm
Solidity	1.35
Maximum blade thickness	20% chord
Trailing edge thickness	5% chord
Cx / Ucasing	0.7
Camber angle	60 deg
Number of blades	15
Reynolds number (exit)	3×10^5
Gas inlet angle	0 deg
Clearance Gaps :	4% chord (4.6 mm)
	2% chord (2.3 mm)
	1% chord (1.2 mm)
Pressure edge radii :	0.5% chord (0.25 gap widths)
	2% chord (1 gap width)
	3% chord (1.5 gap widths)
	5% chord (2.5 gap widths)
Tape thickness	0.06 mm

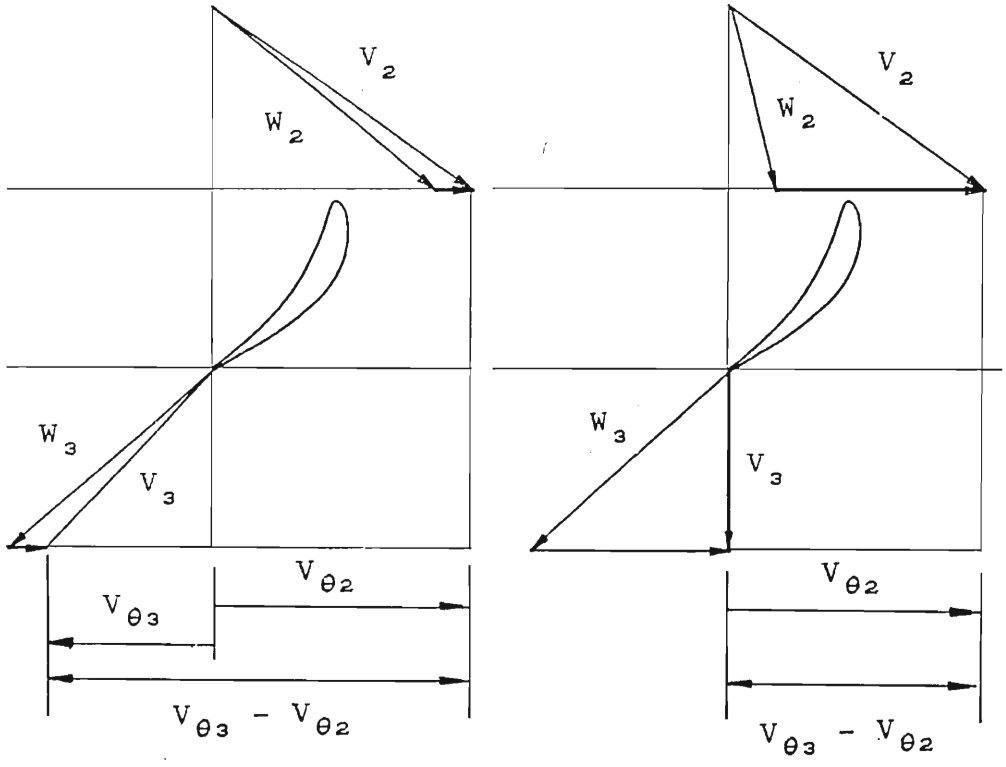

$U(V_{\theta 3} - V_{\theta 2})$ A MAX.

$U(V_{\theta 3} - V_{\theta 2})$ A MIN.

FIGURE 3.2 WORK EXTRACTED BY ROTOR

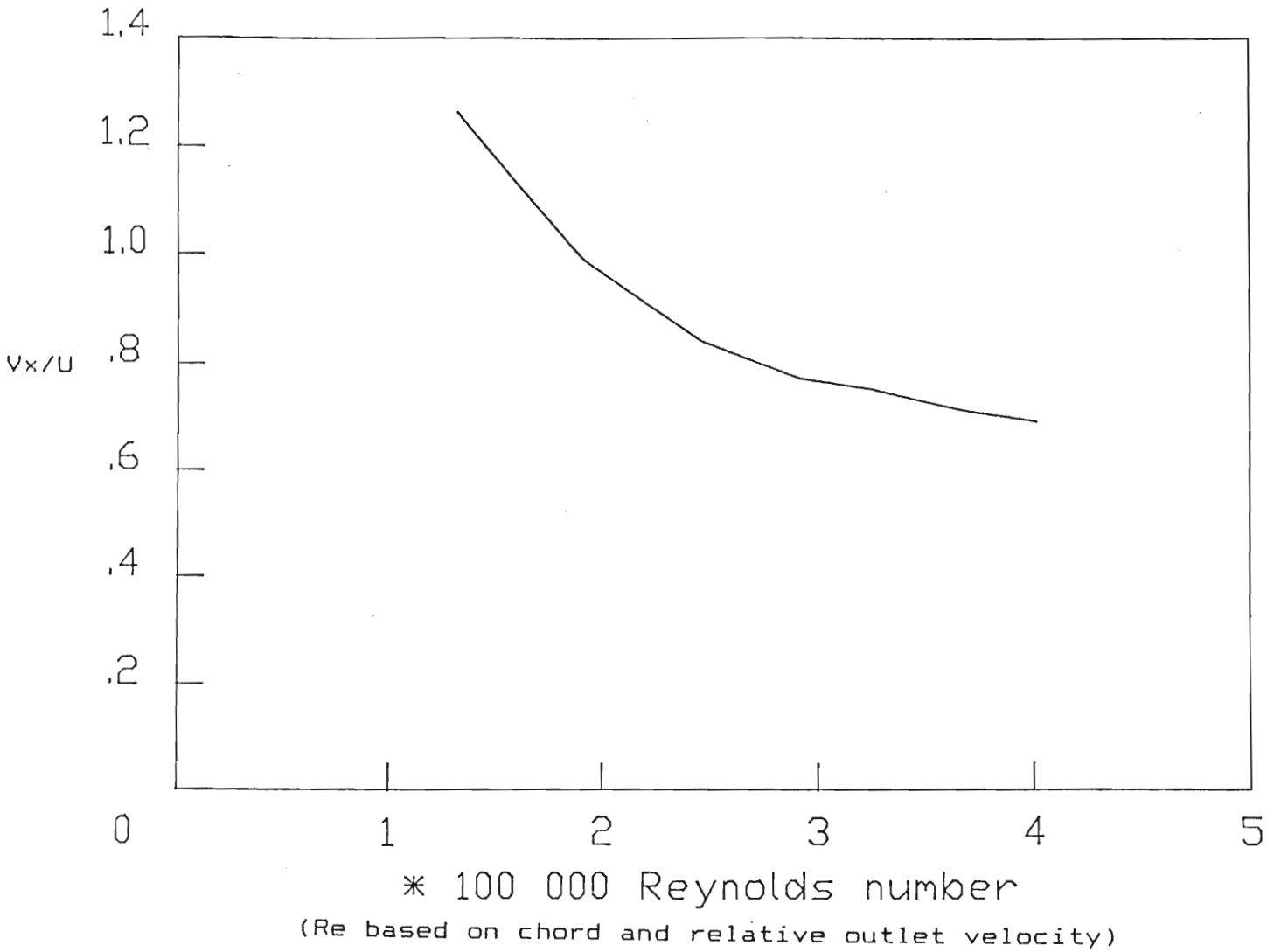

FIGURE 3.3 GRAPH OF Vx/U VERSUS REYNOLDS NUMBER FOR ROTATING CASING TURBINE RIG

3.2 Blades

3.2.1 Profile

The largest profile that fitted in the rotating casing section was selected so as to magnify the microscopic detail of the flow in the tip region. This resulted in a blade with a relatively low aspect ratio.

An untwisted NACA A_3K_7 profile with thickened trailing edge was selected to model a cooled blade. The rotating casing had an axial length of 80 mm. Camber angle and stagger angle for various chord lengths were computed (Appendix 1.a). A camber angle of 60 degrees was chosen. A blade chord of 115 mm resulted from setting the stagger angle to 45.7 degrees for zero inlet angle. From the correlation method by Ainley and Mathieson (1957) a chord/pitch ratio of 0.6 was read giving 15 blades.

A computer program that was able to thicken the trailing edge was used to calculate and plot the blade profile coordinates to scale (Appendix 1.b). The trailing edge was thickened by adding a thickness equal to a factor (.02) times the percentage chord. (i.e. 0mm was added at the leading edge, 1mm at mid chord and 2mm at the trailing edge.)

3.2.2 Blade casting

A master blade was hand made from Jelutong wood and sealed with polyester resin. This blade was used to cast the female mould in two halves from Aeroldit CW 216/HY 216 metal filled epoxy resin using QZ13 release agent. The blades that were to be instrumented with pressure tappings, were cast from Aeroldit CW 2215/HM. The remainder of the blades were cast from a less expensive resin, Aeroldit M-Resin/HR (Figure 3.4).

3.3 Tip geometries and blade instrumentation

A clearance gap of 2% chord (2.3 mm) was used for all experiments in the annular cascade, except for the ones where the effect of clearance was examined. For these, the tip clearance was adjusted to 1%, 2% and 4% of chord by inserting spacers between the blades and hub.

Radii of 2%, 3% and 5% of chord were used to explore the effect of pressure surface edge radius on the separation bubble and blade gap pressure distribution. These pressure corner radii were hand shaped and measured with a radius gauge.

A micropuncture technique developed by Bindon 1987 was used to obtain the detailed static pressure distribution on the blade tip. As shown in Figure 3.5 the blades used for static pressure measurements were slotted at various chordwise stations to create a chamber. The chamber was accessed by a spanwise hole drilled through the blade into the hub. Flexible tubes were connected

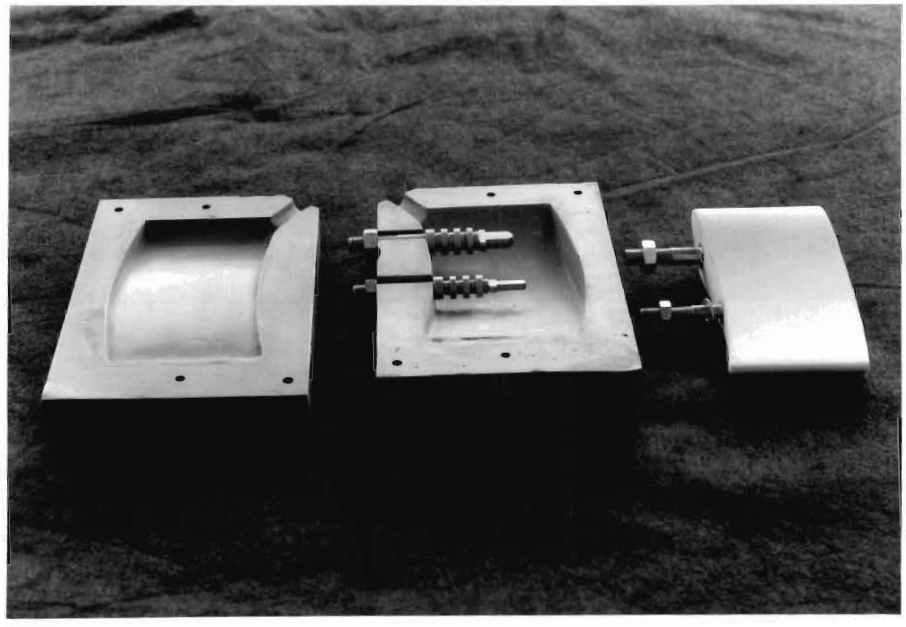

FIGURE 3.4 BLADE CASTING MOULD AND BLADE

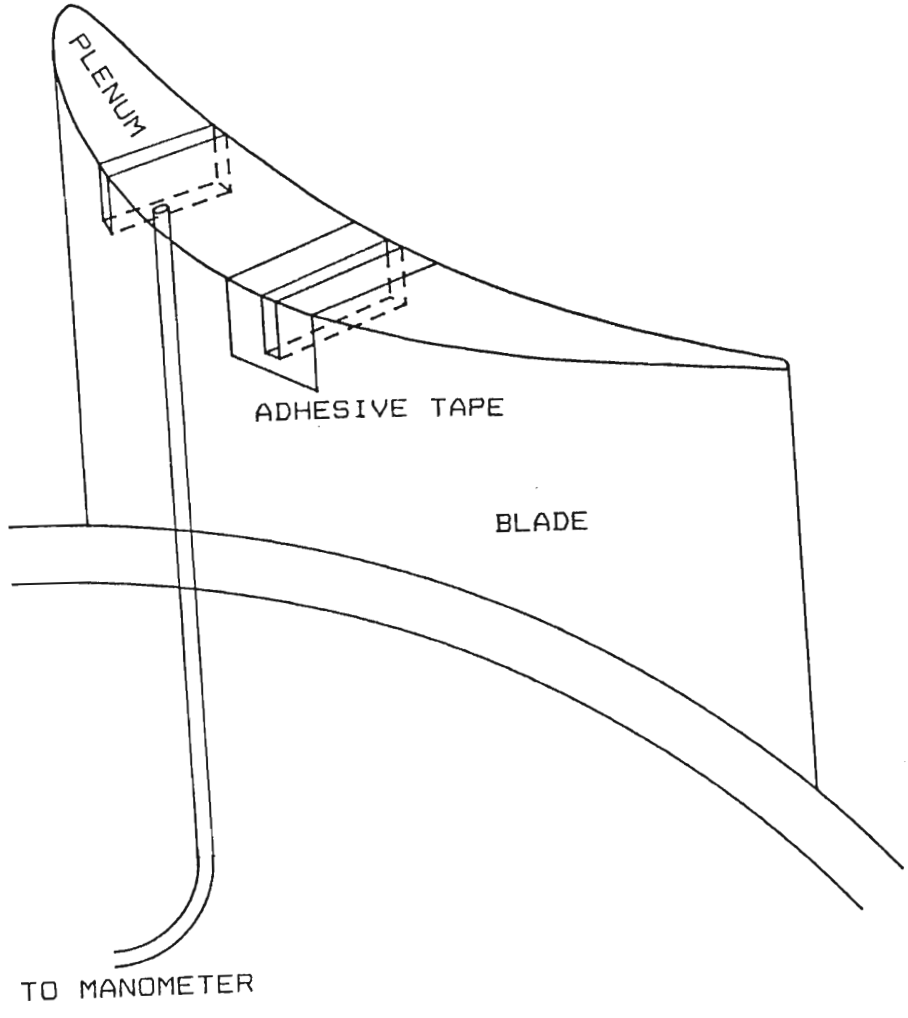

FIGURE 3.5 INSTRUMENTED BLADE FOR STATIC PRESSURE MEASUREMENTS

from the hub through the nose cone to a multitube manometer (see Figure 3.6). The slots were taped over and micropunctured for high resolution static pressure measurements of up to 5 pressure tappings per millimeter. After puncturing, the position of a tapping was measured with a graduated hand held magnifier with a resolution of 0.1 mm. The used holes were blocked using "Lock Tite" non hardening gasket sealer. The blade was instrumented with 19 slots at intervals of 5% chord as shown in Figure 3.7.

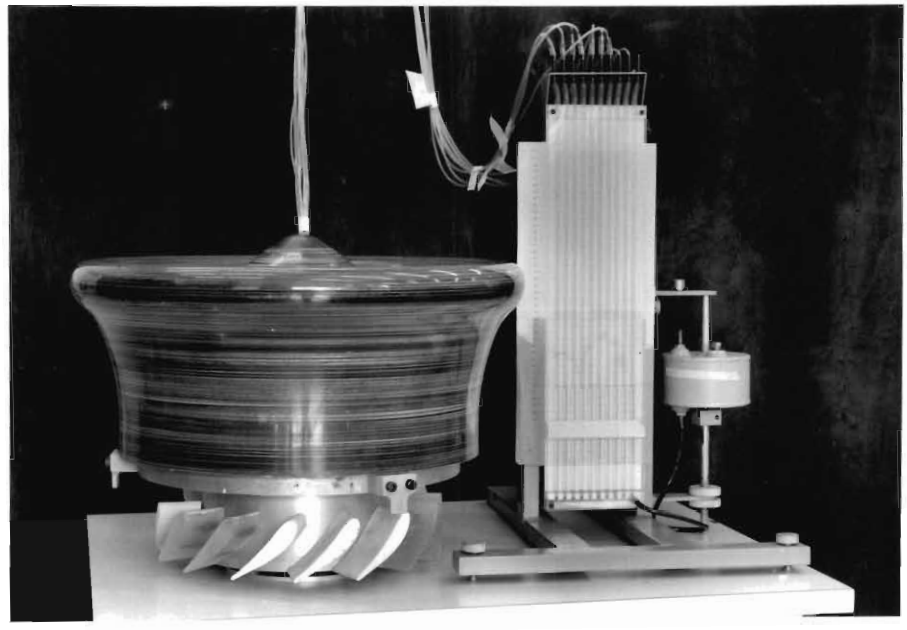

FIGURE 3.6 ANNULAR CASCADE AND MANOMETER

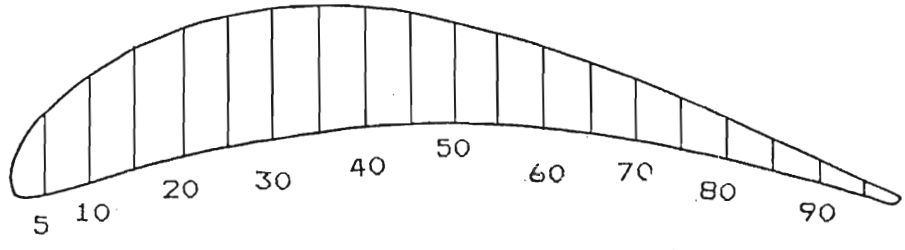

FIGURE 3.7 CHORDWISE LOCATION OF BLADE TIP STATIC PRESSURE MEASUREMENT SLOTS

CHAPTER 4

LINEAR CASCADE AND APPARATUS

In the second part of this experimental program the performance and loss development for various tip geometries were measured using 3 hole and 5 hole pitot static probes in a linear cascade. Traverses were done at the gap exit, the blade exit plane and along the endwall.

4.1 LINEAR CASCADE, BLADES, AND TIP GEOMETRIES

An existing wooden linear cascade was improved using aluminum and perspex walls attached to the wooden bellmouth inlet as shown in Figure 4.1. The inlet dimensions of the cascade were 260mm x 650mm and it was driven from the outlet of a large open section wind tunnel as shown schematically in Figure 4.2.

A proprietary blade profile, as used by Bindon (1986) in previous tip clearance studies was selected so that direct comparison of results would be possible. Six blades of 186 mm chord were used to give a channel between blades 3 and 4 for measurements. The cascade Reynolds number based on chord and cascade exit velocity was 470 000.

Jelutong wood blades were CNC machined in sections of 50 mm. Each blade was made up of five sections to give a blade length of 250 mm. The sections (drilled in a spanwise direction) were pushed onto two 8 mm studs with threaded ends and shoulders for

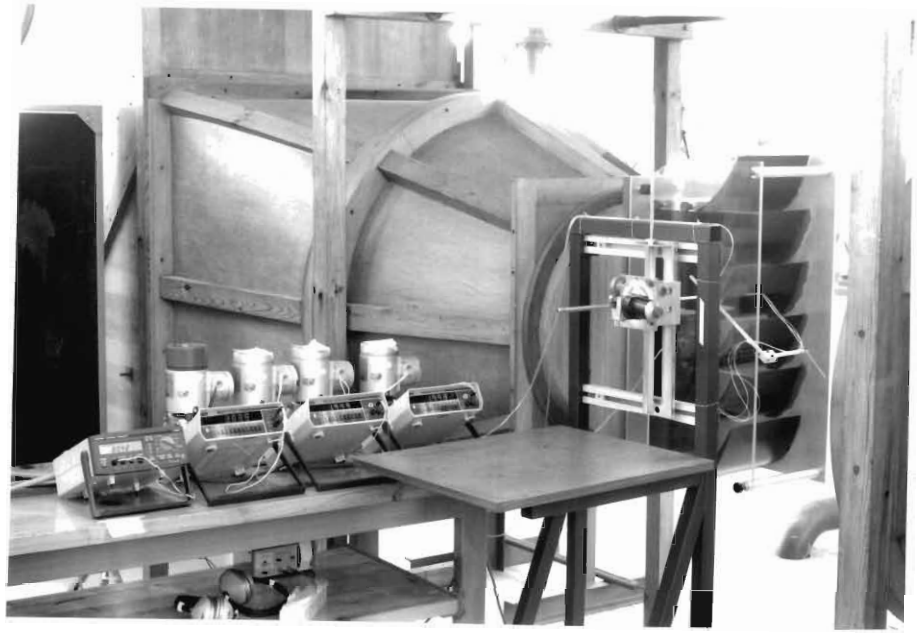

FIGURE 4.1 LINEAR CASCADE AND INSTRUMENTATION

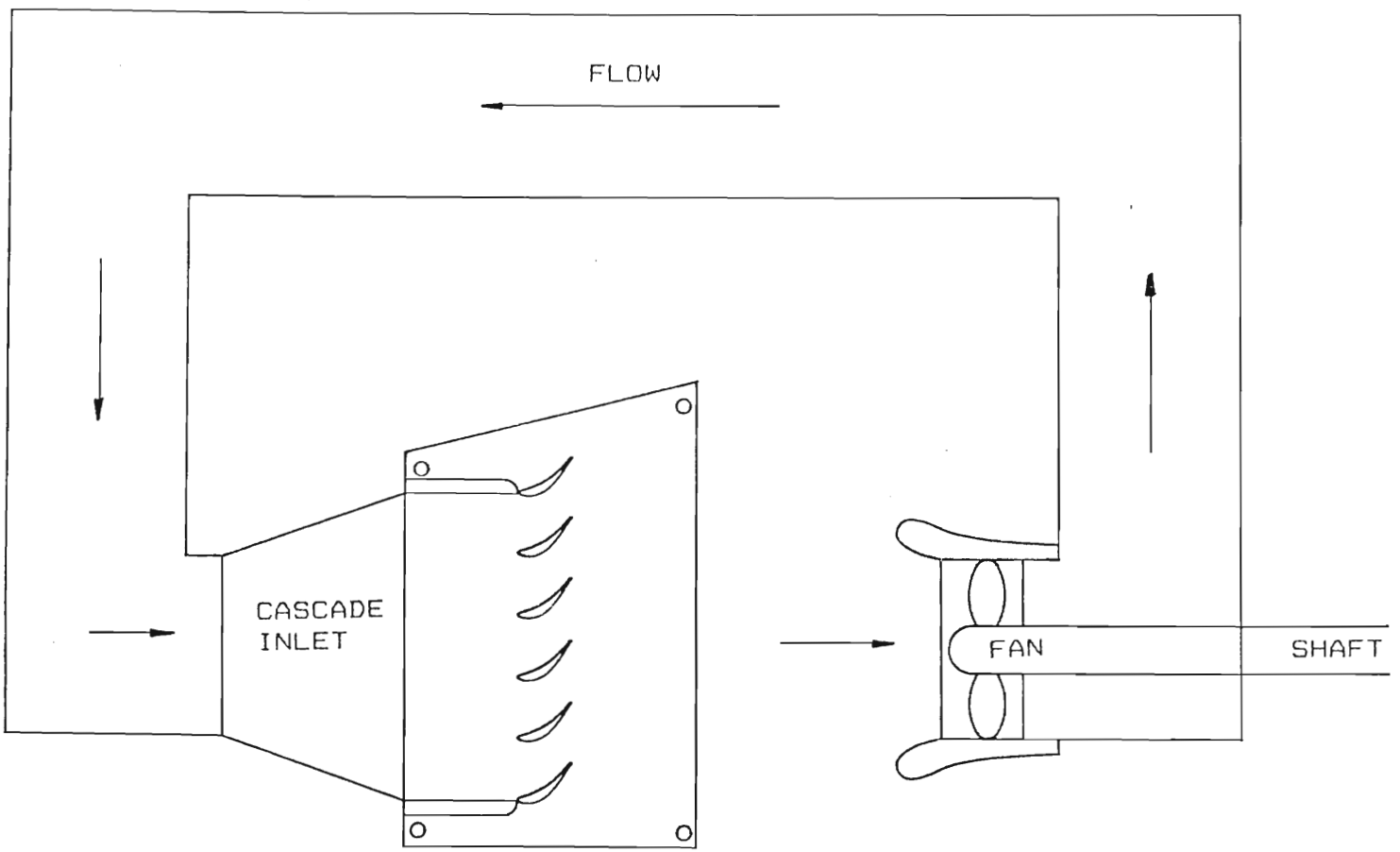

FIGURE 4.2 SCHEMATIC OF OPEN SECTION WIND TUNNEL AND CASCADE

mounting on the hub side of the cascade. Spacers were used for adjusting the tip clearance. In order to stop the perspex wall from deflecting, and thus altering the tip clearance, 4 studs were fitted in the tips of the second and fourth blades from the top. As is illustrated in Figure 4.3 these studs protruded through the endwall allowing lock nuts to be used for fine setting of the tip clearance.

As illustrated in Figure 4.4 the following four blade tip geometries were used.

1) Square tip with zero clearance.
2) Square tip with 2.5% chord clearance.
3) Radiused pressure corner with radius=2.5 x clearance to avoid separation bubble and 2.5% chord clearance.
4) Contoured or radiused suction side squealer with 2.5% chord clearance to avoid bubble formation and to deflect the flow radially. (see Figure 4.4 for profile)

To change the tip geometry of the blades only the tip segments of the four center blades were replaced.

4.2 MEASUREMENT GRID

A 2 dimensional grid was defined in the center channel for taking measurements. Figure 4.5 shows the grid definition in the axial/tangential plane. The spacing for this grid was selected using data obtained from Bindon 1988. The grid was made denser in areas where higher loss was expected. Additional points were added between two grid points if there was a large difference in

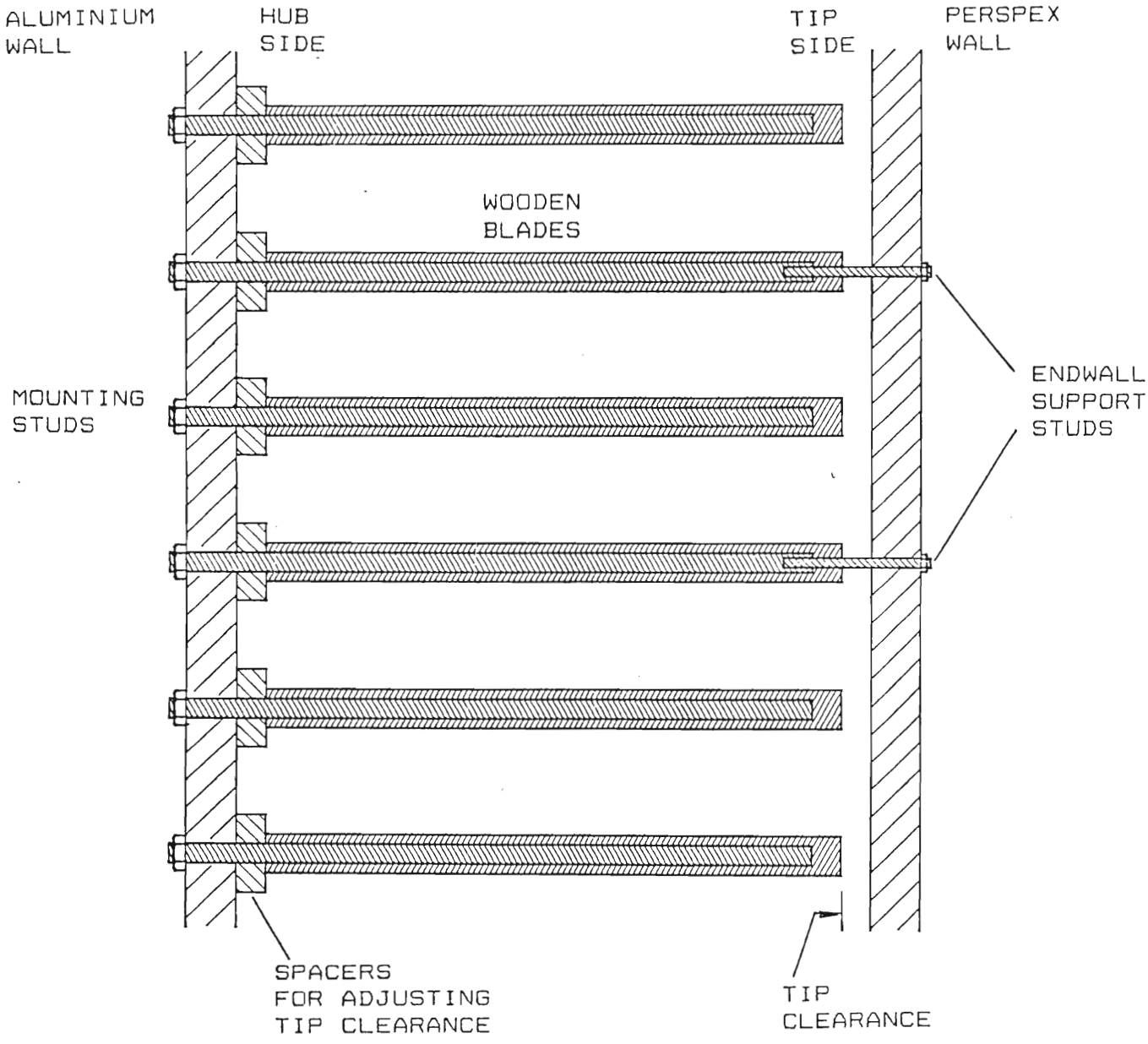

FIGURE 4.3 LINEAR CASCADE WITH TIP CLEARANCE AND TRANSPARENT ENDWALL

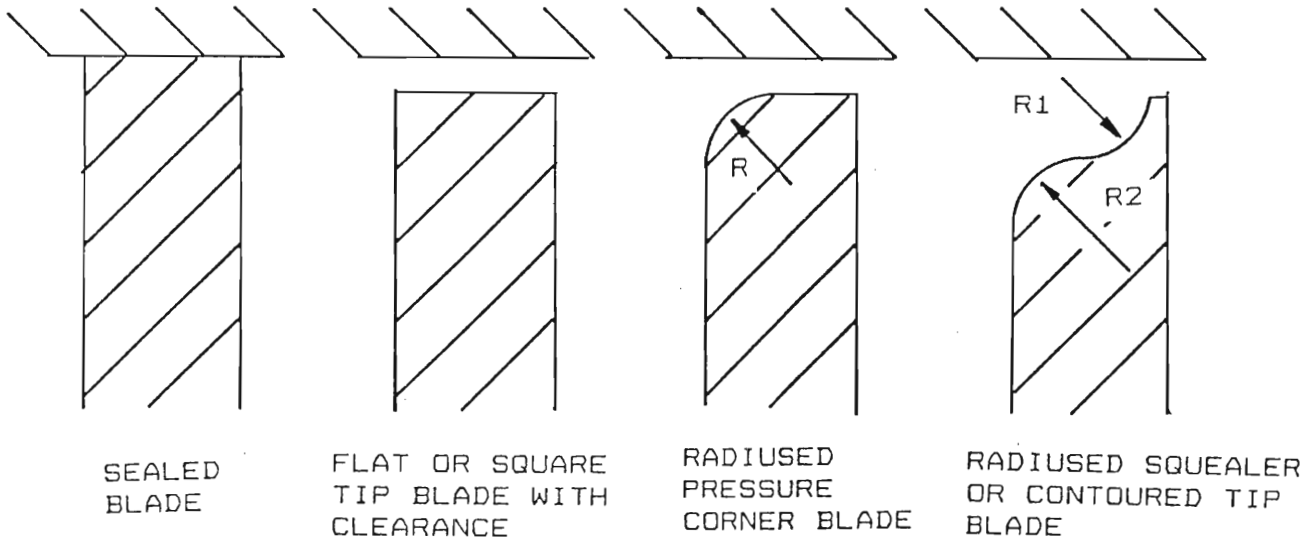

FIGURE 4.4 THE VARIOUS BLADE TIP GEOMETRIES TESTED IN THE LINEAR CASCADE

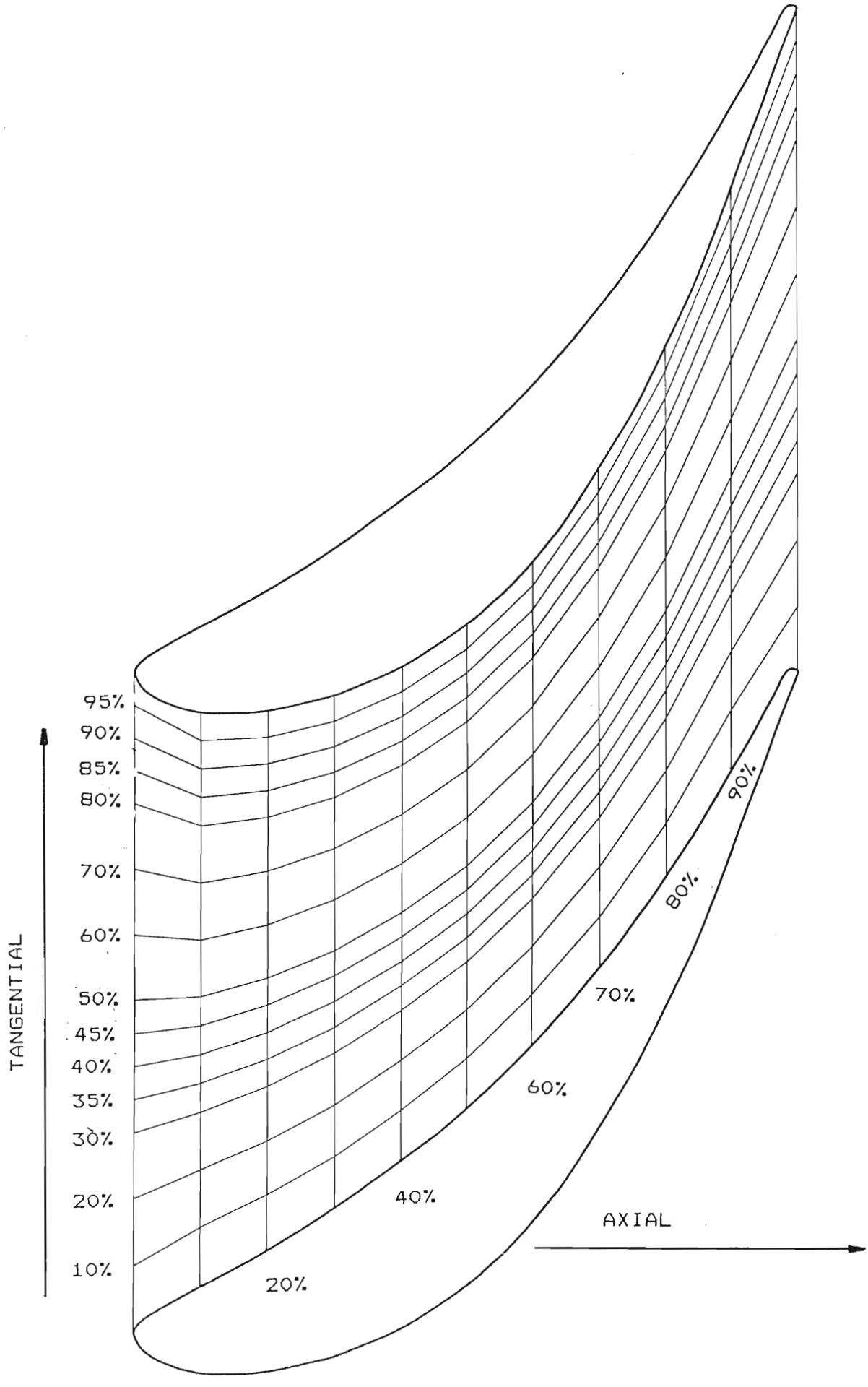

FIGURE 4.5 ENDWALL MEASUREMENT GRID

loss from one grid point to the next. At each grid point the probe was traversed in the radial direction (i.e. into the page) from the endwall up to where zero loss occurred. The spacing for the radial direction was determined during flow measurement and depended on the change in loss or flow angle from the last point. (i.e. if a relatively large difference in loss or flow angle was found from one point to another then more points were added in between.)

The flow exiting the clearance gap was measured on a grid as shown in Figure 4.6. At each grid point the probe was traversed from the endwall to the tip of the blade.

4.3 PROBES

Three probes were used to traverse the cascade flow field. Two of them were 3 hole cobra probes and the third was a 2 hole probe oriented at 90 degrees to the 3 hole probes as shown in Figure 4.7. The 3 hole probes were used to obtain 2 dimensional data of the flow in the axial/tangential plane. The 2 hole probe was used with either of the 3 hole probes to simulate a 5 hole probe so that the radial component of the flow could be measured.

The null and semi-null yaw mode methods were used with the 3 hole probes. In the null yaw mode the probe was rotated about its axis until it faced directly into the flow (i.e. the two outer holes record the same pressure). The flow angle was then recorded from the traverse mechanism. The probe pressures were also

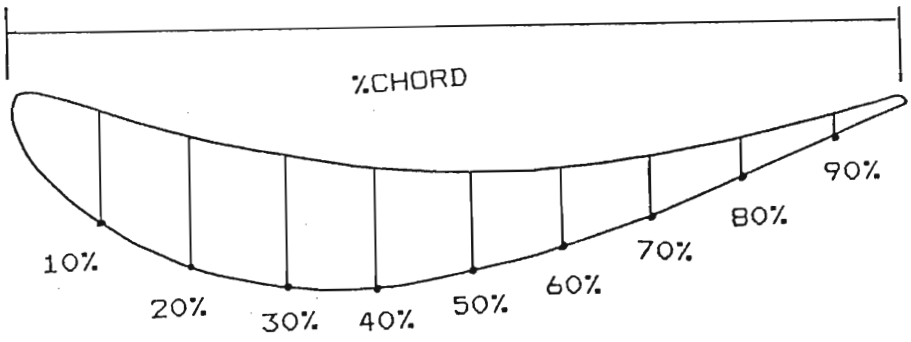

FIGURE 4.6 GAP EXIT MEASUREMENT STATIONS AT 10% CHORDWISE INTERVALS

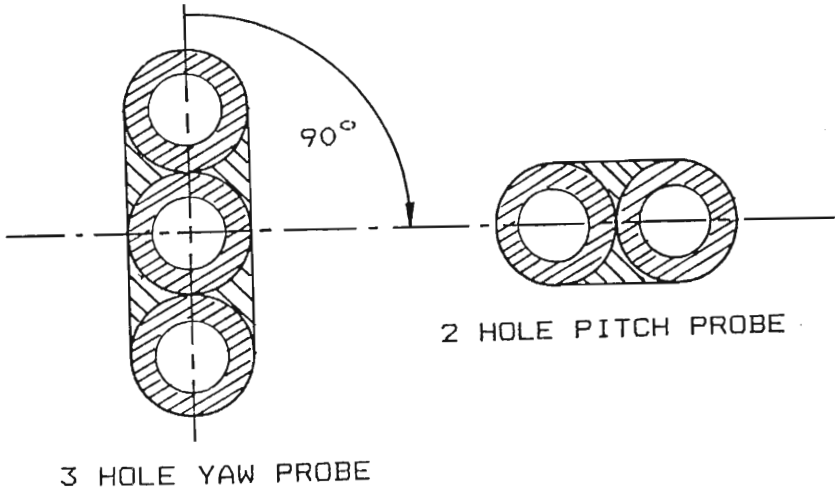

FIGURE 4.7 ORIENTATION OF 2 HOLE PITCH PROBE RELATIVE TO THE 3 HOLE YAW PROBE

recorded to enable calculation of the static and dynamic pressure of the flow. With semi-null yaw mode the probe was rotated until the flow was approximately facing the probe and the pressures of each tube and the probe angle were recorded. The calibration curves were then used to calculate the exact angle, static pressures and dynamic pressures of the flow. The method used to calibrate the probes is discussed in Chapter 5.

At each measurement point the 2 hole probe was rotated to the angle obtained by the 3 hole probe and the two pressures were measured to enable calculation of the radial component of the flow.

All three probes were mounted on a traverse mechanism which rotated for null yawing and traversed in the radial direction. The traverse mechanism was mounted on a stand with slides for movement in the axial and tangential directions as shown in Figure 4.8.

4.3.1 3 Hole yaw probe (exit plane)

A 3 hole cobra probe mounted on a sting as shown in Figure 4.9 accessed the exit plane from the outlet of the cascade. The axis of rotation for this probe was through the center of the head so that the probe head remained at one position in space during null yawing. A schematic of the probe head is shown in Figure 4.10.

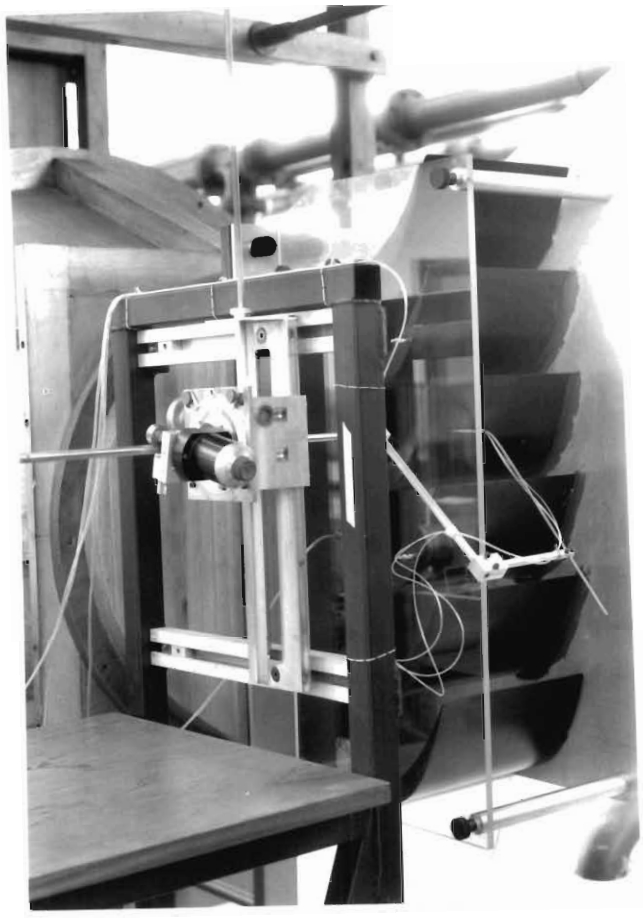

FIGURE 4.8 TRAVERSE MECHANISM STAND WITH SLIDES AND EXIT PLANE PROBE

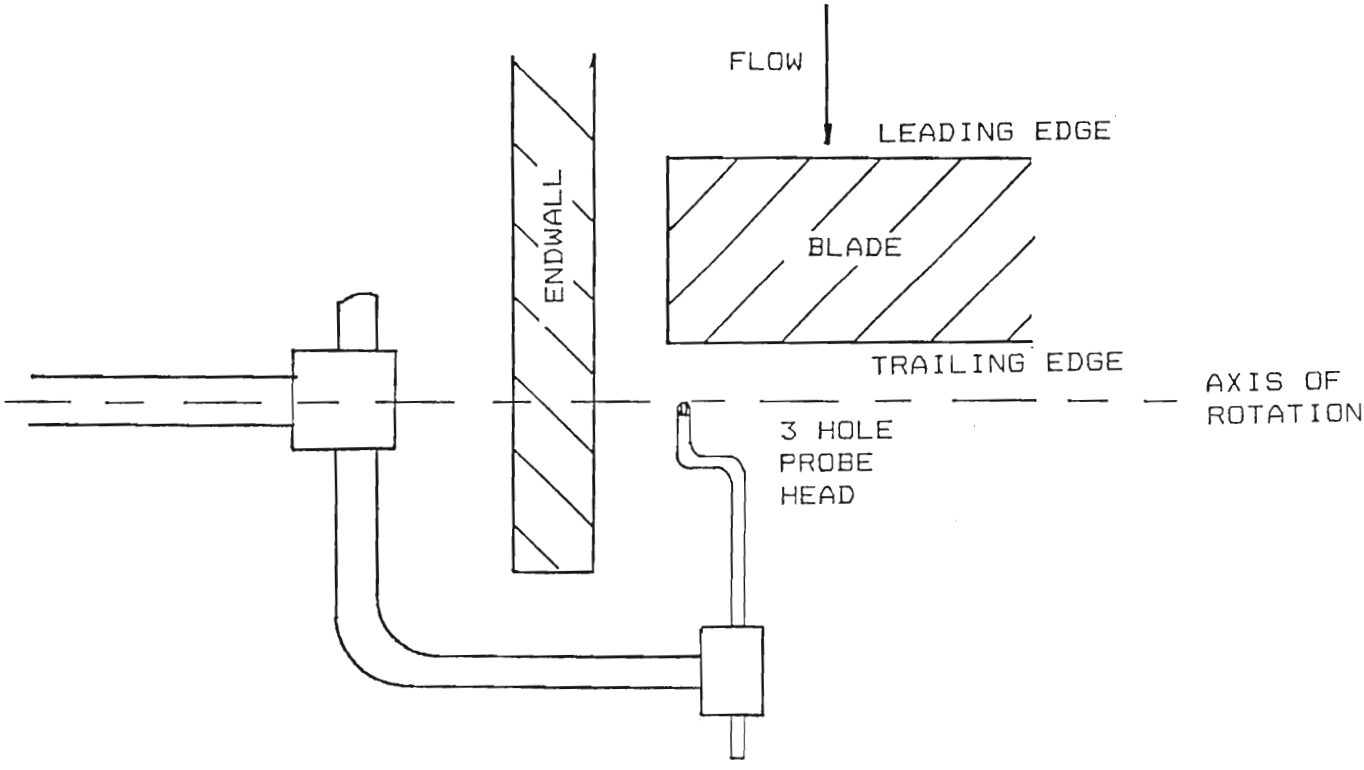

FIGURE 4.9 EXIT PLANE PROBE AND STING

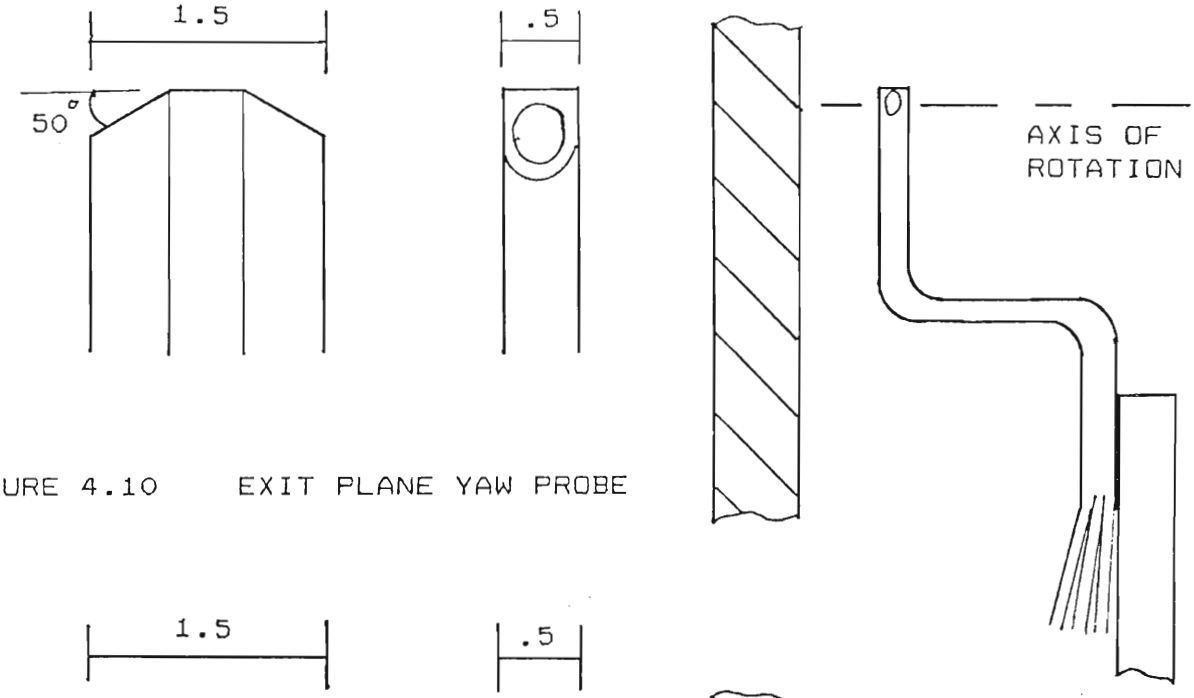

FIGURE 4.10 EXIT PLANE YAW PROBE

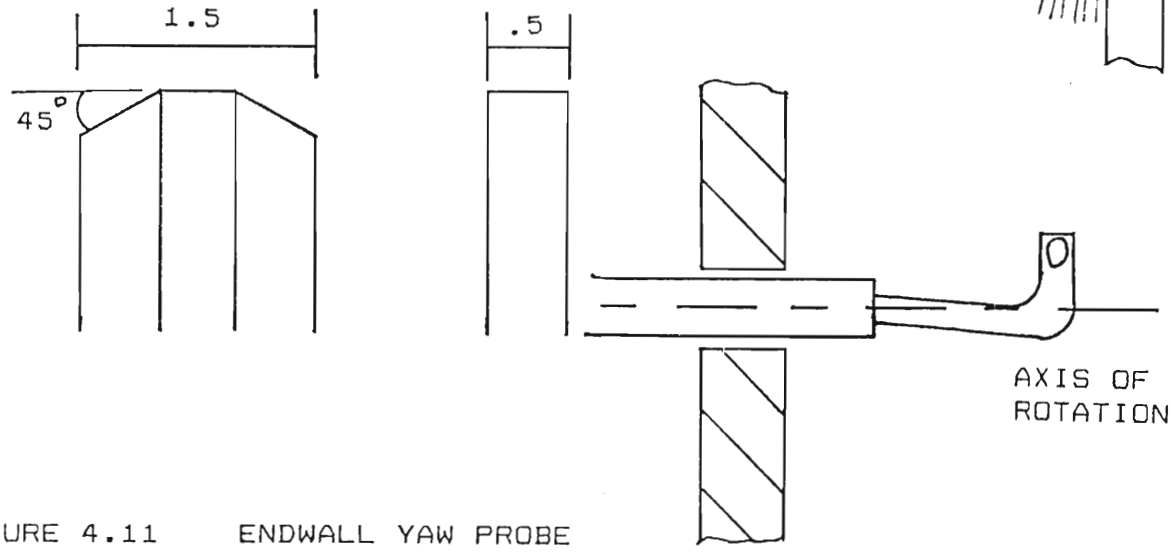

FIGURE 4.11 ENDWALL YAW PROBE

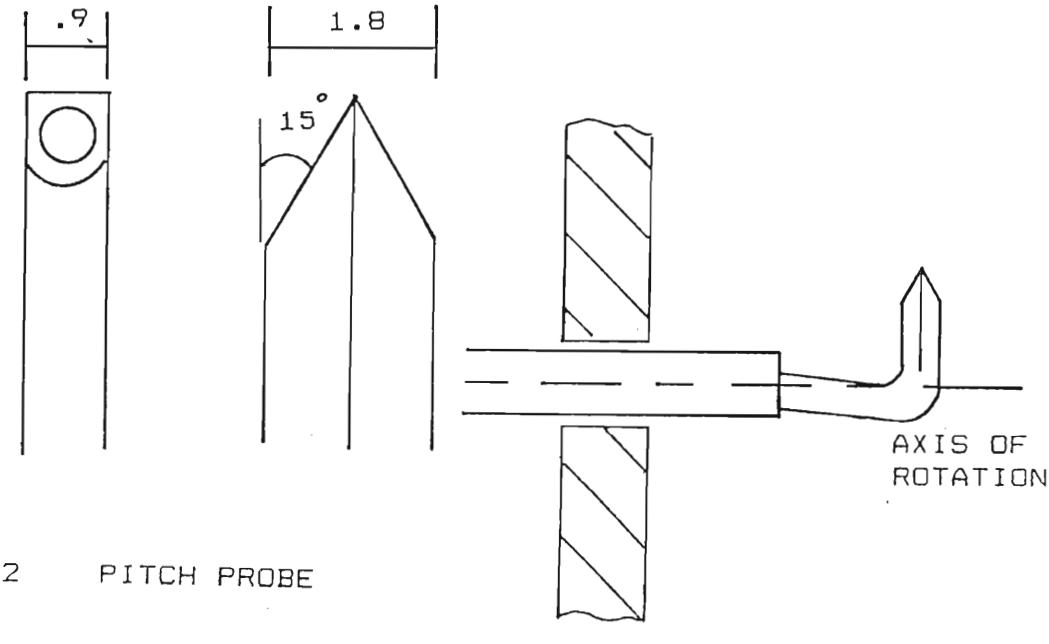

FIGURE 4.12 PITCH PROBE

4.3.2 3 Hole yaw probe (endwall and gap exit)

This probe, in the shape of tightly radiused gooseneck as shown in Figure 4.11, was used (through holes drilled in the endwall at the traverse stations) to access the endwall flow and the gap exit flow. A limitation of this probe was that the tip moved about a radius of 2.5 mm when used in the null or semi null yaw mode but it could be traversed right up to the endwall.

4.3.3 2 Hole pitch probe

The 2 hole pitch probe was orientated at 90^0 to the 3 hole yaw probes (i.e. it measured the radial component of the flow). This probe was also in the shape of a tightly radiused gooseneck (Figure 4.12) and accessed the endwall flow in a similar manner to the above probe. As mentioned earlier this probe was used in conjunction with the above two probes to give 5 hole probe data. During traverses the 2 hole pitch probe was null yawed using data obtained from the 3 hole yaw probes. A 30^0 nose angle made this probe sensitive over a wide angle enabling it to be used in the fixed mode in the radial direction.

4.4 Data acquisition, pressure transducers, and computational facilities

Four Fuji 250 mm H_20 4-20mA differential pressure transducers were used for measuring probe pressures. The transducers were connected in series with a shunt resistor and a constant voltage power supply as shown in Figure 4.13. The voltage across the

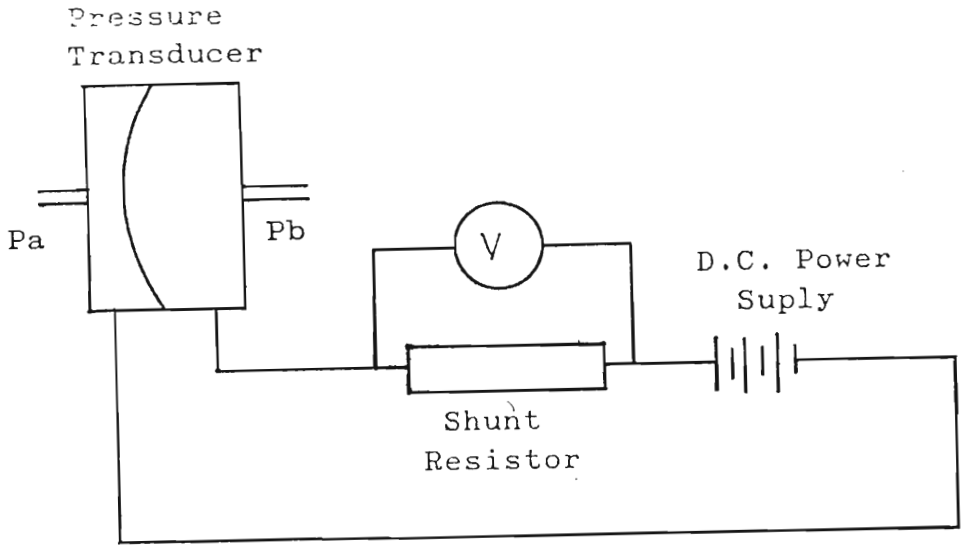

FIGURE 4.13 PRESSURE TRANSDUCER CONNECTION TO VOLT METER

shunt resistor was read by three Keithley and one Phillips voltmeters with HP-IB parallel outputs and connected directly to an HP 86 micro-computer. Traverse positions and angle were entered manually while voltages (function of pressures) were read automatically. At each traverse point several readings were taken and an average was calculated. The data was stored on floppy disc at the end of each radial traverse. (Program listed in Appendix 2.A)

An HP 86 micro computer was used to convert the raw data to dimensionless numbers and to store them on floppy disc (Appendix 2.B). A program by Bindon (1988b) that converted the stationary data to the rotating frame of reference was used to integrate the data. The method used in this program is discussed in Chapter 6. An HP 9000 217 and an IBM PC compatible were used for curve fitting the calibration data for pressure transducers and probes.

CHAPTER 5

PRESSURE TRANSDUCER CALIBRATION, PROBE CALIBRATIONS, CONNECTIONS AND CALCULATION OF DIMENSIONLESS COEFFICIENTS

5.1 Pressure transducer calibration

A total of four pressure transducers were used with the linear cascade. Three transducers were used for measuring the probe pressures and one for measuring inlet total pressure. The transducer zeroes were adjusted to give sufficient range in the positive and negative directions. Each transducer was calibrated using a micro manometer and a syringe (to apply pressures). A computer program was used to automatically read the voltages from the voltmeters (Appendix 3.A). Voltage readings were taken at various pressures for each pressure transducer. A linear regression was done to fit a straight line equation that related voltage across the shunt resistor to pressure. A sample correlation was also calculated to indicate "goodness" of fit of the straight line curve.

The effect of temperature on the pressure transducers was examined by calibrating the transducers at various room temperatures that represented the range encountered while taking measurements. The calibration constants for 3 temperatures are shown in Appendix 3.B. The calibrations done at a room temperature of 23.8 C were used for all the experiments since the maximum error due to temperature drift was seen to be less than one percent.

5.2 Connections for minimum error

When two large numbers are subtracted to obtain a relatively small difference, then the percentage error and zero error are amplified for the difference. This is best illustrated by the following example. If two transducers read voltages of 12v and 10v with an error ±1v (±8% and 10% error respectively) then the difference would be 2v with a maximum possible error ±2v (±100% error). On the other hand if the difference was read directly by one transducer with an error of ±1v then the resultant maximum error would be only ±50%. In order to minimize this error the pressure transducers and probes were connected as shown in Figure 5.1 so that the required pressure differences were measured directly.

5.3 3 Hole Probe Measurement and Calibrations

The three unknowns that must be determined for two dimensional flow measurements are static pressure, dynamic pressure and flow direction or yaw angle. Using a 3 Hole pitot static probe the three unknowns can be calculated. The pressure measured by any tube of the probe represents the static pressure plus a fraction of the dynamic pressure depending on the flow angle.

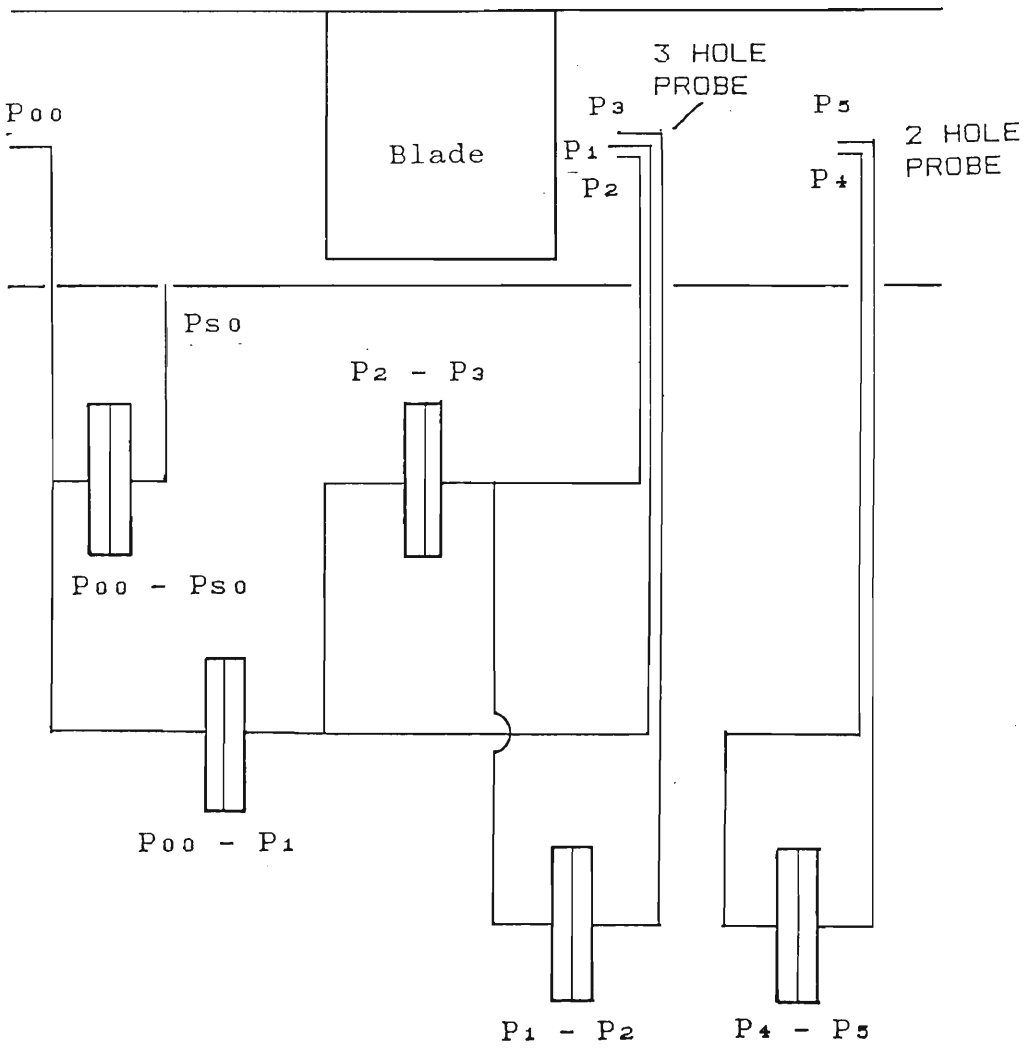

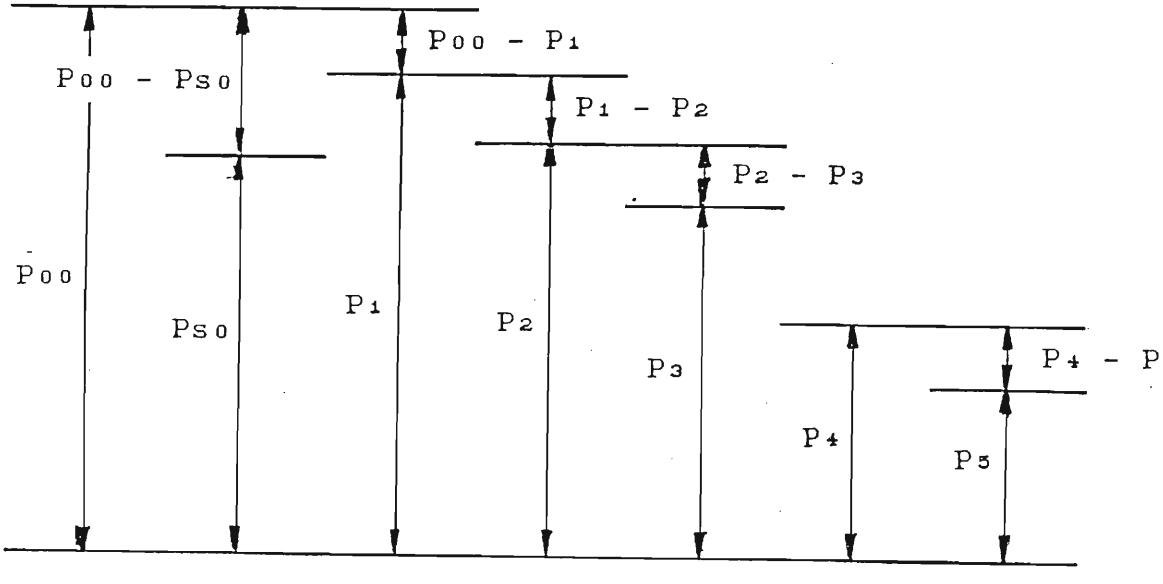

FIGURE 5.1 PRESSURE TRANSDUCER AND PROBE CONNECTIONS FOR MINIMUM ERROR.

The pressure measured by any tube of the probe is :

$$P_i = P_S + K_i q \qquad (i = 1, 2, 3) \qquad (1)$$

$$\text{therefore} \quad K_i = \frac{P_i - P_s}{q} = f(\psi) \qquad (2)$$

where ψ = yaw angle

$$\text{define} \quad K\psi 2 = \frac{P1 - P2}{P1 - P3} \qquad (3)$$

During calibration P1, P2, P3, Pt, Ps was recorded for various yaw angles ψ. Kψ2, K2 and K1 where calculated and plotted against ψ.

$$\text{from (1)} \quad P1 = Ps + K1q \qquad (4)$$

$$\text{and} \quad P2 = Ps + K2q \qquad (5)$$

$$\text{thus} \quad P1 - P2 = (K1 - K2)q \qquad (6)$$

$$\text{or} \quad q = \frac{(P1 - P2)}{(K1 - K2)} \qquad (7)$$

$$\text{from (4) \& (7)} \quad Ps = P1 - K1 \frac{(P1 - P2)}{(K1 - K2)} \qquad (8)$$

Since the probes were used in either null or semi-null yaw modes it was only necessary to calibrate them over a narrow range of yaw angles. The probes were calibrated over a range of -10 degrees to 10 degrees of yaw angle. The calibration curves are shown in Appendix 3.C. The dimensionless coefficients calculated as shown below were used to define the flow at each measurement point.

Loss coefficient:

$$Cl = \frac{\Delta p_0}{q_0} \qquad \text{(defined)}$$

$$= \frac{P_{00} - Pt}{q_0}$$

Now if probe is semi-null yawed then $Pt \approx P_1$

therefore $$Cl = \frac{P_{00} - P_1}{q_0} \qquad (9)$$

Static pressure coefficient:

$$Cp = \frac{P_{s0} - Ps}{q_0} \qquad \text{(defined)}$$

substituting (8) $$= \frac{P_{s0} - P_1 + K_1 \frac{(P_1 - P_2)}{(K_1 - K_2)}}{q_0}$$

therefore $$Cp = \frac{-(P_{00} - P_{s0}) + (P_{00} - P_1) + K_1 \frac{(P_1 - P_2)}{(K_1 - K_2)}}{q_0}$$

Velocity coefficient:

$$Cv = \frac{q}{q_0} \qquad \text{(defined)}$$

substituting (7) $$= \frac{(P_1 - P_2)}{q_0 (K_1 - K_2)}$$

5.4 5 Hole Probe Calibration and measurement method

In order to define the flow in three dimensions, two additional pressure tappings are required in the pitch plane so that the pitch angle can be calculated. As mentioned earlier in Chapter 4, two probes were used to give 5 Hole probe data, the 3 Hole probes were used to obtain data in the yaw direction and a 2 Hole probe was used in the pitch direction. The calibration curves for the 5 Hole probe are shown in Appendix 3.D.

The method used at each measurement point was as follows:

1) Null yaw the 3 Hole probe (i.e. $P_1 - P_2 = 0$)

2) Record ψ, $(P_1 - P_2)$, $(P_{00} - P_{s0})_{yaw}$

3) Set 2 Hole pitch probe at ψ obtained from 3 Hole yaw probe

4) Record $(P_4 - P_5)$, $(P_{00} - P_{s0})_{pitch}$

The tunnel inlet dynamic pressure $(P_{00} - P_{s0})$ was recorded for both probes to enable a correction of the error due to fluctuations of the tunnel wind speed. The value of $(P_4 - P_5)$ was adjusted to be used with the 3 Hole probe to create 5 Hole data as follows.

$$(P_4 - P_5)_{5hole} = (P_4 - P_5) \frac{(P_{00} - P_{s0})_{yaw}}{(P_{00} - P_{s0})_{pitch}}$$

5 Hole Probe Calibration

Define the following coefficients:

$$K\theta = \frac{P_4 - P_5}{P_1 - P_2} \tag{10}$$

$$F(\theta) = \frac{P_t - P_s}{P_1 - P_2} \tag{11}$$

$$G(\theta) = \frac{P_1 - P_t}{P_t - P_s} \tag{12}$$

During calibration $K\theta$, $F(\theta)$ and $G(\theta)$ were plotted against θ.

5 Hole probe data analysis and dimensionless coefficients.

Firstly calculate $K\theta = \frac{P_4 - P_5}{P_1 - P_2}$ and find θ from $K\theta$ vs θ plot

Then find $F(\theta)$ and $G(\theta)$ from plots of $F(\theta)$ and $G(\theta)$ vs θ respectively.

From (11) & (12) $F(\theta)\ (P_1 - P_2) = \frac{P_1 - P_2}{G(\theta)}$ (13)

therefore $\underline{P_t = P_1 - F(\theta)\ G(\theta)\ (P_1 - P_2)}$ (14)

rearanging (11) $P_s = P_t - F(\theta)\ (P_1 - P_2)$ (15)

substituting (14) & (15)

$$\underline{P_s = P_1 - F(\theta)\ (P_1 - P_2)\ (1 + G(\theta))} \tag{16}$$

Loss coefficient :

$$Cl = \frac{P_{00} - P_t}{q_0} \qquad \text{(defined)}$$

substituting (14)

$$= \frac{(P_{00} - P_1) + F(\theta)\, G(\theta)\, (P_1 - P_2)}{q_0}$$

Static pressure coefficient :

$$Cp = \frac{P_{s0} - P_s}{q_0} \qquad \text{(defined)}$$

substituting (16)

$$= \frac{(P_{00} - P_1) - (P_{00} - P_{s0}) + F(\theta)\, (P_1 - P_2)\, (1 + G(\theta))}{q_0}$$

Velocity coefficient :

$$Cv = \frac{P_t - P_s}{q_0} \qquad \text{(defined)}$$

substituting (14) & (16)

$$= \frac{P_1 - F(\theta)\, G(\theta)\, (P_1 - P_2) - P_1 + F(\theta)\, (P_1 - P_2)\, (1 + G(\theta))}{q_0}$$

$$= \frac{F(\theta)\, (P_1 - P_2)\, (1 + G(\theta) - G(\theta))}{q_0}$$

$$= \frac{F(\theta)\, (P_1 - P_2)}{q_0}$$

CHAPTER 6

CALCULATIONS AND INTEGRATION OF RESULTS

6.1 TRANSFORMATION FROM STATIONARY TO ROTATING FRAME OF REFERENCE FOR EVALUATION OF BLADE TIP PERFORMANCE

Rotor blades are often evaluated in stationary linear cascades because of the ease of taking measurements and cost factors. One way of evaluating a stationary cascade is by determining the loss in total pressure which is also a measure of increased entropy. This method however, does not give the full picture of the rotor performance since it ignores the ability of the rotor to deflect the flow or extract work from the flow. Bindon (1988b) developed a method of converting stationary cascade data into rotor data by adding the blade speed vector U to the inlet and outlet velocity as shown in Figure 6.1, to obtain simulated absolute inlet and outlet velocities. This provided a better basis for evaluating tip clearance geometries than merely considering loss or gap discharge coefficient. Bindon's method of evaluating stationary cascade data as if it were a rotor is presented below. The programs are listed in Appendix 4.

For compressible flow and using Figure 6.2 three efficiencies may be defined as follows:

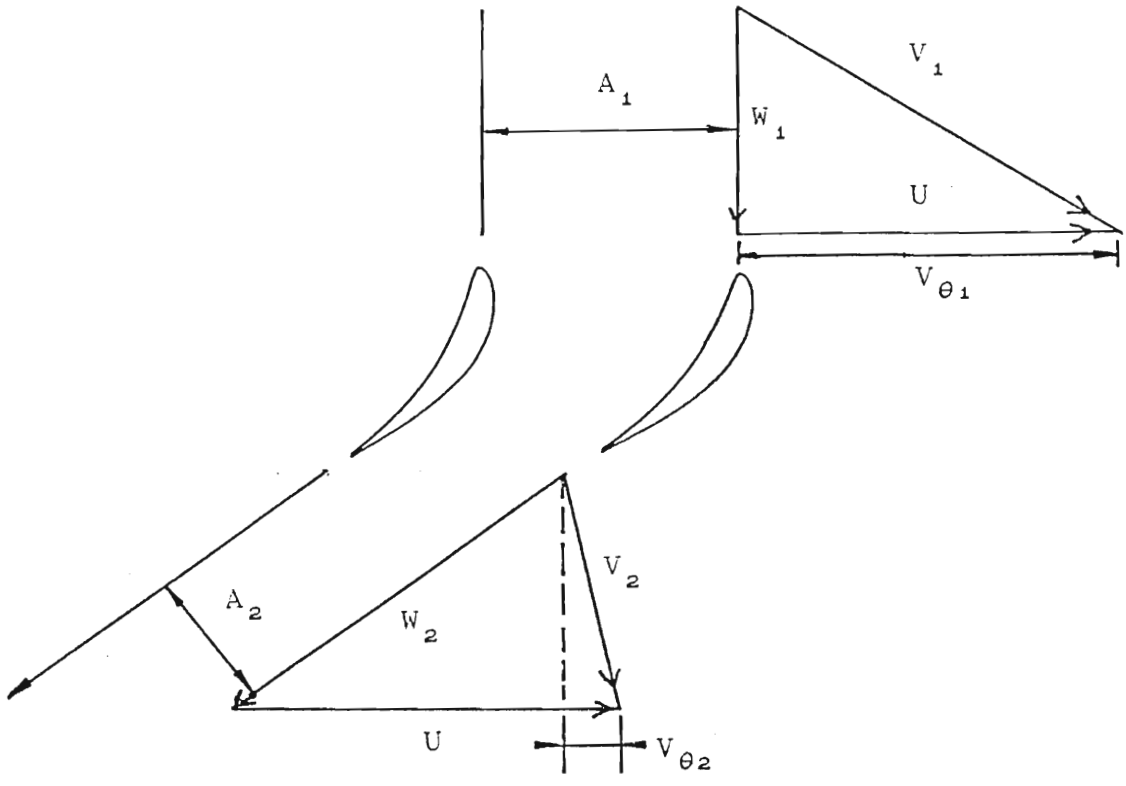

FIGURE 6.1 STATIONARY CASCADE WITH INLET VELOCITY W_1 AND OUTLET VELOCITY W_2 CONVERTED INTO A SIMULATED ROTOR BY ADDING BLADE SPEED U TO CREATE SIMULATED INLET AND OUTLET ABSOLUTE VECTORS V_1 AND V_2.

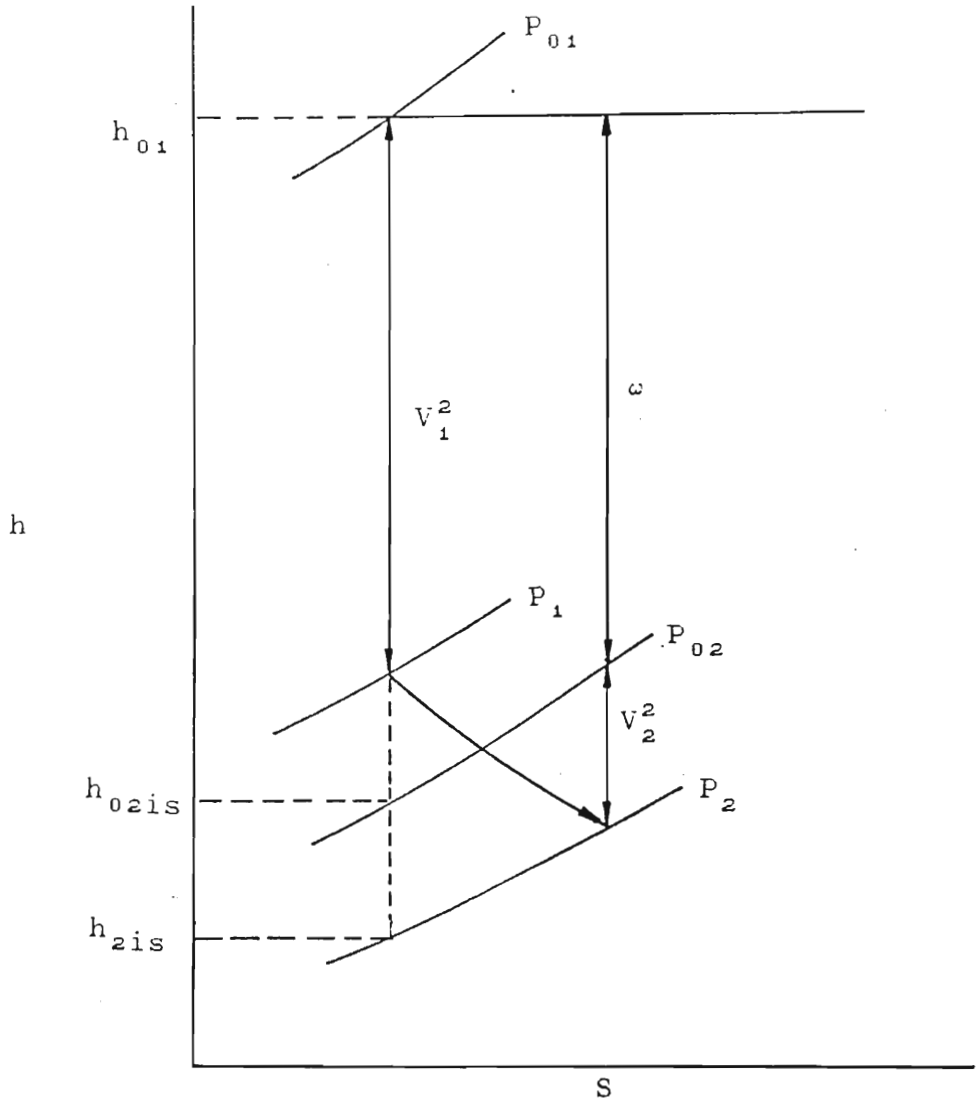

FIGURE 6.2 ENTHALPY ENTROPY DIAGRAM

(I) Total to Total Efficiency

$$\eta_{tt} = \frac{\omega}{h_{01} - h_{02is}}$$

Here the denominator is the ideal work in a loss free rotor with the same total outlet pressure as in the real rotor, or the same outlet static pressure and velocity. This definition should be used in multi-stage turbines where the exhaust velocity from a stage is not lost.

(II) Total to Static Efficiency

$$\eta_{ts} = \frac{\omega}{h_{01} - h_{2is}}$$

Here the denominator is the work from a loss free rotor with the same static outlet pressure and with no kinetic energy in the outlet flow, (ie the outlet flow has no velocity).

(III) Ideal Efficiency

$$\eta_{id} = \frac{\omega}{h_{01} - h_{2is} + .5V^2_{2id}}$$

The denominator is defined in terms of the same static outlet pressure and an ideal outlet velocity. This will have the effect of penalizing a rotor with a high outlet velocity.

The above efficiencies are all rotor efficiencies whereas normally a stage efficiency is calculated that also includes the nozzle loss.

For incompressible flow, the energy balance for the hypothetical rotor is

$$P_1 + .5\rho V_1^2 = P_2 + .5\rho V_2^2 + \Delta p_0 + \rho\omega \qquad (1)$$

The above equation can be applied to a stream tube of fluid. To apply this globally to a flow that has variations within the inlet and outlet flow fields the equation must be written in terms of mass averaged quantities.

The incompressible efficiencies are defined in terms of ideal work when the appropriate pressure differences are applied to a loss free rotor.

$$\eta_{tt} = \frac{\rho\omega}{P_{01} - P_{02}} = \frac{\rho\omega}{\rho\omega + \overline{\Delta p}_0} \qquad (2)$$

$$\eta_{ts} = \frac{\rho\omega}{P_{01} - P_2} = \frac{\rho\omega}{\rho\omega + \overline{\Delta p}_0 + .5\rho\overline{V}_2^2} \qquad (3)$$

$$\eta_{id} = \frac{\rho\omega}{P_{0_1} - P_2 + .5\rho\, V_{2id}^2} = \frac{\rho\omega}{\rho\omega + \overline{\Delta p}_0 + .5\rho\overline{V}_2^2 - .5\rho V_{2id}^2} \qquad (4)$$

Each term in the above equations may be non-dimensionalised with the free stream cascade inlet velocity head $.5\rho W^2$ to obtain the following coefficients.

C_ω = work transfer coefficient = $\dfrac{\rho\omega}{.5\rho W^2}$

$\overline{C}_L$ = mean total pressure loss coefficient for the whole flow field

$$= \frac{\overline{\Delta p}_0}{.5\rho W^2}$$

$\overline{C}_{v2}$ = mean velocity ratio for the whole flow field

$$= \frac{\overline{V}_2}{W}$$

C_{v2id} = ideal velocity ratio = $\dfrac{V_{2id}}{W}$

The above quantities are all mass averaged and are determined by integration of the whole flow field. The efficiencies may be written as follows:

$$\eta_{tt} = \frac{C_\omega}{C_\omega + \overline{C}_L} = \frac{1}{1 + \dfrac{\overline{C}_L}{C_\omega}}$$

$$\eta_{ts} = \frac{C_\omega}{C_\omega + \overline{C}_L + \overline{C}_{v2}^2 - C_{v2id}^2} = \frac{1}{1 + \dfrac{\overline{C}_L}{C_\omega} + \dfrac{\left\{\overline{C}_{v2}^{\,2} - C_{v2id}^{\,2}\right\}}{C_\omega}} \qquad (5)$$

$$\eta_{id} = \frac{C_\omega}{C_\omega + \overline{C}_L + \overline{C}_{V2}^{\,2} + C_{v2id}^2} = \frac{1}{1 + \dfrac{\overline{C}_L}{C_\omega} + \dfrac{\left\{\overline{C}_{v2}^2 + C_{v2id}^2\right\}}{C_\omega}} \qquad (6)$$

The efficiency of the rotor normally takes into account the whole rotor passage from hub to tip. In order to make the efficiency more sensitive to tip clearance losses, only the endwall zone affected by leakage is considered (see Figure 6.3). In Bindon (1988a) a cascade inlet blade height z_1 of 25% chord was found to include the zone affected by tip clearance.

The exit blade height z_2 is found such that the mass flow passing through the exit plane is equal to the mass flow passing through the inlet plane. This exit plane height will depend on the extent, intensity and direction of the tip leakage and secondary flows and is different for each tip shape. The inlet conditions are kept identical for each blade tip shape making the efficiency and rotor work directly comparable since they relate to the same quantity of fluid.

All the coefficients required to calculate the efficiency were calculated by integrating with parallel sided segments and a constant blade speed U. Thus hub tip ratio or radial variations were not required.

The mass flow rate at inlet is

$$\dot{m} = \int_0^{z_1} \rho W_1 S dz_1 \qquad (7)$$

and at the exit plane

$$\dot{m} = \int_0^{S} \int_0^{z_2} \rho W_2 \cos \beta_2 \, dz \, ds \qquad (8)$$

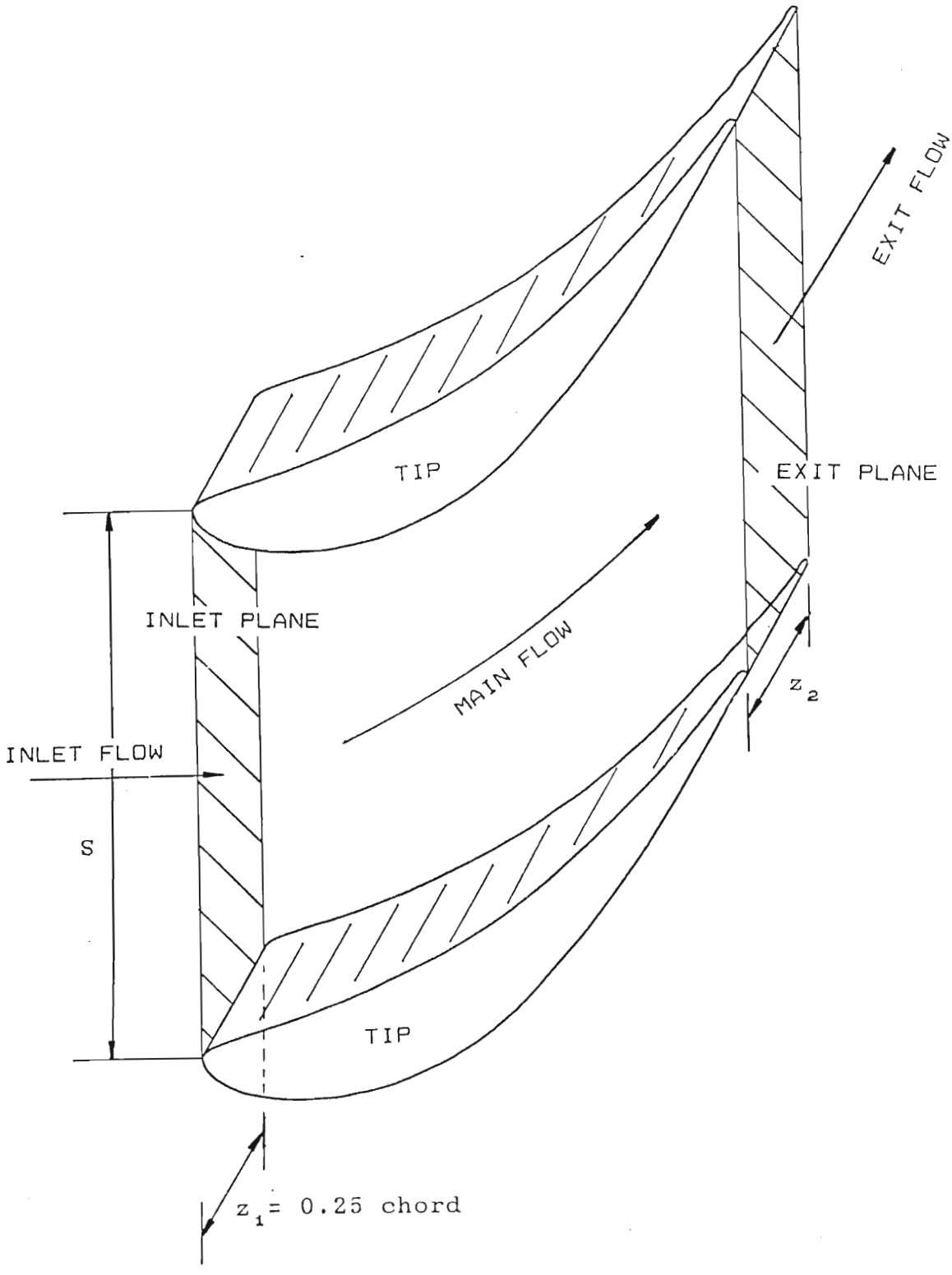

FIGURE 6.3 INTEGRATION HEIGHT Z_2 CALCULATED SUCH THAT INLET AREA HAS THE SAME MASS FLOW RATE AS EXIT AREA AND INCLUDES ALL TIP AND ENDWALL EFFECTS.

Here S is the tangential width of the channel at the plane being considered. To find the exit plane height Z_2, equations (7) and (8) are combined to give

$$\dot{m} = \int_0^{z_1} \rho W_1 S \, dz = \int_0^{S} \int_0^{z_2} \rho W_2 \cos \beta_2 \, dz \, ds \qquad (9)$$

Non dimensionalizing with the mass flow of free-stream inlet fluid through height z_1.

$$C_m = \frac{\dot{m}}{\rho W S z_1} = \int_0^{z_1} \frac{W_1}{W} \frac{dz_1}{z_1} = \int_0^{S} \int_0^{z_2} \frac{W_2}{W} \cos \beta_2 \frac{dz}{z_1} \frac{ds}{S} \qquad (10)$$

Here it is now convenient to make the mass flow coefficient equal to unity to obtain

$$1 = \int_0^{S} \int_0^{z_2} \frac{W_2}{W} \cos \beta_2 \frac{dz}{z_1} \frac{ds}{S}$$

z_2 can be found by iteration or by repetitively integrating for various values of z_2 until the R.H.S. of the equation is equal to unity.

6.2 THE WORK COEFFICIENT

The specific power extracted by the hypothetical rotor can be found by using the Euler work equation. For a fluid element passing through the rotor

$$\omega = UV_{\theta 1} - UV_{\theta 2}$$

The overall work rate

$$\dot{\omega} = \dot{m}\,\bar{\omega} = \sum \dot{dm}\,\omega$$

$$= \sum \dot{dm}\,UV_{\theta 1} - \sum \dot{dm}\,UV_{\theta 2}$$

$$\text{or} \quad \bar{\omega} = \frac{\sum \dot{dm}\,UV_{\theta 1}}{\dot{m}} - \frac{\sum \dot{dm}\,UV_{\theta 2}}{\dot{m}}$$

As shown in Figure 6.1 the inlet velocity to the hypothetical rotor is axial thus $V_{\theta 1}$ is constant and equal to U.

$$\therefore \bar{\omega} = \frac{\sum \dot{dm}\,U^2}{\dot{m}} - \frac{\sum \dot{dm}\,UV_{\theta 2}}{\dot{m}}$$

The work coefficient was defined as

$$\bar{C}_\omega = \frac{\rho\bar{\omega}}{.5\rho W^2} = \frac{\rho \sum \dot{dm}\,U^2}{\dot{m}\ .5\rho W^2} - \frac{\rho \sum \dot{dm}\,UV_{\theta 2}}{\dot{m}\ .5\rho W^2}$$

$$= \frac{\rho \sum_{A_1} \rho W_1\,dA_1\,U^2}{\sum_{A_1} \rho W_1 dA_1\ .5\rho W^2} - \frac{\rho \sum_{A_2} \rho W_2\,dA_2 U\,V_{\theta 2}}{\sum_{A_1} \rho W_1\,dA_1\ .5\rho W^2}$$

Since the flow is uniform in the tangential direction at the inlet to the blade, $dA_1 = S\, dz_1$. At the exit plane $dA_2 = ds \cos \beta_2\, dz_2$

$$\therefore \quad \bar{C}_\omega = \frac{\rho^2 U^2 \sum^{A_1} W_1 S\, dz_1}{0.5\, \rho^2 \sum^{A_1} W_1 S\, dz_1 W^2} - \frac{\rho^2 U \sum^{A_2} W_2 V_{\theta 2}\, ds \cos \beta_2\, dz_2}{0.5\, \rho^2 \sum^{A_1} W_1 S\, dz_1 W^2}$$

$$= 2\frac{U^2}{W^2} - \frac{2U}{W^2} \frac{\sum^{A_2} W_2 \cos \beta_2 V_{\theta 2}\, ds\, dz_2}{\sum^{A_1} W_1 S\, dz_1}$$

devide top and bottom by $W S z_1$

$$= \frac{2U^2}{W^2} - \frac{2U}{W} \frac{\sum^{A_2} \frac{W_2}{W} \frac{V_{\theta 2}}{W} \cos \beta_2 \frac{ds}{S} \frac{dz_2}{z_1}}{\sum^{A_1} \frac{W_1}{W} \frac{dz_1}{z_1}}$$

$$= 2\frac{U^2}{W^2} - \frac{2\frac{U}{W} \int_0^S \int_0^{z_2} \left(\frac{W^2}{W} \frac{V_{\theta 2}}{W} \cos \beta_2 \frac{dz_2}{z_1}\right) \frac{ds}{S}}{\int_0^{z_1} \frac{W_1}{W} \frac{dz_1}{z_1}} \qquad (11)$$

6.3 THE TOTAL PRESSURE LOSS COEFFICIENT

The total pressure loss generated within the rotor may be found from

$$\overline{\Delta p_0} = \overline{\Delta p_{02}} - \overline{\Delta p_{01}}$$

where $\overline{\Delta p_{01}}$ is the total pressure loss at inlet and is mainly due to the inlet and boundary layer

and $\overline{\Delta p_{02}}$ is the total pressure loss at the measurement plane.

Defining the loss coefficient

$$C_L = \frac{\overline{\Delta p_0}}{.5\rho W^2} = \frac{\overline{\Delta p_{02}}}{.5\rho W^2} - \frac{\overline{\Delta p_{01}}}{.5\rho W^2} = \overline{C}_{L2} - \overline{C}_{L1} \qquad (12)$$

The mass averaged total pressure loss at measurement plane may be found from

$$\dot{m}\,\overline{\Delta p_{02}} = \sum d\dot{m}\,\Delta p_{02}$$

$$\therefore \overline{\Delta p_{02}} = \frac{\sum d\dot{m}\Delta p_{02}}{\dot{m}}$$

$$\bar{C}_{L2} = \frac{\overline{\Delta p_{02}}}{0.5\rho W^2} = \frac{\sum \dot{m}\ \Delta p_{02}}{\dot{m}\ 0.5\rho W^2} = \frac{\sum_{A_2} \rho W_2\ dA_2\ \Delta p_{02}}{\sum \rho W_1\ dA_1\ 0.5\ \rho W^2}$$

$$= \frac{\rho \sum W_2\ C_{L2}\ dA_2}{\rho \sum W_1\ dA_1}$$

$$= \frac{\sum \frac{W_2}{W} C_{L2} \frac{dA_2}{A_1}}{\frac{W_1}{W} \frac{dA_1}{A_1}} \qquad \text{divide top and bottom by } WA_1$$

$$= \frac{\sum \frac{W_2}{W} C_{L2}\ \text{Cos}\ \beta_2 \frac{ds}{S} \frac{dz_2}{z_1}}{\sum \frac{W_1}{W} \frac{S\ dz_1}{S\ z_1}} \qquad \left(\frac{dA_2}{A_1} = \text{Cos}\ \beta_2 \frac{ds\ dz_2}{S\ z_1} \right)$$

$$= \frac{\int_0^S \int_0^{z_2} \frac{W_2}{W} \cos \beta_2\ C_{L2} \frac{dz_2}{z_1} \frac{ds}{S}}{\int_0^{z_1} \frac{W_1}{W} \frac{dz_1}{z_1}} \qquad (13)$$

Now to find the mass averaged total pressure loss at inlet

$$\dot{m}\,\overline{\Delta p_{01}} = \sum \dot{m}\,\Delta p_{01}$$

$$\text{Therefore} \quad \overline{\Delta p_{01}} = \frac{\sum \rho W_1\, d_{A1}\, \Delta p_{01}}{\dot{m}}$$

$$\overline{C}_{L1} = \frac{\overline{\Delta p_{01}}}{.5\rho W^2} = \frac{\sum \rho W_1\, d_{A1} \Delta p_{01}}{\sum \rho W_1 dA_1 \quad .5\rho W^2}$$

$$= \frac{\sum W_1\, C_{L1}\, dA_1}{\sum W_1\, dA_1} \quad \text{divide top and bottom by } W\,A_1$$

$$= \frac{\sum \frac{W_1}{W}\, C_{L1}\, \frac{dA_1}{A_1}}{\sum \frac{W_1}{W}\, \frac{dA_1}{A_1}}$$

$$= \frac{\sum \frac{W_1}{W}\, C_{L1}\, \frac{S dz_1}{S\, z_1}}{\sum \frac{W_1}{W}\, \frac{S\, dz_1}{S\, z_1}}$$

$$= \frac{\int_0^{z_1} \frac{W_1}{W} C_{L1} \frac{dz_1}{z_1}}{\int_0^{z_1} \frac{W_1}{W} \frac{dz_1}{z_1}} \qquad (14)$$

Substituting equations (13) and (14) into (12)

$$\overline{C}_L = \frac{\int_0^{z_1} \int_0^{z_2} \left(\frac{W_2}{W} \cos \beta_2 \, C_{L2} \frac{dz_2}{z_1} \right) \frac{ds}{S} - \int_0^{z_1} \frac{W_1}{W} C_{L1} \frac{dz_1}{z_1}}{\int_0^{z_1} \frac{W_1}{W} \frac{dz_1}{z_1}} \qquad (15)$$

It can be seen here that once the total pressure terms C_{L1} or C_{L2} become zero (ie end of boundary layer), then integration may stop.

6.4 OUTLET VELOCITY COEFFICIENT

The mass averaged outlet velocity coefficients may be found as follows:

$$\bar{C}^2_{v2} = \frac{\bar{V}^2_2}{W^2} = \frac{\sum \dot{m}\, dm \, \frac{V_2^2}{W^2}}{\dot{m}}$$

$$= \frac{\sum_{A_2} \rho W_2 dA_2 \frac{V_2^2}{W^2}}{\sum_{A_1} \rho W_1 dA_1}$$

divide top and bottom by WA1

$$= \frac{\sum_{A_2} \frac{W_2}{W} \frac{V_2^2 dA_2}{W^2 A_1}}{\sum_{A_1} \frac{W_1}{W} \frac{dA_1}{A_1}} = \frac{\int_0^S \int_0^{z_2} \frac{W_2}{W} \frac{V_2^2}{W^2} \cos \beta_2 \frac{ds}{S} \frac{dz_2}{z_1}}{\sum \frac{W_1}{W} \frac{Sdz_1}{Sz_1}}$$

$$\bar{C}^2_{v2} = \frac{\int_0^S \int_0^{z_2} \left(\frac{W_2}{W} \frac{V_2^2}{W^2} \cos \beta_2 \frac{dz_1}{z_1} \right) \frac{ds}{s}}{\sum \frac{W_1}{W} \frac{dz_1}{z_1}} \qquad (16)$$

Integration must continue right up to Z_2 since this term is an average kinetic energy.

6.5 IDEAL OUTLET VELOCITY COEFFICIENT

The ideal outlet velocity coefficient that was used in this thesis was the mass averaged quantity at height Z_2, well above the secondary flow and therefore not affected by the nature or extent of the secondary flow. This value does not vary from one case to another and therefore does not influence comparative performance.

$$\frac{\dot{\Delta m}\, V_{2id}^2}{W^2} = \sum^{\dot{\Delta m}} d\dot{m}\, \frac{V_2^2}{W^2}$$

where $\dot{\Delta m}$ is the mass flow through a height dz at a height Z_2 as shown in Figure 6.3.

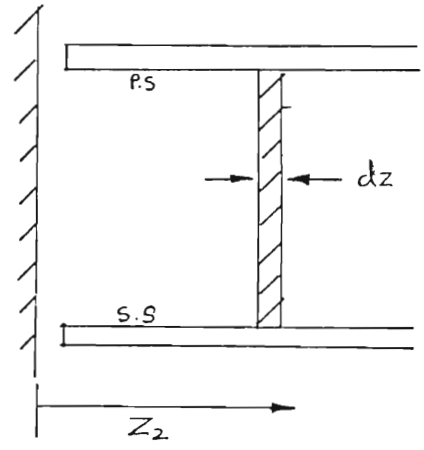

$$\therefore C_{v2id}^2 = \frac{V_{2id}^2}{W^2} = \frac{\sum^{\dot{\Delta m}} d\dot{m}\, \frac{V_2^2}{W^2}}{\dot{\Delta m}}$$

$$= \frac{\sum \rho W_2 dz\, ds \cos\beta_2 \frac{V_2^2}{W^2}}{\sum \rho\, W_2\, dz\, ds \cos\beta_2}$$

$$= \frac{\rho dz \sum W_2 \cos\beta_2 \frac{V_2^2}{W^2}\, ds}{\rho dz \sum W_2 \cos\beta_2\, ds} \qquad \text{(dz is constant at free stream)}$$

divide top and bottom by WS

$$C_{v2id} = \frac{\sum \frac{W_2}{W} \frac{V_2^2}{W^2} \cos\beta_2 \frac{ds}{S}}{\sum \frac{W_2}{W} \cos\beta_2 \frac{ds}{S}} \qquad (17)$$

——————————→

6.6 INTERNAL GAP LOSS AND DISCHARGE COEFFICIENT

The losses generated within the clearance gap where evaluated by integrating the loss coefficient measured at each grid point. This method was the same as used by Bindon (1988a). The gap mass flow coefficient which gives an indication of the actual amount of fluid going through the gap and the discharge coefficient were also calculated.

6.6.1 Internal gap loss integration

In order to obtain a chordwise distribution of loss the losses were integrated one dimensionally at each transverse station. The loss coefficient at each transverse station was defined as

$$C_L' = \frac{\Delta p_o'}{0.5\rho W^2}$$

Integrating this over the gap width

$$= \int_o^{Z_g} \frac{\Delta p_o \rho \; V \; dz}{0.5 \; \rho W^2} = \rho \int_o^{Z_g} \frac{\Delta p_o}{0.5 \; \rho W^2} V \; dz$$

Non-dimensionalizing this with $\rho W Z_g$

$$C_L' = \int_o^{Z_g} C_L \frac{V}{W} \frac{dz}{Zg}$$

——————————>

The mass averaged loss generated by the whole gap was integrated from endwall to tip and from leading edge to trailing edge.

The mass averaged loss coefficient is

$$\bar{C}_L = \frac{\overline{\Delta p_o}}{0.5\ \rho W^2} = \frac{1}{0.5\ \rho W^2} \frac{\int_0^X \int_0^{Z_g} \Delta p_0\ \dot{dm}}{\dot{m}_{ref}} \quad \text{(where X=chord)}$$

$$= \frac{1}{\dot{m}_{ref}} \int_0^{Ss} \int_0^{Z_g} \frac{\Delta p_o}{.5\rho W^2}\ \rho\ V'\ dz\ ds$$

where V' is the velocity component normal to the suction surface

Ss is suction surface distance

and $\dot{m}_{ref} = \rho W A_1 = \rho W z_1 S = \rho W .25 X S$

(since a blade height $z_1 = .25$ chord is considered)

$$\bar{C}_L = \frac{1}{\rho W\ .25\ X\ S} \int_0^{Ss} \int_0^{Z_g} C_L\ \rho V'\ dz\ ds$$

$$= \frac{\rho\ Zg\ X}{\rho .25\ X\ S} \int_0^{Ss} \int_0^{Z_g} C_L \frac{V'}{W} \frac{dz}{Zg} \frac{ds}{X}$$

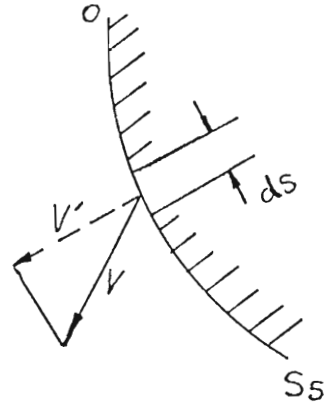

The clearance gap used for all blades was 2.5% chord, thus $Z_g = .025X$

$$\therefore \quad \bar{C}_L = \frac{0.025\ X^2}{.25\ X\ S} \int_0^{Ss/X} \int_0^1 C_L \frac{V'}{W}\ d(z/z_g)\ d(s/X)$$

$$= \frac{.1}{S/X} \int_0^{Ss/X} \int_0^1 C_L \frac{V'}{W}\ d(z/z_g)\ d(s/X)$$

6.6.2 Gap Mass Flow

The gap mass flow is an absolute measure of the gap flow rather than the discharge coefficient which relates to the local pressure and loss.

Gap mass flow coefficient is defined as follows:

$$C_{mg} = \frac{\dot{m}_{gap}}{\dot{m}_{ref}}$$

Using same reference area as before (1 pitch x 0.25 chord)

$$C_{mg} = \frac{\int_0^{Ss} \int_0^{Z_g} \rho V' \, dz \, ds}{\rho W S .25 X}$$

$$= \frac{Z_g X \int_0^{Ss} \int_0^{1} \rho V' \, d(z/Zg) \, d(s/X)}{\rho W S .25 X}$$

$$= \frac{Z_g}{.25S} \int_0^{Ss/x} \int_0^{1} \frac{V'}{W} \, d(z/Z_g) \, d(s/X)$$

6.6.3 Gap Discharge Coefficient

The gap discharge coefficient is a measure of the actual flow through the gap compared to the flow that would flow through if the gap was isentropic. The loss free zone at mid gap height was used to define the isentropic velocity V_{is}. If loss is present at mid gap, then it leads to a slight inaccuracy.

From Bernoulli

$$P_1 + 0.5\rho V_1^2 = P_2 + 0.5\rho V_2^2 + \Delta p_o$$

or $$P_1 - P_2 + 0.5\rho V_1^2 = 0.5\rho V_2^2 + \Delta p_o$$

$$\frac{P_1 - P_2}{.5\rho V_1^2} + 1 = \frac{V_2^2}{V_1^2} + C_L$$

If the pressure coefficient is known, the loss may be set to zero and the isentropic velocity ratio found.

Therefore

$$\left(\frac{V_2}{V_1}\right)_{is}^2 = 1 + C_p$$

or $$\left(\frac{V_2}{V_1}\right)_{is} = \sqrt{1 + C_p}$$

The 1 Dimensional Discharge Coefficient is defined as

$$C_D' = \frac{\dot{m}_{actual}}{\dot{m}_{is}} = \frac{\int_0^{Z_g} \rho V' dz}{\int_0^{Z_g} \rho V_{is}' dz}$$

$$= \frac{\int_0^{Zg} V \sin\theta \, dz}{\int_0^{Zg} V_{is} \sin\theta \, dz}$$

$$= \frac{\int_0^{Z_g} \frac{V}{W} \sin\theta \quad \frac{dz}{Z_g}}{\int_0^{Z_g} \sqrt{1 + C_p} \sin\theta \, \frac{dz}{Z_g}}$$

for the complete gap the overall discharge coefficient was calculated as follows:

$$\bar{C}_D = \frac{\int_0^{S} \int_0^{Zg} \rho V' \, dz \, ds}{\int_0^{S} \int_0^{Zg} \rho V_{is}' \, dz \, ds}$$

$$= \frac{\int_0^{S/X} \int_0^1 V' \, d(z/Zg) \, d(s/X)}{\int_0^{S/X} \int_0^1 V'_{is} \, d(z/Zg) \, d(s/X)}$$

$$= \frac{\int_0^{S/X} \int_0^1 \frac{V}{W} \sin \theta \, d(z/Zg) \, d(s/X)}{\int_0^{S/X} \int_0^1 \sqrt{1 + C_p} \sin \theta \, d(z/Zg) \, d(s/X)}$$

6.7 Conclusion

A method whereby detailed stationary cascade flow field data can be converted into a simulated rotor flow to calculate work transfer and efficiency was presented. The use of this method is demonstrated in Chapter 8 by comparing the endwall region performance of the tip clearance geometries tested. This method could be useful in developing and understanding tip geometries in stationary cascades.

CHAPTER 7

EFFECT OF RELATIVE MOTION, GAP SIZE AND BLADE EDGE RADIUS ON BLADE TIP PRESSURE DISTRIBUTION

The microscopic static pressure measurements and flow visualization done on the blade tips in the annular turbine cascade with rotating outer casing (as described in Chapter 3) are discussed in this chapter. The detailed static pressure distribution and the effect of relative motion between the blade tips and endwall are presented for the flat tip blade. The effect of clearance gap size on the tip pressure distribution and separation bubble for the flat tip blade was also examined. Finally in this chapter, the sharp edged pressure corner at gap inlet was progressively radiused until the separation bubble was eliminated. The effect of increasing this pressure corner radius was shown using flow visualization and static pressure measurements.

The work described in this chapter was all done with relative motion between the endwall and blade tip, except for the case where the rotating casing was kept stationary, to examine the effect of relative motion.

The results described in this chapter are summarized in a paper presented at the ASME Gas Turbine and Aero-Engine Congress, Amsterdam, June 1988. (See Appendix 5).

7.1 DETAILED PRESSURE DISTRIBUTION FOR FLAT-TIPPED BLADE WITH CLEARANCE GAP

The detailed static pressure distributions for the flat tip blade with clearance and relative motion are presented in Figures 7.1.a - 7.1.s for the 19 slots at intervals of 5% chord.

The static pressure distributions recorded here were seen to be similar in shape to those of Bindon (1988a). As the flow turned to enter the gap the static pressure was seen to drop to the lowest value in the form of a very narrow trough at the pressure corner. This is thought to be due to the flow remaining attached as it sharply turns around the corner or small blade edge radius. The flow then diffuses sharply before separating to form the separation bubble. The results obtained here are significant since in Bindon (1987a) only a single measurement was possible to define this phenomenon. An improvement in the resolution of the micro tapping technique has allowed 3 measurements to be taken in the region near the corner to record the pattern. This confirms the existence of these narrow regions of low pressures on sharp edged pressure surfaces. It is important to note that the pressure in the separation bubble and the low pressure trough at the corner are very much lower than even the suction surface pressure. After the separation bubble, the flow reattaches and remains attached for the remainder of the gap. The static pressure remains approximately constant in the attached region up to the suction corner.

Figures 7.2 and 7.3 show a selection of the actual pressure

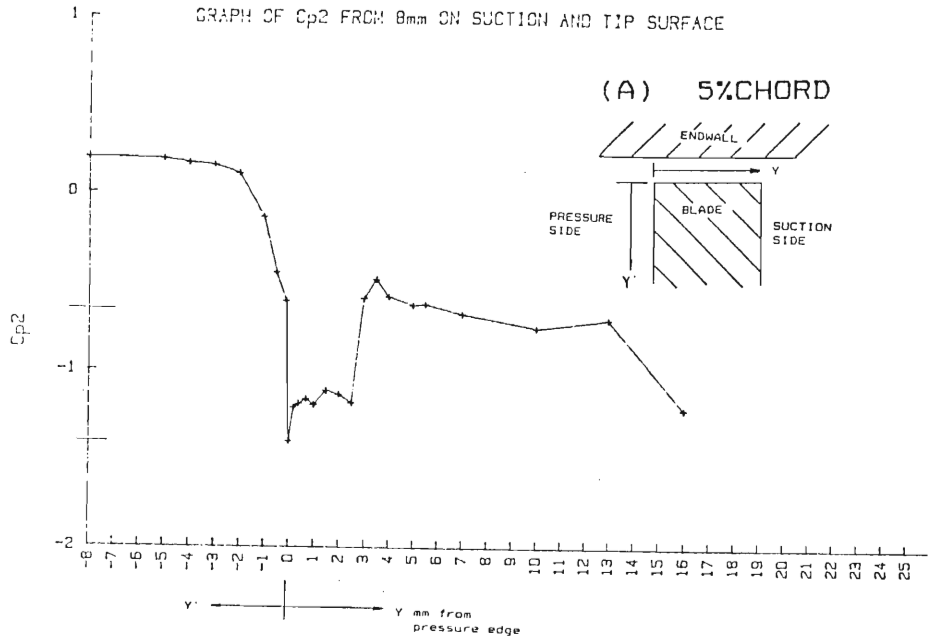

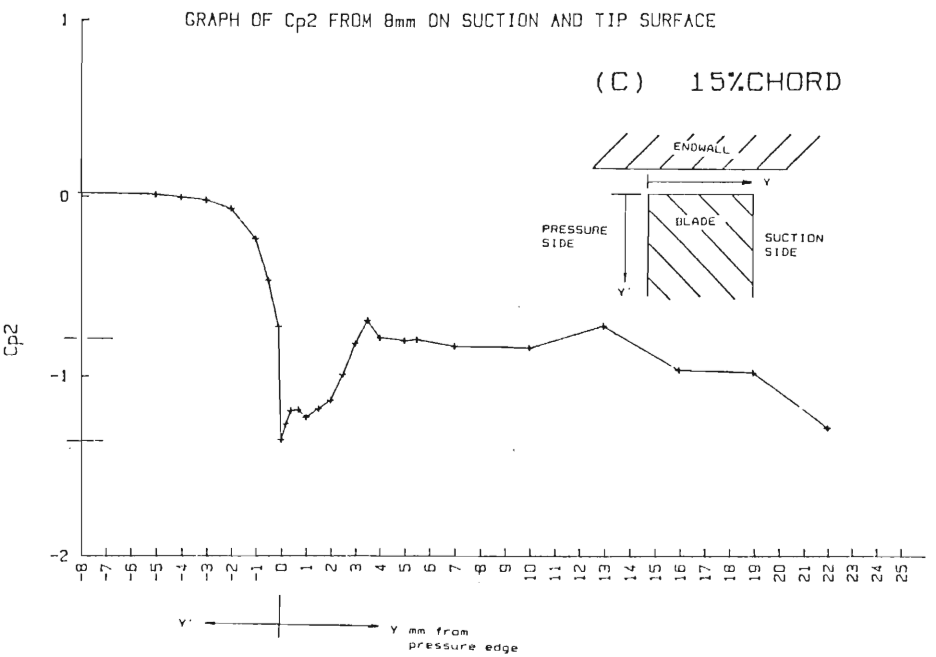

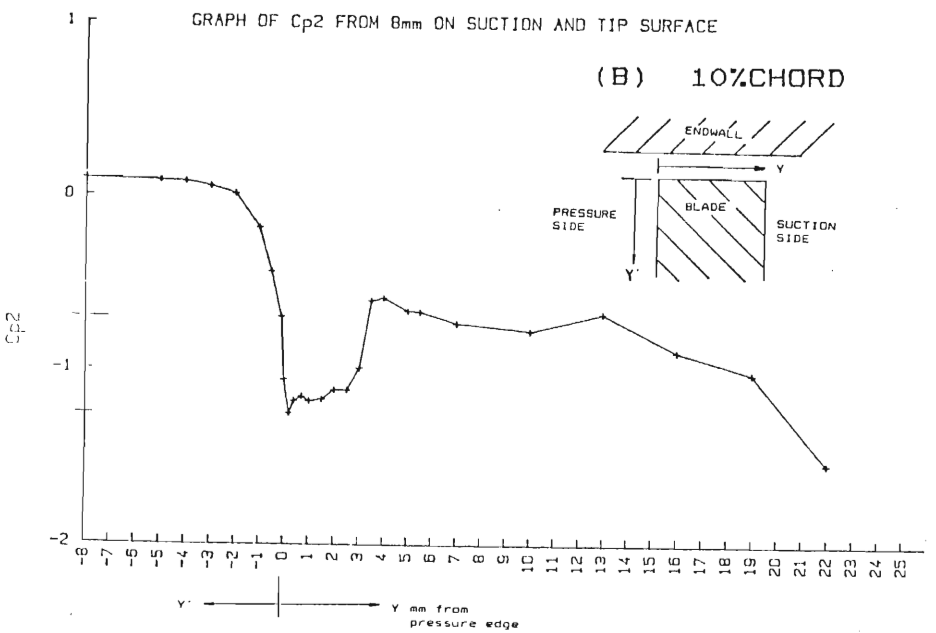

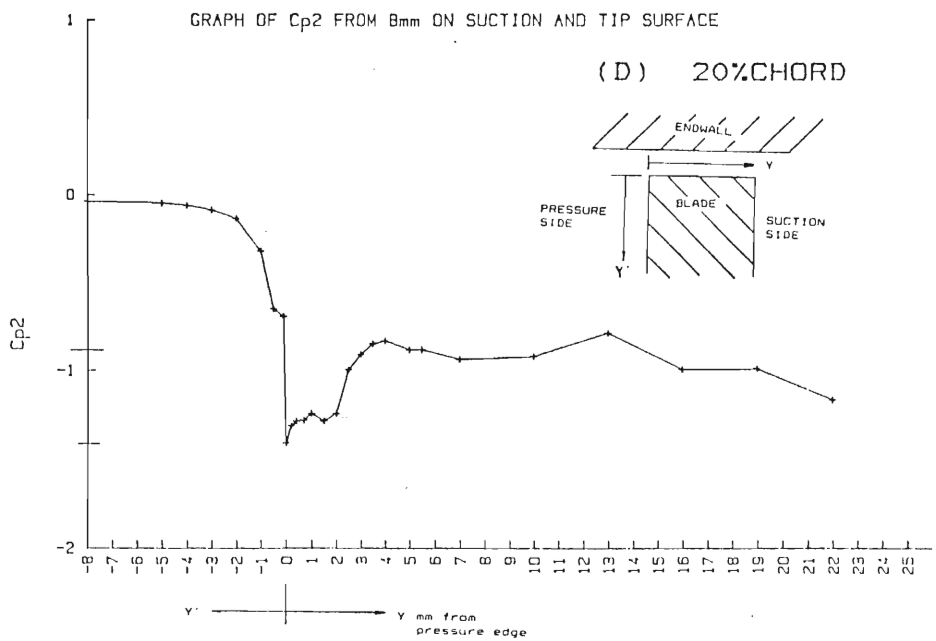

FIGURE 7.1 STATIC PRESSURE DISTRIBUTIONS FOR FLAT TIP BLADE WITH 2% CHORD CLEARANCE AND RELATIVE MOTION

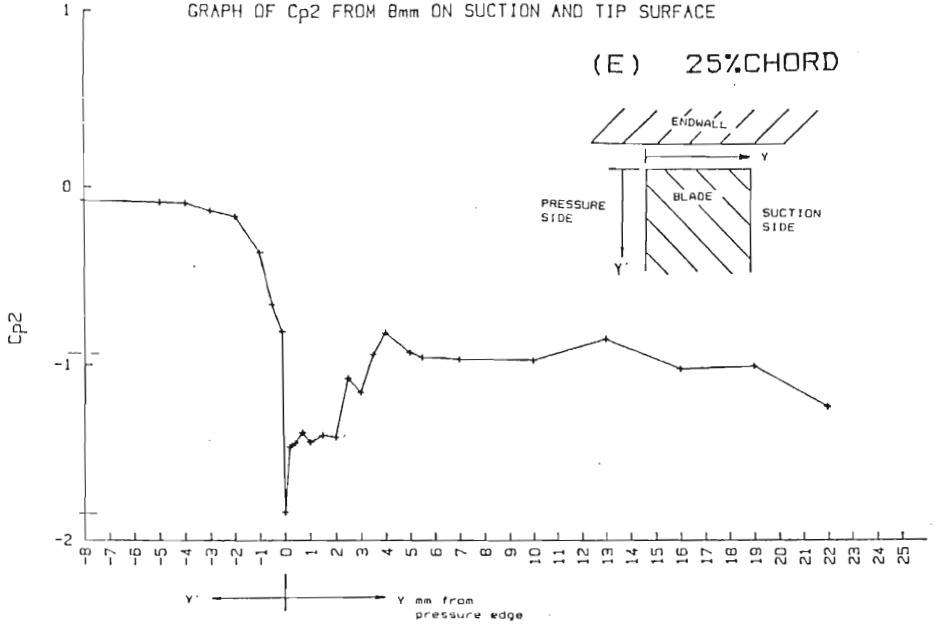
GRAPH OF Cp2 FROM 8mm ON SUCTION AND TIP SURFACE
(E) 25%CHORD
ENDWALL
Y
PRESSURE SIDE
BLADE
SUCTION SIDE
Y'
Cp2
Y mm from pressure edge

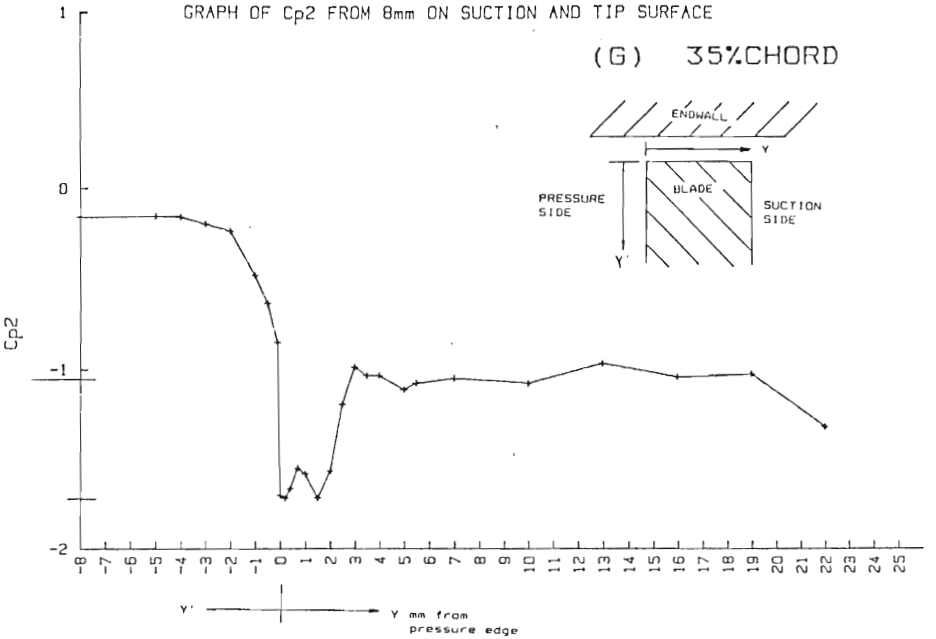
GRAPH OF Cp2 FROM 8mm ON SUCTION AND TIP SURFACE
(G) 35%CHORD
ENDWALL
Y
PRESSURE SIDE
BLADE
SUCTION SIDE
Y'
Cp2
Y mm from pressure edge

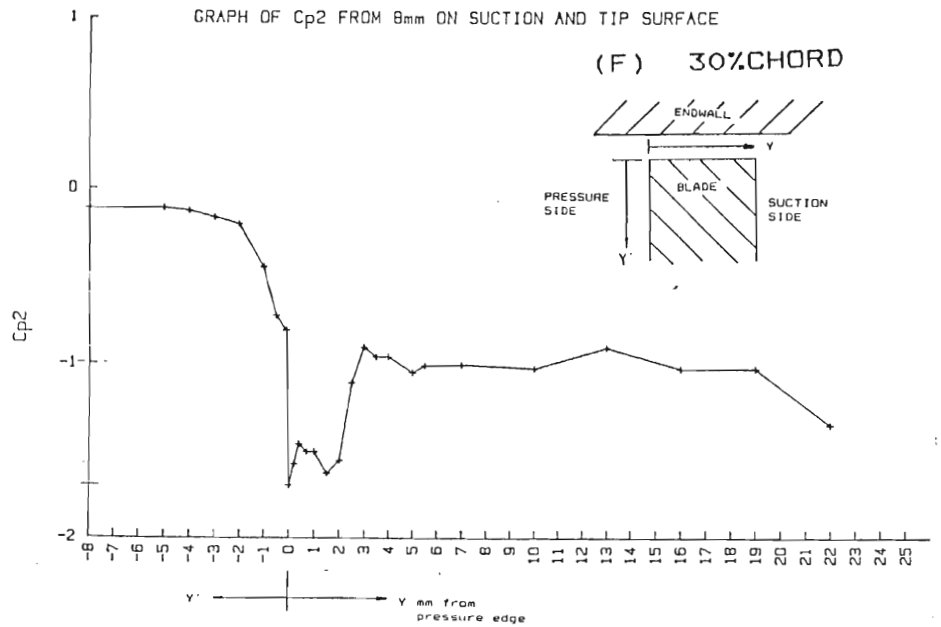
GRAPH OF Cp2 FROM 8mm ON SUCTION AND TIP SURFACE
(F) 30%CHORD
ENDWALL
Y
PRESSURE SIDE
BLADE
SUCTION SIDE
Y'
Cp2
Y mm from pressure edge

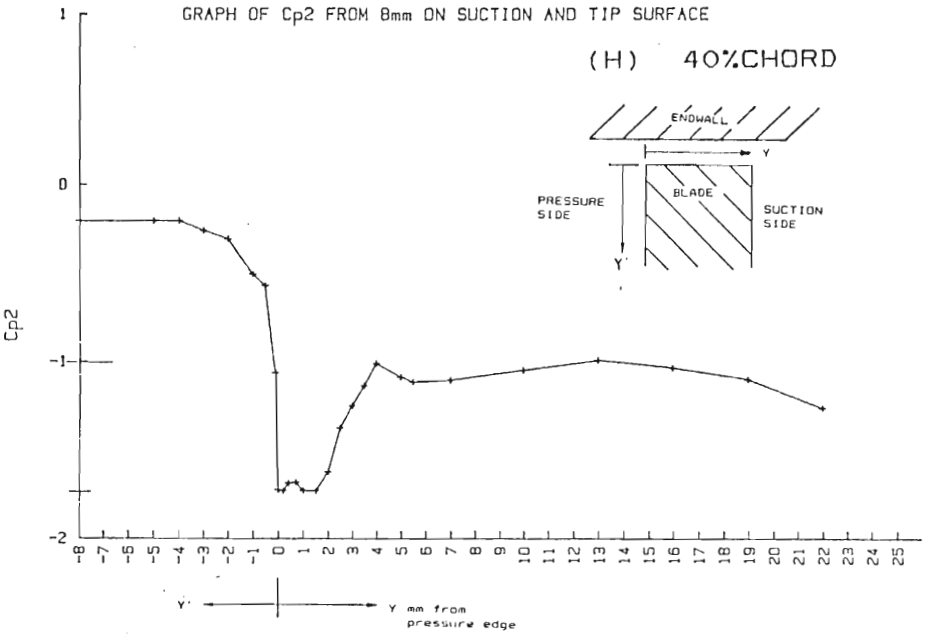
GRAPH OF Cp2 FROM 8mm ON SUCTION AND TIP SURFACE
(H) 40%CHORD
ENDWALL
Y
PRESSURE SIDE
BLADE
SUCTION SIDE
Y'
Cp2
Y mm from pressure edge

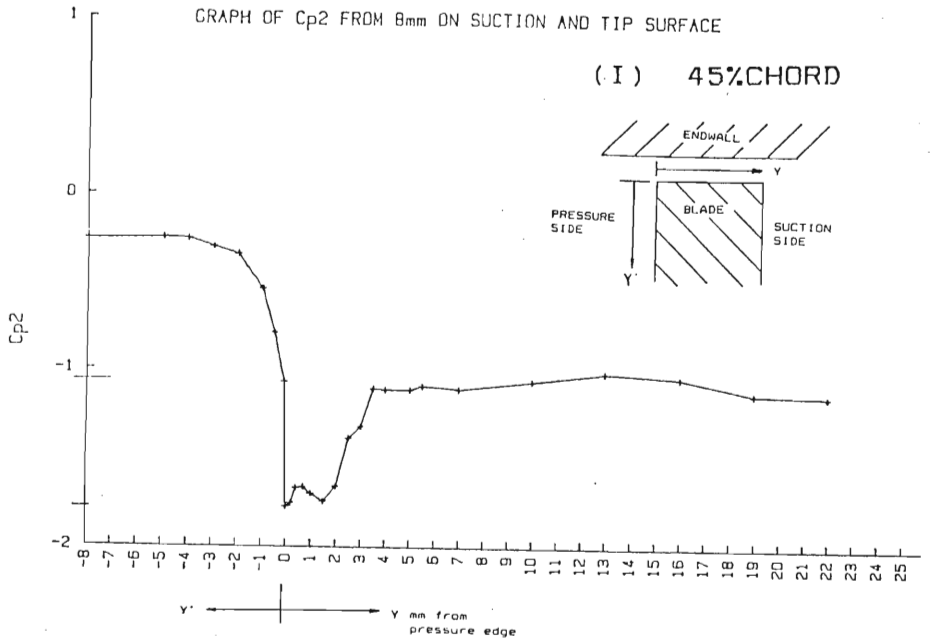
GRAPH OF Cp2 FROM 8mm ON SUCTION AND TIP SURFACE
(I) 45%CHORD
ENDWALL
Y
PRESSURE SIDE
BLADE
SUCTION SIDE
Y'
Cp2
Y mm from pressure edge

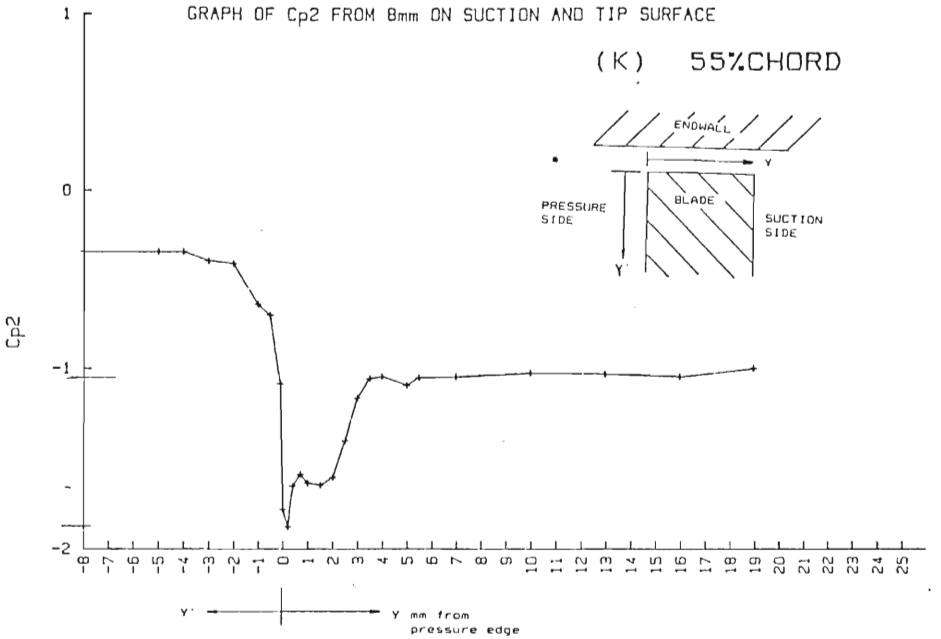
GRAPH OF Cp2 FROM 8mm ON SUCTION AND TIP SURFACE
(K) 55%CHORD
ENDWALL
Y
PRESSURE SIDE
BLADE
SUCTION SIDE
Y'
Cp2
Y mm from pressure edge

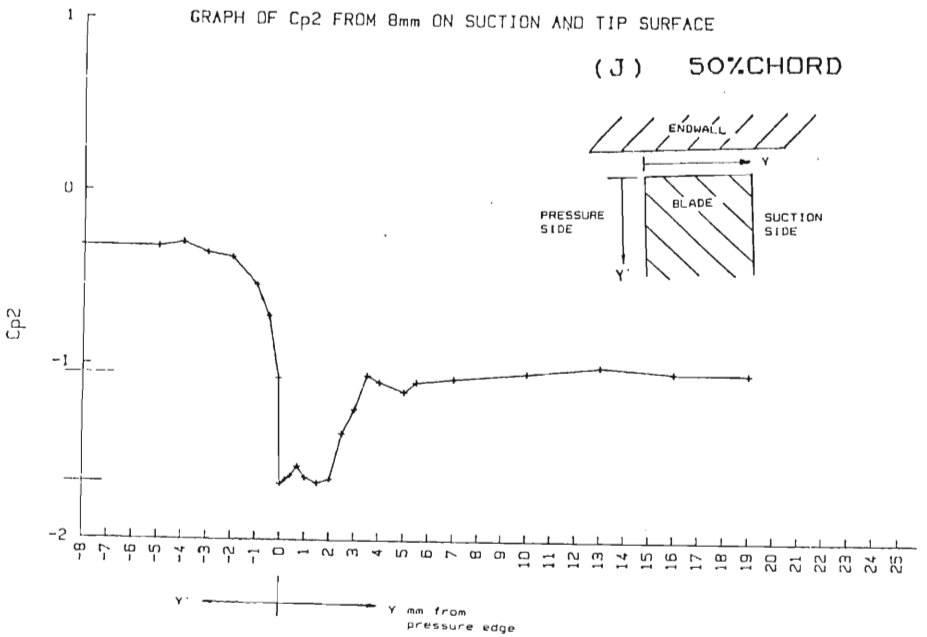
GRAPH OF Cp2 FROM 8mm ON SUCTION AND TIP SURFACE
(J) 50%CHORD
ENDWALL
Y
PRESSURE SIDE
BLADE
SUCTION SIDE
Y'
Cp2
Y mm from pressure edge

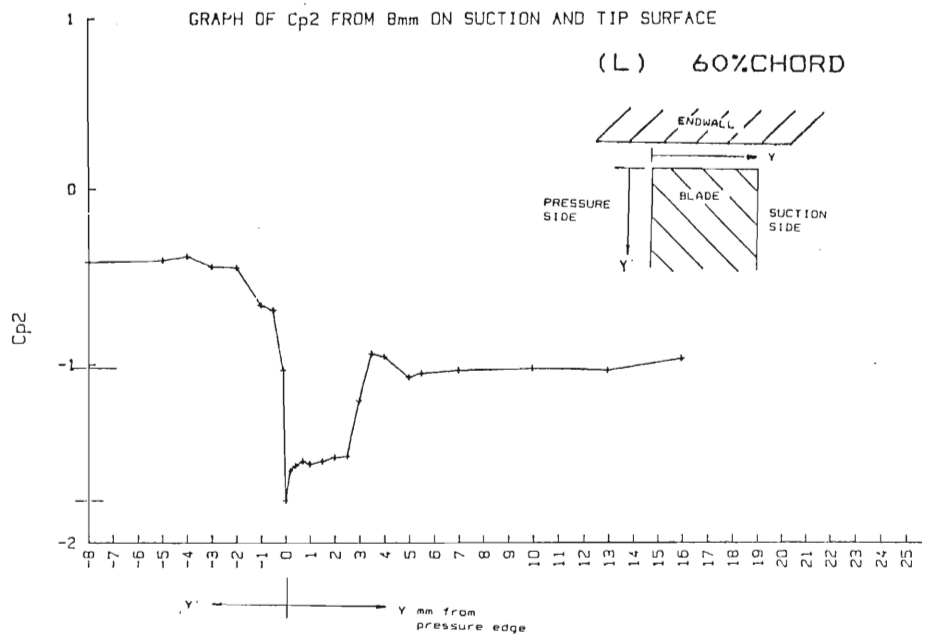
GRAPH OF Cp2 FROM 8mm ON SUCTION AND TIP SURFACE
(L) 60%CHORD
ENDWALL
Y
PRESSURE SIDE
BLADE
SUCTION SIDE
Y'
Cp2
Y mm from pressure edge

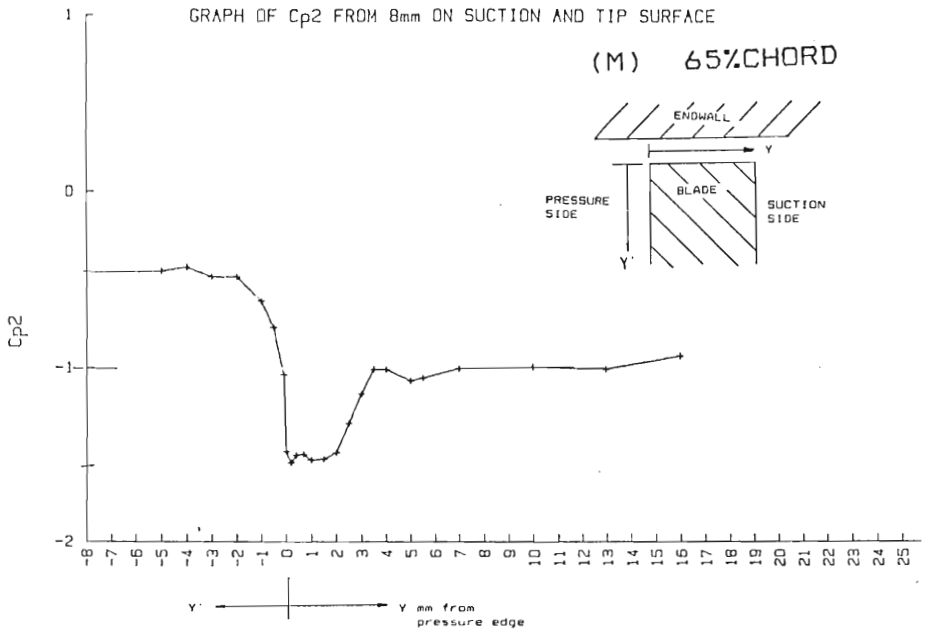
GRAPH OF Cp2 FROM 8mm ON SUCTION AND TIP SURFACE
(M) 65%CHORD
ENDWALL
Y
PRESSURE SIDE
BLADE
SUCTION SIDE
Y'
Cp2
Y' Y mm from pressure edge

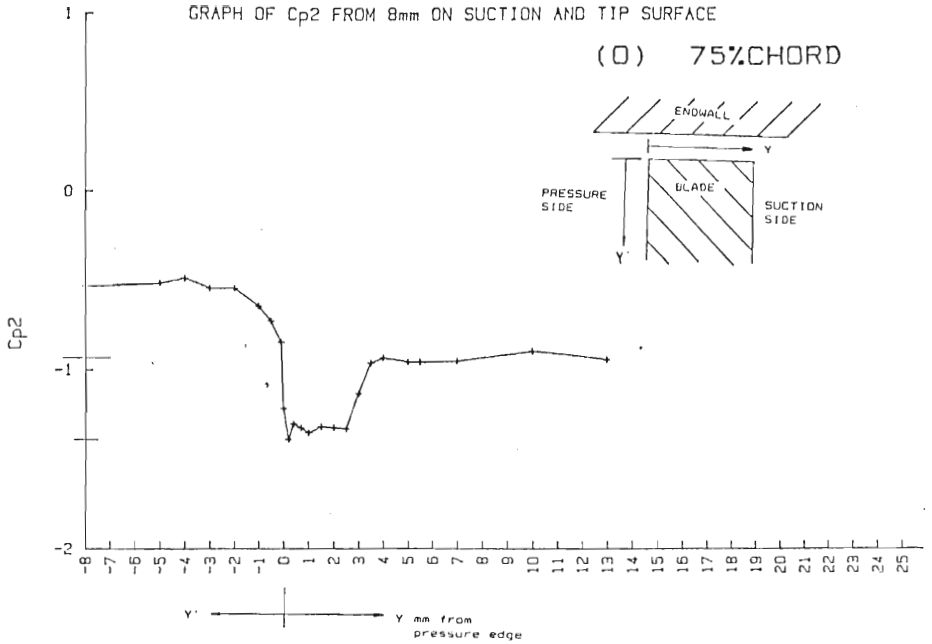
GRAPH OF Cp2 FROM 8mm ON SUCTION AND TIP SURFACE
(O) 75%CHORD
ENDWALL
Y
PRESSURE SIDE
BLADE
SUCTION SIDE
Y'
Cp2
Y' Y mm from pressure edge

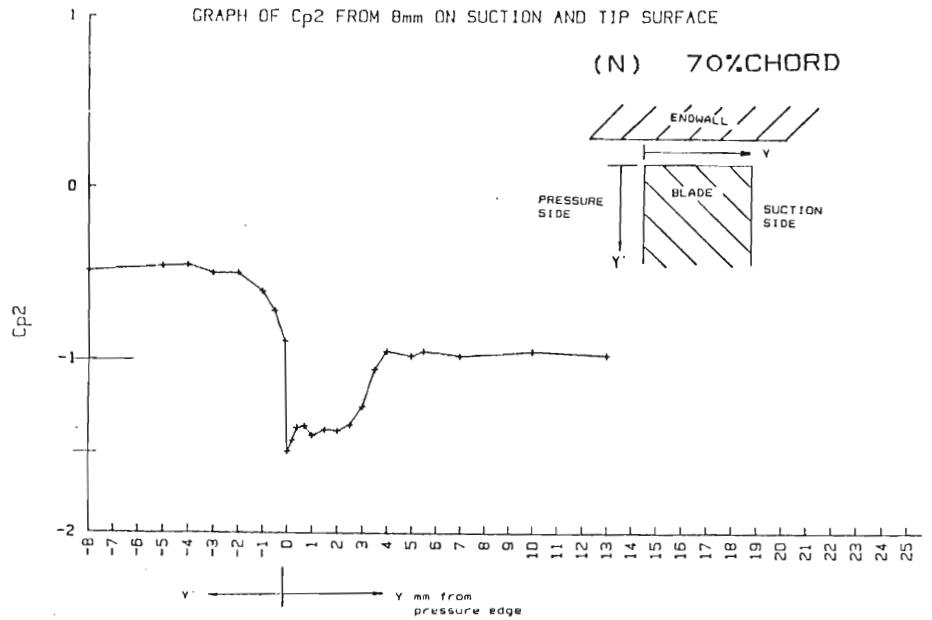
GRAPH OF Cp2 FROM 8mm ON SUCTION AND TIP SURFACE
(N) 70%CHORD
ENDWALL
Y
PRESSURE SIDE
BLADE
SUCTION SIDE
Y'
Cp2
Y' Y mm from pressure edge

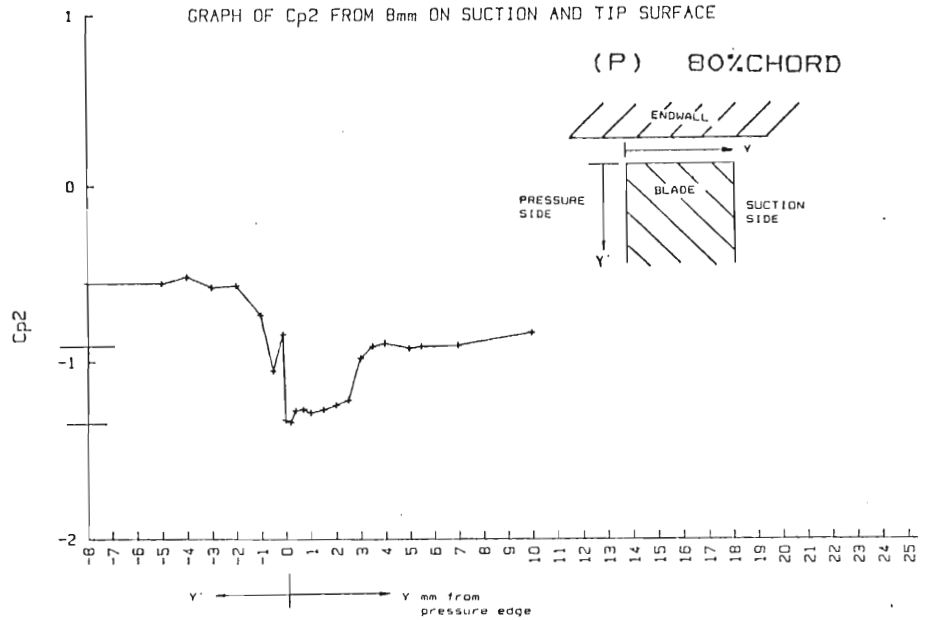
GRAPH OF Cp2 FROM 8mm ON SUCTION AND TIP SURFACE
(P) 80%CHORD
ENDWALL
Y
PRESSURE SIDE
BLADE
SUCTION SIDE
Y'
Cp2
Y' Y mm from pressure edge

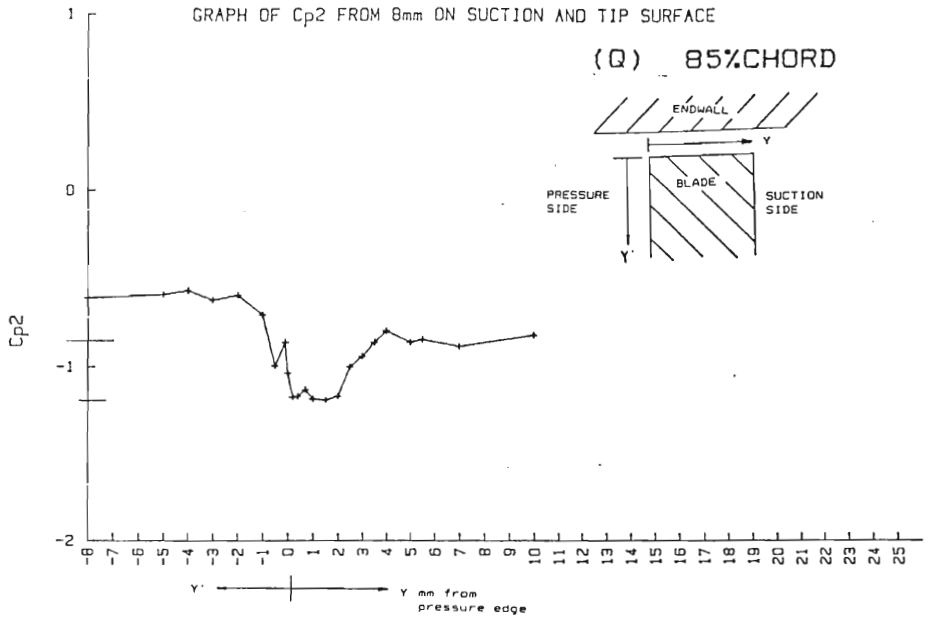
GRAPH OF Cp2 FROM 8mm ON SUCTION AND TIP SURFACE
(Q) 85%CHORD
ENDWALL
Y
PRESSURE SIDE
BLADE
SUCTION SIDE
Y'
Cp2
Y' Y mm from pressure edge

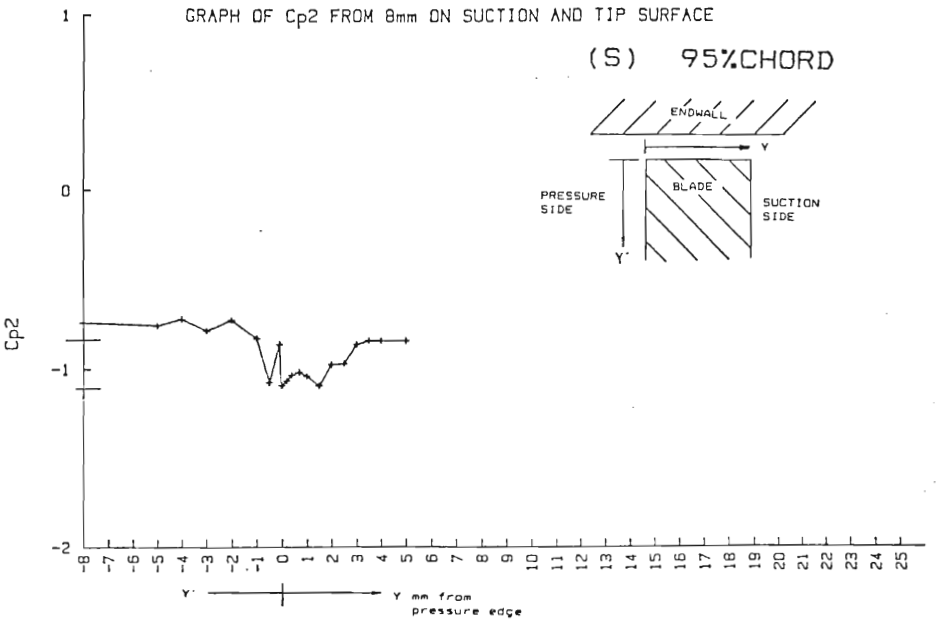
GRAPH OF Cp2 FROM 8mm ON SUCTION AND TIP SURFACE
(S) 95%CHORD
ENDWALL
Y
PRESSURE SIDE
BLADE
SUCTION SIDE
Y'
Cp2
Y' Y mm from pressure edge

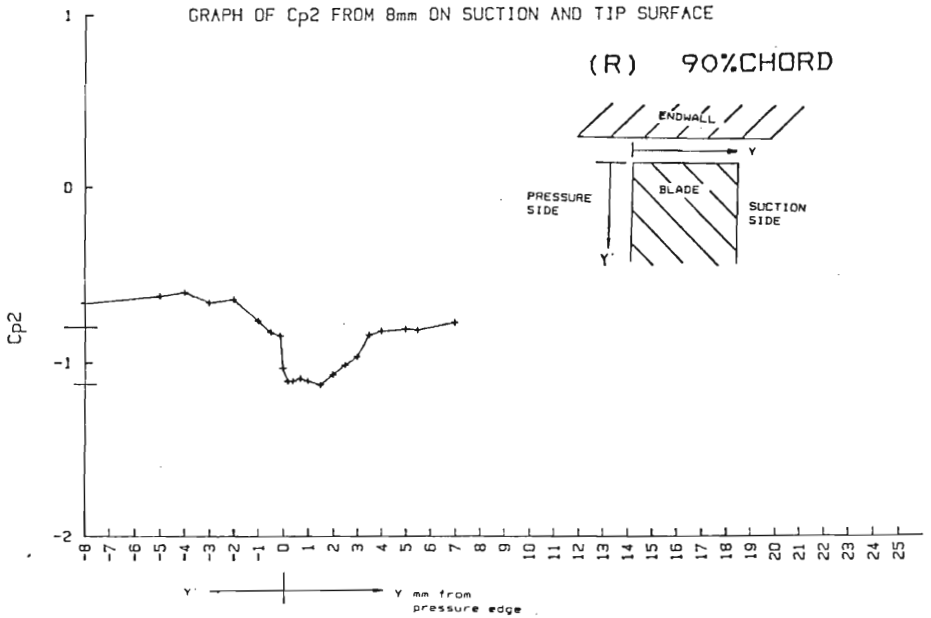
GRAPH OF Cp2 FROM 8mm ON SUCTION AND TIP SURFACE
(R) 90%CHORD
ENDWALL
Y
PRESSURE SIDE
BLADE
SUCTION SIDE
Y'
Cp2
Y' Y mm from pressure edge

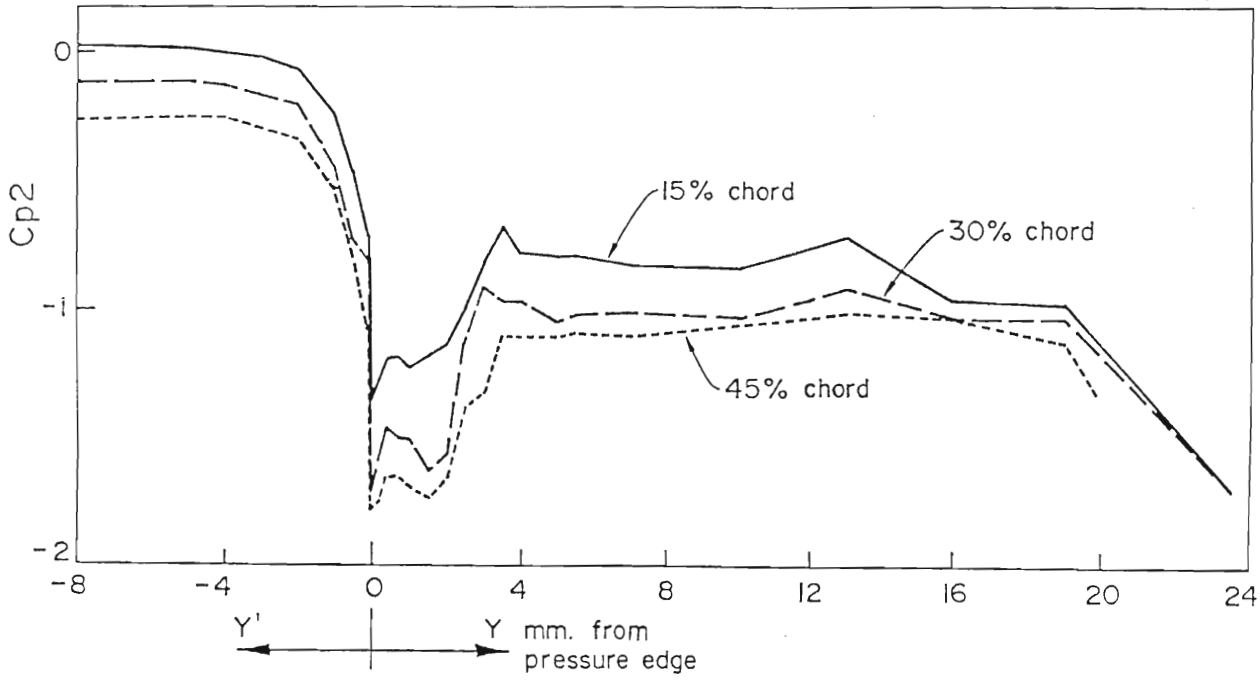

FIGURE 7.2 BLADE PRESSURE DISTRIBUTIONS IN THE CLEARANCE GAP OVER THE FORWARD REGION OF THE PROFILE WHERE PRESSURES ARE FALLING.

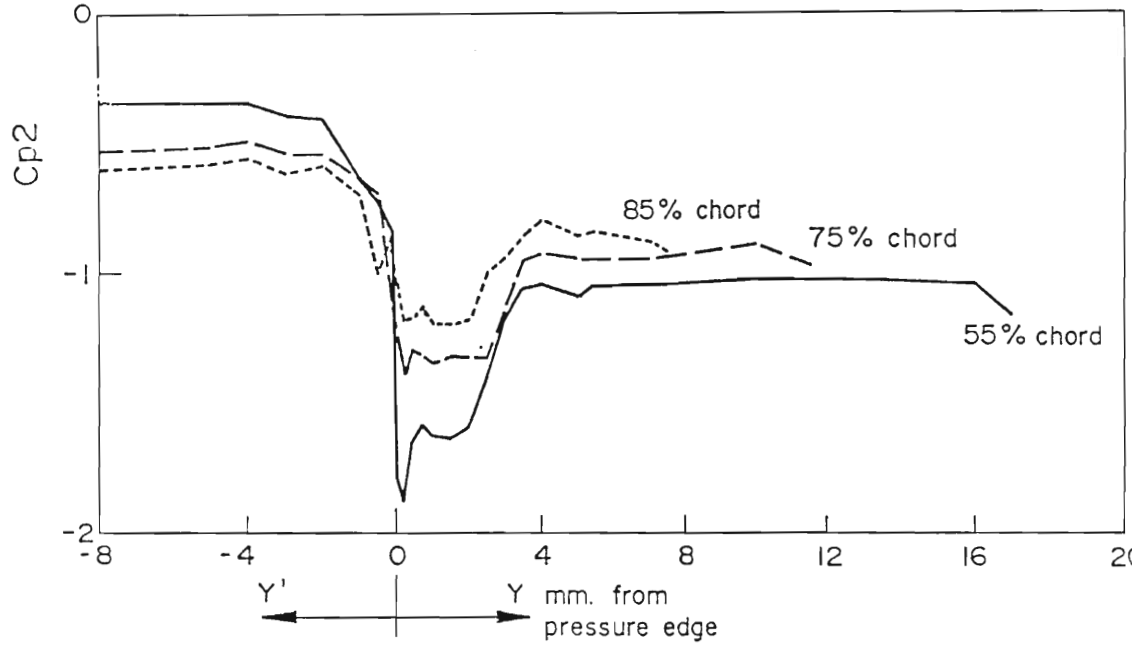

FIGURE 7.3 BLADE PRESSURE DISTRIBUTIONS IN THE CLEARANCE GAP OVER THE REAR REGION OF THE PROFILE WHERE PRESSURES ARE INCREASING

distributions from the pressure surface to suction corner at the blade tip. Figure 7.2 consists of 3 distributions over the forward half of the blade. A chordwise pressure gradient exists within the separation bubble, over the first half of the blade. This gradient which can clearly be seen in Figure 7.2 accelerates the bubble flow towards midchord. Bindon (1986a, 1986b) used smoke flow visualization to demonstrate the strong chordwise corkscrew motion of the bubble flow showing that the flow within the bubble over the forward part of the blade moved towards midchord.

Figure 7.3 shows the pressure distributions over the latter half of the blade tip. Here a steep pressure gradient can be seen within the bubble from midchord, to the trailing edge. This pressure gradient suggests that the flow within the separation bubble is in a chordwise direction from the trailing edge towards midchord. To determine the direction of the flow within the bubble a study was done using oil flow visualization at a clearance gap of 4% chord. Oil was seen to move sluggishly from the trailing edge towards midchord even though the turbine rig was vertical and the oil had to move upwards against gravity.

Figure 7.4 is a schematic of the direction of flow within the separation bubble. It is these flows towards mid chord that cause fluid to accumulate at mid chord as can be seen in Figure 7.5. This accumulated fluid is forced to mix with the gap inlet jet in order to move towards the relatively higher pressure at the gap exit as suggested by Bindon (1988a). Bindon (1988a) suggested that this mixing process may form the major part of the internal

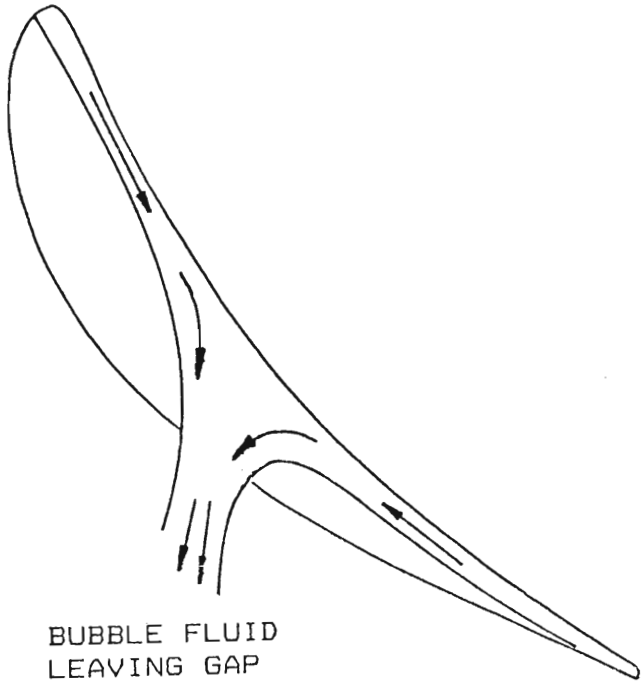

FIGURE 7.4 DIRECTION OF FLOW WITHIN SEPARATION BUBBLE. FLOW OVER FORWARD AND REAR PART OF BLADE IS TOWARDS MIDCHORD WHERE IT MIXES WITH THE MAIN LEAKAGE FLOW.

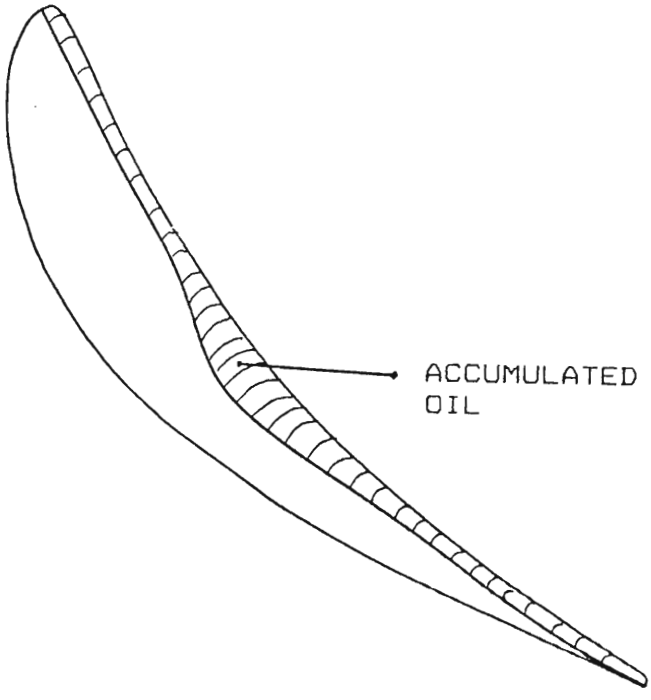

FIGURE 7.5 FLOW ACCUMULATION AT MIDCHORD

gap loss and that it appeared to play an important role in decreasing the mass flow rate through the gap.

An interesting result, not seen before, was that the pressure begins to fall to suction surface pressure well within the parallel walls of the tip and endwall. Studying Figures 7.2 and 7.3, it can be seen that this effect decreases from leading edge to trailing edge.

Figure 7.6 compares the static pressures on the suction and pressure corners between a blade with clearance and a blade with no clearance. To obtain the zero clearance blade loading, the gap was sealed with felt and the rotating casing was kept stationary. Figure 7.6 clearly demonstrates how the static pressure at the suction and pressure corners drops well below the suction surface pressure encountered on the blade with the sealed gap. This corresponds to linear cascade measurements taken by Bindon (1987a). The pressure surface (with clearance) curve was generated by taking the minimum measured pressure at the pressure surface corner.

In Figure 7.7 the average separation bubble pressure and the pressure of the reattached flow after the bubble is shown. It can be seen that the flow leaving the separation bubble has to move to a higher pressure. The only way it can do this is by mixing with the high velocity (kinetic energy) flow coming through the gap over the bubble. The chordwise pressure distribution within the bubble can also clearly be seen from Figure 7.7. The lowest pressure within the bubble is found at around mid chord.

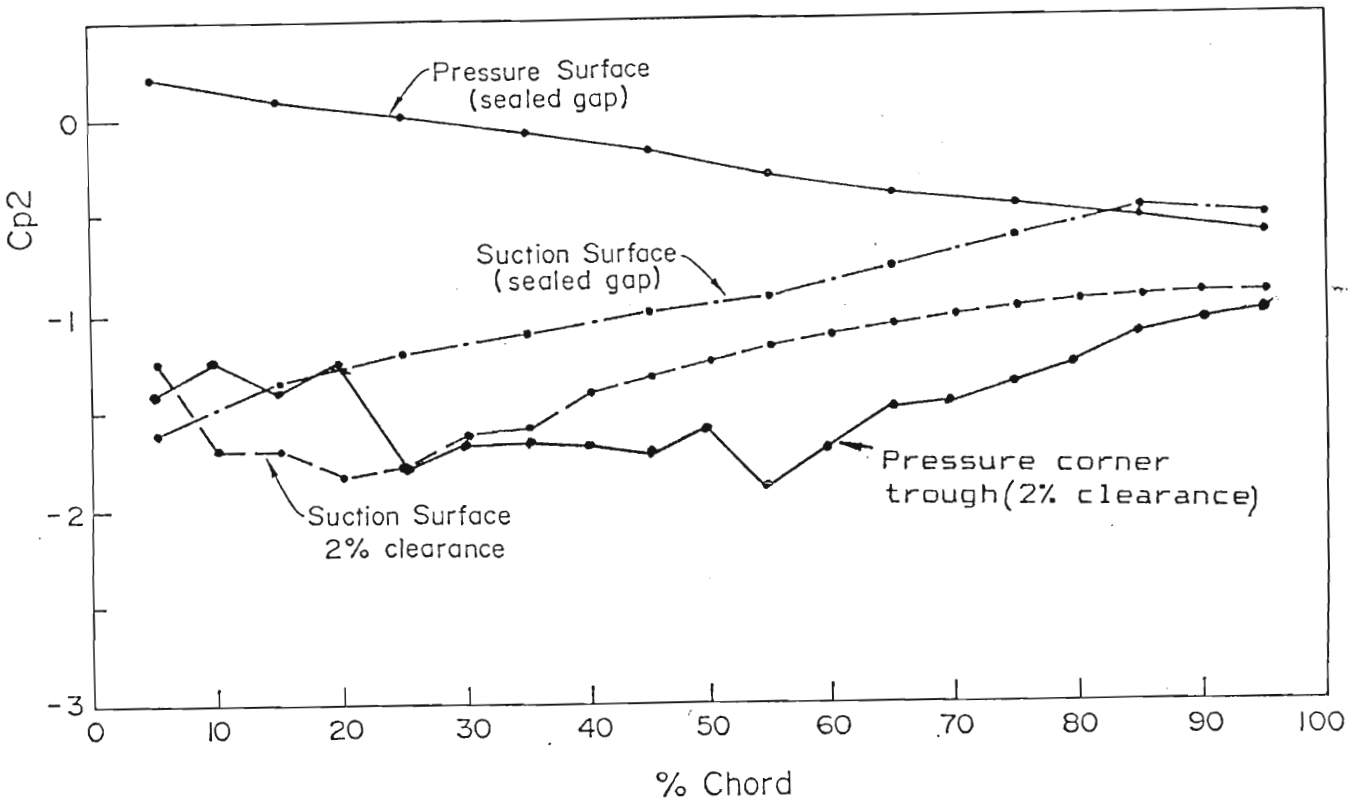

FIGURE 7.6 EFFECT OF CLEARANCE ON BLADE PROFILE PRESSURE DISTRIBUTIONS

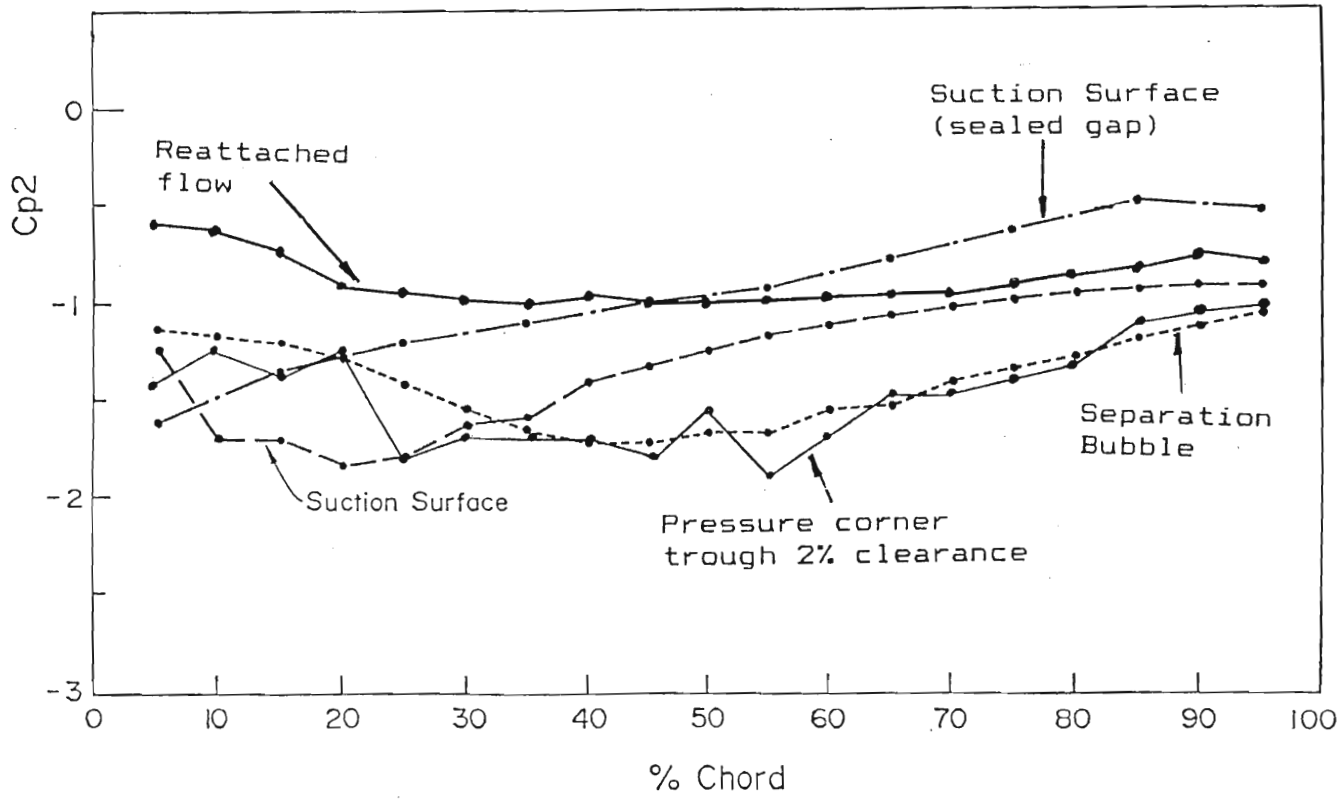

FIGURE 7.7 GAP TIP PRESSURE DISTRIBUTIONS OF PRESSURE CORNER TROUGH, SEPARATION BUBBLE, REATTACHED FLOW AND SUCTION CORNER.

7.2 THE EFFECT OF RELATIVE MOTION ON STATIC PRESSURE DISTRIBUTION

The effect of having relative motion between the blade tip and the endwall was examined by keeping the rotating wall stationary. The pressure distributions were only taken at 4 stations namely 30%, 40%, 50% and 60% of chord. The relative motion of the casing in an axial turbine is in the opposite direction to that of the leakage flow as shown in Figure 7.8.

Figure 7.9 (a,b,c,d) show the distribution obtained with the stationary casing and compare these to the case with relative motion. These results are seen to be similar to those obtained in the linear cascade of Bindon (1987a). The pressure level and width of the separation bubble was little affected by relative motion. The pressure level was affected mostly at mid chord. This coincides with the area where the mixed out bubble flow emerges. In Bindon (1987c) a relatively loss free core layer was seen over most of the gap except for midchord where the mixed out bubble flow is thought to emerge.

In the areas where the boundary layers of the casing and tip do not interact the effect is minimal. The pressures found in the area after the separation bubble (i.e. the attached flow) are significantly higher (about 14%) for the case with relative motion. As mentioned earlier the wall motion is in the opposite direction to the leakage flow. This creates additional viscous shear within the clearance gap causing the amount of fluid leaking through the gap to decrease and thus increasing the

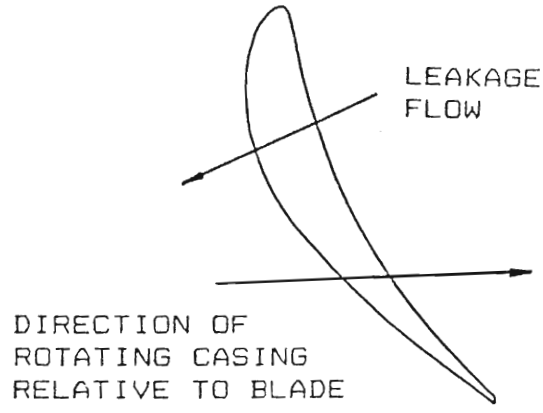

FIGURE 7.8 DIRECTION OF ROTATING WALL RELATIVE TO LEAKAGE FLOW.

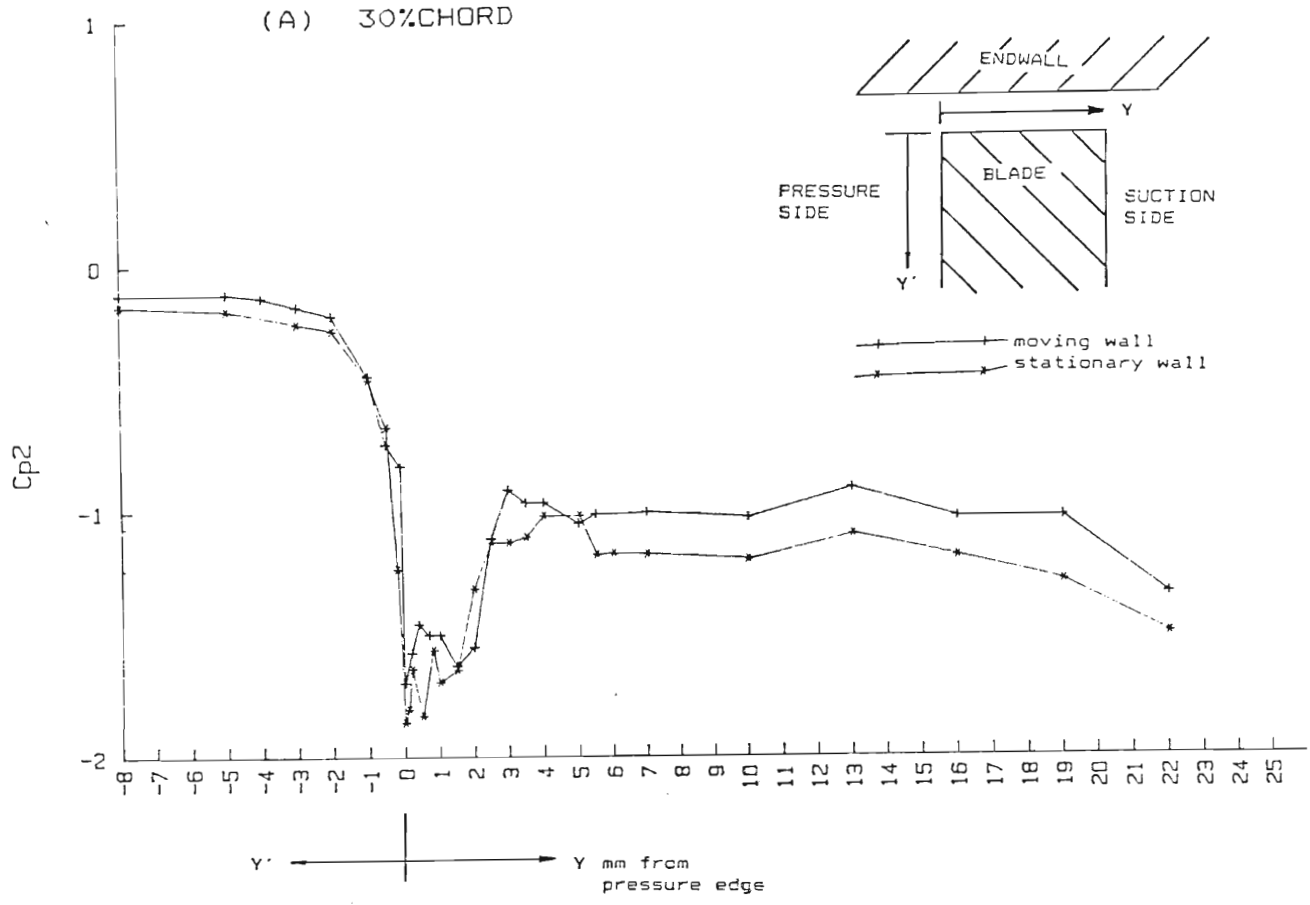

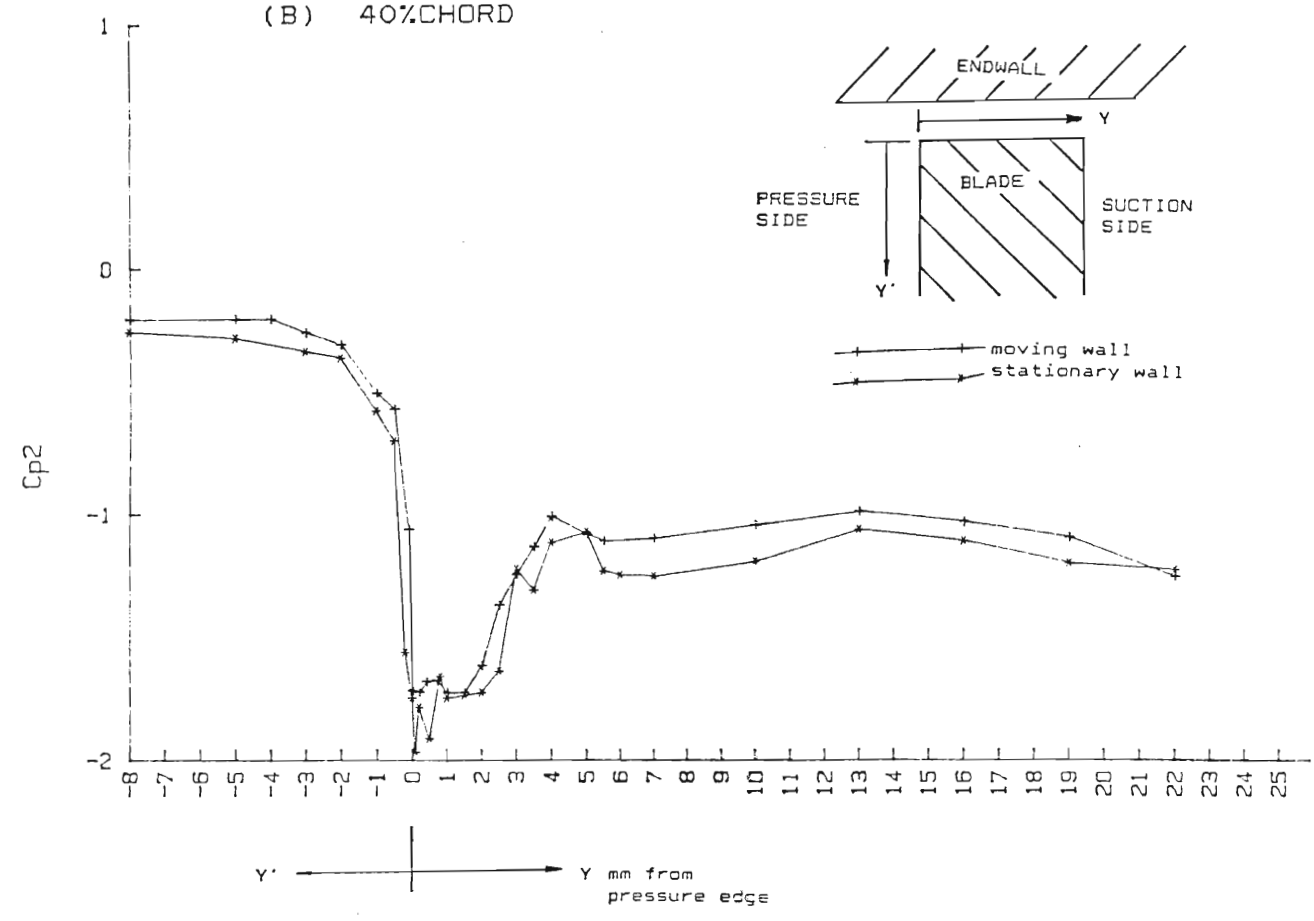

FIGURES 7.9 EFFECT OF RELATIVE MOTION ON THE BLADE PRESSURE DISTRIBUTIONS IN THE TIP CLEARANCE GAP.

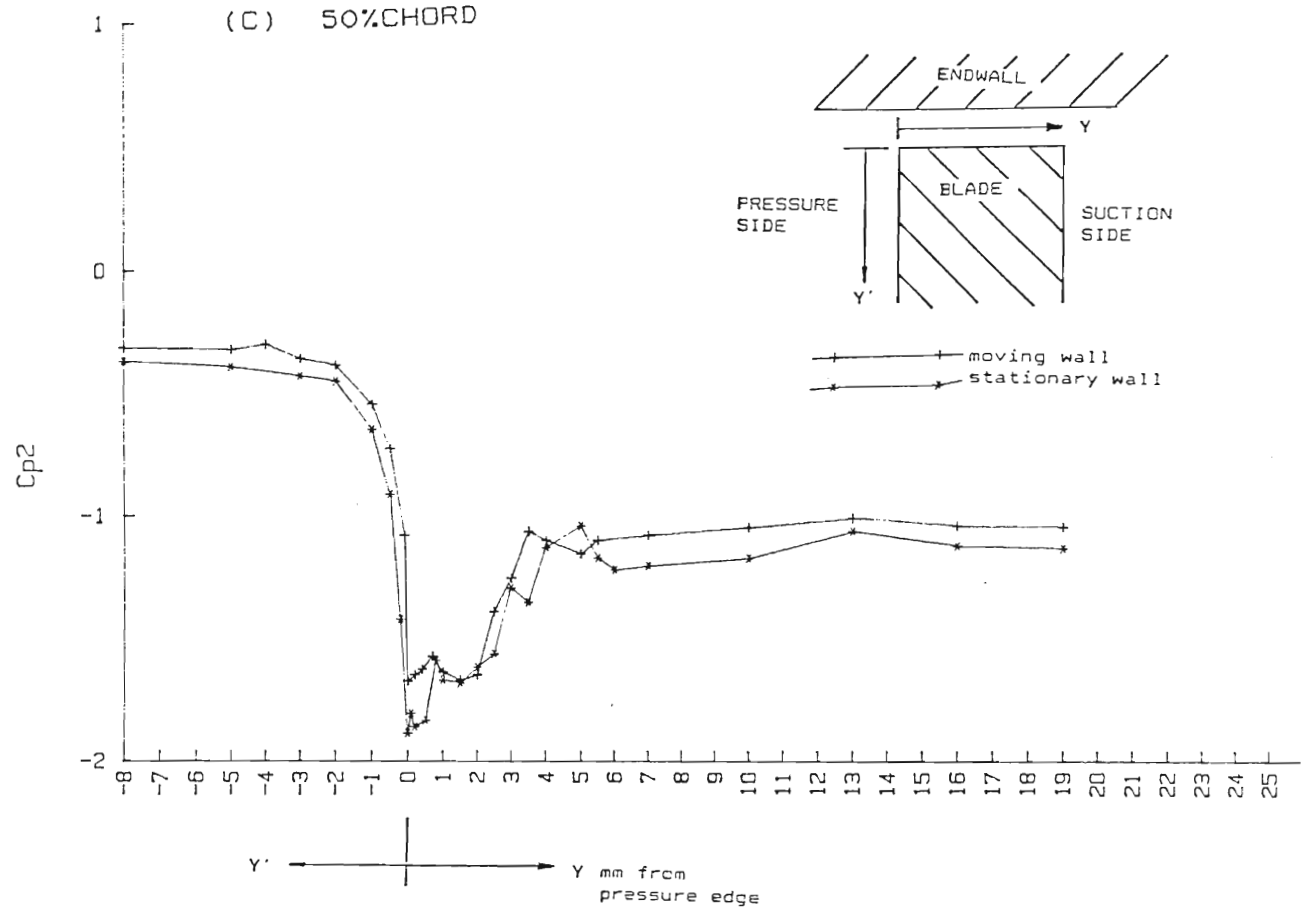
(C) 50%CHORD
ENDWALL
Y
BLADE
PRESSURE SIDE
SUCTION SIDE
Y'
moving wall
stationary wall
Cp2
1
0
-1
-2
-8 -7 -6 -5 -4 -3 -2 -1 0 1 2 3 4 5 6 7 8 9 10 11 12 13 14 15 16 17 18 19 20 21 22 23 24 25
Y'
Y mm from pressure edge

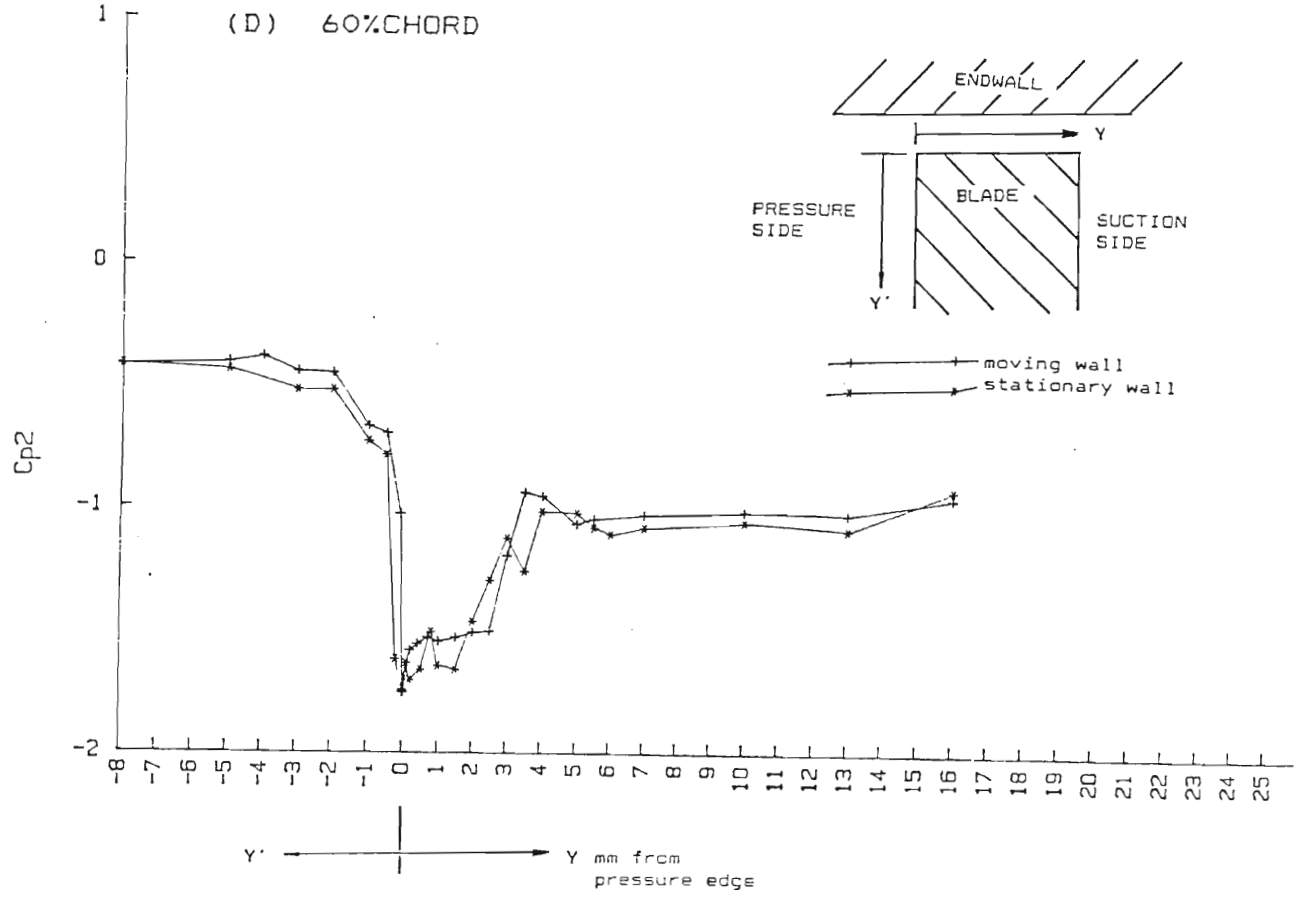
(D) 60%CHORD
ENDWALL
Y
BLADE
PRESSURE SIDE
SUCTION SIDE
Y'
moving wall
stationary wall
Cp2
1
0
-1
-2
-8 -7 -6 -5 -4 -3 -2 -1 0 1 2 3 4 5 6 7 8 9 10 11 12 13 14 15 16 17 18 19 20 21 22 23 24 25
Y'
Y mm from pressure edge

static pressure. If this leakage flow is decreased then it is reasonable to assume that the leakage vortex downstream of the clearance gap will be decreased in strength which was in agreement to the findings of Graham (1985).

An oil flow visualization study was also done on the blade with the wall held stationary but there was no noticeable difference between the stationary and rotating wall cases.

7.3 THE EFFECT OF CLEARANCE GAP SIZE ON THE CLEARANCE FLOW

The effect of gap size on the clearance flow was examined in the annular cascade with relative motion between the casing and blade tip. Static pressure distributions were taken at the slots at 30%, 40%, 50% and 60% chord, and oil flow visualization was done and photographed through the transparent rotating casing. The oil flow could not be seen at the trailing edge since it was hidden by the metal casing.

Studying the flow visualization photographs in Figure 7.10 it can clearly be seen that the bubble width increases with clearance. The bubble also tends to widen with chordwise distance and at the 4% clearance gap, the accumulation of fluid can clearly be seen at midchord. Figure 7.11 shows graphs of bubble width versus clearance gap size for the 4 chordwise stations at which measurements were taken. From these graphs it is obvious that the bubble width increases with clearance gap size. This is similar to what Bindon (1986b; 1987b) found by using smoke flow visualization. Moore & Moore (1986) claimed that the bubble width

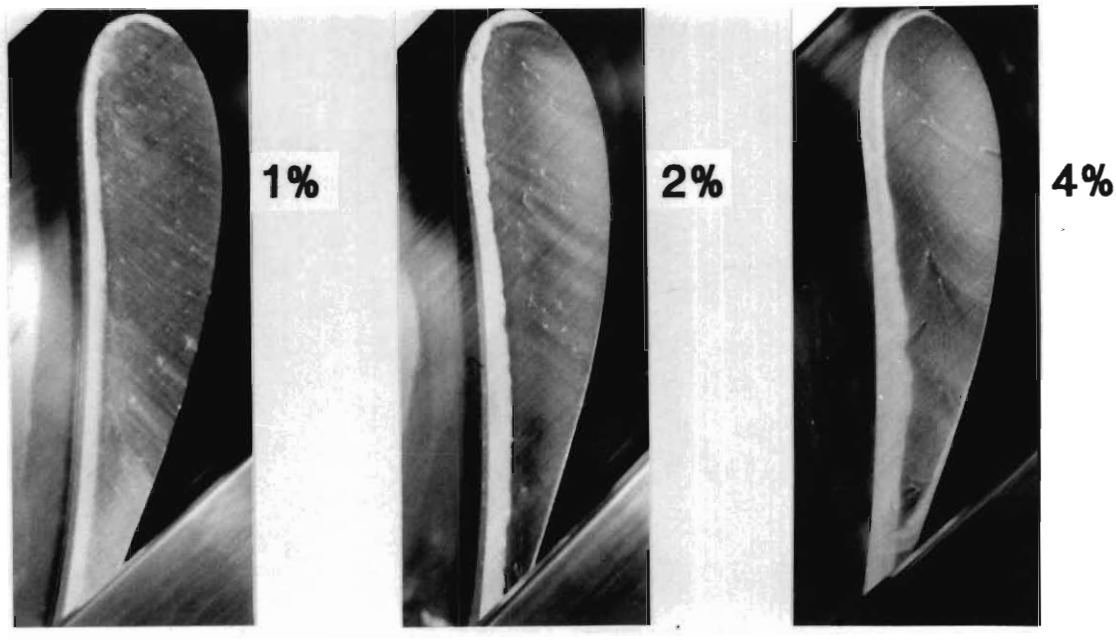

FIGURE 7.10 EFFECT OF GAP SIZE ON SEPARATION BUBBLE WIDTH
(SEPARATION BUBBLE SHOWN BY WHITE AREA ON PRESSURE SIDE OF TIP)

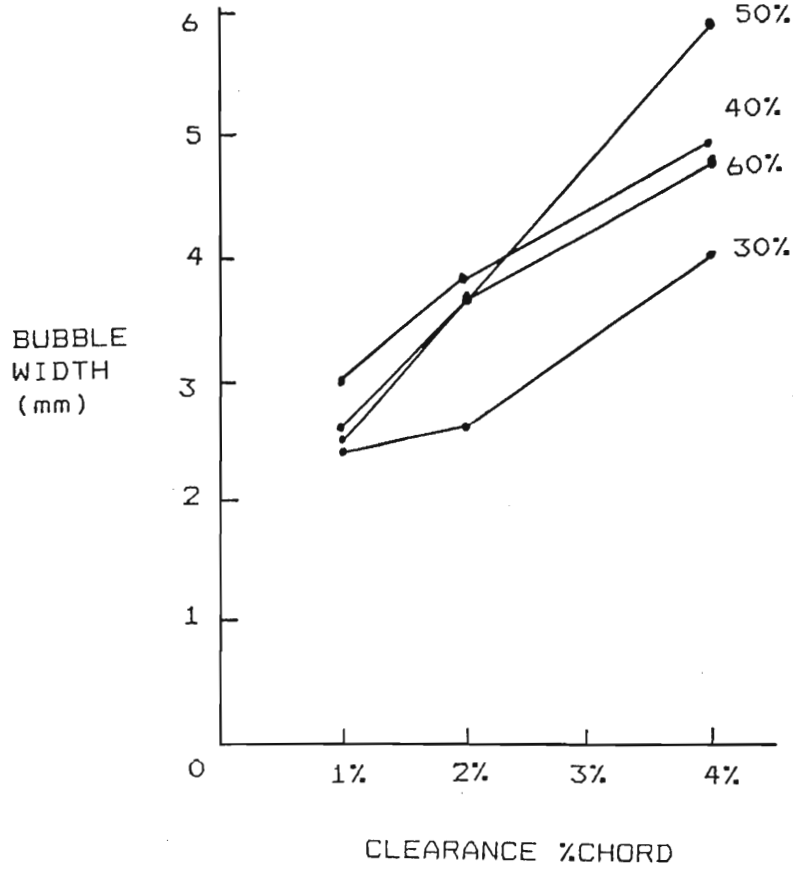

FIGURE 7.11 GRAPH OF BUBBLE WIDTH VERSUS GAP SIZE

was twice the gap size. From Figure 7.11 this can be seen to be an approximation as the bubble width varies anything from 0.9 to 2.6 times the gap size. Moore & Moore (1986) also did not show that width of the separation bubble varied with axial distance.

The bubble widths seen on the oil flow visualization photographs were measured and are indicated on the pressure distributions with arrows (Figures 7.12 a,b,c,d). The edge of the visible separation bubble was seen to closely coincide with the end of the pressure rise. As is shown in Figure 7.13 the pressure rise after the separation bubble signifies reattachment. At the reattachment point the flow is in a direction towards the tip surface causing the flow to stagnate and thus increase the static pressure. The pressure distributions of Bindon (1986a) were analyzed in this manner and his results also showed an increase in bubble width with gap size.

As shown in Figure 7.12(a,b,c,d), the separation bubble pressure was strongly dependent on gap size, but the relationship was not monotonic. A minimum pressure was found for the 2% clearance case. This was true for all readings taken from 30% to 60% of chord. This trend can also be seen in results of Bindon (1986a).

In the attached region after the separation bubble, the static pressure was seen to increase with gap size. This effect is probably due to the fact that, as the clearance is increased, the effect that the "vena-contracta" has on the clearance gap flow is decreased, and thus the pressure levels encountered are not as extreme.

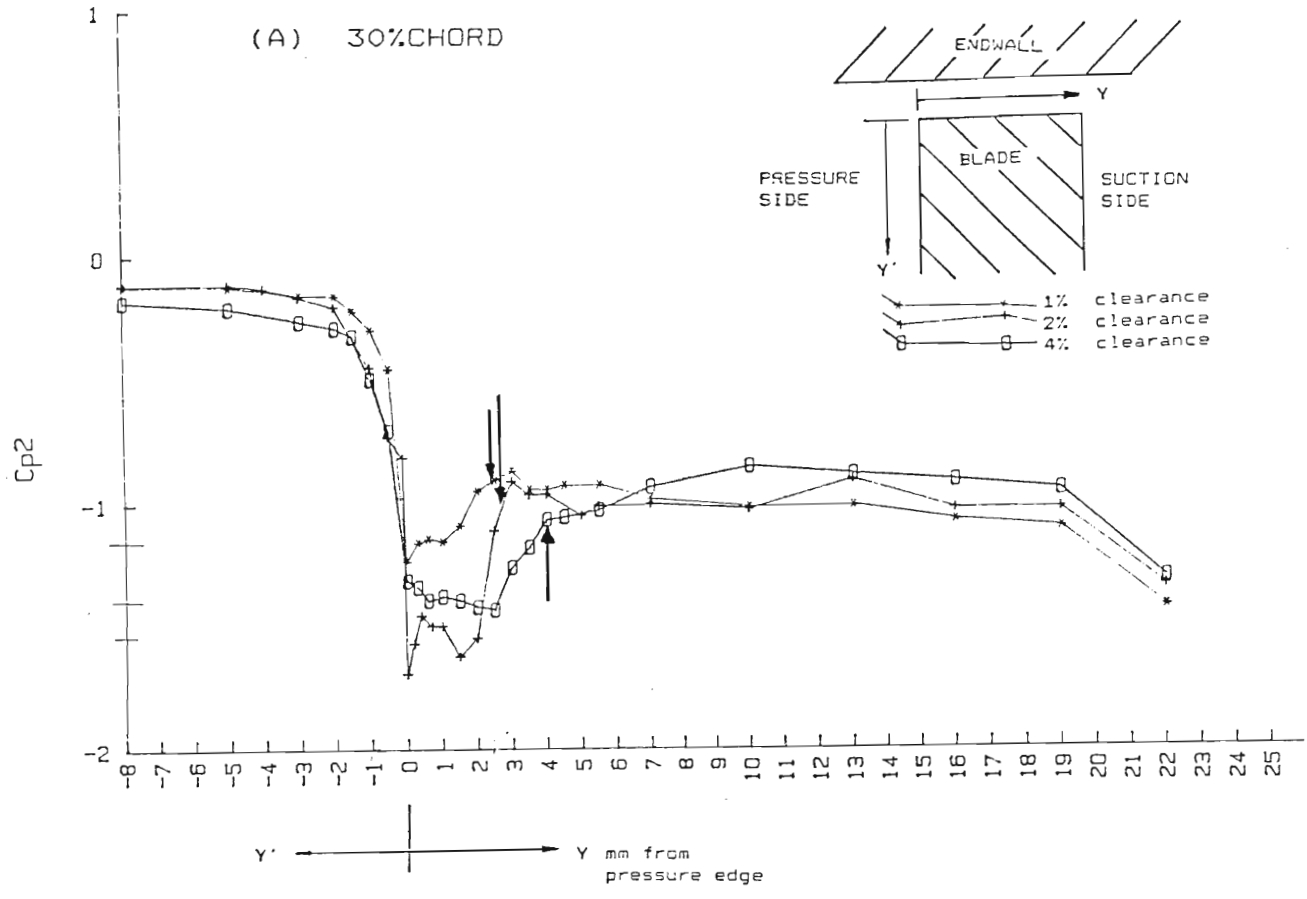

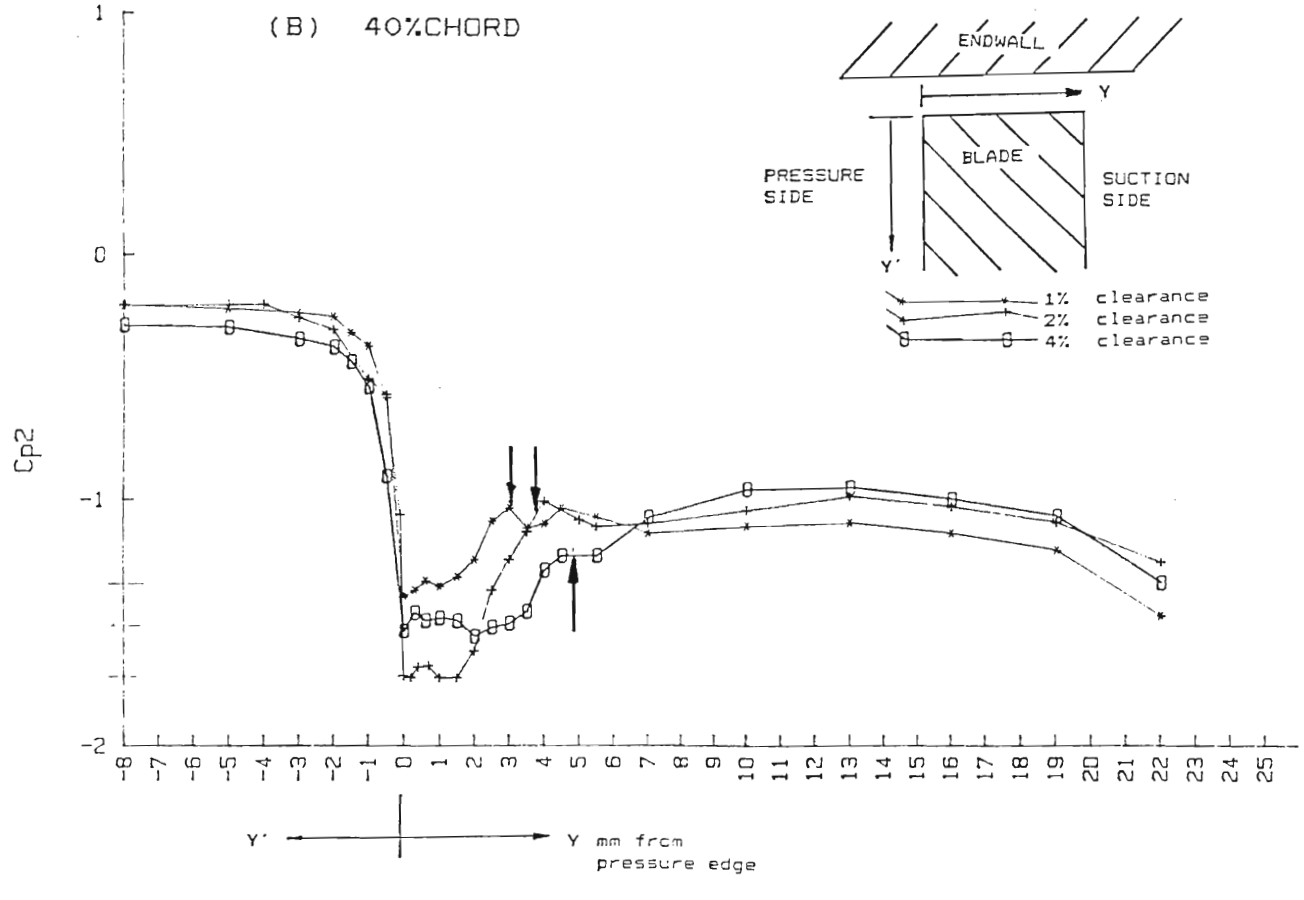

FIGURE 7.12 EFFECT OF GAP SIZE ON THE PRESSURE DISTRIBUTION

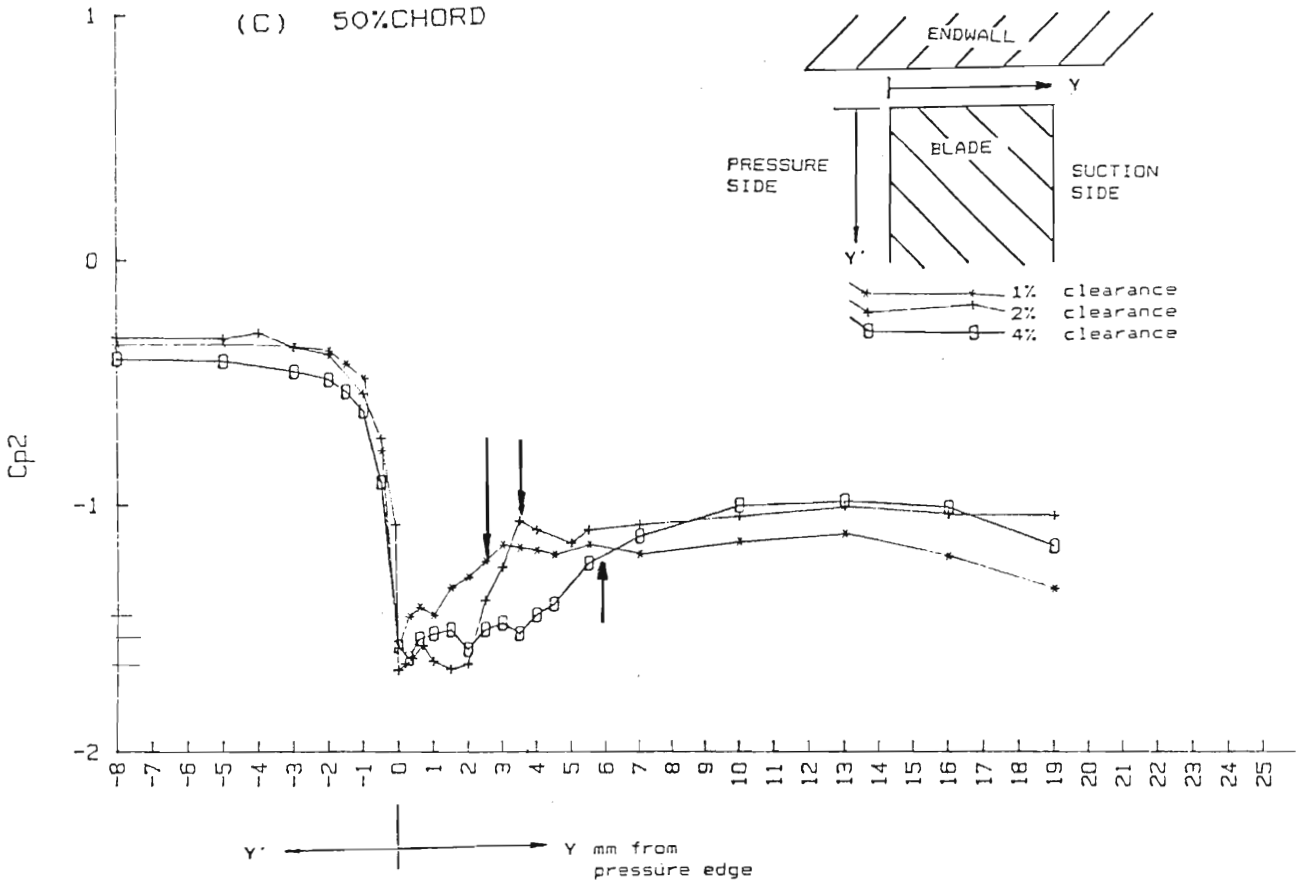
(C) 50%CHORD
ENDWALL
Y
BLADE
PRESSURE SIDE
SUCTION SIDE
Y'
1% clearance
2% clearance
4% clearance
Cp2
1
0
-1
-2
-8 -7 -6 -5 -4 -3 -2 -1 0 1 2 3 4 5 6 7 8 9 10 11 12 13 14 15 16 17 18 19 20 21 22 23 24 25
Y'
Y mm from pressure edge

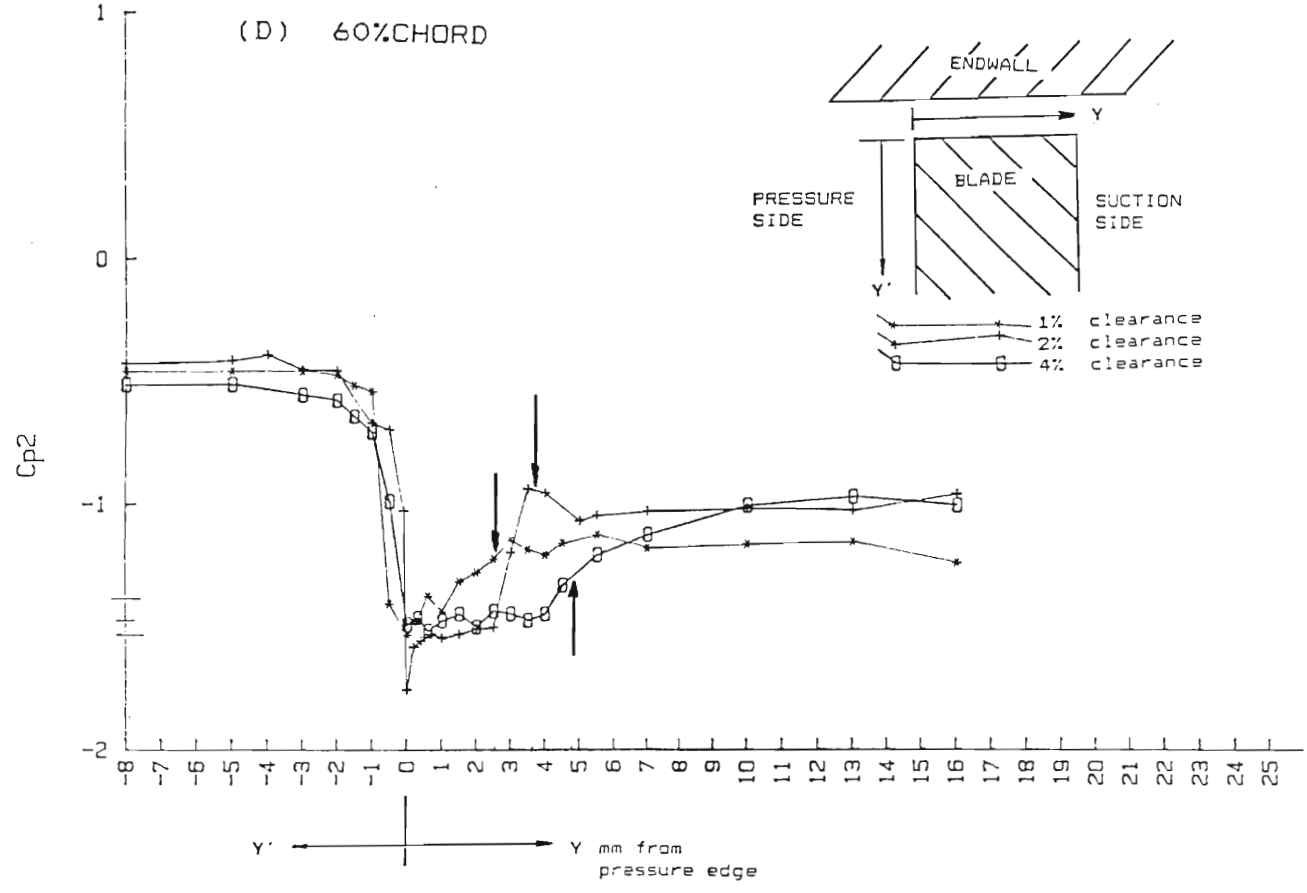
(D) 60%CHORD
ENDWALL
Y
BLADE
PRESSURE SIDE
SUCTION SIDE
Y'
1% clearance
2% clearance
4% clearance
Cp2
1
0
-1
-2
-8 -7 -6 -5 -4 -3 -2 -1 0 1 2 3 4 5 6 7 8 9 10 11 12 13 14 15 16 17 18 19 20 21 22 23 24 25
Y'
Y mm from pressure edge

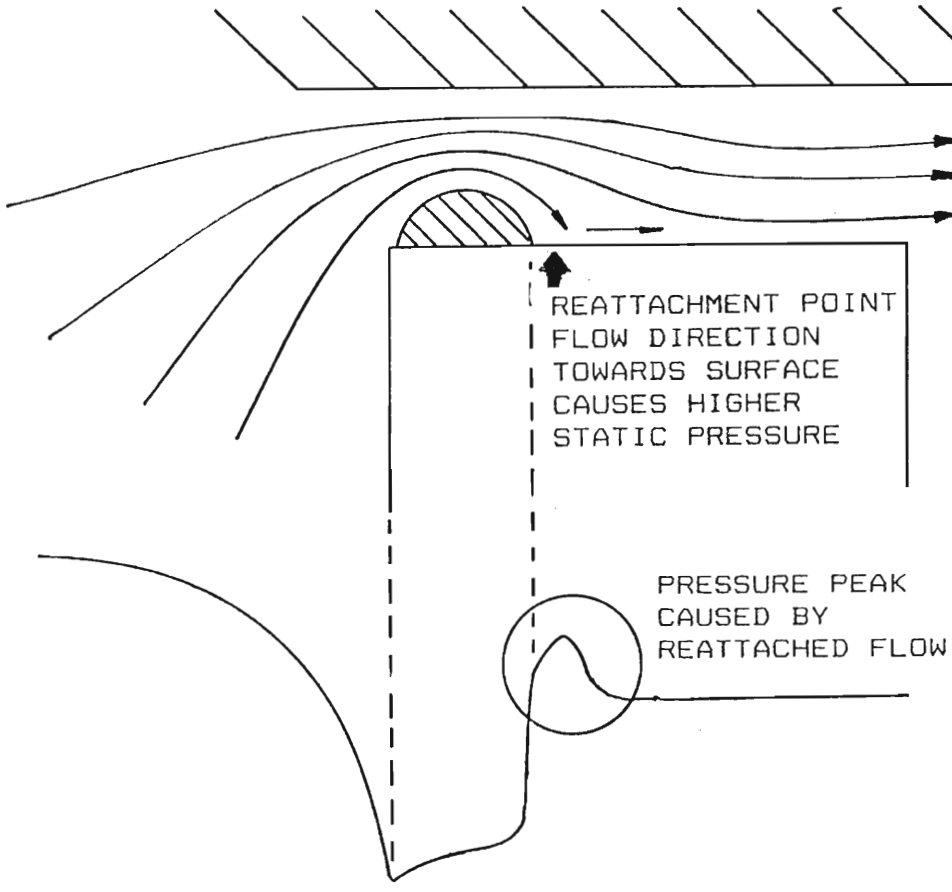

FIGURE 7.13 REATACHED FLOW CAUSES SMALL PRESSURE RISE

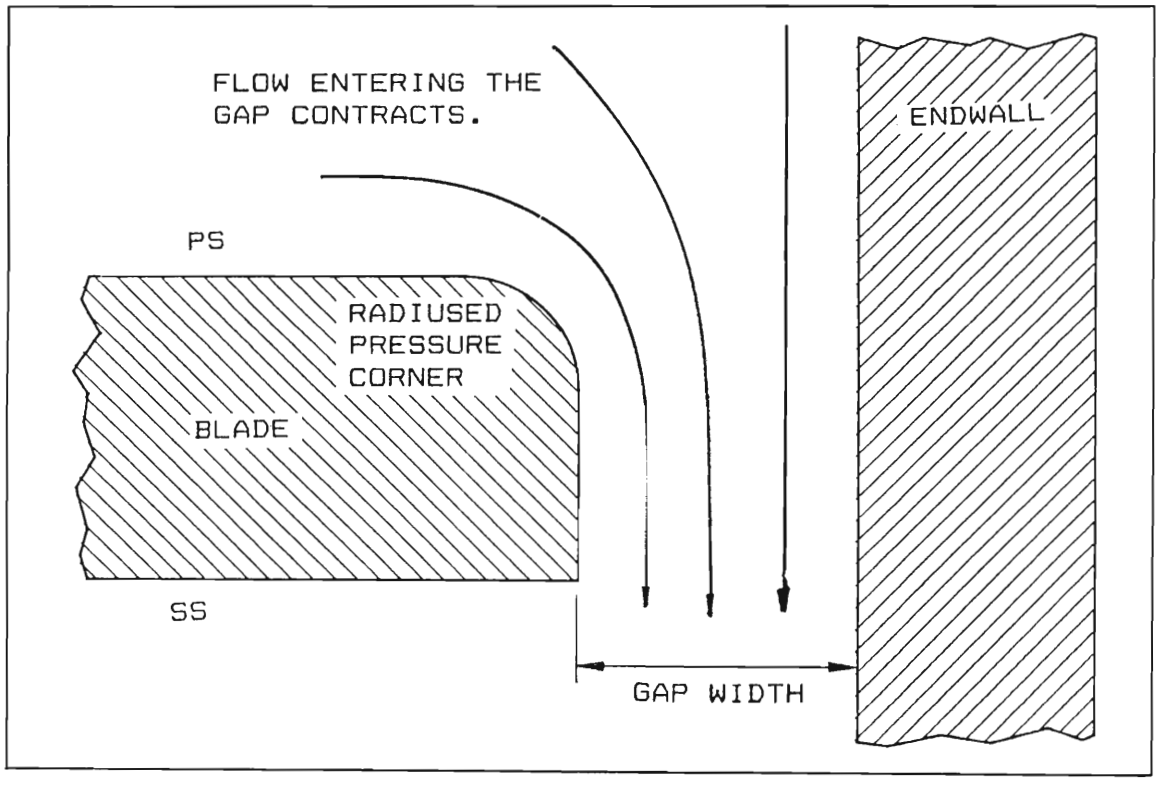

FIGURE 7.14 RADIUSED PRESSURE CORNER TO ELIMINATE SEPARATION BUBBLE

The pressures at the suction surface corner do not follow the pattern found in the attached flow regime. A possible explanation here is that, as the clearance is increased, the vortex strength is also increased causing a longer depression on the suction surface.

7.4 THE EFFECT OF BLADE EDGE RADIUS ON THE CLEARANCE GAP FLOW

Bindon (1988a) showed that some 40% of the overall loss in the tip region was generated within the gap. This internal gap loss was mainly associated with the separation bubble. Bindon (1986a, 1987a) did a brief study on the effect of radiusing the pressure edge corner and found that this decreased the corner pressure depression caused by the flow remaining attached around the corner. It was thus important to find out at what radius the bubble could be eliminated and what effect this would have on the clearance gap flow.

As shown in Figure 7.14, as the flow enters the gap it undergoes a sudden contraction. The rate at which the flow contracts (and thus whether the separation takes place or not) is dependent on the inlet pressure corner radius. Tests were done at a fixed gap width of 2% chord, and once the critical radius had been established as a ratio of gap width, a single test was done at a smaller gap width for confirmation. The separation bubble was monitored using surface oil flow visualization and static pressure measurements. Due to machining limitations the flat (or square) tipped blade had a finite radius at the pressure corner. This pressure corner radius was measured and found to be 1/4 gap

widths (0.5% chord). This radius was gradually increased until the separation bubble had disappeared. Tests were done at radii of 0.25, 0.5, 1, 1.5, 2.5 gap widths (0.5%, 1%, 2%, 3%, 5% chord).

Flow visualization was done over the complete blade whereas pressure distributions were only taken at 30%, 40%, 50% and 60% chord slots. The pressure distributions for the different radii were plotted on the same axis for comparison. A method was used whereby the actual surface distance on the radiused corner was projected on to the square surfaced blade tip. This transformation is shown in Figure 7.15.

Figure 7.16 shows the surface flow visualization for pressure edge radii of .25, 1, 1.5 and 2.5 gap widths (.5%, 2%, 3%, and 5% chord). For the blade with the smallest radius the separation bubble can clearly be seen to extend from the leading edge right up to the trailing edge. The blade with the pressure edge radius of 2% chord was seen to have a thin separation bubble with reattachment from leading edge up to about midchord. This separation bubble seems to be very thin and only starts part way around the radius. From midchord to the trailing edge the flow appears to remain separated over the surface. Increasing the radius further to 3% chord, the flow appears to have even a smaller separation zone over the first half of the blade with no separation evident from midchord to the trailing edge. At 5% chord pressure edge radius the flow remains attached all the way around the corner and for the remainder of the gap surface.

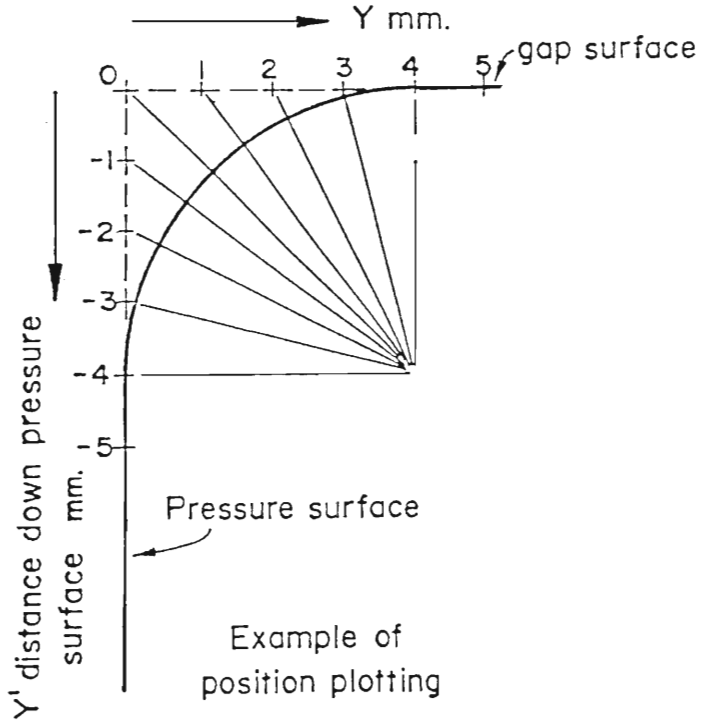

FIGURE 7.15 METHOD USED FOR PLOTING PRESSURE DISTRIBUTIONS FOR RADIUSED PRESSURE CORNER BLADES

.5% 2% 3% 5%

FIGURE 7.16 SURFACE OIL FLOW VISUALIZATION SEEN THROUGH MOVING TRANSPARENT CASING SHOWING GAP SEPARATION BUBBLE FOR INCREASING PRESSURE EDGE RADIUS AND A CLEARANCE GAP OF 2% CHORD

Figure 7.17 (a,b,c,d) shows the pressure distributions for pressure edge radii of 0.25, 0.5, 1, 1.5 and 2.5 gap widths. For the sharp edge case or 0.25 gap width radius, the typical pressure depression due to the separation bubble is clearly shown. At a pressure edge radius of 0.5 gap widths, this depression is decreased, but the general shape is still evident. The end of the pressure rise after the separation bubble depression, coincides with the point of reattachment seen in the flow visualization. For the larger radii the depression is seen to decrease even further until at a pressure edge radius of 2.5 gap widths, the pressure drops from the pressure surface to suction surface in a monotonic fashion. In the area of attached flow after the separation bubble, the pressure was lowest for the blade tip with a pressure edge radius of 2.5 gap widths. This is probably due to the fact that since the flow remained attached right through the gap, the higher velocities reached, caused a lower static pressure. The pressure in this region strongly depends on how much loss is generated within the gap.

In order to confirm that a pressure edge radius of 2.5 gap widths eliminates separation within the clearance gap, a single test was done at a different gap size. The clearance gap size was set at 0.8% chord and a blade with an edge radius of 2% chord (2.5 gap widths) was tested. Here no signs of separation were noticed, confirming that a pressure edge radius of 2.5 gap width avoids separation.

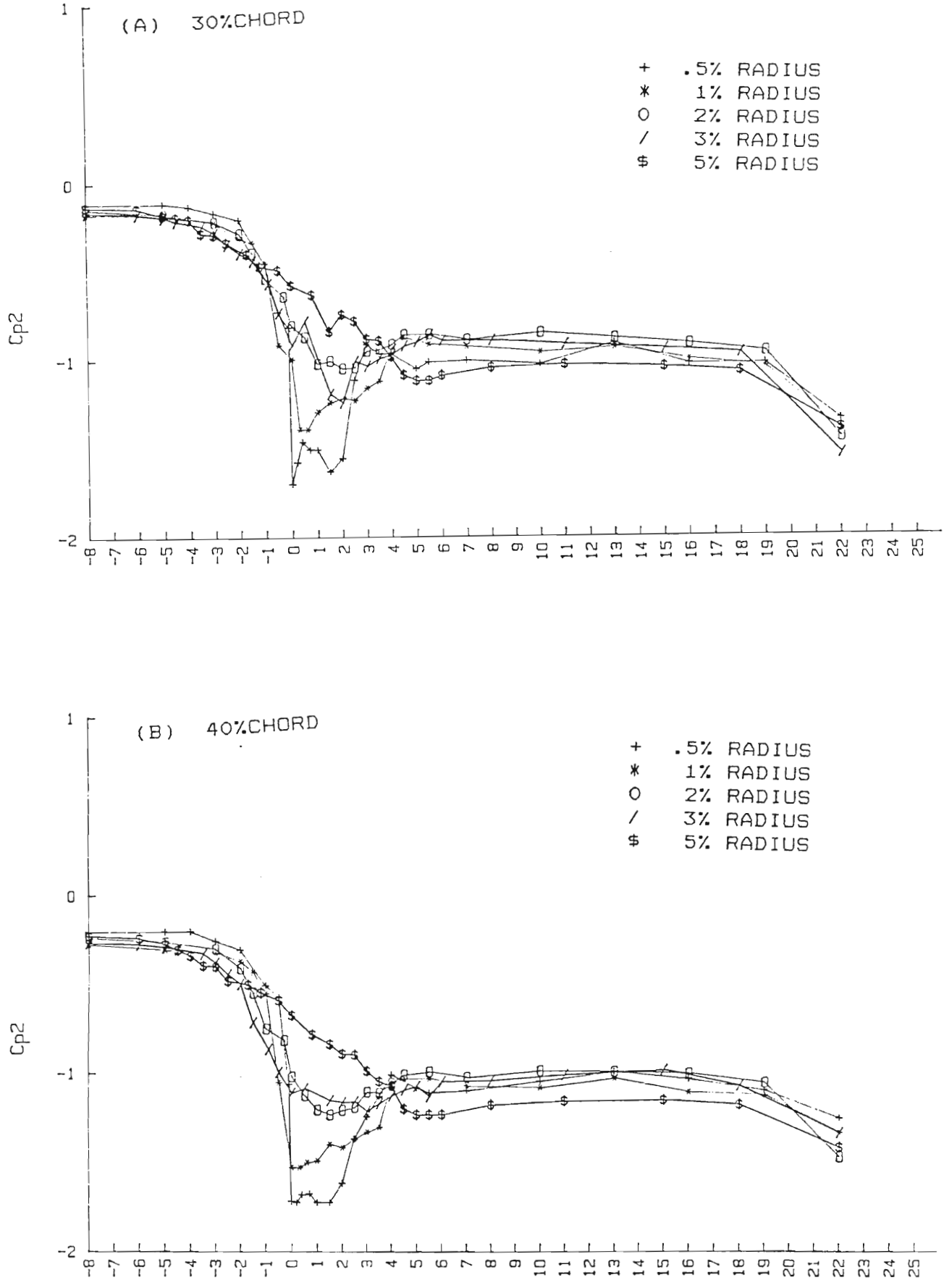

FIGURE 7.17 EFFECT OF PRESSURE EDGE RADIUS ON THE SEPARATION BUBBLE AND THE BLADE GAP PRESSURE DISTRIBUTION

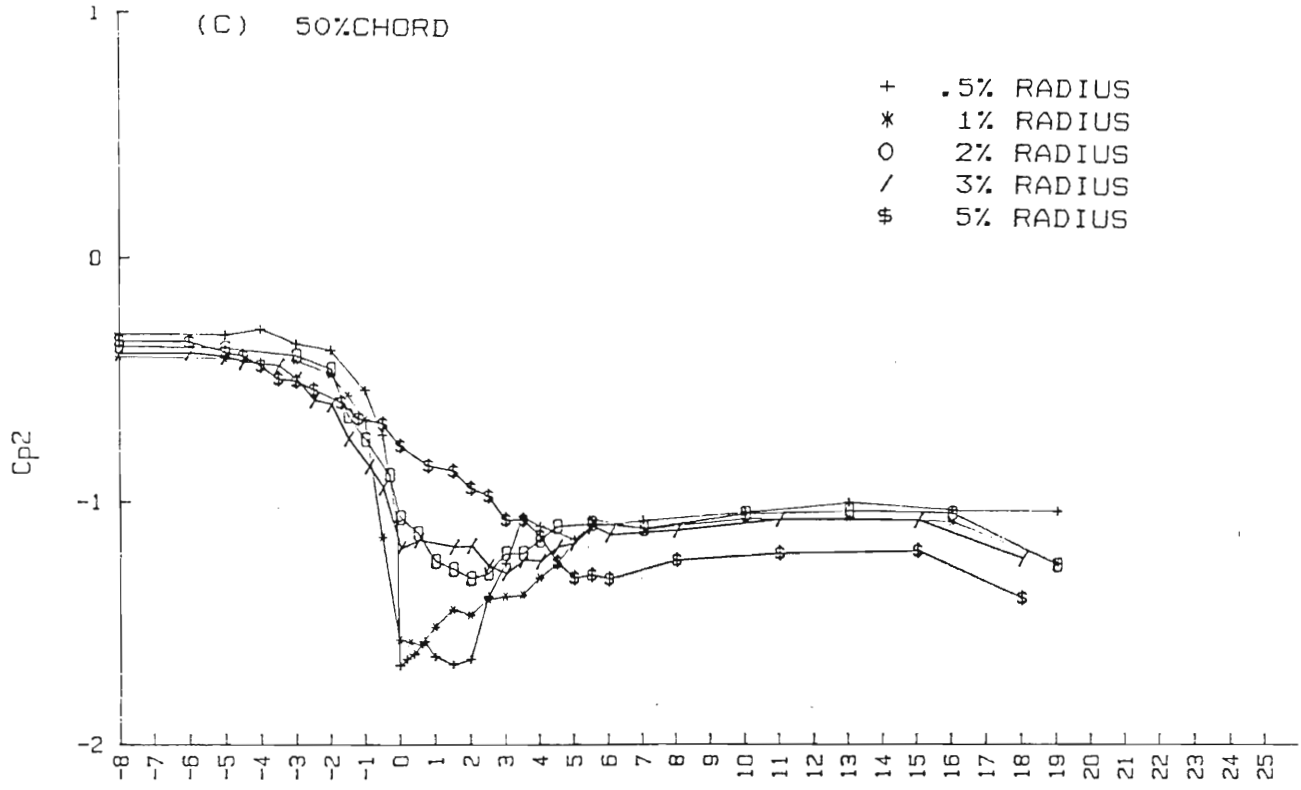
(C) 50%CHORD
+ .5% RADIUS
* 1% RADIUS
O 2% RADIUS
/ 3% RADIUS
$ 5% RADIUS
Cp2
1
0
-1
-2
-8 -7 -6 -5 -4 -3 -2 -1 0 1 2 3 4 5 6 7 8 9 10 11 12 13 14 15 16 17 18 19 20 21 22 23 24 25

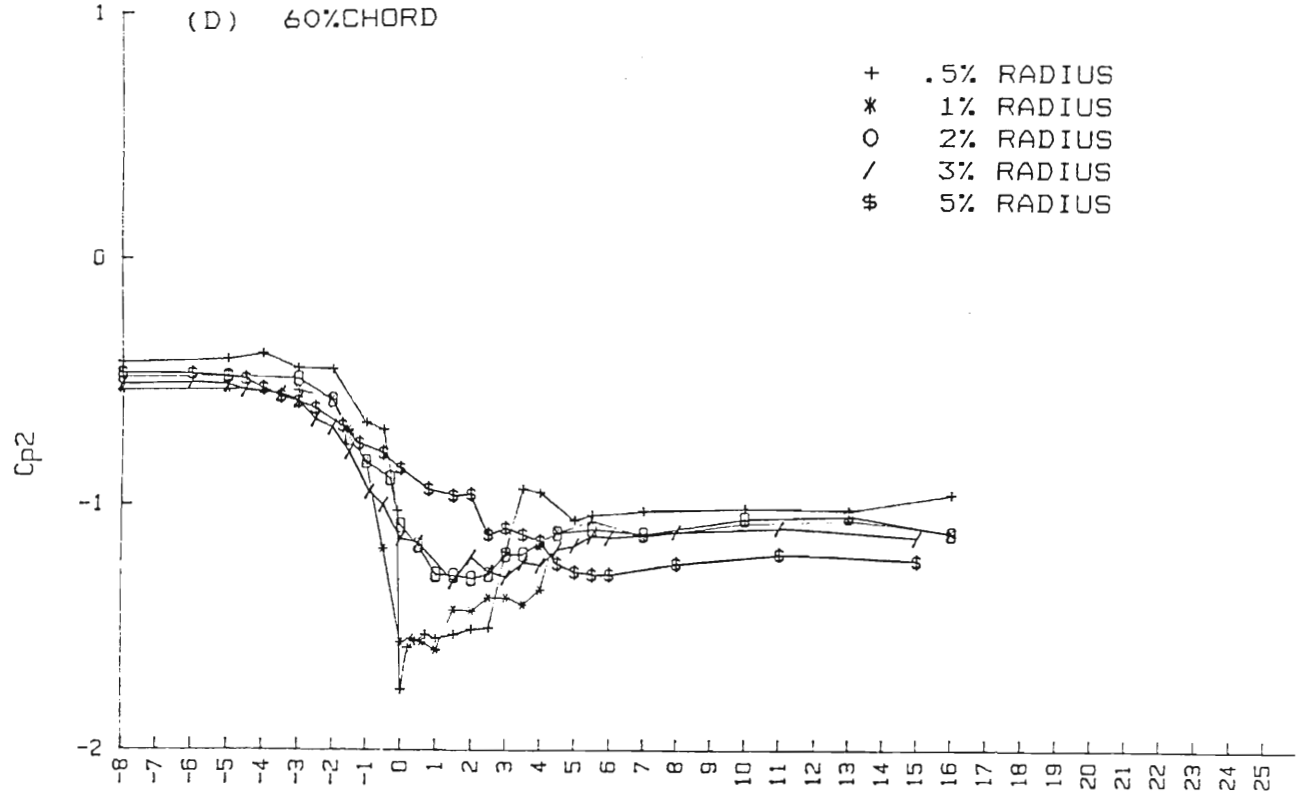
(D) 60%CHORD
+ .5% RADIUS
* 1% RADIUS
O 2% RADIUS
/ 3% RADIUS
$ 5% RADIUS
Cp2
1
0
-1
-2
-8 -7 -6 -5 -4 -3 -2 -1 0 1 2 3 4 5 6 7 8 9 10 11 12 13 14 15 16 17 18 19 20 21 22 23 24 25

CHAPTER 8

PERFORMANCE EVALUATION OF 3 BLADE TIP GEOMETRIES

The results discussed in this chapter were obtained from pitot static measurements taken in the linear cascade (described in Chapter 4). In Section 7.2 it was seen that relative motion between the blade tips and the rotating casing did not have a marked effect on the nature of the tip clearance flow. The most significant result with relative motion seemed to be a decrease in flow rate through the gap. Since the endwall and tip boundary layers do not interact viscously over the majority of the gap, it can be assumed that the effect of relative motion would be similar on different blade tip geometries. The relative performance of different blade tip geometries could thus be examined in a large linear cascade with a stationary endwall for ease of taking measurements.

As mentioned in Chapter 4 a proprietary blade profile as used by Bindon (1986a, 1986b) was used so that results could be directly compared. The boundary layer at inlet to the cascade was measured using a 0.9mm diameter single hole total pressure probe. The static pressure was measured from a tapping in the endwall. As shown in Figure 8.1 the velocity profile was quite different to that obtained by Bindon (1986a). The boundary layer was thus thickened using a 4mm diameter trip wire 190mm upstream of the blade leading edges. The thickened boundary layer velocity profile was seen to be similar in shape to that obtained by Bindon.

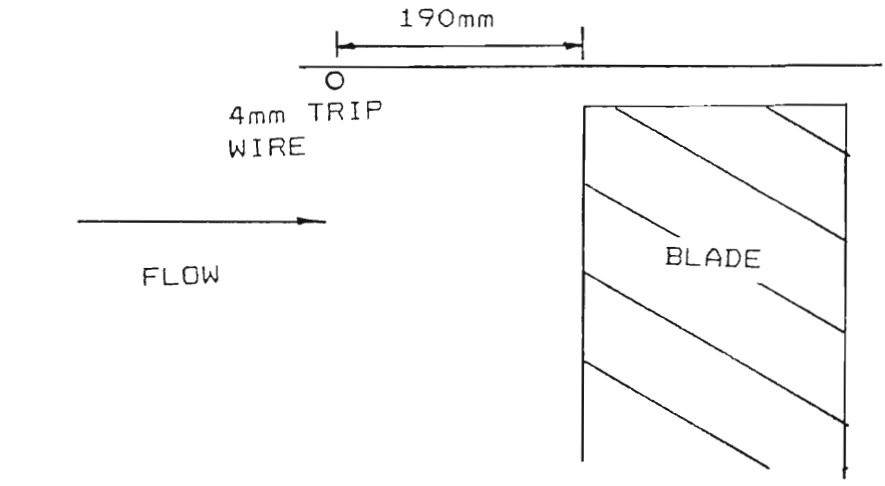

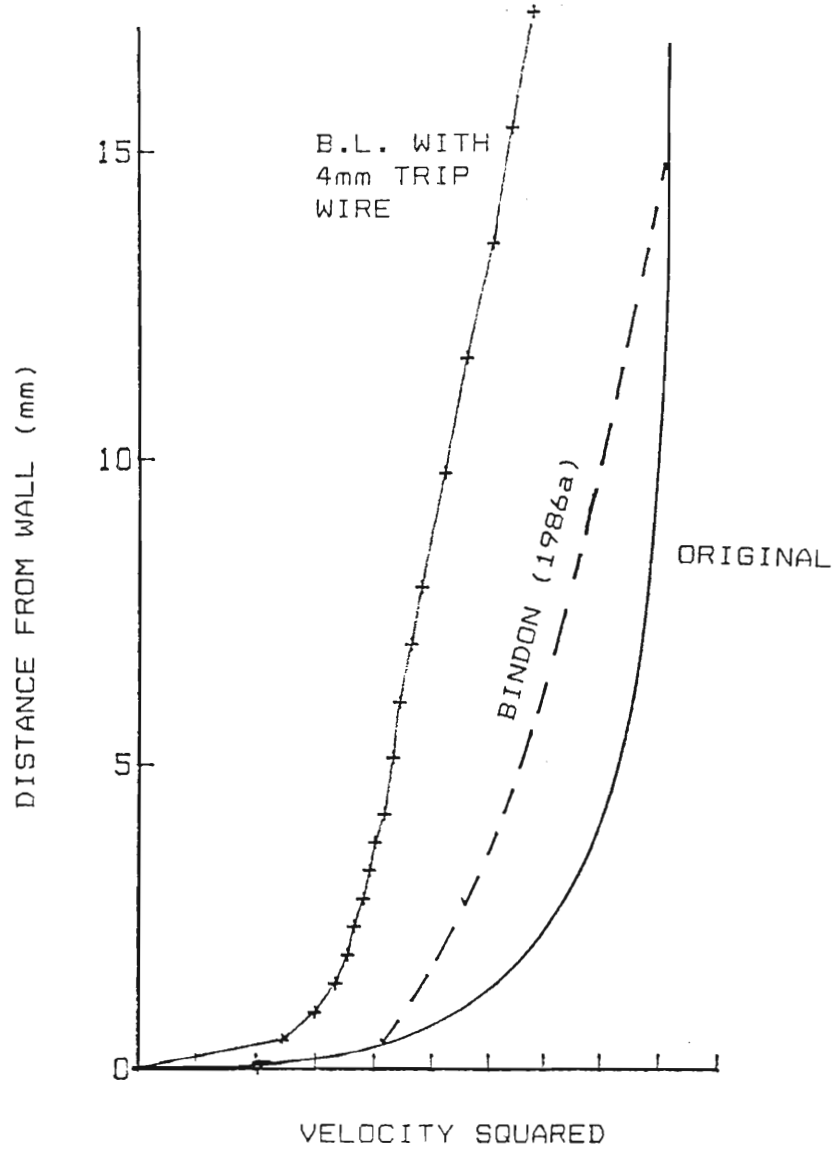

FIGURE 8.1 INLET BOUNDRY LAYER

The flow field was measured for a blade with zero clearance so that the secondary losses without tip leakage could be calculated. As discussed in Chapter 4 and shown in Figure 4.4 three tip geometries were used, a flat tip edged reference blade and two rounded tip designs that minimized the size and formation of the separation bubble. The first rounded tip had a pressure side edge with a radius of 2,5 gap widths to avoid the formation of a separation bubble as found in Section 7.4. As shown in Figure 8.2 the second tip was intended to deflect the leakage flow radially into the gap. This would reduce the gapwise velocity component or alternatively, the resulting "vena-contracta" would reduce the effective flow area. The contours that deflected the flow were generous so as to avoid separation within the gap. A tip clearance of 2,5% chord was used for all three blade tip shapes.

The integrated results for the 3 blade tip geometries and for the zero clearance case are presented in Table 8.1 for comparison. These results were calculated using Bindon's method as described in Chapter 6. The overall loss was split up into the loss generated within the gap, the mixing loss and the secondary loss. The results for the three blade tip geometries are presented in Table 8.2 as percentages of the overall loss for comparison. The results of Bindon (1988) are also tabulated.

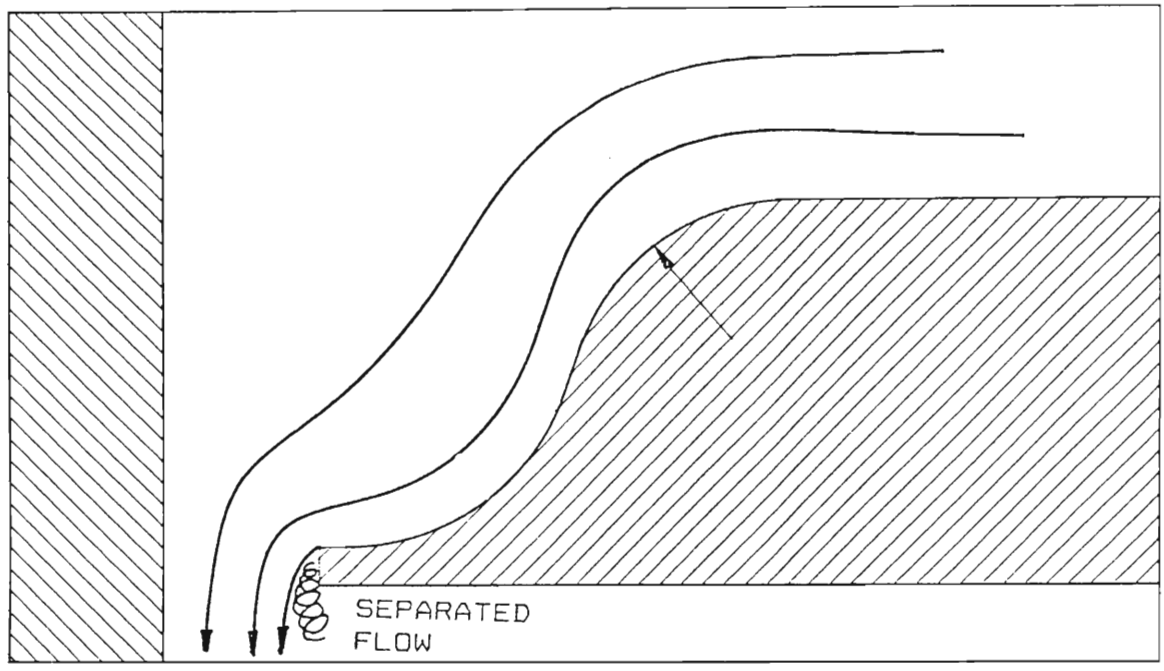

FIGURE 8.2 RADIUSED SQUEALER (OR CONTOURED) TIP BLADE

Schematic of Geometry			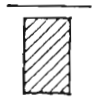		
Rotor eff ts	η_{ts}	97.70	76.90	74.09	80.68
Rotor eff tt	η_{tt}	98.38	87.81	86.56	88.82
Loss coef.	C_L	0.152	0.874	0.964	0.843
Internal gap loss	C_{lg}	-----	0.270	0.062	0.062
Gap exit loss	C_{lge}	-----	0.307	0.099	0.099
Mixing loss	C_{lm}	0.152	0.452	0.750	0.629
Work coef	C_ω	9.225	7.869	6.212	6.700
Exit height	z_2	1.046	1.123	1.112	1.179
Gap mass flow coef	C_f	-----	0.240	0.287	0.256
Gap discharge coef	C_d	-----	0.824	0.926	0.920
Vel coef	C_{v2}	1.194	1.862	1.994	1.600
Ideal vel coef	C_{v2id}	1.129	0.845	0.785	0.839

TABLE 8.1 INTEGRATED RESULTS FOR VARIOUS TIP GEOMETRIES

	BINDON (1988a)			
Schematic of Geometry		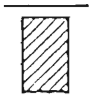		
Internal gap loss	39%	30.9%	6.4%	7.4%
Mixing loss	48%	51.7%	77.8%	74.6%
Secondary loss	13%	17.4%	15.8%	18.0%

TABLE 8.2 PERCENTAGE LOSS DUE TO SECONDARY LOSS, INTERNAL GAP LOSS AND MIXING LOSS FOR VARIOUS BLADE TIP GEOMETRIES

8.1 INTERNAL GAP LOSS AND MIXING LOSS

The amount of loss generated within the clearance gap effects the overall performance of the blade. Bindon (1988a) showed that for a flat tip blade, this accounted for a large proportion of the overall loss produced by the leakage flow. It was thus important to evaluate the internal gap loss generated by each of the three blade tip geometries. The loss entering the clearance gap is relatively small and is mainly due to the inlet boundary layer on the endwall. The gap inlet flow is however difficult to measure since it undergoes intense directional change over a small area.

The loss at gap exit is somewhat simpler to measure since the flow leaves the gap almost parallel to the endwall. The flow leaving the clearance gap was traversed at the gap exit with a 3-hole pitot static probe. The flow was traversed at 9 discrete traverse points at 10% chordwise intervals. The gap exit loss distributions at each traverse point for the three blade tips are presented in Figures 8.3, 8.4 and 8.5. The loss distributions all have a "bucket" shape and have a loss free area at the midpoint between the endwall and tip. For most of the distributions this midpoint area has zero loss. As shown in Figure 8.6 the loss seen at the gap exit may be split up into two components. The loss on the endwall side is due to the inlet boundary layer plus the loss generated on the endwall within the gap. On the tip side of the gap the loss is all generated by the boundary layers and separated flow on the tip. The loss that occurs on the endwall side of the gap at exit was calculated for each of the three

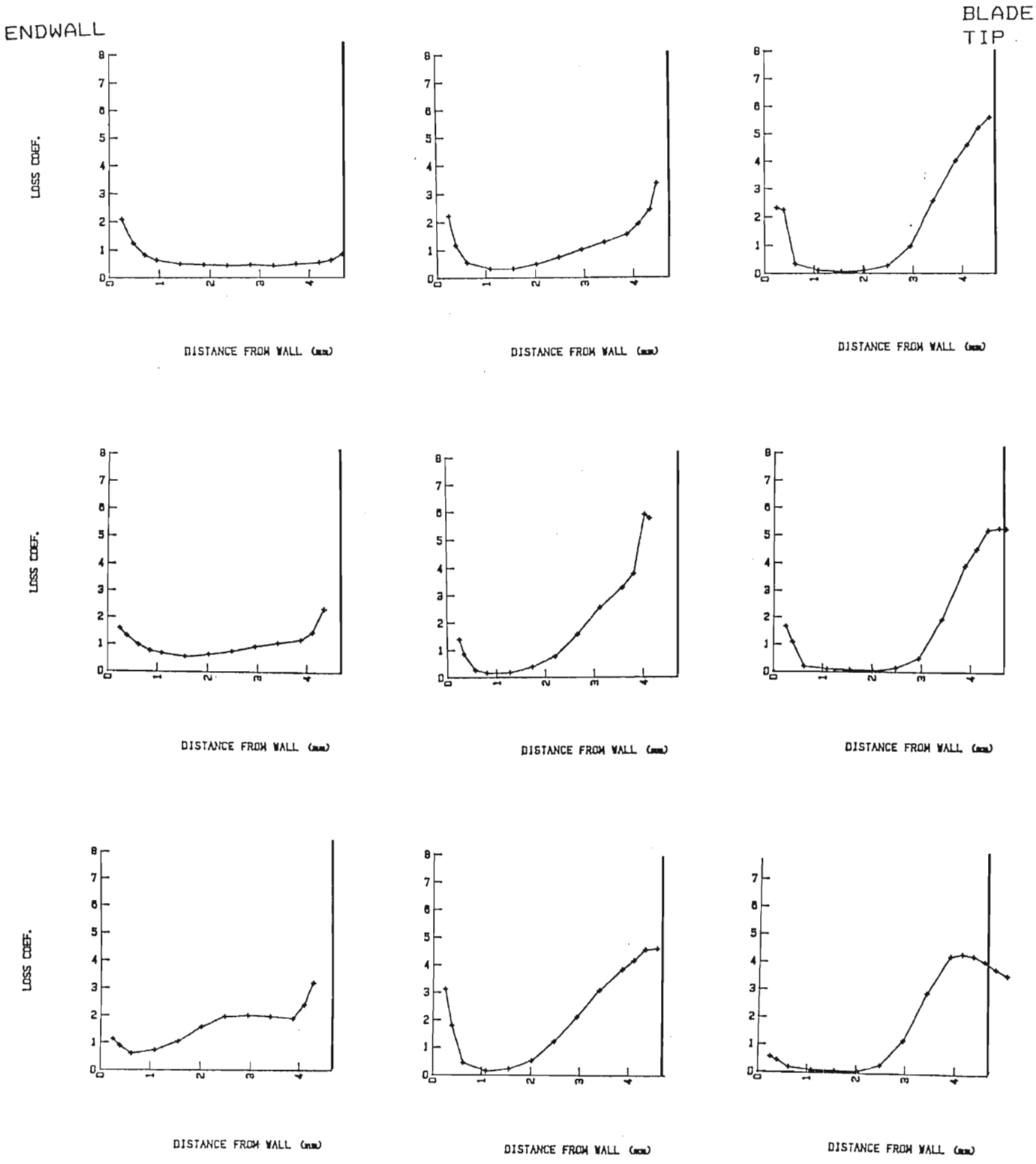

FIGURE 8.3 FLAT OR SQUARE TIP BLADE GAP EXIT LOSS DISTRIBUTIONS

ENDWALL

BLADE TIP

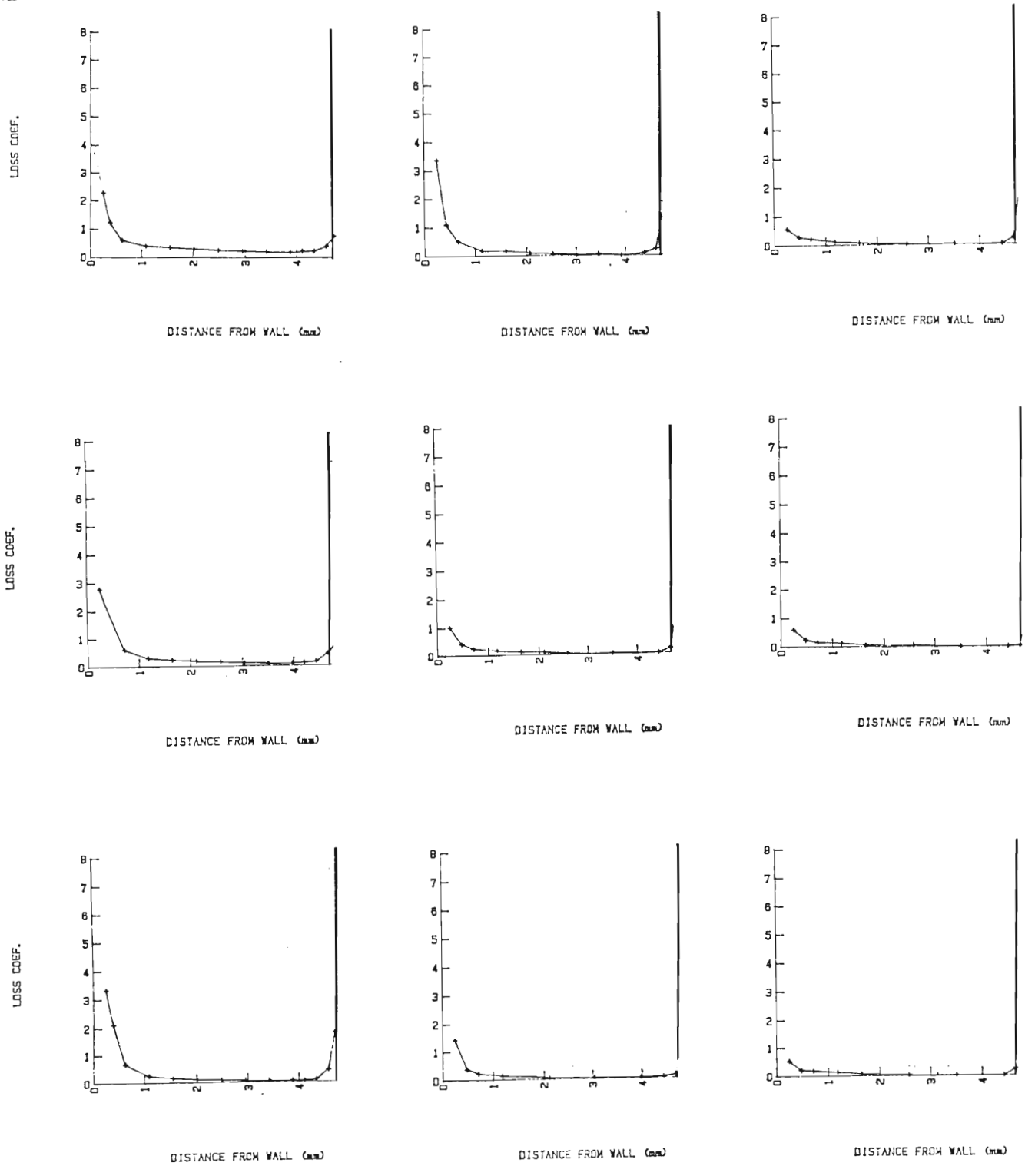

FIGURE 8.4 RADIUSED TIP BLADE GAP EXIT LOSS DISTRIBUTIONS

ENDWALL

BLADE TIP

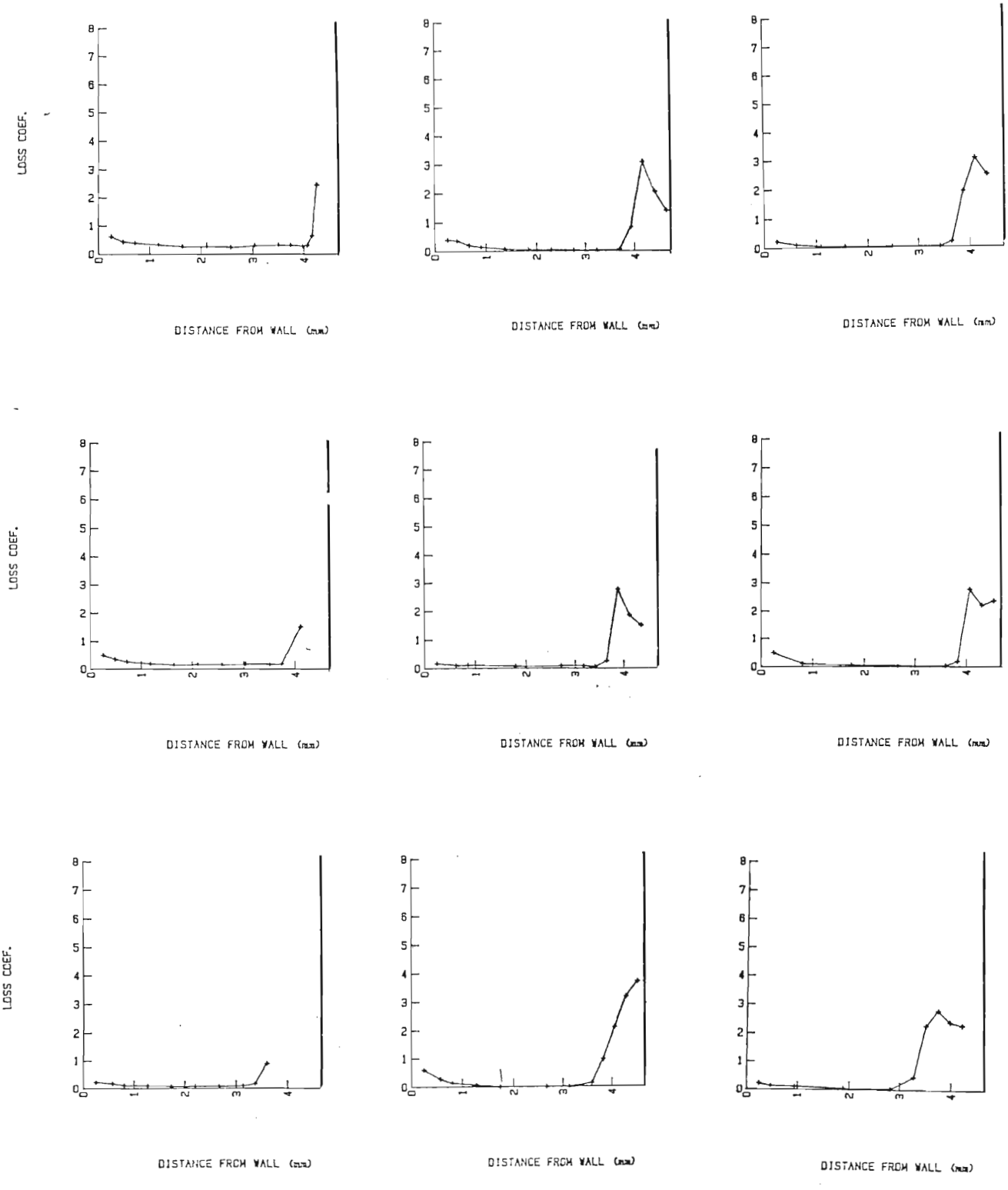

FIGURE 8.5 RADIUSED SQUEALER OR CONTOURED TIP BLADE LOSS DISTRIBUTIONS

blades. A loss coefficient of 0.058, 0.060 and 0.037 was calculated for the square, radiused and contoured tip blades respectively.

For the flat tip and radiused pressure corner blades the loss on the endwall side is due to both inlet loss and loss that was generated on the endwall in the gap. For the contoured blade the loss seen in the endwall side and gap exit is mainly due to the inlet loss since the path of the clearance gap flow is too short for endwall loss to develop.

As mentioned earlier the loss entering the clearance gap is mainly caused by the inlet boundary layer and should not vary much for different blade tip geometries since upstream flow conditions do not change. The gap inlet loss calculated for the contoured tip blade was thus used to represent the inlet loss to all three blades.

The loss developed on the endwall within the gap was calculated by subtracting the inlet loss from the gap exit loss on the endwall side. Sjolander and Amrud (1986) showed that for a flat tip blade the flow separated on the endwall due to the diffusion required of the flow after the separation bubble as shown in Figure 8.6. It was thus thought that the flat tip blade would generate the highest loss on the endwall within the clearance gap. Contrary to this the radiused tip blade showed a marginally higher loss coefficient of 0.023 as opposed to 0.021 for the flat tip blade. This is probably due to the higher mass flow rate experienced through the gap by the radiused tip blade.

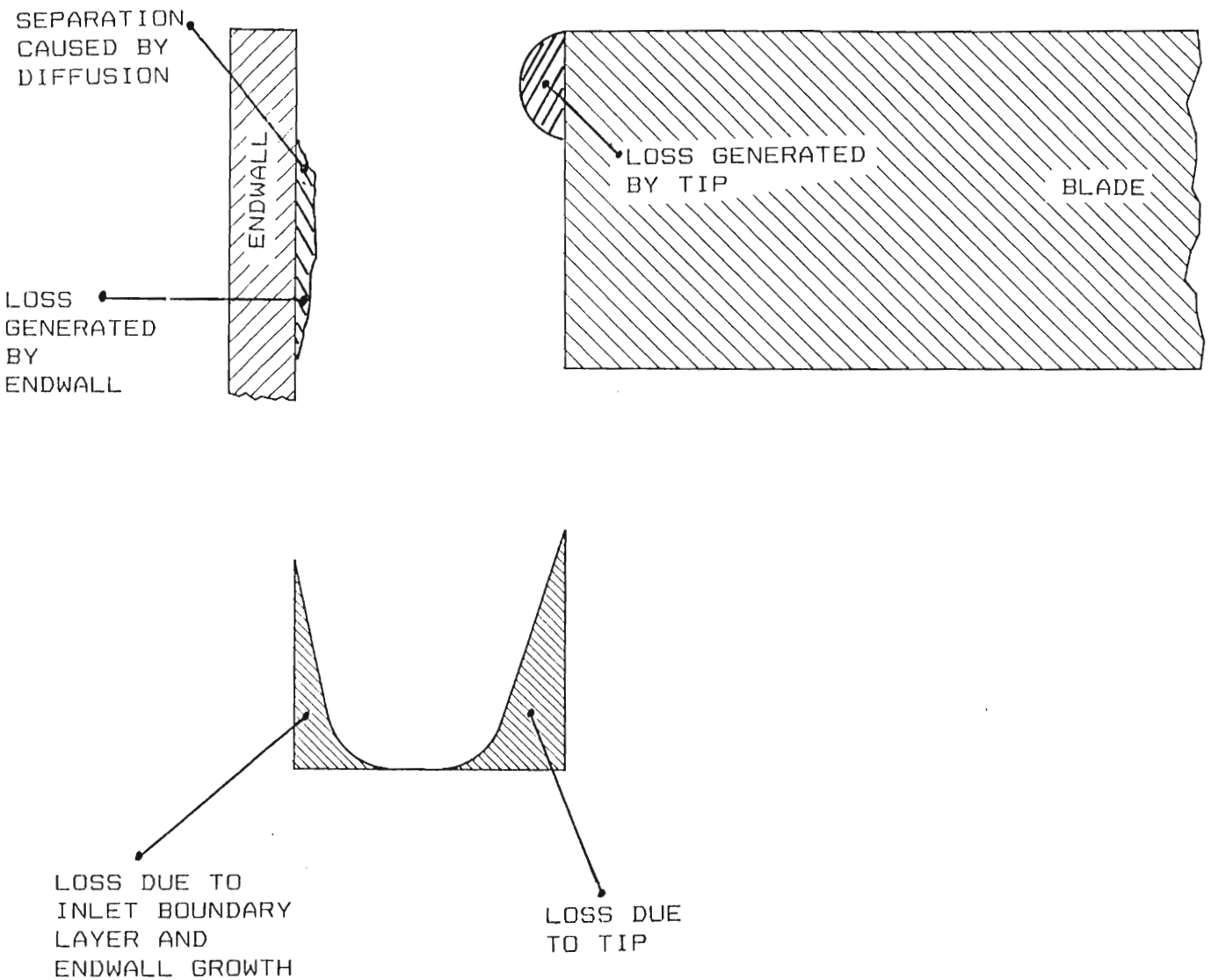

FIGURE 8.6 TYPICAL LOSS PROFILE AT GAP EXIT

Figure 8.7 shows the distribution of loss with chord for the flat tip blade and compares this to that of Bindon (1988). The distribution is quite different from what Bindon (1988) found for the same blade geometry in a different cascade. The single high loss region at midchord was not seen in this experiment. This suggests that tip clearance flows are very sensitive and are not easily repeated for different cascades and that results would not be applicable for different blade tip geometries.

The sharp peak previously seen by Bindon (1988) in the gap exit loss distribution was associated with bubble flow leaving the gap at the point of lowest static pressure. In the present study two peaks were seen suggesting that the separated flow within the bubble leaves the gap in a more evenly distributed manner. Yaras et al (1988) showed two total pressure troughs at the gap exit which would correspond to the two high loss peaks. The total integrated internal gap loss as a percentage of the overall loss was 30,9% whereas Bindon (1988) found a higher loss of 38%.

The chordwise loss distribution for the three blade tip geometries are presented in Figure 8.8. The radiused and contoured tip blades were seen to have a much lower loss distribution than the flat tip blade. This is as expected since separation of the flow within the gap was avoided. The internal gap loss as a percentage of overall loss was 6.4% for the radiused tip blade and 7.4% for the contoured tip.

The distributions of mass flow coefficient and discharge coefficient are presented in Figure 8.9 and Figure 8.10

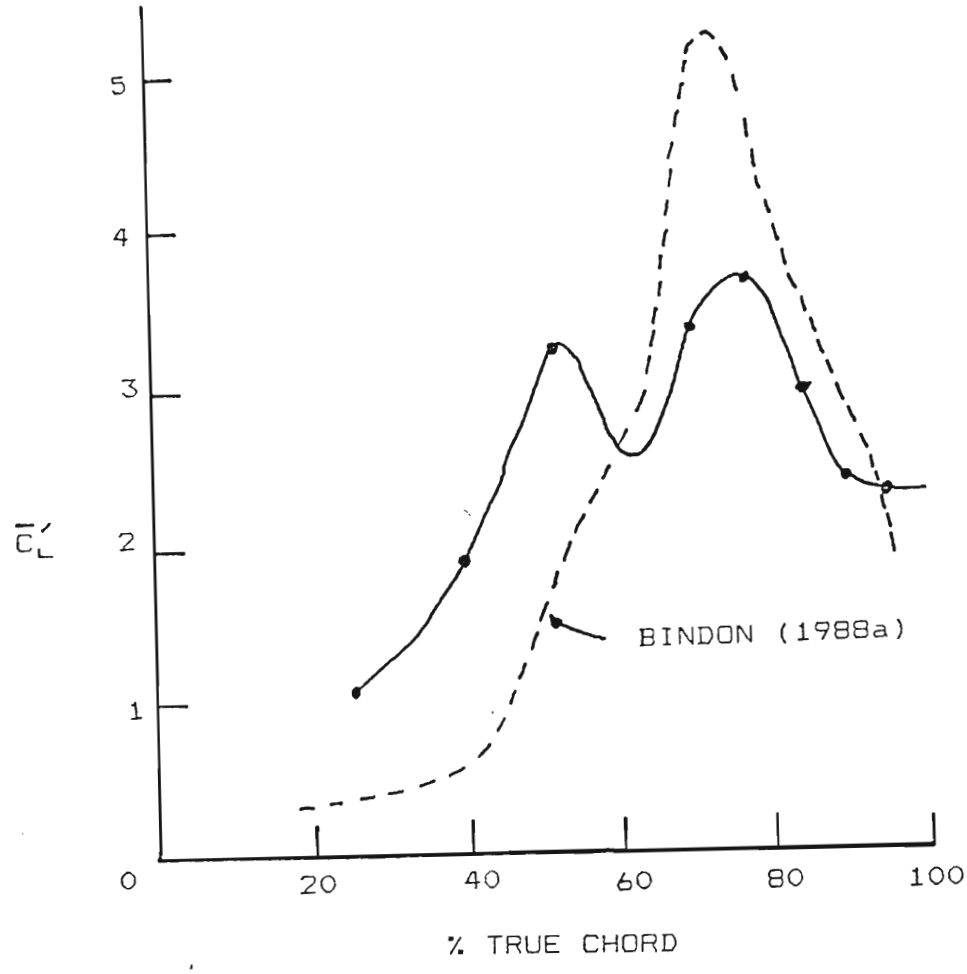

FIGURE 8.7 GAP EXIT LOSS DISTRIBUTION FOR FLAT TIP BLADE

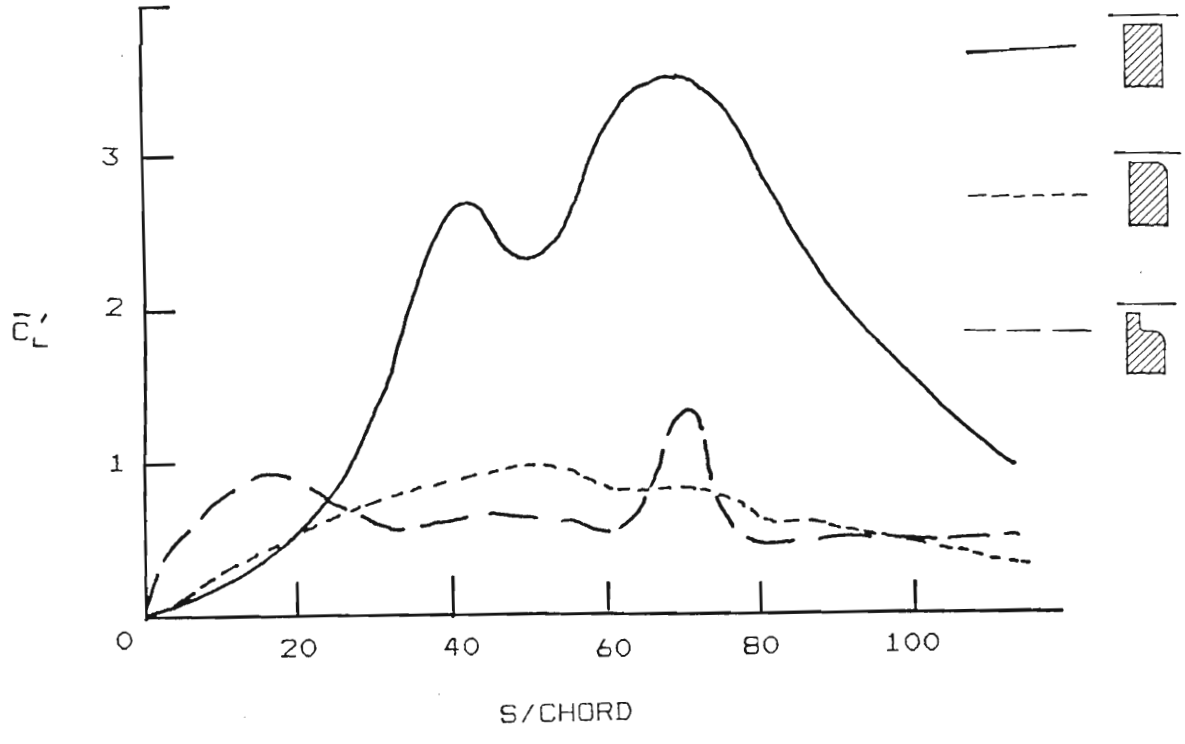

FIGURE 8.8 CHORDWISE GAP EXIT LOSS DISTRIBUTION FOR THREE BLADE TIPS

respectively. The integrated results are presented in Table 8.1. The radiused tip blade had the highest mass flow rate through the gap of some 20% more than that of the flat tip blade. This is the main reason for the bad overall performance of the radiused tip blade. This additional leakage flow produced the very large mixing loss which penalized this blade. The contoured tip blade had about 6.7% more leakage flow than the flat tip blade.

The mixing loss was calculated by subtracting the internal gap loss and the secondary loss from the overall loss. The overall loss calculated for the blade with zero clearance gap was assumed to be the secondary loss. The mixing loss coefficient for the square, radiused and contoured tip blades was 0.452, 0.75 and 0.629 respectively. This follows the same pattern as that obtained for the leakage mass flow rate. The radiused tip blade had the highest mass flow rate through the gap and thus produced the highest mixing loss. The lowest mixing loss was created by the flat tip blade which also had the lowest leakage mass flow rate through the gap.

The radiused tip blade had 66% more mixing loss than the flat tip blade for an increase in mass flow rate of only 20%. The contoured tip blade experienced 39% more mixing loss for an increase in mass flow rate of 6,7%. It therefore appears that for a relatively small increase in leakage mass flow rate the mixing loss increases dramatically.

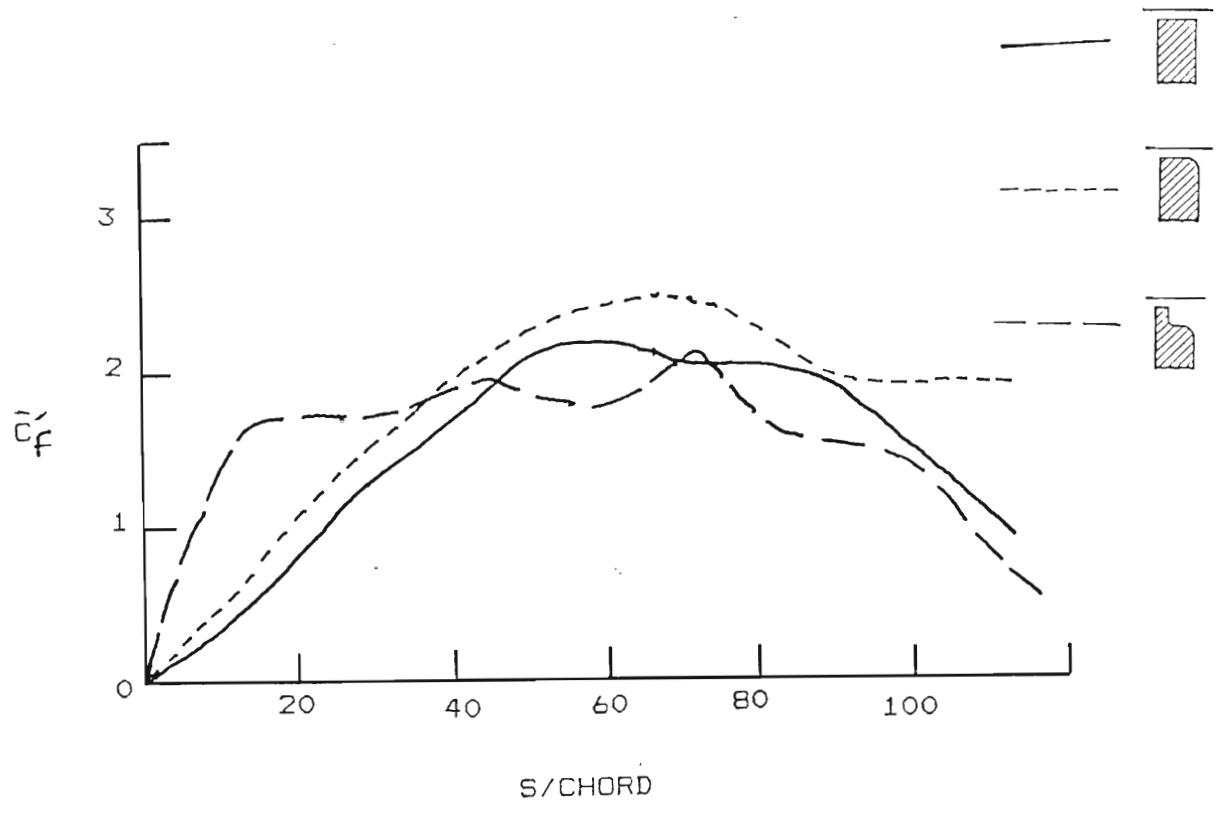

FIGURE 8.9 MASS FLOW COEFFICIENT DISTRIBUTION FOR THREE BLADE TIPS

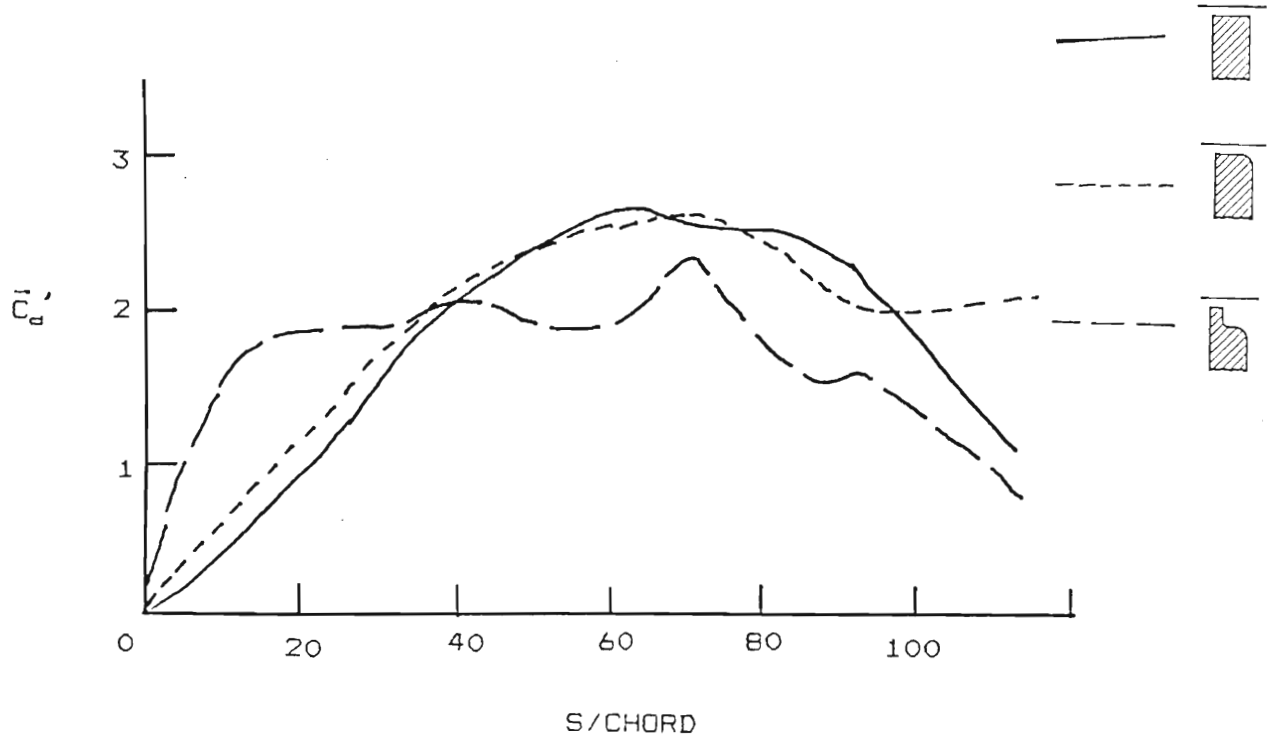

FIGURE 8.10 MASS DISCHARGE COEFFICIENT DISTRIBUTION FOR THREE BLADE TIPS

8.2 EXIT PLANE AND ENDWALL TRAVERSES

The development of the leakage flow mixing vortex for the flat tip blade was examined by measuring the flow between two blades at 6 planes normal to the axial direction, ranging from 40% axial to the exit plane. The exit plane was traversed for all the blades so that relative performance of each blade could be examined. The flow was traversed with a 3-hole yaw and a 2-hole pitch pitot static probe to make up 5-hole probe data as described in Chapter 4.

Secondary flow diagrams were drawn for each measurement plane. These diagrams show the velocity component of the flow projected on a plane normal to the free steam velocity. The gradual development of the leakage vortex for the flat tip blade is shown in Figure 8.11 for planes from 40% to 100% axial. At all the planes the leakage jet stays parallel to the wall until it suddenly lifts off to roll and form the vortex. The vortex grows steadily up to 80% axial chord from where it seems to grow much faster. The length of the leakage jet vectors show that the leakage flow is relatively undeflected. The flow can also be seen entering the clearance gap.

The leakage vortex patterns for the three blade tip geometries are presented in Figure 8.12. The contoured tip blade has a vortex center that is the furthest away from the suction surface. The radiused tip blade leakage vortex occupies the largest area and is some 25% wider than the contoured tip blade. This causes the very high mixing loss experienced by the radiused tip blade. The contoured tip blade seems to have the smallest diameter

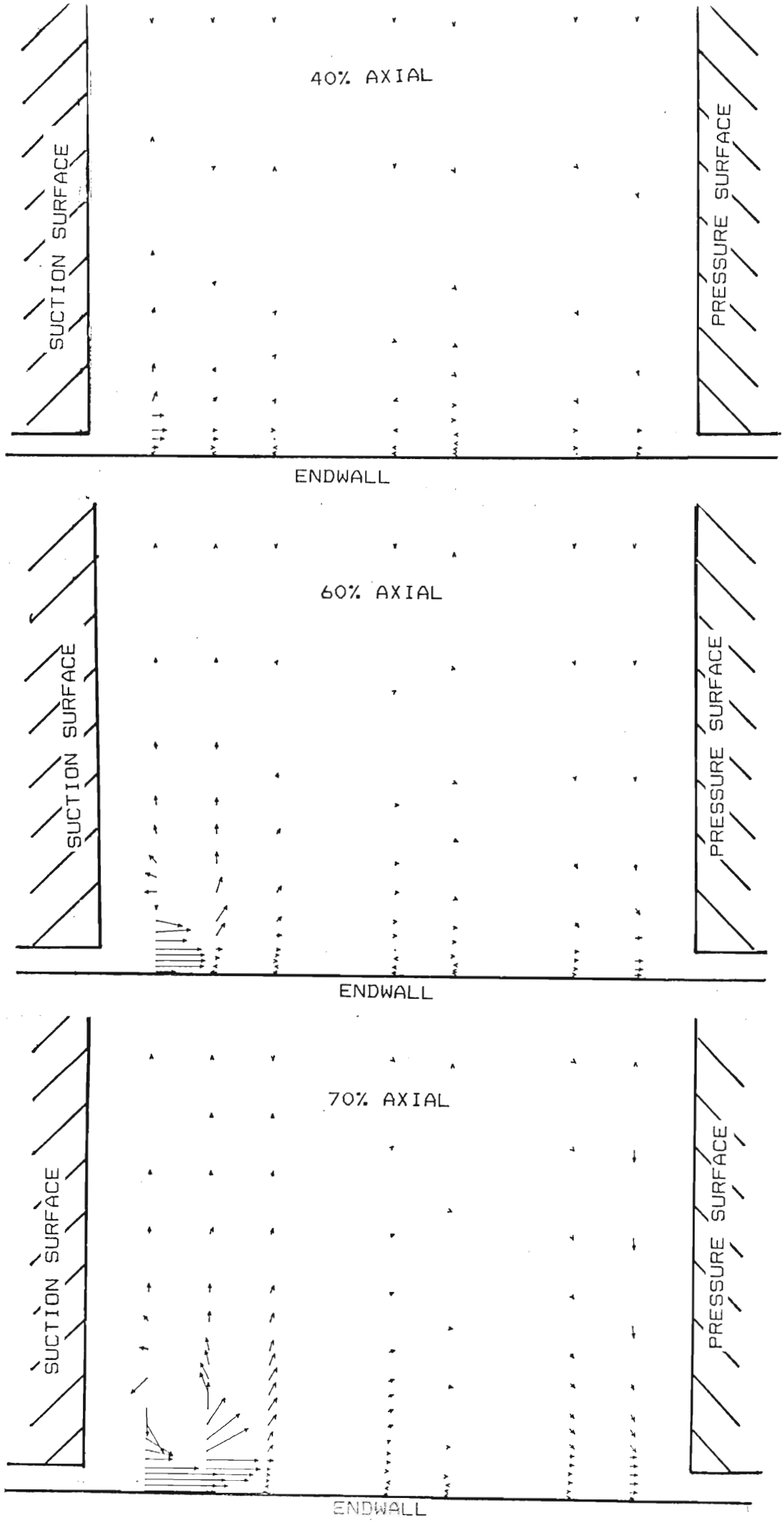

FIGURE 8.11 SECONDARY FLOW DIAGRAM SHOWING

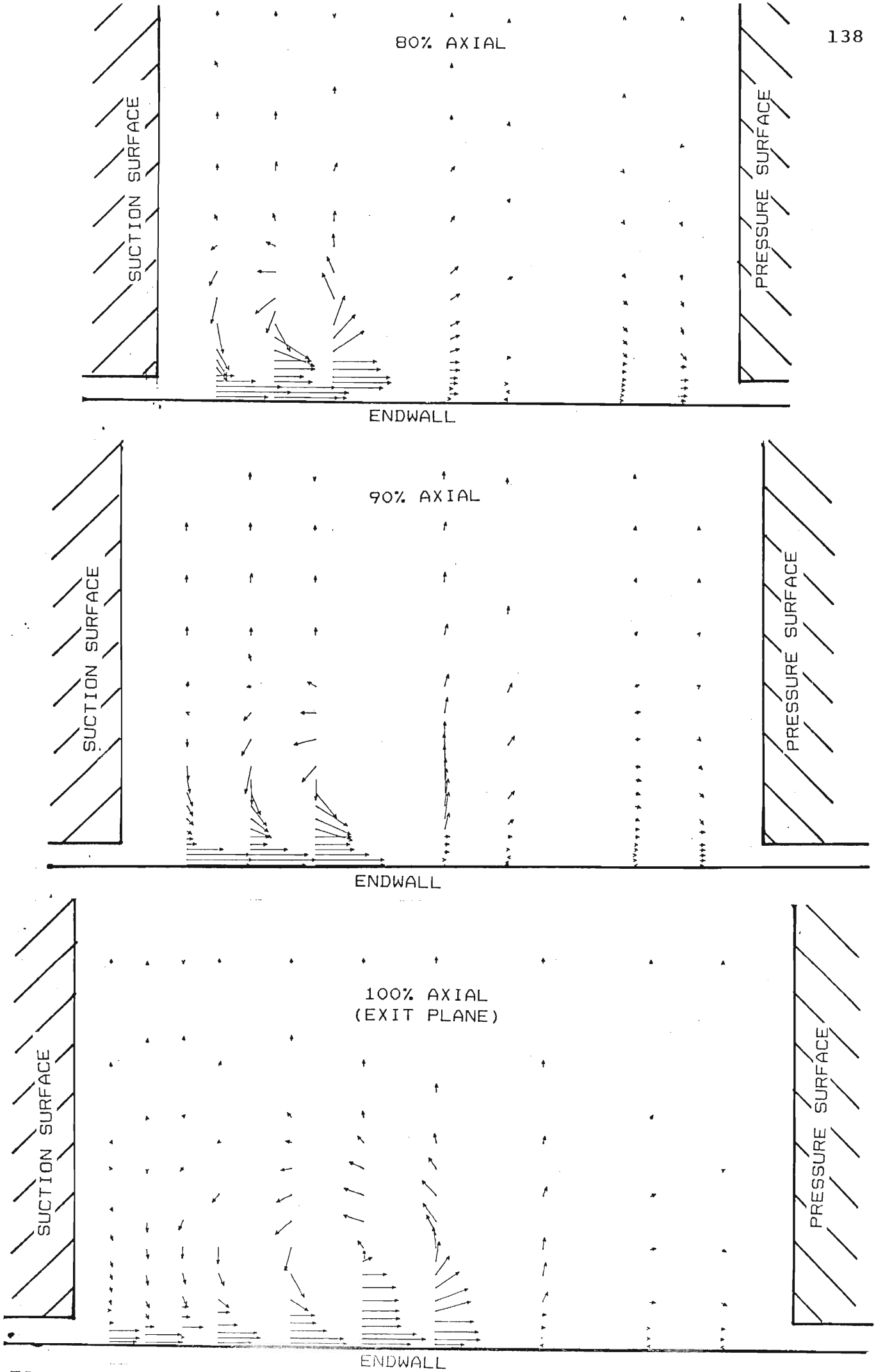

FIGURE 8.11 (CONTINUED)

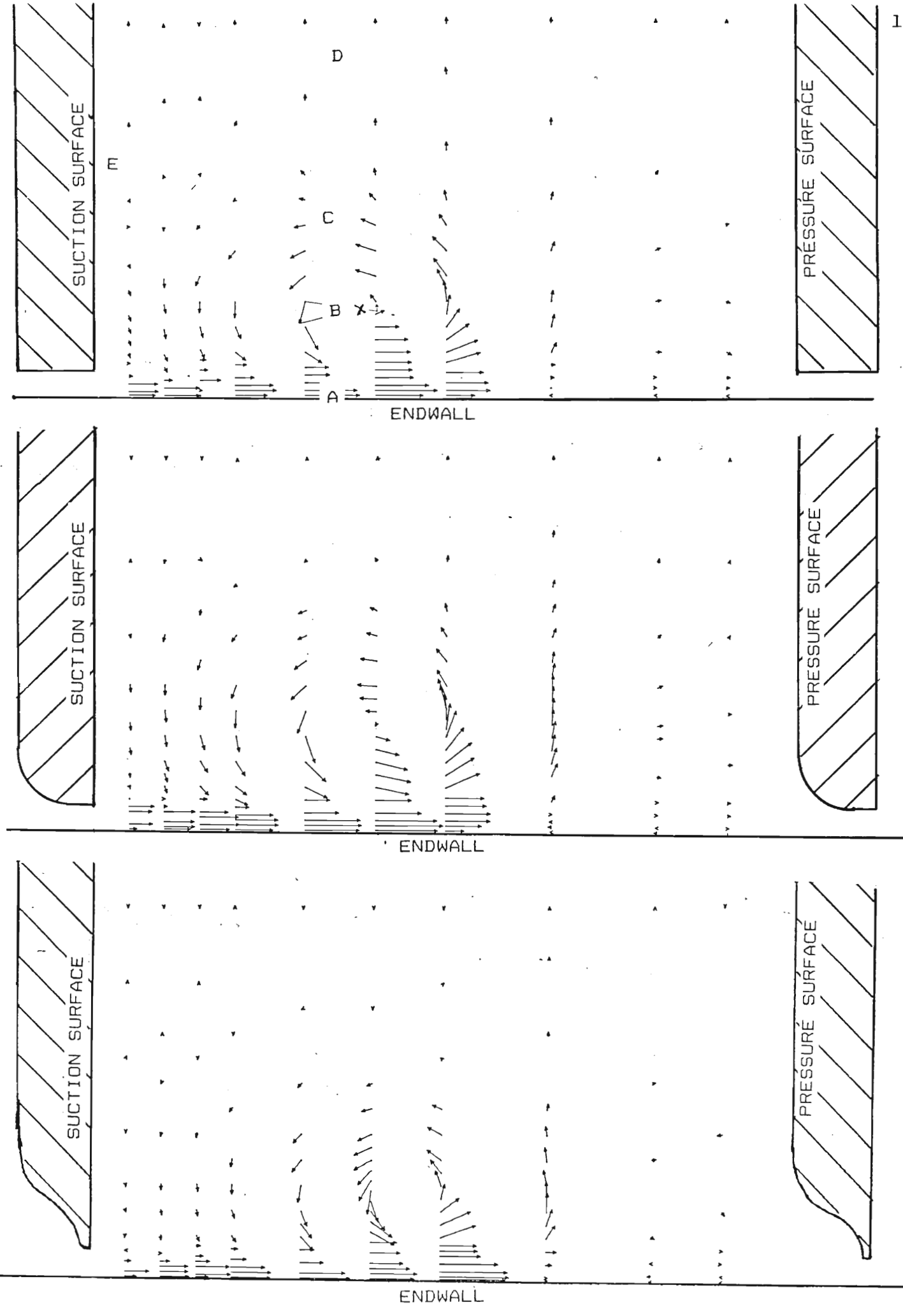

FIGUR 8.12 SECONDARY FLOW DIAGRAMS AT EXIT PLANE FOR THREE BLADE TIP GEOMETRIES

leakage vortex.

The loss coefficient and efficiency contour plots at exit plane for the 4 blades (including the zero clearance blade) are presented in Figure 8.13 and Figure 8.14 respectively. The zero clearance blade represents the loss generated by secondary flow. The loss contours are all similar in shape to what was presented by Bindon (1988). The large loss region with a high loss core at the center of the leakage vortex can be seen in all the blades with tip clearance. Extreme shear is shown by the contour lines in the leakage jet region. The radiused tip blade once again has the largest area affected by shear at the leakage jet.

8.3 CASCADE PERFORMANCE AT EXIT PLANE

The overall performance of each blade tip geometry was evaluated by measuring the flow at the cascade exit plane. The cascade exit plane contains the sum of all the components of loss, namely, internal gap loss, leakage flow mixing loss and secondary flow loss. The flow at the exit plane describes the overall performance of the cascade but does not explain how the loss was generated or how the leakage flow developed.

Table 8.1 presents the results for the simulated rotor analysis and it can be seen that the contoured tip blade had the best overall performance in terms of both efficiencies and work transfer. On the other hand the radiused tip blade displayed the worst performance. The total to static efficiency for the contoured blade was 4.9% higher than the flat tipped blade,

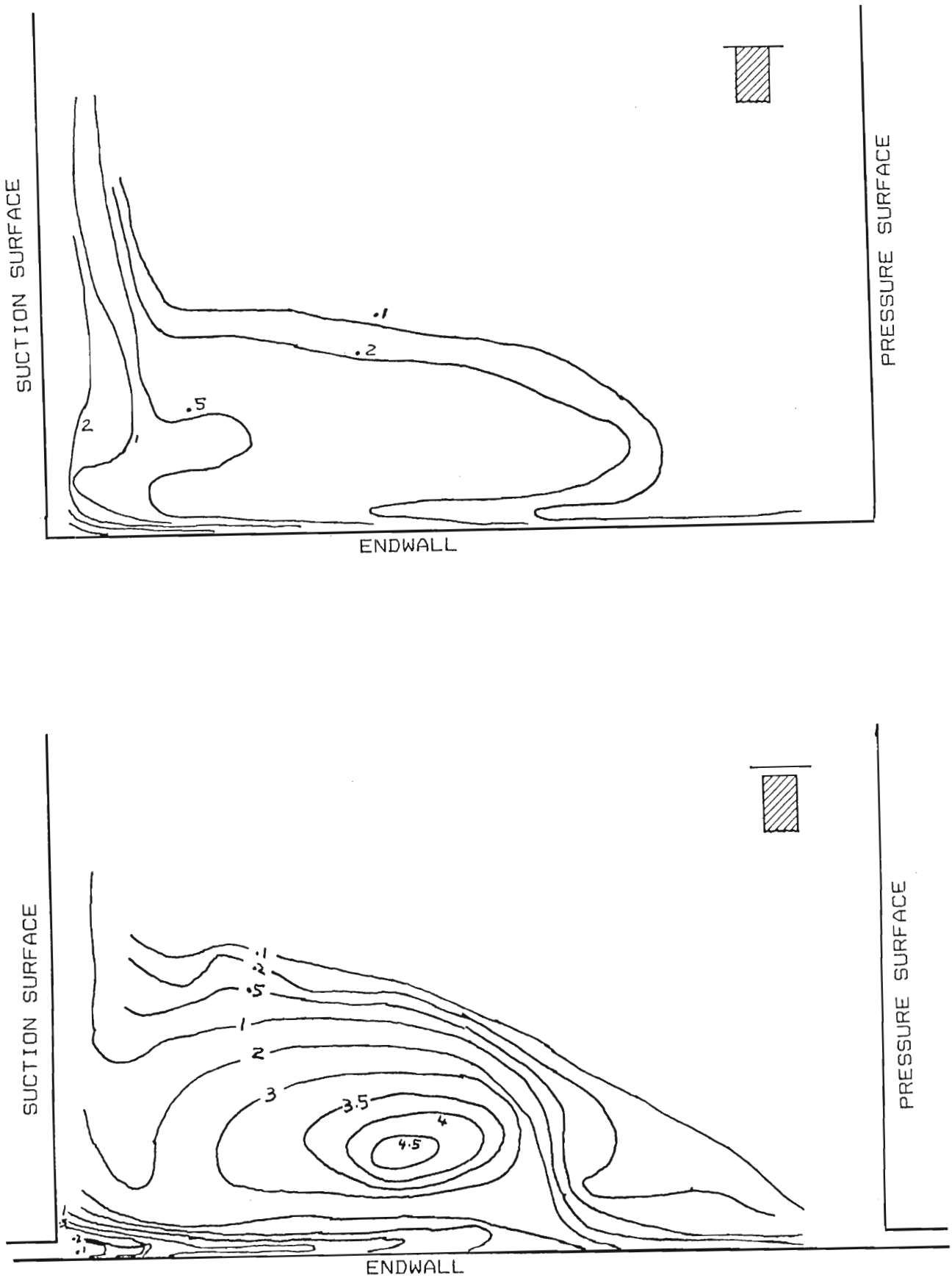

FIGURE 8.13 EXIT PLANE LOSS CONTOURS FOR 3 BLADE TIP GEOMETRIES AND ZERO CLEARANCE BLADE

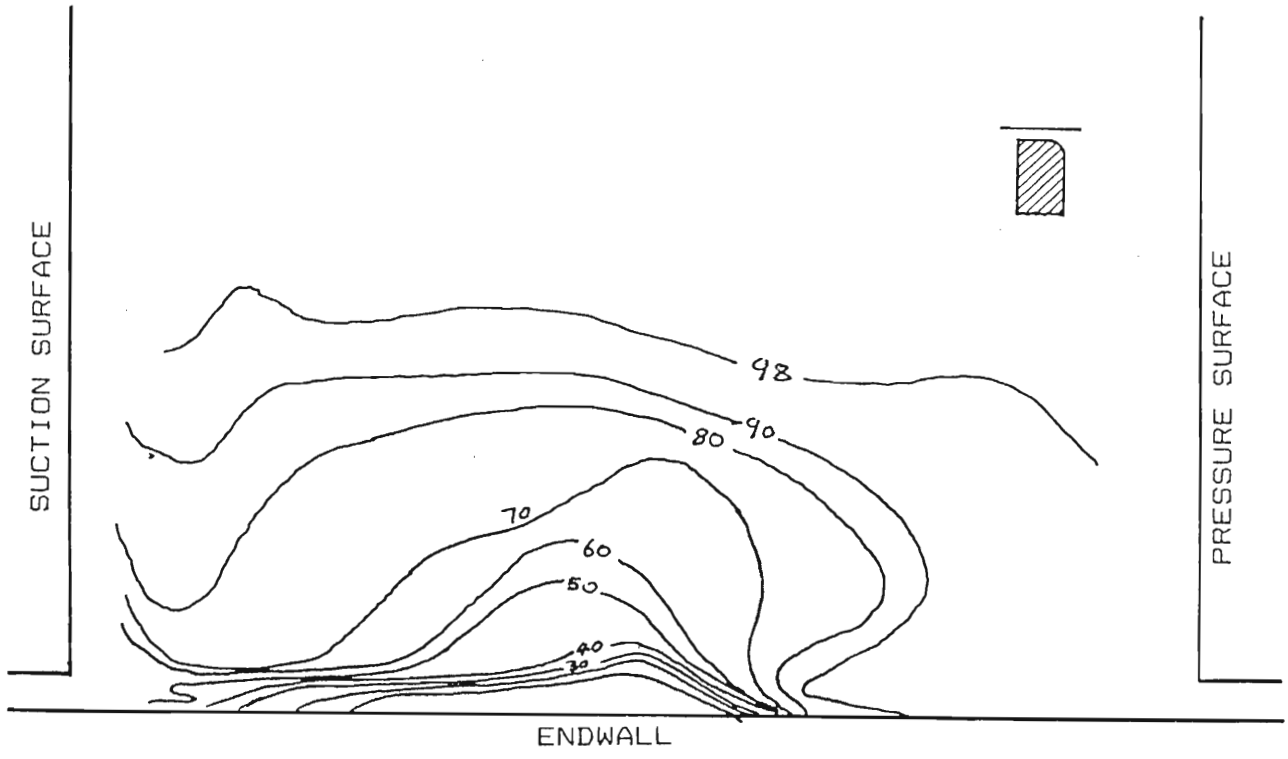

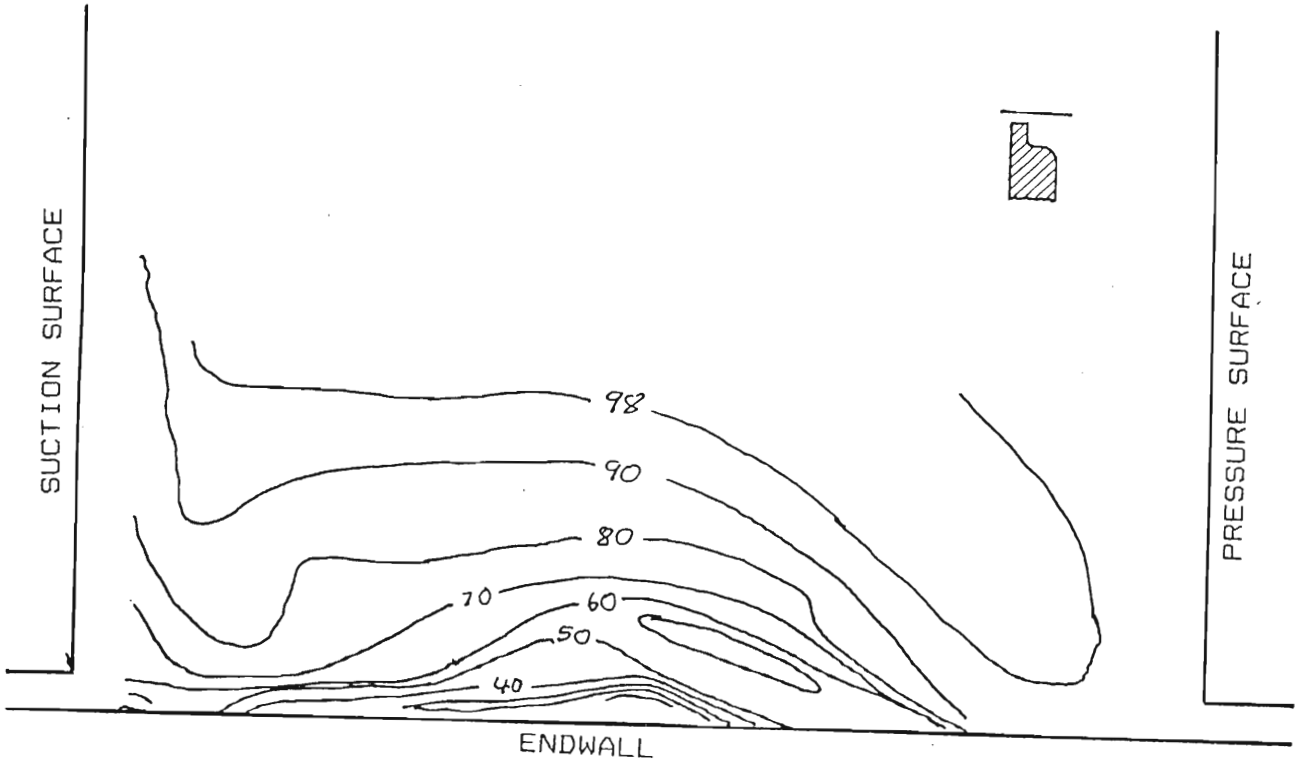

FIGURE 8.13 (CONTINUED)

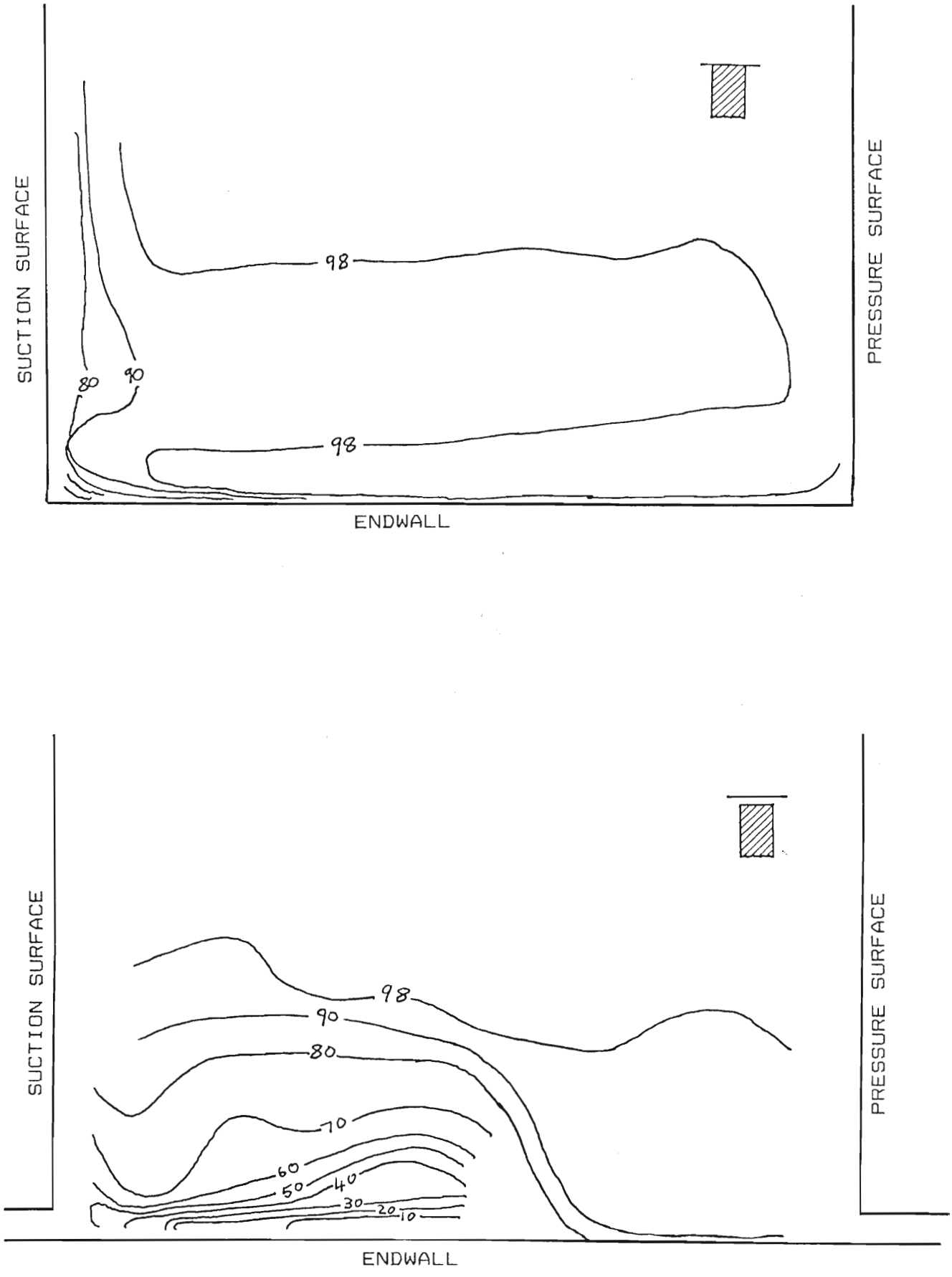

FIGURE 8.14 EXIT PLANE EFFICIENCY CONTOURS FOR 3 BLADE TIP GEOMETRIES AND ZERO CLEARANCE

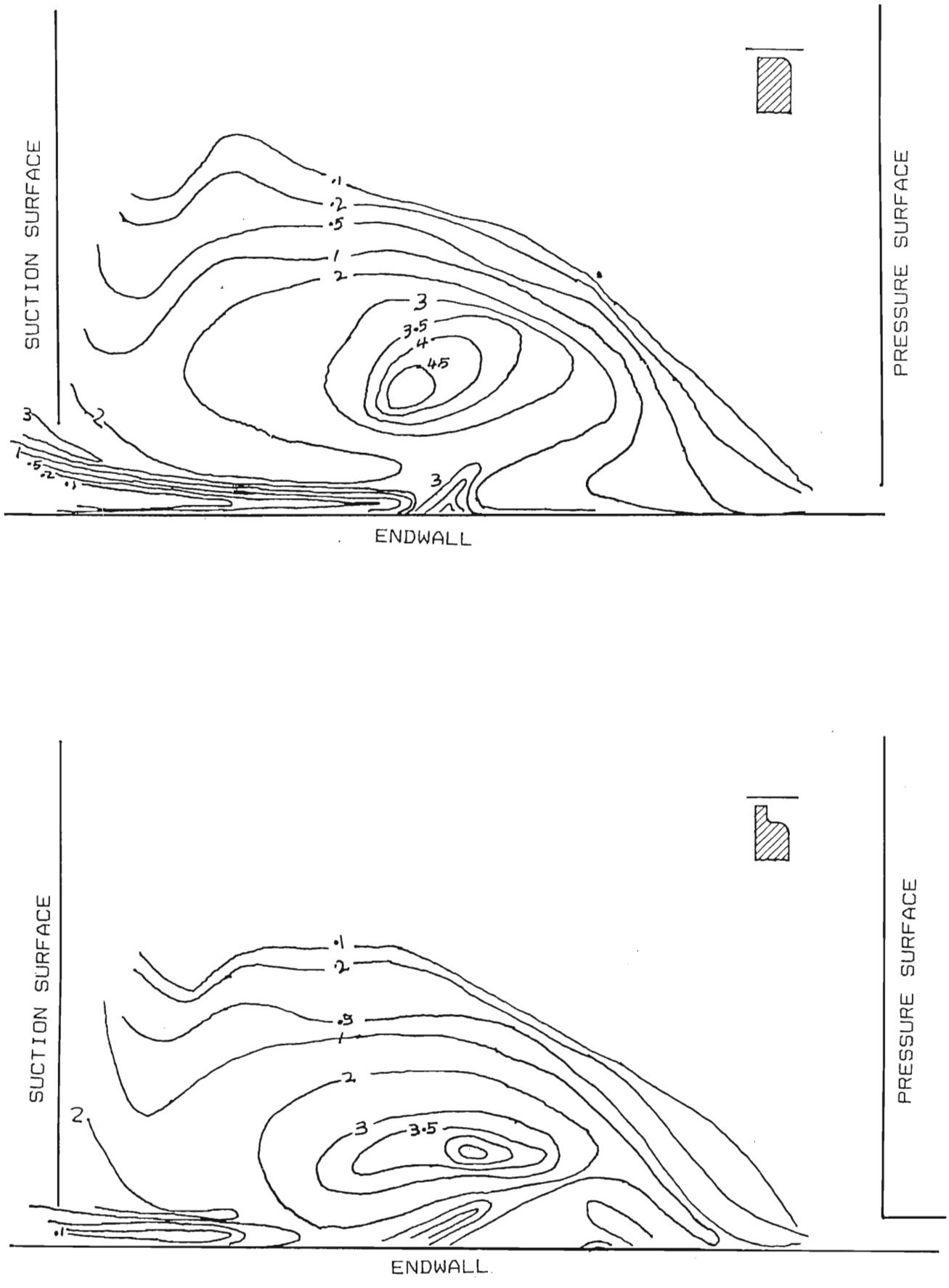

FIGURE 8.14 (CONTINUED)

whereas the radiused tip blade was 3.7% lower. The total to total efficiency differences relative to the flat tip blade were not as high. The contoured tip blade was only 1,2% more efficient than the flat tip blade and the radiused tip blade was only 1,4% less. The above efficiency figures are all for a blade height of .25% chord. Therefore to obtain the overall efficiency improvement the above figure must be divided by 4 and by the aspect ratio. For example, for a long blade of aspect ratio 2 the total to static efficiency improvement for the contoured tip blade is 0,613%.

The overall total to total efficiencies for the three blades are all higher than the total to static efficiencies. This was as expected since the total to total efficiency assumes that the kinetic energy at rotor exit was not lost but will be used in subsequent stages. The surprising result here is that the total to total efficiencies improvement for the contoured tip blade is much lower than the total to static efficiency improvement. This is explained by the small kinetic energy C_2, leaving the contoured tip blade. On the other hand the radiused tip blade had a very high kinetic energy at exit causing the total to total efficiency to be high.

It is interesting to note that the radiused tip blade had the lowest efficiency since this blade tip was initially selected to decrease the overall loss. As mentioned in Section 8.1 the extra leakage mass flow rate through the gap due to the streamlined tip geometry caused a much larger mixing loss. This offset any advantage gained by the radiused tip's ability to create very

little loss within the clearance gap.

The relative performance of the different blade tips can also be compared by considering the total pressure loss coefficient. As discussed in Chapter 6 this method does not however take into account the ability of the rotor to extract work from the flow. Although it is logical it would be difficult to prove that the simulated rotor efficiency analysis method is a more reliable quantity. The simulated rotor efficiency does not require much extra effort to calculate since only a few extra lines of computer program are required and therefore it can easily be used to obtain extra information on which to assess a blade.

The mass averaged absolute outlet velocity coefficients for the four blades are presented in Table 8.1. It is important to note that the outlet velocities for the three blades with tip clearance are much higher than the blade with zero clearance. Figure 8.15 shows the mean flow velocity diagrams for the three blades with clearance and compares them to the zero clearance blade. From these velocity diagrams it can clearly be seen that tip clearance reduces the overall deflection and increases the axial velocity. This reduces the ability of the rotor to extract work from the flow.

Figure 8.16 presents the velocity diagrams at various points in the exit plane flow field for the square tip blade. The flow in the free stream is loss free and the vector diagram shows that the flow leaves in an axial direction with no swirl velocity. In the blade wake, high loss is experienced causing the axial velocity to be very low and the flow to leave with a high swirl

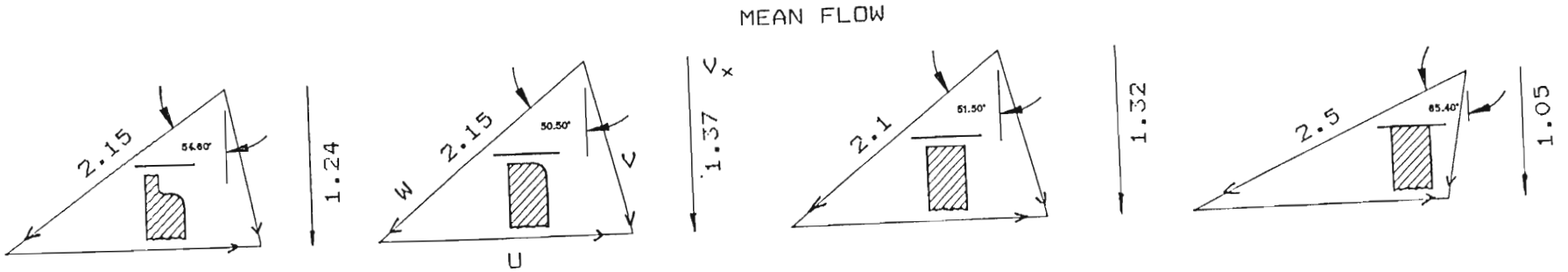

FIGURE 8.15 MEAN FLOW FIELD OUTLET VELOCITY TRIANGLES FOR ZERO CLEARANCE AND 3 BLADE TIP GEOMETRIES

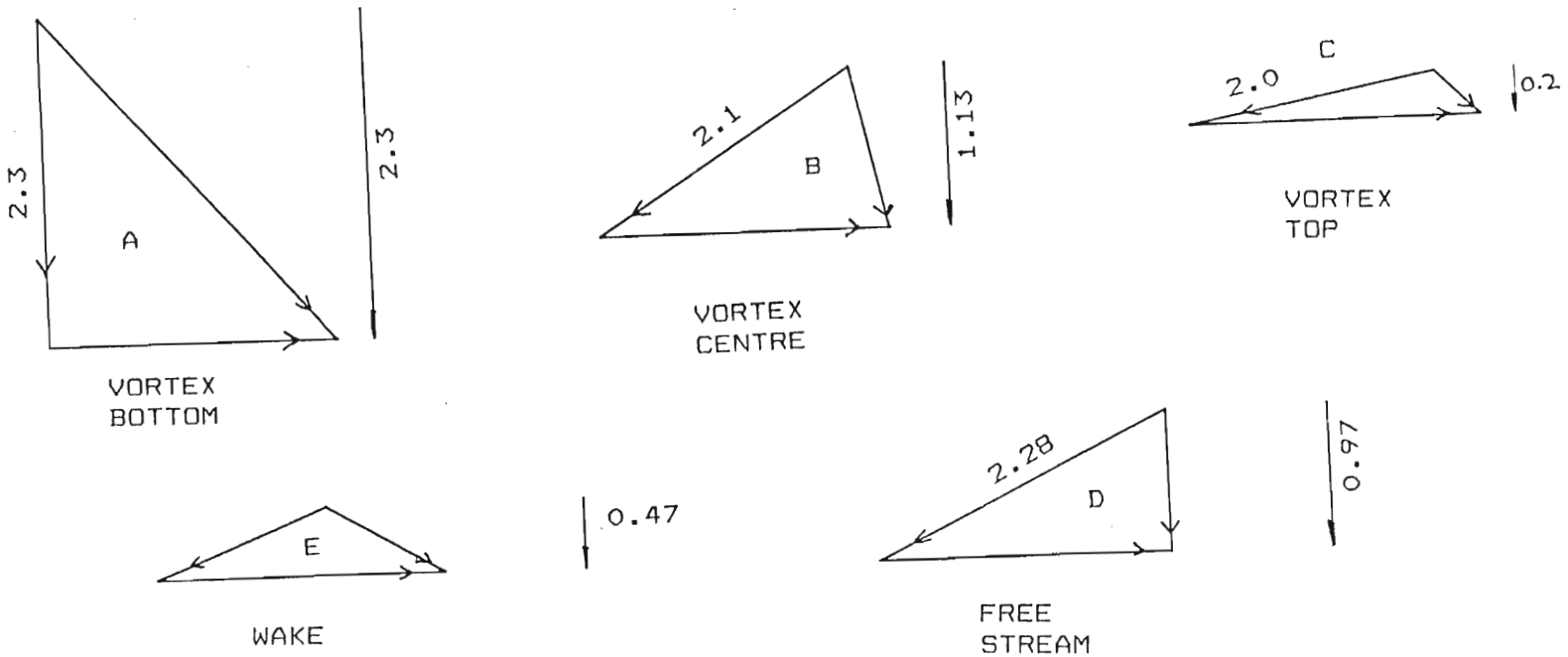

FIGURE 8.16 VELOCITY TRIANGLES AT VARIOUS POINTS MARKED IN THE EXIT PLANE FLOW FIELD IN FIGURE 8.12 OF THE FLAT TIP BLADE SHOWING THE INFLUENCE OF THE FLOW PHENOMENA ON EXIT SWIRL AND LOCAL WORK TRANSFER.

velocity. Thus in the wake the rotor work transfer is reduced both due to high entropy generation and due to bad deflection. The most interesting velocity diagrams are those in the vortex region. In the vortex center the loss generation is high but, due to the low static pressure, the relative velocity W_2 is as high as that in the free stream. Since the direction of the absolute outlet velocity is almost axial, a small swirl velocity leaves the rotor. The flow in the center of the vortex therefore has good deflection and work transfer even though high loss was produced. At the top of the vortex the flow is deflected even more giving even better work transfer and a very small axial outlet velocity. At the bottom of the vortex where the flow is fairly loss free, the flow comes through almost completely undeflected and with a very high axial velocity, hence almost no work is extracted from this part of the flow.

CHAPTER 9

CONCLUSIONS

During the course of this research program, two experimental rigs were used to study tip clearance micro-flow phenomena and to evaluate the performance of various tip geometries.

The first rig was an annular cascade with a rotating casing that provided a relatively simple way of creating the relative motion between the blade tip and endwall. This allowed the effect of relative motion on the flow within the gap, to be studied. Relative motion was found to have little effect on the general shape of the pressure distribution on the blade tip. This is explained by the loss free flow between the blade tip boundary layer and the casing boundary layer that indicated that the two boundary layers do not interact viscously. The pressure depression caused by the separation bubble was little affected by relative motion, however in the reattached flow regime after the separation bubble, the pressures were higher due to the reduced leakage flow and reduced distortion of the suction surface. The reduction in leakage flow was due to the direction of the rotating casing which was opposite to that of the leakage flow. Relative motion would thus be important in determining the leakage mass flow rate and the formation of leakage vortex and associated loss formation rather than in determining the basic nature of the flow.

The existence of the very low and narrow pressure trough on the pressure surface corner of the flat tip blade was confirmed by using a higher resolution pressure tapping technique which provided more data in this region than had been reported previously. This low pressure, is thought to be caused by the flow remaining attached around the corner before it separated to from the separation bubble.

It was found that the width of the separation bubble and the static pressure within it both depend on the clearance gap width. The bubble width was found to vary with chord, with the widest part of the separation bubble at midchord. The bubble width was also seen to increase as the clearance gap increased but the relationship was not linear. The relationship of separation bubble pressure to gap size was not monotonic. A minimum separation bubble pressure was recorded at a clearance gap of 2% chord. The reattachment line at the end of the separation bubble was seen to coincide with a slight pressure peak.

A chordwise pressure gradient that accelerates the flow in the separation bubble, from the leading edge towards midchord was once again found. A pressure gradient was also found from the trailing edge to midchord, and by using oil flow visualization it was confirmed that flow within the separation bubble moves from the trailing edge towards midchord. It is thought that the flow within the separation bubble emerges at midchord and mixes with the high velocity leakage jet to form a large proportion of the internal gap loss and to reduce the leakage mass flow rate.

The pressure corner radius of the tip was increased gradually up to a radius of 2.5 gap widths at which all signs of separation within the clearance gap disappeared. The deep pressure depression associated with the separation bubble also disappeared at a pressure corner radius of 2.5 gap widths.

The second experimental rig used was a linear cascade that provided a means of evaluating the performance of two blade tip shapes that were designed to prevent the formation of the separation bubble within the clearance gap, and to compare them to a conventional flat tip blade. Both modified blade tip shapes were found to substantially reduce internal gap loss generation which was responsible for some 31% of overall cascade loss. It was found that simply radiusing the pressure corner decreased the internal gap loss but, due to the extra leakage mass flow the mixing loss increased by a large amount, making this blade the least efficient. The contoured tip blade that was shaped to avoid separation within the clearance gap and to shed the flow radially, was found to be the most efficient blade tip in spite of a fairly large mixing loss.

The formation of the separation bubble within the clearance gap was eliminated with the two modified tip geometries and thus the internal gap loss was greatly reduced. However the relationship between this internal gap loss and the formation of mixing loss was not established. The leakage jet showed a more even distribution of loss than previous measurements, where a high loss concentration was found at midchord. The fact that the previous results were not repeatable indicates that tip clearance

flow and loss formation is sensitive to tip geometry and flow conditions. The overall inlet gap loss was also not the same as previously measured by Bindon (1988a).

The formation of mixing loss appeared to depend very strongly on the leakage mass flow rate. Therefore new tip geometry designs should have a low entropy generation in the gap and at the same time keep the leakage flow rate to a minimum.

Bindon's method of converting stationary cascade flow field data into a simulated rotor flow, was used to calculate work transfer and efficiency. This gave additional insight into the performance of the blade tip geometries rather than merely considering loss generation. The ability of the rotor to deflect the flow and the amount of kinetic energy leaving the rotor were both taken into account in evaluating the performance of the various tip geometries.

The radiused tip and the improved contoured tip blades investigated in this thesis were primarily studied to enhance the understanding of the basic tip flow phenomena. In practice the increase in overall performance of the blade obtained due to any blade tip geometry will depend on the blade length. This is due to the tip losses only affecting the tip region and the rest of the blade being unaffected .The development of more efficient blade tip geometries may be possible following the methodology used in this study.

REFERENCES

Ainley D G, Mathieson G C R, 1957 "A method of performance estimation for axial flow turbines", Aeronautical Research Council, R & M 2974

Bindon J P, 1986a "Pressure and flow field measurements of axial turbine tip clearance flow using a linear cascade" Cambridge University, Whittle Laboratory Report CUED/A-Turbo TR123

Bindon J P, 1986b "Visualization of axial turbine tip clearance flow using a linear cascade" Cambridge University, Whittle Laboratory Report CUED/A-Turbo TR123

Bindon J P, 1987a "Pressure distributions in the tip clearance region of an unshrouded axial turbine as effecting the problem of tip burnout", ASME Paper 87-GT-230

Bindon J P, 1987b "Visualization of tip clearance flow in a linear turbine cascade", AIAA 8th International Symposium on Air Breathing Engines, Cincinnati, June 1987, page 436-444, Paper No. ISABE 87-7032.

Bindon J P, 1987c "Measurements of the tip clearance flow structure on the endwall and within the clearance gap of an axial turbine cascade". Proceedings of the I Mech E, International Conference on Turbomachinery Efficiency Prediction and Improvement, Cambridge, September 1987, page 43-52, Paper NO C273/87.

Bindon J P, 1988a "The measurement and formation of tip clearance loss", ASME Paper 88-GT-203

Bindon J P, 1988b, University of Natal Durban, Private communication.

Bindon and Morphis, 1988 "The development of axial turbine leakage loss for two profiled tip geometries using linear cascade data". University of Natal, Durban, IZMAR Report, Activity Code A9.3, Blade Tip Flow Fields.

Booth T C, Dodge P R, Hepworth H K, 1982 "Rotor tip leakage: Part 1-Basic methodology" ASME Transactions, J of Engineering for power, V 104, Jan 1982, p 154

Gearhart W S, 1964 "Tip clearance flow in turbomachines", The Pennsylvania State University Science and Engineering Ordnance Research Lab, TM 506.2491-04.

Graham J A H, 1985 "Investigation of a tip clearance cascade in a water analogy rig", ASME Paper No. 85-IGT-65.

Mayle R E, Metzger D E, 1982 " Heat Transfer at the tip of an unshrouded turbine blade" The 7th International Heat Transfer Conference, Munich, v3, p87.

Moore J G, J Moore 1986 "The effects of Reynolds Number on flow through a tip gap" Virginia Polytechnic Institute and State University, Blacksburg, Virginia, 24061, Turbo Research Group, Report No. JM/86-9

Moore J, Tilton J G, 1987 "Tip leakage flow in a linear turbine cascade" ASME Paper No. 87-GT-222
Moore J, 1987, Virginia Polytechnic Institute and State University, Private communication.

Morphis G, Bindon J P, 1988 "The effects of relative motion, blade edge radius and gap size on blade tip pressure distribution in an annular turbine cascade with clearance" ASME Paper No. 88-GT-256

Offenberg L S, Fisher J D, Vander Hoek T J, 1987 "An experimental investigation of turbine casing treatments" AIAA/SAE/ASME/ASEE 23rd joint Propulsion Conference, Paper No. AIAA-87-1919

Rains D A, 1954 "Tip clearance flows in axial flow compressors and pumps" California Institute of Technology, Hydrodynamics Laboratory Report No. 5 1954

Sjolander S A, Amrud K K, 1986 "Effects of tip clearance on blade loading in a planar cascade of turbine blades" ASME Paper No. 86-GT-245

Wadia A R, Booth T C, 1982 "Rotor tip leakage : Part 2 -Design optimization through viscous analysis and experiment" ASME Transactions, J of Engineering for power, V 104, Jan 1982, p162

Yaras M, Zhu Yingkang, Sjolander S A, 1988 "Flow field in the tip gap of a planar cascade of turbine blades"
ASME Paper No. 88-GT-29

APPENDIX 1.A

```
5  ! PROGRAM "CHORD"
10 ! PROGRAM TO CALCULATE GAMMA , ALPHA 2 ,THETA ,F
20 ! ********************************************
25 PRINTER IS 601
30 DEG
60 DISP "INPUT WIDTH"
70  INPUT W
75 PRINT "WIDTH IS:",W
76 PRINT @ PRINT
77 PRINT "  C                GAMMA                    THETA=ALPHA(2)"
78  PRINT @ PRINT
80 FOR K=0 TO 15
90 C=K*5+W
130 G=ACS (W/C)
140 F=TAN (G)/.6574
150 PHI(2)=ATN (F*.1602)
160 THETA=G+PHI(2)
170 PRINT C,G,THETA
180 NEXT K
190 END
```

```
WIDTH IS:          80

  C                GAMMA                THETA=ALPHA(2)

 80                0                    0
 85                19.7499227957        24.7501291765
 90                27.2660444507        34.424542236
 95                32.6368975035        41.5072486974
 100               36.8698976458        47.2272724521
 105               40.3675935442        52.0712479136
 110               43.3417582272        56.2931515083
 115               45.9207901521        60.0458891367 ← SELECTED VALUE
 120               48.1896851042        63.4300497182
 125               50.2081805004        66.515938671
 130               52.0201275551        69.3549104173
 135               53.6587969062        71.9857573389
 140               55.1500954209        74.4385680959
 145               56.514623377         76.7371857538
 150               57.7690473645        78.9008423669
 155               58.9270490279        80.9452846902
```

APPENDIX 1.B

```
10 ! PROGRAM "BL7"
20 ! PROGRAM TO GENERATE AND PLOT A3K7 BLADE PROFILE
30 ! AND TO THICKEN TRAILING EDGE
40 ! ************************************************
50 CLEAR
60 PRINTER IS 601
70 DIM X(24)
80 DIM PXT(24)
90 DIM PYT(24)
100 DIM PXB(24)
110 DIM PYB(24)
120 DIM Y(24)
130 DIM DA(24)
140 DIM DB(24)
150 DIM SR(30)
160 DIM A(24)
170 DIM B(24)
180 DIM DX(24)
190 DIM DY(24)
200 DIM R(24)
210 DIM THE(24)
220 ASSIGN# 1 TO  "BLADE DATA"
230 FOR K=1 TO 24
240 READ# 1 ; X(K),Y(K),A(K),B(K)
250 NEXT K
260 OUTPUT 602 ;"VS12"
270 PLOTTER IS 602
280 GCLEAR
290 MOVE 80,10
300 LORG 5
310 CSIZE 3.5
320 LABEL "PERCENTAGE CHORD"
330 DEG
340 LDIR 90
350 MOVE 10,50
360 LABEL "Y"
370 MOVE 80,90
380 CSIZE 3 @ LDIR 0
390 LOCATE 20,160,20,95
400 SCALE -10,210.75,-60,60
410 ! LAXES 5,2,-10,-30,2,10
420 DISP "INPUT CHORD LENGTH (mm)"
430 INPUT C
440 DISP "INPUT WIDTH (mm)"
450 INPUT W
460 DISP "INPUT LABEL:"
470 INPUT R$
480 DISP "INPUT THICKNESS FACTOR"
490 INPUT L
500 G=ACS (W/C)
510 F=TAN (G)/.6574
520 PHI(2)=ATN (F*.1602)
530 SR(1)=0
540 Z=2
550 R=0
```

```
560 FOR K=1 TO 23
570 DX(K)=X(K+1)-X(K)
580 DY(K)=F*Y(K+1)-F*Y(K)
590 R(K)=SQR (DX(K)^2+DY(K)^2)
600 THE(K)=ATN (DY(K)/DX(K))
610 R=R+R(K)
620 SR(K+1)=SR(K)+R(K)
630 NEXT K
640 D=R/100
650 FOR K=2 TO 24
660 Z=1
670 Z=Z+1
680 IF Z=24 THEN GOTO 710
690 IF D*A(K)<= SR(Z) THEN GOTO 710
700 GOTO 670
710 IF K>17 THEN GOTO 740
720 I=K
730 GOTO 750
740 I=18
750 PXT(K)=X(Z-1)+(D*A(K)-SR(Z-1))*COS (THE(Z-1))-(B(K)+A(I)*L)*SIN (THE(Z-1))
760 PYT(K)=F*Y(Z-1)+(D*A(K)-SR(Z-1))*SIN (THE(Z-1))+(B(K)+A(I)*L)*COS (THE(Z-1))

770 PXB(K)=X(Z-1)+(D*A(K)-SR(Z-1))*COS (THE(Z-1))+(B(K)+A(I)*L)*SIN (THE(Z-1))
780 PYB(K)=F*Y(Z-1)+(D*A(K)-SR(Z-1))*SIN (THE(Z-1))-(B(K)+A(I)*L)*COS (THE(Z-1))

790 NEXT K
800 PXT(1)=0
810 PYT(1)=0
820 PXB(1)=0
830 PYB(1)=0
840 ! 1 GOTO 890
850 PRINT "PXT                    PYT                PXB                    PYB"
860 FOR K=1 TO 24
870 PRINT PXT(K),PYT(K),PXB(K),PYB(K)
880 NEXT K
890 MOVE X(1),F*Y(1)
900 LORG 5
910 LABEL R$
920 MOVE X(1),F*Y(1)
930 FOR J=2 TO 24
940 PLOT X(J),F*Y(J),-1
950 LORG 5
960 LABEL R$
970 MOVE X(J),F*Y(J)
980 NEXT J
990 MOVE PXT(1),PYT(1)
1000 LORG 5
1010 LABEL R$
1020 MOVE PXT(1),PYT(1)
1030 FOR J=2 TO 24
1040 PLOT PXT(J),PYT(J),-1
1050 LORG 5
1060 LABEL R$
1070 MOVE PXT(J),PYT(J)
1080 NEXT J
1090 MOVE PXB(1),PYB(1)
1100 LORG 5
1110 LABEL R$
1120 MOVE PXB(1),PYB(1)
1130 FOR J=2 TO 24
1140 PLOT PXB(J),PYB(J),-1
1150 LORG 5
```

```
1160 LABEL R$
1170 MOVE PXB(J),PYB(J)
1180 NEXT J
1190 DISP "TO RUN AGAIN PRESS 0:"
1200 INPUT X
1210 IF X=0 THEN GOTO 800
1220 END
1230 NEXT J
```

TOP AND BOTTOM BLADE SURFACE COORDINATES

PXT	PYT	PXB	PYB
0	0	0	0
-1.50690805899	3.5248033017	3.22287047813	-1.61925530894
-1.14336217008	5.79199642106	4.85178604708	-2.26654773122
.48102597002	9.19269243663	7.56824282508	-2.92261413189
5.15261292912	13.747798263	12.2519489537	-3.24263504555
10.8146556764	16.558204926	16.3707547224	-2.91881433753
16.6227892085	18.1326952834	20.5995582229	-2.28360477818
22.3818366644	18.9821269115	25.0133452375	-1.64872296508
28.0867685468	19.2942999073	29.5525168208	-1.07904193931
33.6989990356	19.0995800726	34.2163814114	-.50559423111
39.2145876436	18.6675652653	38.9844041388	-.11902462099
44.6358644672	17.8755236585	43.839276174	.26753333903
49.9724818771	16.8413621241	48.7618736557	.5823694205
55.2207593858	15.6220150583	53.7509413758	.81679574157
60.3987474375	14.2627484158	58.7855645679	.96020576296
65.5146524847	12.8070719139	63.8566792891	1.00092059847
70.5769141409	11.3006545084	68.9576739523	.93030845764
75.607309303	9.77736446467	74.0673365222	.73354006157
80.5988306183	8.17478691873	79.1937352827	.49018861445
85.5758868124	6.63088309767	84.3164153178	.09105652855
90.5613009493	5.16464434436	89.4094527973	-.49329890692
95.6477531082	3.77732843426	94.3782578062	-1.2673901583
100.366059776	1.45464780628	99.6339402243	-1.4546478065
100.366059776	1.45464780628	99.6339402243	-1.4546478065

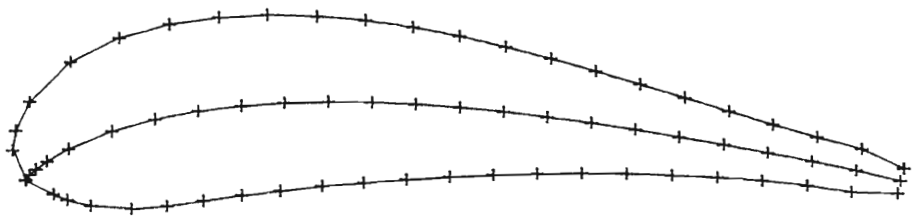

A3K7 BLADE PROFILE WITH THICKENED TRAILING EDGE

APPENDIX 2.A

```
10  ! PROGRAM "ENTER RES"
20 ! PROGRAM TO ENTER DATA FROM 4 PRESSURE TRANSDUCERS **********************
30 ! VERSION ON 5/8/1988
40 OPTION BASE 1
50 CLEAR
60 PRINTER IS 601
70 DIM RES(50,6)
80 FOR I=1 TO 50
90 FOR J=1 TO 6
100 RES(I,J)=0
110 NEXT J
120 NEXT I
130 ! ============================================================
140 !                        INPUTS
150 ! ============================================================
160 CAT
170 DISP "INPUT FILE NAME TO STORE DATA:"
180 INPUT F$
190 DISP "DO YOU WANT TO CREATE FILE ?"
200 INPUT QF$
210 DISP "INPUT TEMPERATURE:" @ INPUT TEMP
220 DISP "INPUT PRESSURE (mm Hg):" @ INPUT H
230 DISP "INPUT  % AXIAL FROM LEADING EDGE :" @ INPUT A
240 DISP "INPUT  % TANGE FROM BOTTOM BLADE :" @ INPUT T
250 DISP
260 DISP
270 PRINT "=================================================="
280 PRINT "READINGS FOR RADIUSED TIP BLADE  2.5%CHORD CLEARANCE"
290 PRINT "=================================================="
300 PRINT " PRESS TRANSDUCERS CONECTED FOR MINIMUM ERROR"
310 PRINT " ENDWALL PROBE"
320 PRINT @ PRINT
330 PRINT "          % AXIAL =",A,"DATA STORED IN FILE :",F$
340 PRINT "          --------------                    ------------------------------"
350 PRINT "          % TANG. =",T
360 PRINT "          --------------"
370 PRINT
380 PRINT "          TEMPERATURE (CELCIUS) =",TEMP
390 PRINT "          PRESSURE (mm Hg) =",H @ PRINT @ PRINT
400 PRINT
410 PRINT "                                        (P01-P1)     (P2-P3)      (P1-P2)      (P01-PS1)
420 PRINT "NO.    ANGLE(DEG)   DIST.(TURNS) PT1=V*1000  PT2=V*1000  PT3=V*1000   PT4 =V"
430 PRINT "===    ==========  ============ ==========  ==========  ==========   ======"
440 PRINT @ PRINT
450 DISP "TO STOP ENTERING DATA TYPE -9999-"
460 DISP "TO REPEAT LAST READING   TYPE -5555-"
470 SL=0
480 FOR I=1 TO 100
490 K=I
500 GOTO 550
510 DISP "INPUT NO. AT WHICH TO RESTART:" @ INPUT I
520 SL=SL+K-I
530 IF I=K THEN GOTO 550
540 PRINT "ABOVE READINGS ARE ERRONEOUS NEXT READINGS ARE REPETITION" @ SL=SL+1
550 DISP "INPUT DISTANCE FROM WALL (NO. OF TURNS) ;"
```

```
560 INPUT RES(I,2)
570 DISP "INPUT REFERENCE ANGLE:"
580 INPUT RES(I,1)
590 IF RES(I,1)=9999 OR RES(I,2)=9999 THEN RES(I,1)=0 @ RES(I,2)=0 @ GOTO 860
600 IF RES(I,1)=5555 OR RES(I,2)=5555 THEN I=I-1 @ GOTO 510
610 SUM1=0 @ SUM2=0 @ SUM3=0 @ SUM4=0
620 ENTER 628 ; RES6
630 FOR M=1 TO 5
640 ENTER 622 ; RES3@ SUM1=SUM1+RES3
650 ENTER 624 ; RES4@ SUM2=SUM2+RES4
660 ENTER 626 ; RES5@ SUM3=SUM3+RES5
670 ENTER 628 ; RES6@ SUM4=SUM4+RES6
680 NEXT M
690 RES(I,3)=SUM1/5
700 RES(I,4)=SUM2/5
710 RES(I,5)=SUM3/5
720 RES(I,6)=SUM4/5
730 DISP "    DATA NUMBER:",I
740 DISP "        DISTANCE:",RES(I,2)
750 DISP "REFERENCE ANGLE:",RES(I,1)
760 DISP
770 DISP RES(I,3)
780 DISP RES(I,4)
790 DISP RES(I,5)
800 DISP
810 DISP RES(I,6)
820 DISP
830 PRINT USING 840 ; I,RES(I,1),RES(I,2),RES(I,3),RES(I,4),RES(I,5),RES(I,6)
840 IMAGE DDD,4X,SDDD,9X,SDD.DD,7X,DDDD,9X,DDDD,9X,DDDD,9X,D.DDDD
850 NEXT I
860 ! ******** STORE DATA **********
870 N=I-1
880 IF QF$="Y" OR QF$="YES" THEN GOTO 900
890 GOTO 930
900 CREATE F$,6*N+20,8
910 DISP "FILE CREATED:",F$
920 DISP "================================="
930 ASSIGN# 1 TO  F$
940 PRINT# 1 ; N
950 PRINT# 1 ; TEMP
960 PRINT# 1 ; H
970 FOR I=1 TO N
980 PRINT# 1 ; RES(I,1),RES(I,2),RES(I,3),RES(I,4),RES(I,5),RES(I,6)
990 NEXT I
1000 ASSIGN# 1 TO  *
1010 DISP "DATA STORED !!"
1020 CAT
1030 PRINT CHR$ (12)
1040 DISP "********************  THE  END  ***************************"
1050 END
```

```
10 ! PROGRAM "ENTERPRE"
20 ! PROGRAM TO ENTER DATA FROM PRESSURE TRANSDUCERS FOR PITCH PROBE *******
30 ! VERSION ON 4/10/1988
40 OPTION BASE 1
50 CLEAR
60 PRINTER IS 601
70 DIM RES(50,4)
80 FOR I=1 TO 50
90 FOR J=1 TO 4
100 RES(I,J)=0
110 NEXT J
120 NEXT I
130 ! ================================================================
140 !                        INPUTS
150 ! ================================================================
160 CAT
170 DISP "INPUT FILE NAME TO STORE DATA:"
180 INPUT F$
190 DISP "DO YOU WANT TO CREATE FILE ?"
200 INPUT QF$
210 DISP "INPUT TEMPERATURE:" @ INPUT TEMP
220 DISP "INPUT PRESSURE (mm Hg):" @ INPUT H
230 DISP "INPUT  % AXIAL FROM LEADING EDGE :" @ INPUT A
240 DISP "INPUT  % TANGE FROM BOTTOM BLADE :" @ INPUT T
250 DISP
260 DISP
270 PRINT "============================================================"
280 PRINT "PITCH READINGS FOR RADIUSED TIP BLADE  2.5%CHORD CLEARANCE"
290 PRINT "============================================================"
300 PRINT "PITCH PROBE"
310 PRINT @ PRINT
320 PRINT "          % AXIAL =",A,"DATA STORED IN FILE :",F$
330 PRINT "          --------------                    ------------------------------"
340 PRINT "          % TANG. =",T
350 PRINT "          --------------"
360 PRINT
370 PRINT "          TEMPERATURE (CELCIUS) =",TEMP
380 PRINT "          PRESSURE (mm Hg) =",H @ PRINT @ PRINT
390 PRINT
400 PRINT "      SET YAW                    (P4-P5)        (P01-PS1)"
410 PRINT "NO.   ANGLE(DEG)  DIST.(TURNS)  PT2=V*1000     PT4 =V"
420 PRINT "===   ==========  ============  ==========     ======"
430 PRINT @ PRINT
440 DISP "TO STOP ENTERING DATA TYPE -9999-"
450 DISP "TO REPEAT LAST READING   TYPE -5555-"
460 SL=0
470 FOR I=1 TO 100
480 K=I
490 GOTO 540
500 DISP "INPUT NO. AT WHICH TO RESTART:" @ INPUT I
510 SL=SL+K-I
520 IF I=K THEN GOTO 540
530 PRINT "ABOVE READINGS ARE ERRONEOUS NEXT READINGS ARE REPETITION" @ SL=SL+1
540 DISP "INPUT DISTANCE FROM WALL (NO. OF TURNS) :"
550 INPUT RES(I,2)
560 DISP "SET AND INPUT YAW ANGLE:"
570 INPUT RES(I,1)
580 IF RES(I,1)=9999 OR RES(I,2)=9999 THEN RES(I,1)=0 @ RES(I,2)=0 @ GOTO 780
590 IF RES(I,1)=5555 OR RES(I,2)=5555 THEN I=I-1 @ GOTO 500
600 SUM1=0 @ SUM2=0 @ SUM3=0 @ SUM4=0
```

```
610 ENTER 628 ; RES2
620 FOR M=1 TO 5
630 ENTER 624 ; RES1@ SUM1=SUM1+RES1
640 ENTER 628 ; RES2@ SUM2=SUM2+RES2
650 NEXT M
660 RES(I,3)=SUM1/5
670 RES(I,4)=SUM2/5
680 DISP "    DATA NUMBER:",I
690 DISP "       DISTANCE:",RES(I,2)
700 DISP "YAW ANGLE:",RES(I,1)
710 DISP
720 DISP RES(I,3)
730 DISP RES(I,4)
740 DISP
750 PRINT USING 760 ; I,RES(I,1),RES(I,2),RES(I,3),RES(I,4)
760 IMAGE DDD,4X,SDDD,9X,SDD.DD,7X,DDDD.D,7X,D.DDDD
770 NEXT I
780 ! ******** STORE DATA **********
790 N=I-1
800 IF QF$="Y" OR QF$="YES" THEN GOTO 820
810 GOTO 850
820 CREATE F$,4*N+20,8
830 DISP "FILE CREATED:",F$
840 DISP "==================================="
850 ASSIGN# 1 TO  F$
860 PRINT# 1 ; N
870 PRINT# 1 ; TEMP
880 PRINT# 1 ; H
890 FOR I=1 TO N
900 PRINT# 1 ; RES(I,1),RES(I,2),RES(I,3),RES(I,4)
910 NEXT I
920 ASSIGN# 1 TO  *
930 DISP "DATA STORED !!"
940 CAT
950 PRINT CHR$ (12)
960 DISP "********************  THE  END  ***************************"
970 END
```

APPENDIX 2.B

```
10  ! PROGRAM "CALCPRES"
20 ! ************************************************************
30 ! PROGRAM TO READ RESULTS , CHANGE VOLTS TO PRESSURES ,
40 ! CALCULATE KPSI2 , FIND PSI , FIND Pstat ,FIND P01-P02
50 ! P4-P5 FROM PITCH PROBE
60 ! RADIUSED TIP EXIT  TRAVERSES USING ENDWALL PROBE + PITCH PROBE
70 ! PRESURE TRANSDUCERS CONNECTED FOR MIN ERROR
80 ! ************************************************************
90 OPTION BASE 1
100 CLEAR
110 PRINTER IS 601
120 DISP "************************************************"
130 DISP " THIS PROGRAM READS YAW DATA FROM :D700"
140 DISP "             READS PITCH DATA FROM :D700"
150 DISP "           AND STORES DATA ON :D700"
160 DISP "************************************************"
170 DISP "PRESS CONT WHEN THE FLOPPY DRIVES ARE READY "
180 DISP "------------------------------------------------"
190 PAUSE
200 ! GOTO 360
210 ! ========================================================
220 ! FILE DATA
230 ! ========================================================
240 DIM AX(6)
250 DIM TA(20)
260 ! % AXIAL
270 DATA 100
280 ! % TANGENTIAL
290 DATA 10,20,35,50,60,70,80,85,90,95
300 FOR I=1 TO 1
310 READ AX(I)
320 NEXT I
330 FOR I=1 TO 10
340 READ TA(I)
350 NEXT I
360 ! ============================================================
370 ! DIMENSION AND ZERO ARRAYS
380 ! ============================================================
390 DIM RES(50,6)
400 DIM PRESS(50,6)
410 DIM COEF(50,6)
420 DIM CALC(50,6)
430 DIM DIMLESS(50,6)
440 DIM PITCH(50,4)
450 DIM PP(50,4)
460 DIM PPI(50,4)
470 DISP "INITIALIZING ARAYS !"
480 FOR I=1 TO 50
490 FOR J=1 TO 4
500 PITCH(I,J)=0
510 PP(I,J)=0
520 PPI(I,J)=0
530 NEXT J
540 NEXT I
550 FOR I=1 TO 50
```

```
560 FOR J=1 TO 6
570 RES(I,J)=0
580 PRESS(I,J)=0
590 COEF(I,J)=0
600 CALC(I,J)=0
610 DIMLESS(I,J)=0
620 NEXT J
630 NEXT I
640 ! ============================================================
650 ! MAIN LOOP
660 ! ============================================================
670 FOR V=1 TO 1
680 FOR W=1 TO 10
690 RES$="RTA"&VAL$ (AX(V))&"T"&VAL$ (TA(W))
700 PITCH$="PRTA"&VAL$ (AX(V))&"T"&VAL$ (TA(W))
710 CALC$="5DRTEXIT"&VAL$ (TA(W))
720 DISP RES$,PITCH$,CALC$
730 ! ============================================================
740 ! INPUTS
750 ! ============================================================
760 CR$="Y" @ GOTO 820
770 DISP "ENTER NAME OF FILE IN WHICH TO STORE DIMENSIONLESS DATA:"
780 INPUT CALC$
790 CAT
800  DISP "ENTER NAME OF RESULTS DATA FILE"
810  INPUT RES$
820 ! ============================================================
830 ! READ RESULTS ARRAYS FROM DISC
840 ! ============================================================
850 MASS STORAGE IS ":D700"
860 ASSIGN# 1 TO  RES$
870 READ# 1 ; N
880 READ# 1 ; T
890 READ# 1 ; H
900 FOR I=1 TO N
910 READ# 1 ; RES(I,1),RES(I,2),RES(I,3),RES(I,4),RES(I,5),RES(I,6)
920 NEXT I
930 MASS STORAGE IS ":D700"
940 ASSIGN# 2 TO  PITCH$
950 READ# 2 ; NP
960 READ# 2 ; TP
970 READ# 2 ; HP
980 FOR I=1 TO NP
990 READ# 2 ; PITCH(I,1),PITCH(I,2),PITCH(I,3),PITCH(I,4)
1000 NEXT I
1010 ! ============================================================
1020 ! CALCULATE DISTANCE FROM WALL AND PRESSURES USING P.TR.CALIBRATIONS
1030 ! ============================================================
1040 ! YAW PROBE
1050 ! *********
1060 ! PRESS(I,1)=REFFERENCE ANGLE (YAW ANGLE)
1070 ! PRESS(I,2)=ACTUAL DISTANCE FROM WALL FOR YAW PROBE
1080 ! PRESS(I,3)=P.T.1 = P01-P1
1090 ! PRESS(I,4)=P.T.2 = P2-P3
1100 ! PRESS(I,5)=P.T.3 = P1-P2
1110 ! PRESS(I,6)=P.T.4 = P01-PS1 FOR YAW PROBE
1120 ! PITCH PROBE
1130 ! ***********
1140 ! PP(I,1)=ACTUAL DISTANCE FROM WALL FOR PITCH PROBE
1150 ! PP(I,2)=P.T.2 =(P4-P5)
```

```
1160 ! PP(I,3)=P.T.4 =(P01-PS1) FOR PITCH PROBE
1170 ! ============================================================
1180 DENSITY=13600*9.81*H/1000/287.1/(273+T)
1190 DISP "AIR DENSITY IS :",DENSITY
1200 FOR I=1 TO N
1210 PRESS(I,1)=RES(I,1)
1220 PRESS(I,2)=(RES(1,2)-RES(I,2))*4.65+.25
1230 PRESS(I,3)=-1172.0759+587.0971*RES(I,3)/1000
1240 PRESS(I,4)=-1153.2179+578.0121*RES(I,4)/1000
1250 PRESS(I,5)=-1165.9342+583.8912*RES(I,5)/1000
1260 PRESS(I,6)=-610.42495+758.1216*RES(I,6)
1270 NEXT I
1280 FOR I=1 TO NP
1290 PP(I,1)=(RES(1,2)-PITCH(I,2))*4.65+.25
1300 PP(I,2)=-1153.2179+578.0121*PITCH(I,3)/1000
1310 PP(I,3)=-610.425+758.1216*PITCH(I,4)
1320 NEXT I
1330 ! ============================================================
1340 ! INTERPOLATE TO FIND PITCH DATA AT SAME POINTS AS YAW DATA
1350 ! ============================================================
1360 ! PPI(I,1)=P4-P5 AT YAW DATA POINT
1370 ! PPI(I,2)=P01-PS1 AT YAW DATA POINT
1380 ! PPI(I,3)=P4-P5 WITH WIND TUNNEL CORRECTION
1390 ! ============================================================
1400 PPI(1,1)=PP(1,2)
1410 PPI(1,2)=PP(1,3)
1420   FOR I=2 TO N
1430 FOR J=2 TO NP
1440 IF PRESS(I,2)<PP(1,1) THEN GOTO 1460
1450 GOTO 1490
1460 PPI(I,1)=PP(1,2)
1470 PPI(I,2)=PP(1,3)
1480 GOTO 1530
1490 IF PRESS(I,2)<PP(J,1) THEN GOTO 1510
1500 NEXT J
1510   PPI(I,1)=PP(J,2)-(PP(J,2)-PP(J-1,2))*(PP(J,1)-PRESS(I,2))/(PP(J,1)-PP(J-1,1))
1520   PPI(I,2)=PP(J,3)-(PP(J,3)-PP(J-1,3))*(PP(J,1)-PRESS(I,2))/(PP(J,1)-PP(J-1,1))
1530   NEXT I
1540 ! ============================================================
1550 ! CONVERT P4-P5 TO TUNNEL SETTING USED WITH YAW TRAVERSE
1560 ! ============================================================
1570 FOR I=1 TO N
1580 PPI(I,3)=PPI(I,1)*PRESS(I,6)/PPI(I,2)
1590 NEXT I
1600 ! ============================================================
1610 ! CALCULTE Ktheta, FIND theta ,FIND COEFICIENTS
1620 ! ============================================================
1630 ! COEF(I,1)=Ktheta=(P4-P5)/(P1-P2)
1640 ! COEF(I,2)=theta=PITCH ANGLE
1650 ! COEF(I,3)=(Pt-Ps)/(P1-P2)
1660 ! COEF(I,4)=(P1-Pt)/Pt-Ps)
1670 ! COEF(I,5)
1680 ! COEF(I,6)
1690 ! ============================================================
1700 ! CALIBRATION CURVES FOR ENDWALL + PITCH PROBES 5-HOLE CAL.
1710 ! ============================================================
1720 FOR M=1 TO NP
1730 IF PP(M,1)<5 THEN GOTO 1750
1740 GOTO 1760
1750 NEXT M
```

```
1760 FOR I=1 TO N
1770 IF PRESS(I,2)<PP(M,1) THEN GOTO 1790
1780 GOTO 1810
1790 COEF(I,2)=0
1800 GOTO 1880
1810 COEF(I,1)=PPI(I,3)/PRESS(I,5)
1820 A=-1.390701
1830 B=-19.32034
1840 C=.778482
1850 D=.292109
1860 E=.020172
1870 COEF(I,2)=A+B*COEF(I,1)+C*COEF(I,1)^2+D*COEF(I,1)^3+E*COEF(I,1)^4
1880 A=1.293291
1890 B=-.002852
1900 C=-.000303
1910 D=-.000011
1920 E=.000000455616
1930 COEF(I,3)=A+B*COEF(I,2)+C*COEF(I,2)^2+D*COEF(I,2)^3+E*COEF(I,2)^4
1940 A=-.011014
1950 B=-.002949
1960 C=-.000381
1970 D=.000001083042
1980 COEF(I,4)=A+B*COEF(I,2)+C*COEF(I,2)^2+D*COEF(I,2)^3
1990 NEXT I
2000 ! ============================================================
2010 ! CALCULATE DIMENSIONLESS COEFICIENTS AND TOTAL ANGLE
2020 ! ============================================================
2030 ! CALC(I,1)=YAW ANGLE
2040 ! CALC(I,2)=PITCH ANGLE
2050 ! CALC(I,3)=LOSS
2060 ! CALC(I,4)=VELOCITY DIFF.
2070 ! CALC(I,5)=STATIC PRESS DIFF.
2080 ! CALC(I,6)=UPSTREAM Q
2090 ! ============================================================
2100 FOR I=1 TO N
2110 CALC(I,1)=PRESS(I,1)
2120 CALC(I,2)=COEF(I,2)
2130 CALC(I,3)=PRESS(I,3)+COEF(I,3)*COEF(I,4)*PRESS(I,5)
2140 CALC(I,4)=COEF(I,3)*PRESS(I,5)
2150 CALC(I,5)=-PRESS(I,6)+PRESS(I,3)+COEF(I,3)*PRESS(I,5)*(1+COEF(I,4))
2160 CALC(I,6)=PRESS(I,6)
2170 NEXT I
2180 ! ============================================================
2190 ! PRINT AND STORE DIMENSIONLESS COEFICIENTS AND ANGLES
2200 ! ============================================================
2210 ! CONVERT P4-P5 TO WIND TUNNEL SETTING AT YAW MEASUREMENT
2220 PRINT "============================================================"
2230 PRINT "CLEARANCE=2.5% CHORD=4.65mm ,RADIUSED TIP EXIT TRAVERSE "
2240 PRINT "------------------------------------------------------------"
2250 PRINT "PRESURE TRANSDUCERS CONECTED FOR MIN ERROR"
2260 PRINT "PRESURE TRANSDUCER CALIBRATION 4/8/88 T=23.5"
2270 PRINT "ENDWALL PROBE + PITCH PROBE USED"
2280 PRINT
2290 PRINT "DATA STORED IN FILE ",CALC$
2300 PRINT "------------------  ==========="
2310 PRINT @ PRINT
2320 PRINT "NO.   DIST.(mm)     YAW       PITCH     LOSS COEF     VEL.COEF      PRESS
2330 PRINT "===   =========     ===       =====     =========     ========      ======
2340 FOR I=1 TO N
2350 DIMLESS(I,1)=PRESS(I,2)
```

```
2360 DIMLESS(I,2)=CALC(I,1)
2370 DIMLESS(I,3)=CALC(I,2)
2380 DIMLESS(I,4)=CALC(I,3)/CALC(I,6)
2390 DIMLESS(I,5)=CALC(I,4)/CALC(I,6)
2400 DIMLESS(I,6)=CALC(I,5)/CALC(I,6)
2410 PRINT USING 2420 ; I,DIMLESS(I,1),DIMLESS(I,2),DIMLESS(I,3),DIMLESS(I,4)
IMLESS(I,5),DIMLESS(I,6)
2420 IMAGE DD,4X,DDD.D,7X,SDD.DD,5X,SDD.DD,6X,DD.DDDD,6X,DDD.DDD,6X,DDD.DDD
2430 NEXT I
2440 PRINT CHR$ (12)
2450 MASS STORAGE IS ":D700"
2460 IF CR$="Y" OR CR$="YES" THEN GOTO 2480
2470 GOTO 2510
2480 CREATE CALC$,N*6+20,8
2490 DISP "CREATED FILE :",CALC$
2500 DISP "======================================="
2510 ASSIGN# 2 TO  CALC$
2520 PRINT# 2 ; N
2530 FOR I=1 TO N
2540 PRINT# 2 ; DIMLESS(I,1),DIMLESS(I,2),DIMLESS(I,3),DIMLESS(I,4),DIMLESS(I,5),
 ,DIMLESS(I,6)
2550 NEXT I
2560 DISP "DATA STORED IN FILE ",CALC$
2570 ! END
2580  NEXT W
2590  NEXT V
2600 MASS STORAGE IS ":D700"
2610 END
2620 END
2630 END
2640 ! % AXIAL
2650 DATA 20,40,60,70,80,90
2660 ! % TANGENTIAL
2670 DATA 10,20,35,50,70,80,90,95
2680 FOR I=1 TO 6
2690 READ AX(I)
2700 NEXT I
2710 FOR I=1 TO 8
2720 READ TA(I)
2730 NEXT I
2740 FOR V=6 TO 6
2750 FOR W=1 TO 8
2760 RES$="DRTA"&VAL$ (AX(V))&"T"&VAL$ (TA(W))
2770  DISP "PURGING ",RES$
2780  PURGE RES$
2790 NEXT W
2800 NEXT V
2810 END
```

APPENDIX 3.A

```
10  ! PROGRAM "CALIBRATIO"
20 ! PRESSURE TRANSDUCER CALIBRATION PROGRAM
30 PRINTER IS 601
40 CLEAR
50 DIM H(20)
60 DIM V(20)
70 DIM P(20)
80 FOR I=1 TO 20
90 H(I)=0
100 V(I)=0
110 P(I)=0
120 NEXT I
130 DISP "ENTER TRANSDUCER NO. OR NAME:"
140 INPUT T$
150 DISP "ENTER SELECT CODE:"
160 INPUT SC
170 PRINT "PRESSURE TRANSDUCER CALIBRTION"
180 PRINT "==============================" @ PRINT @ PRINT
190 PRINT "TRANSDUCER :",T$,SC
200 PRINT "================================================" @ PRINT @ PRINT
210 DISP "ENTER DENSITY OF MANOMETER FLUID (mm)"
220 INPUT D
230 PRINT "MANOMETER DENSITY:",D,"mm" @ PRINT @ PRINT
240 PRINT "HEIGHT(mm)              VOLTS (v)              PRESSURE(Pa)"
250 PRINT "=========               =========              ============" @ PRINT
260 I=0
270 DISP "TO STOP ENTERING POINTS TYPE -9999-"
280 DISP "INPUT MANOMETER HEIGHT IN mm:"
290 I=I+1
300 INPUT H(I)
310 IF H(I)=9999 THEN GOTO 370
320 ENTER SC ; V
330 V(I)=V/1000
340 P(I)=D*9.81*H(I)/1000
350 PRINT H(I),V(I),P(I)
360 GOTO 280
370 ! ~~~~~~~~~~~X    ,Y    ~~~~~~~~~~~~~~~~~~~~~~~~~~~~~~~~~~~~
380 DISP "~~~~~~~~~~LINEAR REGRESSION~~~~~~~~~~" @ PRINT @ PRINT
390 PRINT "~~~~~~~~~~LINEAR REGRESSION~~~~~~~~~~"
400 SX=0
410 SY=0
420 SXY=0
430 SXX=0
440 SYY=0
450 SX2=0
460 SY2=0
470 n=I-1
480 FOR J=1 TO n
490 SX=SX+V(J)
500 SY=SY+P(J)
510 SXY=SXY+V(J)*P(J)
520 SX2=SX2+V(J)*V(J)
530 SY2=SY2+P(J)*P(J)
540 NEXT J
550 SXX=SX2-SX*SX/n
```

```
560 SYY=SY2-SY*SY/n
570 b=(n*SXY-SX*SY)/(n*SX2-SX*SX)
580 a=SY/n-b*SX/n
590 r=b*SQR (SXX/SYY)
600 PRINT "~~~~~P=a+bV :V IN VOLTS , P IN Pa"
610 PRINT "a=",a
620 PRINT "b=",b
630 PRINT "SAMPLE CORRELATION _r_:",r
640 END
```

APPENDIX 3.B

Pressure transducer calibration constants for 3 different room temperature.

Temp		23	23.8	25
Pressure transducer	constant			
1	a	-1167.6	-1172.1	-1187.0
	b	585.6	587.1	593.8
	r	.999999	.999998	.999201
2	a	-1153.8	-1153.2	-1161.5
	b	578.7	578.0	581.62
	r	.999996	.999996	.999989
3	a	-1161.6	-1165.9	-1176.9
	b	561.5	583.89	588.3
	r	.999997	.999992	.999993
4	a	-617.1	-610.4	-612.6
	b	765.05	758.1	761.9
	r	.999891	.999986	.999981

$P = a + bV$ where P = pressure (Pa)

V = volts

a,b = calibration constants

r = sample corolation

APPENDIX 3.C

3 HOLE PROBE CALIBRATION COEFFICIENTS

$K1 = AX^2 + BX + C$

COEFFICIENTS	
A	.998782813853
B	-.00182847402597 X
C	-8.30898268398E-5 X^2

X angle	Ymeasured	Ycalculated	Deviation
-6.00000	1.00820	1.00676	.00144
-4.00000	1.00140	1.00477	-.00337
-2.00000	1.00330	1.00211	.00119
0.00000	1.00330	.99878	.00452
2.00000	.99070	.99479	-.00409
4.00000	.98440	.99014	-.00574
6.00000	.99400	.98482	.00918
8.00000	.97640	.97884	-.00244
10.00000	.97150	.97219	-.00069

Average deviation .00362813852814
Maximum deviation .00917926406926

$K2 = AX^2 + BX + C$

COEFFICIENTS	
A	.233016883117
B	.0230358225108 X
C	.000159794372294 X^2

X angle	Ymeasured	Ycalculated	Deviation
-6.00000	.10400	.10055	.00345
-4.00000	.13850	.14343	-.00493
-2.00000	.18750	.18758	-.00008
0.00000	.23560	.23302	.00258
2.00000	.27820	.27973	-.00153
4.00000	.32310	.32772	-.00462
6.00000	.38250	.37698	.00552
8.00000	.43100	.42753	.00347
10.00000	.47550	.47935	-.00385

Average deviation .00333641173641
Maximum deviation .00551558441558

$K3 = AX^2 + BX + C$

COEFFICIENTS	
A	.284041731602
B	-.0276917532468 X
C	6.58549783556-5 X^2

X angle	Ymeasured	Ycalculated	Deviation
-6.00000	.45450	.45256	.00194
-4.00000	.39010	.39586	-.00576
-2.00000	.34470	.33969	.00501
0.00000	.28890	.28404	.00486
2.00000	.22010	.22892	-.00882
4.00000	.16880	.17433	-.00553
6.00000	.13280	.12026	.01254
8.00000	.06400	.06672	-.00272
10.00000	.01220	.01371	-.00151

Average deviation .00540990860991
Maximum deviation [illegible]

$$Kpsi2 = AX^2 + BX + C$$

COEFFICIENTS	
A	1.07856008658
B	-.077319004329 X
C	.00219891774892 X^2

X angle	Ymeasured	Ycalculated	Deviation
-6.00000	1.63300	1.62164	.01136
-4.00000	1.41160	1.42302	-.01142
-2.00000	1.24000	1.24199	-.00199
0.00000	1.07500	1.07856	-.00356
2.00000	.92460	.93272	-.00812
4.00000	.81100	.80447	.00653
6.00000	.71000	.69381	.01619
8.00000	.60000	.60074	-.00074
10.00000	.51700	.52526	-.00826

Average deviation .00757577681578
Maximum deviation .016129004329

(COEFFICIENTS A,B,C ARE CALCULATED USING MULTIPLE REGRESSION)

GRAPHS OF CALIBRATION COEFFICIENTS AGAINST YAW ANGLE

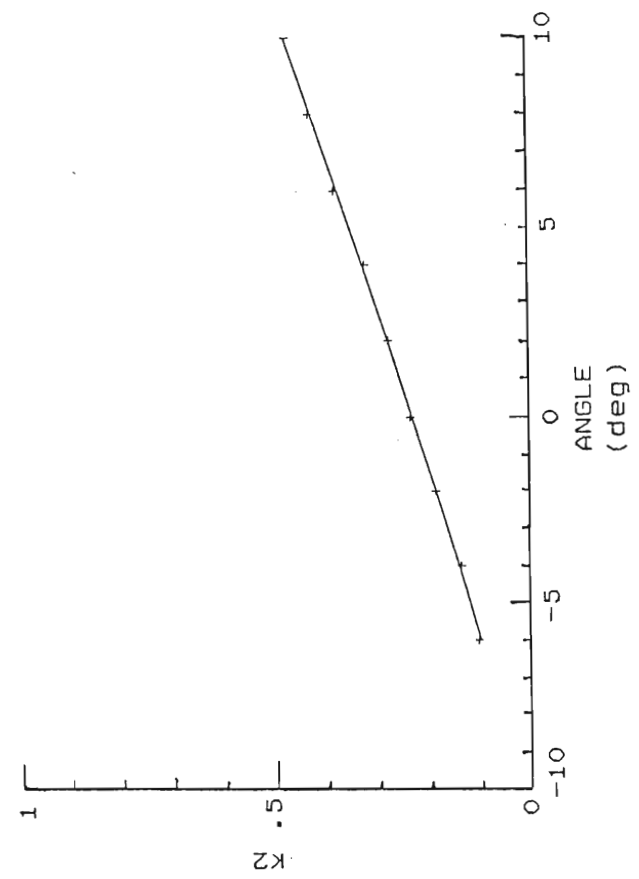

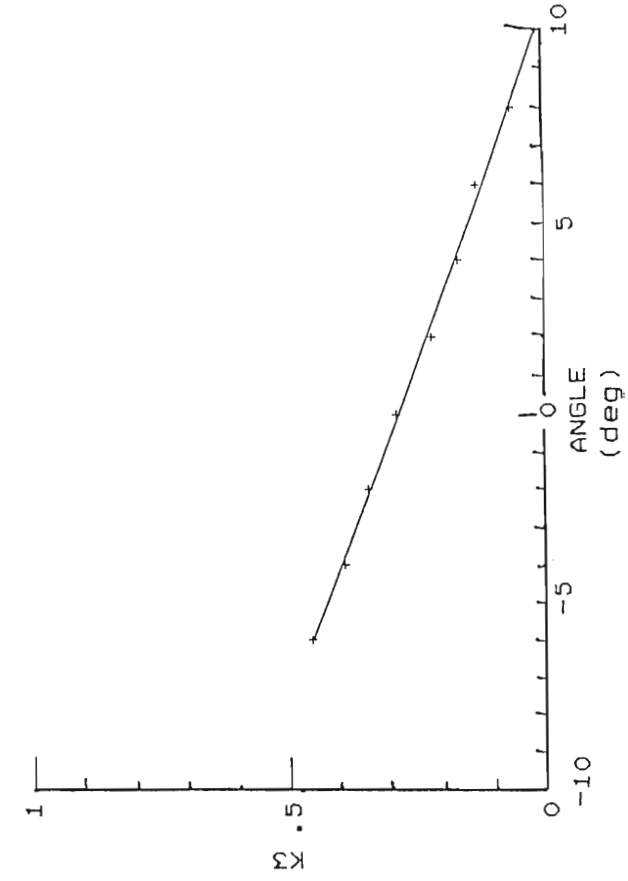

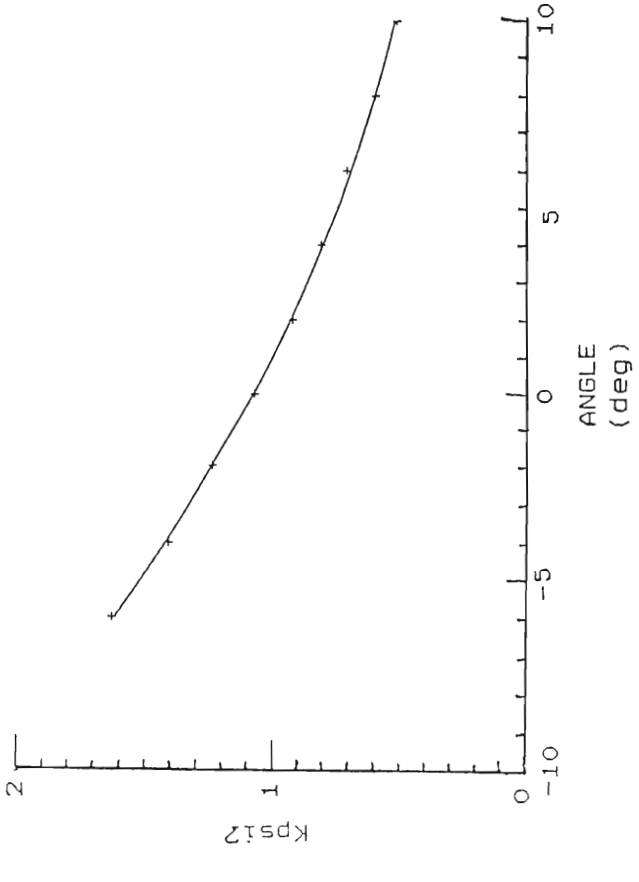

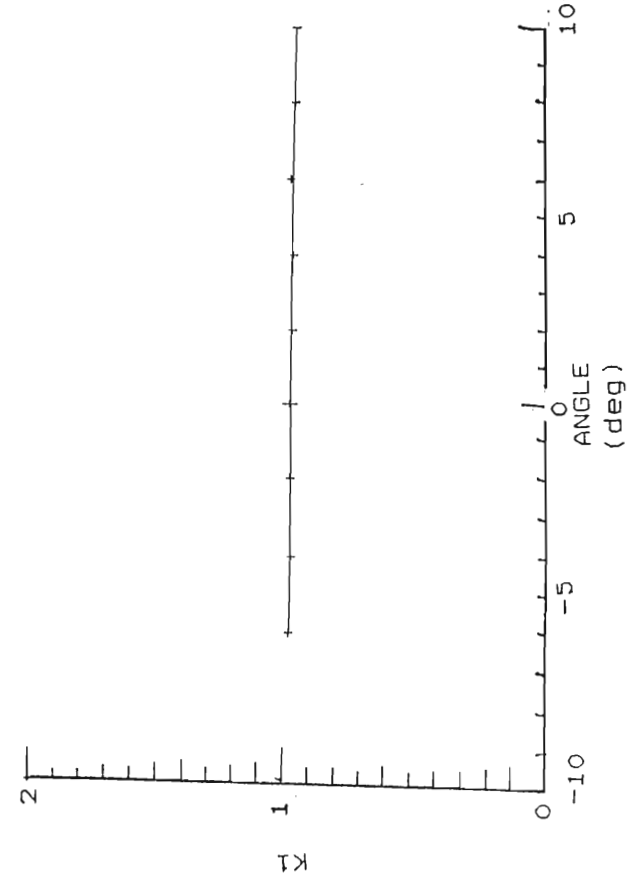

APPENDIX 3.D

5 HOLE PROBE CALIBRATION COEFFICIENTS

ANGLE (DEG)	(P4-P5)/(P1-P2)	(P1-Pt)/(Pt-Ps)	(Pt-Ps)/(P1-P2)
-60	13.166196418	-1.41402549122	8.7366930445
-50	6.67753099868	-1.00128905715	4.93170679371
-40	2.66042100544	-.539601103521	2.50746560362
-30	1.81491160182	-.315900620368	2.11011696526
-20	.974410327601	-.103829349113	1.52824706336
-10	.572424271606	-1.61946012387E-2	1.23633751967
0	-.285789264001	-9.56611991697E-3	1.13951062201
10	-.930365679771	-5.45442612972E-2	1.07209688842
20	-1.37791988677	-.238425427322	1.14826657231
30	-1.69566484838	-.414888967757	1.22634327648
40	-1.89803258454	-.66298167409	1.34079724819
50	-2.10724105971	-.98660375413	1.40839530792
60	-5.53384759258	-1.31456769105	3.67209528373

ANGLE	Pt-P1 (Pa)	P2-P3 (Pa)	P1-P2 (Pa)
-60	1456.1226302	52.45753939	117.86738144
-50	1038.4618244	362.56103104	210.2973584
-40	563.970029	278.11346323	416.81967584
-30	310.6963832	157.94474764	466.10009312
-20	100.9853348	56.79263014	636.42115616
-10	15.4453019	6.8523847	771.4168016
0	9.1046543	-34.82228771	835.23610976
10	52.2562838	-27.19252799	893.62522976
20	231.4969979	31.706905	845.570984
30	406.040936	-68.34698951	798.04224032
40	658.8449042	-125.39678378	741.17123744
50	984.0379325	-159.037088	708.18138464
60	1293.9077291	120.89417203	268.04419808

Pt-Ps
1029.7711316
1037.12491112
1045.16100008
983.525714
972.60876296
953.73153512
951.76041896
958.05282824
970.94089544
978.67373576
993.7603556
997.39933928
984.2808356

Model fitting results for: PTPSP1P2

Independent variable	coefficient	std. error	t-value	sig.level
CONSTANT	1.293291	0.142248	9.0918	0.0000
ANGLE	-0.002852	0.005103	-0.5589	0.5915
ANGLE^2	-0.000303	0.000221	-1.3730	0.2070
ANGLE^3	-0.000011	1.878431E-6	-5.9611	0.0003
ANGLE^4	4.556167E-7	6.026843E-8	7.5598	0.0001

R-SQ. (ADJ.) = 0.9851 SE= 0.269553 MAE= 0.174309 DurbWat= 2.418
Previously: 0.0000 0.000000 0.000000 0.000
13 observations fitted, forecast(s) computed for 0 missing val. of dep. var.

Model fitting results for: P1PTPTPS

Independent variable	coefficient	std. error	t-value	sig.level
CONSTANT	-0.011014	0.010776	-1.0221	0.3334
ANGLE	-0.002949	0.000488	-6.0434	0.0002
ANGLE^2	-0.000381	5.759889E-6	-66.0767	0.0000
ANGLE^3	1.083042E-6	1.795961E-7	6.0304	0.0002

R-SQ. (ADJ.) = 0.9973 SE= 0.025772 MAE= 0.016821 DurbWat= 3.293
Previously: 0.9877 0.054892 0.041440 1.067
13 observations fitted, forecast(s) computed for 0 missing val. of dep. var.

Model fitting results for: ANGLE

Independent variable	coefficient	std. error	t-value	sig.level
CONSTANT	-1.390701	2.010724	-0.6916	0.5087
P4P5	-19.32034	1.298576	-14.8781	0.0000
P4P5^2	0.778482	0.174811	4.4533	0.0021
P4P5^3	0.292109	0.044093	6.6249	0.0002
P4P5^4	-0.020172	0.003372	-5.9822	0.0003

R-SQ. (ADJ.) = 0.9792 SE= 5.622868 MAE= 3.380914 DurbWat= 1.220
Previously: 0.8986 12.402426 8.727349 1.578
13 observations fitted, forecast(s) computed for 0 missing val. of dep. var.

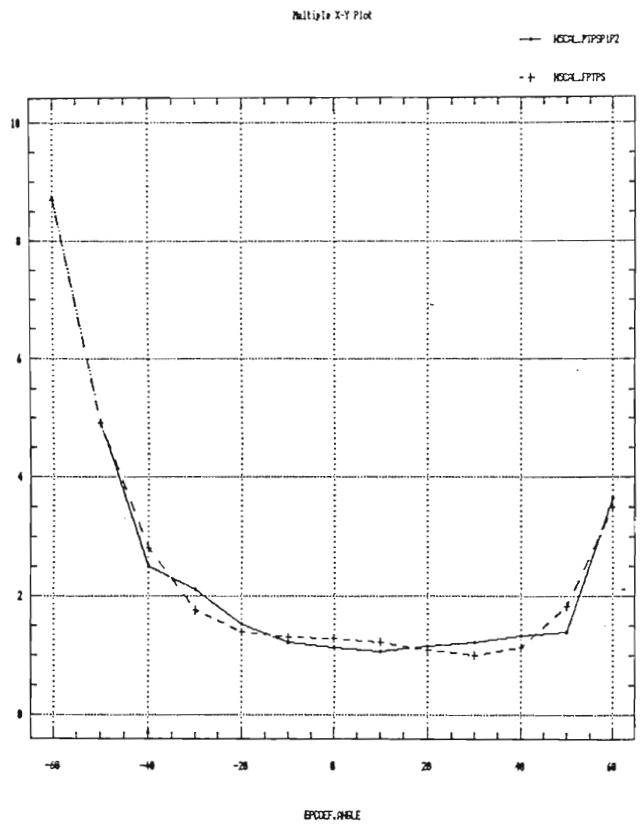
Multiple X-Y Plot
MSCAL_MIPSPIP2
MSCAL_FPIPS
EPCOEF.ANGLE

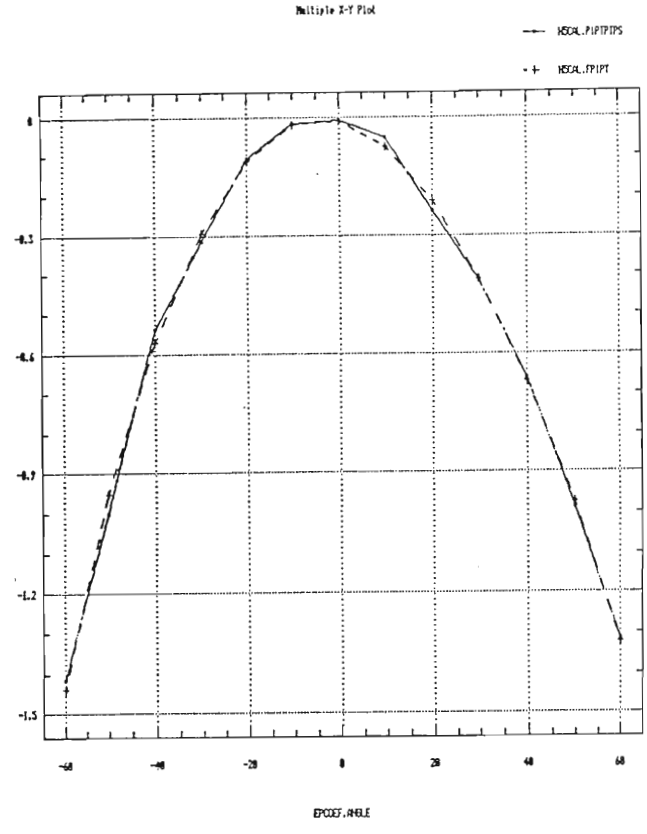
Multiple X-Y Plot
MSCAL.MIPIPIPS
MSCAL.FPIPT
EPCOEF.ANGLE

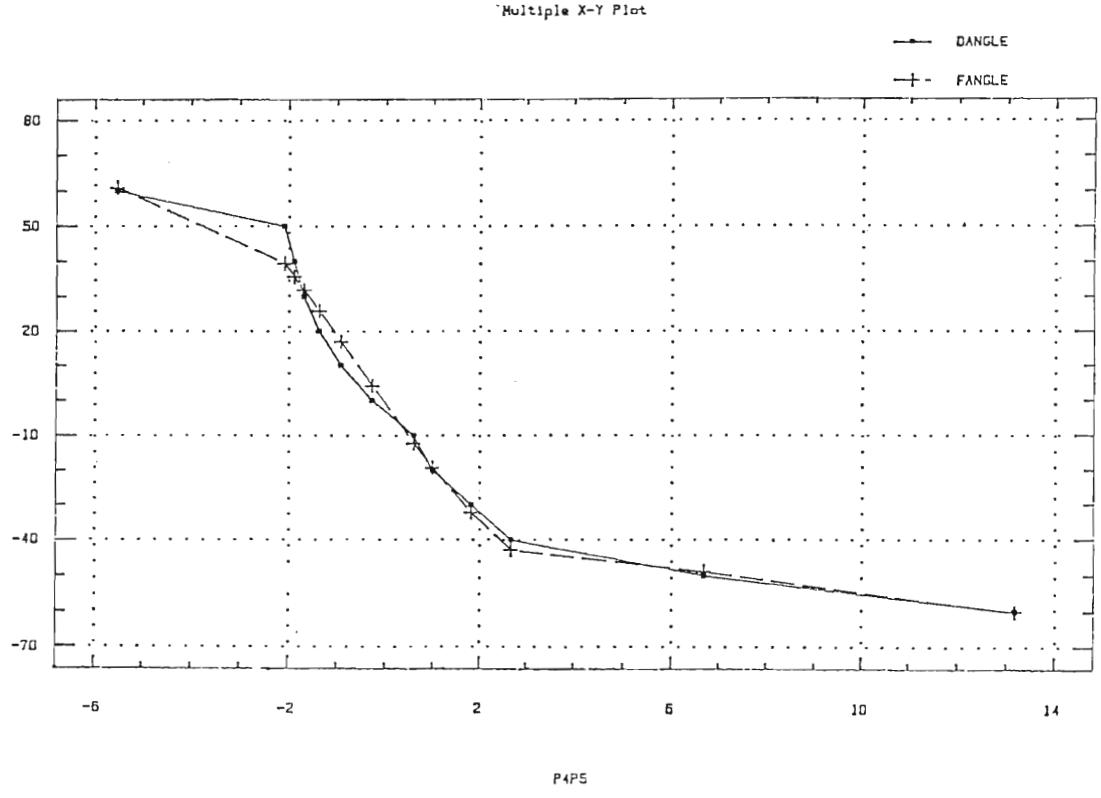
Multiple X-Y Plot
DANGLE
FANGLE
80
50
20
-10
-40
-70
-6
-2
2
6
10
14
P4P5

APPENDIX 4.A

PROGRAM 'SPLN INT'

PROGRAM WRITTEN BY PROFESSOR J P BINDON

INTERGRATES 5-HOLE DATA RESULT OBTAINED FROM PROGAM 'CALCPRES' TO CALCULATE SIMULATED ROTOR PERFORMANCE

```
10   PRINT
20   CLEAR
30  PRINT "          EXIT BOUNDARY LAYER INTEGRATION       "
40  PRINT "            (Spline fit in pitch dir)           "
50  PRINT "            SIMULATED ROTOR PERFORMANCE         "
60  PRINT "                 ( SPLN INT )                   "
70  DEG
80  PAGESIZE 24
90  R$=CHR$ (13)
100  PRINT @ PRINT
110  DIM V(4,15)
120  ! Variable for pitchwise integration , 1 2 3 4 allocated as needed
130  DIM Z(15,31),B2(15,31),CL2(15,31),W2S(15,31),W2W(15,31),PSI(15,31)
140  DIM S(15),M(15),TRAV$(15)
150  DIM WC(15,31),CP2(15,31)
160  DIM CT(15,31),C2S(15,31)
170 DIM XB(15),YB(15),B(15),s(15),G(15)
180 !
190 ! Z(mm) becomes Z2/Z1, W2W is W2/W, WC is W2/W*Cos(B2), W2S is (W2/W)^2
200 ! CT is C02/W, C2S is C2^2/W^2
210 !
220 ! Inlet Boundary Layer Data
230 Z1=186/4 @ ! ie 1/4 chord
240 Clin=.13709 @ ! Inlet BL loss coeff
250 !
260 ! Creating traverse DATA
270 READ Case$,Ze,N
280 FOR n=1 TO N @ READ S(n)@ NEXT n
290 ! DATA "Radiused Edge",1.111595,12,.02,.1,.2,.35,.5,.6,.7,.8,.85,.9,.95,1.02

300    DATA "Square Edge",1.12343286,12,.02,.1,.2,.35,.5,.6,.7,.8,.85,.9,.95,1.0
2
310 !  DATA "Zero Clearance",1.0464554,13,.02,.1,.2,.3,.4,.5,.6,.7,.8,.85,.9,.95
,1.02
320 ! DATA "Radiused Squealer",1.178707,12,.02,.1,.2,.35,.5,.6,.7,.8,.85,.9,.95,
1.02
330 PRINT @ PRINT Case$ @ PRINT
340 !
350 !   Input Data from Disc and Create Required Quantities
360 !
370 FOR n=2 TO N-1
380 TRAV$(n)="5DSTEXIT"&VAL$ (S(n)*100) @ DISP "Input of ";TRAV$(n)
390 ASSIGN# 1 TO  TRAV$(n)
400 READ# 1 ; M(n)
```

```
410 FOR m=1 TO M(n)
420 READ# 1 ; Z(n,m),B2(n,m),PSI(n,m),CL2(n,m),W2S(n,m),CP2(n,m)
430 Z(n,m)=Z(n,m)/Z1
440 W2W(n,m)=SQR (W2S(n,m))
450 WC(n,m)=W2W(n,m)*COS (B2(n,m))*COS (PSI(n,m))
460 IF CL2(n,m)<0 THEN CL2(n,m)=0 @ BEEP @ DISP "Loss Coef neg and set zero at Z
=";Z(n,m)*Z1
470 NEXT m
480 !
490 ! Creating Wall Values
500 !
510 Z(n,0)=0
520 W2W(n,0)=0
530 CL2(n,0)=1+CP2(n,1)
540 CP2(n,0)=CP2(n,1)
550 B2(n,0)=B2(n,1)
560 WC(n,0)=WC(n,1)
570 NEXT n
580 !
590 PRINT "           Determining The Exit Plane Integration Height"
600 K=1
610 Cmze=0
620 DISP "Ze is ";Ze;" Recalculate ? (Y/N) " @ INPUT A$@ IF A$ <> "Y" THEN 800
630 FOR n=2 TO N-1
640 Cmv=0
650 FOR m=1 TO M(n)
660 IF Z(n,m)<= Ze THEN Cmv=Cmv+(WC(n,m)+WC(n,m-1))/2*(Z(n,m)-Z(n,m-1)) @ GOTO 7
20
670 DZ=Ze-Z(n,m-1)
680 PM=WC(n,m-1)
690 PM1=WC(n,m)-PM
700 Cmv=Cmv+(PM+PM1*DZ/2/(Z(n,m)-Z(n,m-1)))*DZ
710 GOTO 730
720 NEXT m
730 V(K,n)=Cmv @ ! PRINT "Cmv at n=";n;"  is ";Cmv
740 NEXT n
750 GOSUB 1610 @ Cmze=AREA
760 BEEP
770 DISP "Mass Flow Coeff Cmze = ";Cmze;"   for Ze = ";Ze
780 IF ABS (Cmze-1)>.00001 THEN Ze=Ze+.75*(1-Cmze)*Ze @ GOTO 630
790 !
800 PRINT @ PRINT " Exit Height Ze is ";Ze
810 PRINT @ PRINT " Integrating for Work Coef Cw, Loss Coeff Cl and C2bar"
820 !
830 Phi=.5
840 Cw=0 @ Cl=0 @ C2bar=0 @ Ctm=0
850 !
860 PRINT "Pitch       Cl         Cw        C2b     Ctheta"
870 FOR n=2 TO N-1
880 !
890 FOR m=1 TO M(n)
900 CT(n,m)=W2W(n,m)*SIN (B2(n,m))-1/Phi @ !    Ctheta
```

```
910 C2S(n,m)=CT(n,m)^2+WC(n,m)^2 @ !            C2^2/W^2
920 NEXT m
930 !
940 CT(n,0)=-(1/Phi) @ ! wall value
950 C2S(n,0)=1/Phi^2 @ ! wall value
960 Cww=0 @ C11=0 @ C2b=0 @ Ctmm=0
970 !
980 FOR m=1 TO M(n)
990 !
1000 IF Z(n,m)<= Ze THEN 1150
1010 DZ=Ze-Z(n,m-1)
1020 PM=WC(n,m-1)*CT(n,m-1)
1030 PM1=WC(n,m)*CT(n,m)-PM
1040 Cww=Cww+(PM+PM1*DZ/2/(Z(n,m)-Z(n,m-1)))*DZ
1050 PM=WC(n,m-1)*CL2(n,m-1)
1060 PM1=WC(n,m)*CL2(n,m)-PM
1070 C11=C11+(PM+PM1*DZ/2/(Z(n,m)-Z(n,m-1)))*DZ
1080 PM=WC(n,m-1)*C2S(n,m-1)
1090 PM1=WC(n,m)*C2S(n,m)-PM
1100 C2b=C2b+(PM+PM1*DZ/2/(Z(n,m)-Z(n,m-1)))*DZ
1110 PM=CT(n,m-1)
1120 PM1=CT(n,m)-PM
1130 Ctmm=Ctmm+(PM+PM1*DZ/2/(Z(n,m)-Z(n,m-1)))*DZ
1140 GOTO 1200
1150 Cww=Cww+(WC(n,m)*CT(n,m)+WC(n,m-1)*CT(n,m-1))/2*(Z(n,m)-Z(n,m-1))
1160 C11=C11+(WC(n,m)*CL2(n,m)+WC(n,m-1)*CL2(n,m-1))/2*(Z(n,m)-Z(n,m-1))
1170 C2b=C2b+(WC(n,m)*C2S(n,m)+WC(n,m-1)*C2S(n,m-1))/2*(Z(n,m)-Z(n,m-1))
1180 Ctmm=Ctmm+(CT(n,m)+CT(n,m-1))/2*(Z(n,m)-Z(n,m-1))
1190 NEXT m
1200 V(1,n)=C11 @ V(2,n)=Cww @ V(3,n)=C2b @ V(4,n)=Ctmm
1210 PRINT USING "DDD,2X,D.DDDDDD,2X,SD.DDDDD,2X,DD.DDDDD,2X,SD.DDDDD" ; S(n)*10
0;C11;Cww;C2b;Ctmm
1220 NEXT n
1230 !
1240 PRINT @ PRINT @ PRINT "Extrapolated endpoints at S=.02 and S=1.02 for Splin
e Integration"
1250 ! FOR n=2 TO N-1 @ PRINT V(2,n) @ NEXT n
1260 K=2 @ GOSUB 1610 @ Cw=2/Phi^2+2/Phi*AREA
1270 K=1 @ GOSUB 1610 @ C12=AREA @ C1bar=C12-C1in
1280 K=3 @ GOSUB 1610 @ C2bar=AREA
1290 K=4 @ GOSUB 1610 @ Ctm=AREA
1300 !
1310 BEEP @ PRINT @ PRINT @ !              Printing out Results
1320 PRINT "Phi = ";Phi;R$
1330 PRINT "Work Coeff Cw                          = ";Cw;R$
1340 PRINT "Exit Loss Coeff C12                    = ";C12;R$
1350 PRINT "Cascade Loss Coeff C12-C1in = C1bar  = ";C1bar;R$
1360 PRINT "Mean Outlet Velocity Coef C2bar^2/W^2 = ";C2bar;R$
1370 PRINT "Mean Ctheta / W                        = ";Ctm;R$
1380 A1=ASN (Ctm/SQR (C2bar)) @ PRINT "Mean Alpha2 = ";A1;R$
1390 Cxm=SQR (C2bar)*COS (A1) @ PRINT "Mean Cx     = ";Cxm;R$
1400 B2m=ATN ((1/Phi+Ctm)/Cxm) @ PRINT "Mean Beta2  = ";B2m;R$
```

```
1410 !
1420 PRINT "Finding C2id^2/W^2 at furthest point from endwall";R$
1430 !
1440 FOR n=2 TO N-1
1450 m=M(n)
1460 V(3,n)=WC(n,m)*C2S(n,m) @ ! C2id
1470 V(2,n)=WC(n,m) @ !          Cme
1480 NEXT n
1490 K=2 @ GOSUB 1610 @ Cme=AREA @ K=3 @ GOSUB 1610 @ C2id=AREA/Cme
1500 PRINT "C2id^2 / W^2                                    = ";C2id
1510 !
1520 PRINT "Tip Region Turbine Efficiency (ts)              = ";Cw/(Cw+C1bar+C2bar-C2id
);R$;R$
1530 PRINT "Tip Region Turbine Efficiency (tt)              = ";Cw/(Cw+C1bar);R$;R$
1540 Cp=Cw+C1bar+C2bar
1550 PRINT "Driving Pressure Coeff (Po1-P2/.5 Ro W2) = ";Cp;R$
1560 PRINT "Work Coeff Cwp                                  = ";Cw/Cp;R$
1570 !
1580 DISP "Enter new Phi value (or type 0 to end)";@ INPUT Phi
1590 IF Phi>0 THEN 840
1600 END
1610 ! ****************   SUB INTUN   ************************
1620 ! Y data is supplied via array V(n,m) and integration may be done on any
1630 ! row n by specifying K
1640 ! X data is in array S(n)
1650 V(K,1)=V(K,2)-(V(K,3)-V(K,2))*.8 @ V(K,N)=V(K,N-1)+(V(K,N-1)-V(K,N-2))*1.41
521 ! generating first and last array points 1 and N by extrapolating
1660 Xent=1 @ IF K=1 THEN DISP "If extrapolated endpoints ";V(1,1);"  and ";V(1,
N);" are OK, type in zero" @ INPUT Xent
1670 IF K=1 AND Xent<> 0 THEN DISP "Type in desired value at 0" @ INPUT V(1,1)
1680 IF K=1 AND Xent<> 0 THEN DISP "Type in desired value at 1" @ INPUT V(1,N)
1690 PRINT "K = ";K,V(K,1),V(K,N)
1700 FOR I=1 TO N @ XB(I)=S(I) @ YB(I)=V(K,I) @ NEXT I
1710 E=.000001
1720 FOR I=2 TO N-1
1730 H=XB(I+1)-XB(I-1)
1740 XX=XB(I)-XB(I-1)
1750 B(I)=.5*XX/H
1760 T=((V(K,I+1)-V(K,I))/(XB(I+1)-XB(I))-(V(K,I)-V(K,I-1))/XX)/H
1770 s(I)=2*T
1780 G(I)=3*T
1790 NEXT I
1800 s(1)=0 @ s(N)=0
1810 W=8-4*SQR (3)
1820 U=0
1830 FOR I=2 TO N-1
1840 T=W*(-s(I)-B(I)*s(I-1)-(.5-B(I))*s(I+1)+G(I))
1850 H=ABS (T)
1860 IF H>U THEN U=H
1870 s(I)=s(I)+T
1880 NEXT I
1890 IF U>= E THEN 1820
1900 AREA=0
```

```
1910 FOR I=1 TO N-1
1920 H=XB(I+1)-XB(I)
1930 AREA=AREA+(.5*H*(V(K,I)+V(K,I+1))-1/24*H^3*(s(I)+s(I+1)))
1940 NEXT I
1950 RETURN
```

APPENDIX 4.B

PROGRAM 'GAP EXIT I'

PROGRAM WRITTEN BY PROFESSOR J P BINDON

CALCULATES LOSS AT GAP EXIT, GAP MASS FLOW RATE AND
DISCHARGE COEFFICIENT

```
10  PRINT
20  CLEAR
30  PRINT "          GAP EXIT LOSS & DISCHARGE COEFF INTEGRATION          "
40  PRINT "               WITH REFERENCE TO SUCTION SURFACE               "
50  PRINT "                   (Spline fit in pitch dir)                   "
60  PRINT "                         (GAP EXIT I)                          "
70  DEG
80  PAGESIZE 24
90  R$=CHR$ (13)
100  PRINT @ PRINT
110 DIM V(4,15)
120 ! Variable for pitchwise integration , 1 2 3 4 allocated as needed
130 DIM Z(15,31),B2(15,31),CL2(15,31),W2S(15,31),W2W(15,31)
140 DIM S(15),Ss(15),Alb(15),M(15),TRAV$(15),Mm(15),St(15)
150 DIM WC(15,31),CP2(15,31)
160 DIM CisC(15,31),C2S(15,31)
170 DIM XB(15),YB(15),B(15),s(15),G(15)
180 !
190 ! WC   is W2/W x Cos(90-Gamma+B2)  Alb is Blade ss Angle
200 ! CisC is Cis/W x Cos(90-Gamma+B2)
210 ! S  is s/Chord where  s  is distance along surface from le
220 ! Ss is Suc Side   pos of trav
230 ! St is true chord pos of trav
240 ! W2W  is W2/W,  W2S is (W2/W)^2
250 !
260 !
270 ! Creating Chordwise traverse Positions
280 READ Case$,Code$,N@ PRINT Case$
290 FOR n=1 TO N @ READ St(n),Ss(n),Alb(n),S(n)
300 Ss(n)=Ss(n)/100 @ S(n)=S(n)/100 @ NEXT n
310 ! DATA "Radiused Edge    ","DRTGAP",11
320   DATA "Square Tip       ","DSTGAP",11
330 ! DATA "Radiused Squealer","DRSGAP",11
340   DATA 0,0,-90,0,10,25.6,14,18.8,20,40,28.4,29.7,30,52.2,42,40
350   DATA 40,62,50.5,50,50,70.2,59,60,60,77.3,64,70.2,70,83.7,67,80.8
360   DATA 80,89.7,70,91.9,90,95,71.5,102.8,100,100,72.5,113.3
370 PRINT @ PRINT
380 !
390 ! Performing input and Calculations for each Chord position
400 !
```

```
410 FOR n=2 TO N-1
420 TRAV$(n)=Code$&VAL$ (St(n))
430 DISP "READING ";TRAV$(n);"  s/X=";S(n);"  Alpha ss=";Alb(n)
440 ASSIGN# 1 TO  TRAV$(n)
450 READ# 1 ; M(n)@ M(n)=M(n)+1 @ ! Create last trav point on blade
460 FOR m=1 TO M(n)-1
470 READ# 1 ; K,Z(n,m),B2(n,m),CL2(n,m),W2S(n,m),CP2(n,m)
480 W2W(n,m)=SQR (W2S(n,m))
490 WC(n,m)=W2W(n,m)*COS (90-Alb(n)+B2(n,m))
500 CisC(n,m)=SQR (1+CP2(n,m))*COS (90-Alb(n)+B2(n,m))
510 IF WC(n,m)<0 THEN BEEP @ DISP "Neg Leakage Comp Set Zero at ";S(n)*100;"%, R
eading no ";m;" 90-Alb+B2 = ";90-Alb(n)+B2(n,m) @ WC(n,m)=0
520 IF CL2(n,m)<0 THEN CL2(n,m)=0 @ ! If loss goes neg set to zero
530 NEXT m
540 !
550 ! Creating Edge Values
560 !
570 Z(n,0)=0
580 Z(n,M(n))=Z(n,M(n)-1)+.25
590 W2W(n,0)=0
600 W2W(n,M(n))=0
610 CL2(n,0)=1+CP2(n,1)
620 CL2(n,M(n))=1+CP2(n,M(n)-1)
630 CP2(n,0)=CP2(n,1)
640 CP2(n,M(n))=CP2(n,M(n)-1)
650 B2(n,0)=B2(n,1)
660 B2(n,M(n))=B2(n,M(n)-1)
670 WC(n,0)=0
680 WC(n,M(n))=0
690 CisC(n,0)=SQR (1+CP2(n,0))*COS (90-Alb(n)+B2(n,0))
700 CisC(n,M(n))=SQR (1+CP2(n,0))*COS (90-Alb(n)+B2(n,M(n)))
710 NEXT n
720 !
730 GOTO 780 @ DISP "Display data ? (Y/N)" @ INPUT A$@ IF A$="N" THEN 780
740 FOR n=2 TO N-1 @ DISP Ss(n)*100;"% Chord" @ DISP "Zmm   Cl    WCosB  WisCosB
   B2" @ FOR m=0 TO M(n)
750 DISP USING "D.DD,DD.DDD,DDD.DDD,DDD.DDD,DDDD.DD" ; Z(n,m),CL2(n,m),WC(n,m),C
isC(n,m),B2(n,m) @ NEXT m
760 INPUT A$@ IF A$="0" THEN 780
770 NEXT n
780 PRINT "."
790 PRINT "% Chord   1D Loss  Losscomp  1D dis coef   Beta mean  1dMassF Cf  Int
Cisdz  S/C"
800 FOR n=2 TO N-1
810 !
820 ! Generating array V for spline subroutine INTUN
830 ! Integrating firstly at each Chordwise station
840 Clp=0 @ Cdp=0 @ Top=0 @ Bot=0 @ B2mn=0 @ Cl=0
850 Zg=Z(n,M(n))-Z(n,0)
860 FOR m=1 TO M(n)
870 dZ=(Z(n,m)-Z(n,m-1))/Zg
880 Cl=Cl+(WC(n,m)+WC(n,m-1))/2*(CL2(n,m)+CL2(n,m-1))/2*dZ
890 Clp=Clp+(W2W(n,m)+W2W(n,m-1))/2*(CL2(n,m)+CL2(n,m-1))/2*dZ
900 B2mn=B2mn+(WC(n,m)+WC(n,m-1))/2*(B2(n,m)+B2(n,m-1))/2*dZ
```

```
910 Top=Top+(WC(n,m)+WC(n,m-1))/2*dZ
920 Bot=Bot+(CisC(n,m)+CisC(n,m-1))/2*dZ
930 NEXT m
940 V(1,n)=Cl
950 V(2,n)=Top
960 V(3,n)=Bot
970 PRINT USING "DDD,5X,DD.DDDD,5X,DD.DDDD,5X,DD.DDDD,5X,DDD.DD,5X,DD.DDDD,3X,DD
.DDDD,3X,DDD.D" ; Ss(n)*100,Clp,Cl,Top/Bot,B2mn/Top,Top,Bot,S(n)*100
980 NEXT n
990 PRINT @ PRINT
1000 !
1010 ! Integrating Loss in chordwise direction
1020 V(1,1)=V(1,2)-(V(1,3)-V(1,2))*(S(2)-S(1))/(S(3)-S(2))
1030 IF V(1,1)<0 THEN BEEP @ DISP "L H value was ";V(1,1) @ V(1,1)=0
1040 V(1,N)=V(1,N-1)+(V(1,N-1)-V(1,N-2))*(S(N)-S(N-1))/(S(N-1)-S(N-2))
1050 IF V(1,N)<0 THEN V(1,N)=0
1060 PRINT "Loss Coef Endpoint data  ";V(1,1);"   ";V(1,N)
1070 !
1080 PRINT "Integrated Loss up to each chord pos
           % Chord  Loss (spline) Loss (Trapez rule)"
1090 Np=N @ Sum=0
1100 FOR N=2 TO Np
1110 IF N=2 THEN AREA=0 @ GOTO 1130
1120 K=1 @ GOSUB 1440
1130 Sum=Sum+.1/.7*(V(1,N)+V(1,N-1))/2*(S(N)-S(N-1))
1140 PRINT USING "DDD,6X,D.DDDDD,9X,D.DDDDD" ; Ss(N)*100,.1/.7*AREA,Sum
1150 NEXT N @ PRINT @ PRINT
1160 !
1170 ! Integrating for overall Discharge Coeff and Flow Coeff
1180 !
1190 N=Np
1200 V(2,1)=V(2,2)-(V(2,3)-V(2,2))*(S(2)-S(1))/(S(3)-S(2))
1210 IF V(2,1)<0 THEN V(2,1)=0
1220 V(2,N)=V(2,N-1)+(V(2,N-1)-V(2,N-2))*(S(N)-S(N-1))/(S(N-1)-S(N-2))
1230 IF V(2,N)<0 THEN V(2,N)=0
1240 PRINT "Flow Coef Endpoint data  ";V(2,1);"   ";V(2,N)
1250 K=2 @ GOSUB 1440 @ Top=AREA
1260 V(3,1)=V(3,2)-(V(3,3)-V(3,2))*(S(2)-S(1))/(S(3)-S(2))
1270 IF V(3,1)<0 THEN V(3,1)=0
1280 V(3,N)=V(3,N-1)+(V(3,N-1)-V(3,N-2))*(S(N)-S(N-1))/(S(N-1)-S(N-2))
1290 IF V(3,N)<0 THEN V(3,N)=0
1300 PRINT "Discharge Coef Endpoint data  ";V(3,1);"   ";V(3,N)
1310 K=3 @ GOSUB 1440
1320 PRINT @ PRINT "Spline integrated"
1330 PRINT "Discharge Coeff for whole gap = ";Top/AREA
1340 PRINT "Gap Mass Flow Coeff           = ";.1/.7*Top
1350 PRINT @ PRINT "Trapezoidally integrated"
1360 Top=0 @ AREA=0
1370 FOR n=2 TO N
1380 Top=Top+(V(2,n)+V(2,n-1))/2*(S(n)-S(n-1))
1390 AREA=AREA+(V(3,n)+V(3,n-1))/2*(S(n)-S(n-1))
1400 NEXT n
```

```
1410 PRINT "Discharge Coeff for whole gap = ";Top/AREA
1420 PRINT "Gap Mass Flow Coeff           = ";.1/.7*Top
1430 BEEP @ BEEP @ BEEP @ END
1440 ! ****************   SUB INTUN   ************************
1450 FOR I=1 TO N @ XB(I)=S(I) @ YB(I)=V(K,I) @ NEXT I
1460 E=.000001
1470 FOR I=2 TO N-1
1480 H=XB(I+1)-XB(I-1)
1490 XX=XB(I)-XB(I-1)
1500 B(I)=.5*XX/H
1510 T=((V(K,I+1)-V(K,I))/(XB(I+1)-XB(I))-(V(K,I)-V(K,I-1))/XX)/H
1520 s(I)=2*T
1530 G(I)=3*T
1540 NEXT I
1550 s(1)=0 @ s(N)=0
1560 W=8-4*SQR (3)
1570 U=0
1580 FOR I=2 TO N-1
1590 T=W*(-s(I)-B(I)*s(I-1)-(.5-B(I))*s(I+1)+G(I))
1600 H=ABS (T)
1610 IF H>U THEN U=H
1620 s(I)=s(I)+T
1630 NEXT I
1640 IF U>= E THEN 1570
1650 AREA=0
1660 FOR I=1 TO N-1
1670 H=XB(I+1)-XB(I)
1680 AREA=AREA+(.5*H*(V(K,I)+V(K,I+1))-1/24*H^3*(s(I)+s(I+1)))
1690 NEXT I
1700 RETURN
```

APPENDIX 4.C

PROGRAM 'GAP INLET'

PROGRAM WRITTEN BY PROFESSOR J P BINDON

CALCULATES LOSS INLETING THE GAP BY ITEGRATING THE LOSS
FROM THE ENDWALL UP TO LOSS FREE ZONE AT GAP EXIT FOR
THE CONTOURED TIP BLADE

```
10  PRINT
20  CLEAR
30  PRINT "                    GAP INLET LOSS INTEGRATION                    "
40  PRINT "                 WITH REFERENCE TO SUCTION SURFACE                "
50  PRINT "                     (Spline fit in pitch dir)                    "
60  PRINT "                           (GAP INLET I)                          "
70  DEG
80  PAGESIZE 24
90  R$=CHR$ (13)
100  PRINT @ PRINT
110 DIM V(4,15)
120 ! Variable for pitchwise integration , 1 2 3 4 allocated as needed
130 DIM Z(15,31),B2(15,31),CL2(15,31),W2S(15,31),W2W(15,31)
140 DIM S(15),Ss(15),Alb(15),M(15),TRAV$(15),Mm(15),St(15)
150 DIM WC(15,31),CP2(15,31)
160 DIM CisC(15,31),C2S(15,31)
170 DIM XB(15),YB(15),B(15),s(15),G(15)
180 !
190 ! WC   is W2/W x Cos(90-Gamma+B2)  Alb is Blade ss Angle
200 ! CisC is Cis/W x Cos(90-Gamma+B2)
210 ! S  is s/Chord where  s  is distance along surface from le
220 ! Ss is Suc Side   pos of trav
230 ! St is true chord pos of trav
240 ! W2W  is W2/W,  W2S is (W2/W)^2
250 !
260 !
270 ! Creating Chordwise traverse Positions
280 READ Case$,Code$,N@ PRINT Case$
290 FOR n=1 TO N @ READ St(n),Ss(n),Alb(n),S(n)
300 Ss(n)=Ss(n)/100 @ S(n)=S(n)/100 @ NEXT n
310 ! DATA "Radiused Edge    ","DRTGAP",11
320   DATA "Square Tip       ","DSTGAP",11
330 ! DATA "Radiused Squealer","DRSGAP",11
340   DATA 0,0,-90,0,10,25.6,14,18.8,20,40,28.4,29.7,30,52.2,42,40
350   DATA 40,62,50.5,50,50,70.2,59,60,60,77.3,64,70.2,70,83.7,67,80.8
360   DATA 80,89.7,70,91.9,90,95,71.5,102.8,100,100,72.5,113.3
370 PRINT @ PRINT @ PRINT "M(n)"
380 !
390 ! Performing input and Calculations for each Chord position
400 !
```

```
410 FOR n=2 TO N-1
420 TRAV$(n)=Code$&VAL$ (St(n))
430 DISP "READING ";TRAV$(n);"  s/X=";S(n);"  Alpha ss=";Alb(n)
440 ASSIGN# 1 TO  TRAV$(n)
450 READ# 1 ; M(n)
460 ! SQUARE TIP
470 DATA 6,6,3,4,4,4,5,5,5
480 ! RADIUSED TIP
490 ! DATA 6,7,8,7,7,6,6,6,6
500 ! RADIUSED SQUEALER
510 ! DATA 6,5,5,6,4,5,4,4,4
520 READ M(n)@ PRINT M(n)
530 FOR m=1 TO M(n)
540 READ# 1 ; K,Z(n,m),B2(n,m),CL2(n,m),W2S(n,m),CP2(n,m)
550 W2W(n,m)=SQR (W2S(n,m))
560 WC(n,m)=W2W(n,m)*COS (90-Alb(n)+B2(n,m))
570 CisC(n,m)=SQR (1+CP2(n,m))*COS (90-Alb(n)+B2(n,m))
580 IF WC(n,m)<0 THEN BEEP @ DISP "Neg Leakage Comp Set Zero at ";S(n)*100;"%, R
eading no ";m;" 90-Alb+B2 = ";90-Alb(n)+B2(n,m) @ WC(n,m)=0
590 IF CL2(n,m)<0 THEN CL2(n,m)=0 @ ! If loss goes neg set to zero
600 NEXT m
610 !
620 ! Creating Edge Values
630 !
640 Z(n,0)=0
650 Z(n,M(n))=Z(n,M(n)-1)+.25
660 W2W(n,0)=0
670 CL2(n,0)=1+CP2(n,1)
680 CP2(n,0)=CP2(n,1)
690 B2(n,0)=B2(n,1)
700 WC(n,0)=0
710 CisC(n,0)=SQR (1+CP2(n,0))*COS (90-Alb(n)+B2(n,0))
720 NEXT n
730 !
740 GOTO 790 @ DISP "Display data ? (Y/N)" @ INPUT A$@ IF A$="N" THEN 790
750 FOR n=2 TO N-1 @ DISP Ss(n)*100;"% Chord" @ DISP "Zmm   Cl    WCosB  WisCosB
   B2" @ FOR m=0 TO M(n)
760 DISP USING "D.DD,DD.DDD,DDD.DDD,DDD.DDD,DDDD.DD" ; Z(n,m),CL2(n,m),WC(n,m),C
isC(n,m),B2(n,m) @ NEXT m
770 INPUT A$@ IF A$="0" THEN 790
780 NEXT n
790 PRINT "."
800 PRINT "% Chord   1D Loss  Losscomp  1D dis coef   Beta mean  1dMassF Cf  Int
Cisdz  S/C"
810 FOR n=2 TO N-1
820 !
830 ! Generating array V for spline subroutine INTUN
840 ! Integrating firstly at each Chordwise station
850 Clp=0 @ Cdp=0 @ Top=0 @ Bot=0 @ B2mn=0 @ Cl=0
860 Zg=4.65
870 FOR m=1 TO M(n)
880 dZ=(Z(n,m)-Z(n,m-1))/Zg
890 Cl=Cl+(WC(n,m)+WC(n,m-1))/2*(CL2(n,m)+CL2(n,m-1))/2*dZ
900 Clp=Clp+(W2W(n,m)+W2W(n,m-1))/2*(CL2(n,m)+CL2(n,m-1))/2*dZ
```

```
910 B2mn=B2mn+(WC(n,m)+WC(n,m-1))/2*(B2(n,m)+B2(n,m-1))/2*dZ
920 Top=Top+(WC(n,m)+WC(n,m-1))/2*dZ
930 Bot=Bot+(CisC(n,m)+CisC(n,m-1))/2*dZ
940 NEXT m
950 V(1,n)=Cl
960 V(2,n)=Top
970 V(3,n)=Bot
980 PRINT USING "DDD,5X,DD.DDDD,5X,DD.DDDD,5X,DD.DDDD,5X,DDD.DD,5X,DD.DDDD,3X,DD
.DDDD,3X,DDD.D" ; Ss(n)*100,Clp,Cl,Top/Bot,B2mn/Top,Top,Bot,S(n)*100
990 NEXT n
1000 PRINT @ PRINT
1010 !
1020 ! Integrating Loss in chordwise direction
1030 V(1,1)=V(1,2)-(V(1,3)-V(1,2))*(S(2)-S(1))/(S(3)-S(2))
1040 IF V(1,1)<0 THEN BEEP @ DISP "L H value was ";V(1,1) @ V(1,1)=0
1050 V(1,N)=V(1,N-1)+(V(1,N-1)-V(1,N-2))*(S(N)-S(N-1))/(S(N-1)-S(N-2))
1060 IF V(1,N)<0 THEN V(1,N)=0
1070 PRINT "Loss Coef Endpoint data  ";V(1,1);"   ";V(1,N)
1080 !
1090 PRINT "Integrated Loss up to each chord pos
          % Chord  Loss (spline) Loss (Trapez rule)"
1100 Np=N @ Sum=0
1110 FOR N=2 TO Np
1120 IF N=2 THEN AREA=0 @ GOTO 1140
1130 K=1 @ GOSUB 1190
1140 Sum=Sum+.1/.7*(V(1,N)+V(1,N-1))/2*(S(N)-S(N-1))
1150 PRINT USING "DDD,6X,D.DDDDD,9X,D.DDDDD" ; Ss(N)*100,.1/.7*AREA,Sum
1160 NEXT N @ PRINT @ PRINT
1170 !
1180 BEEP @ BEEP @ BEEP @ END
1190 ! *****************   SUB INTUN   ************************
1200 FOR I=1 TO N @ XB(I)=S(I) @ YB(I)=V(K,I) @ NEXT I
1210 E=.000001
1220 FOR I=2 TO N-1
1230 H=XB(I+1)-XB(I-1)
1240 XX=XB(I)-XB(I-1)
1250 B(I)=.5*XX/H
1260 T=((V(K,I+1)-V(K,I))/(XB(I+1)-XB(I))-(V(K,I)-V(K,I-1))/XX)/H
1270 s(I)=2*T
1280 G(I)=3*T
1290 NEXT I
1300 s(1)=0 @ s(N)=0
1310 W=8-4*SQR (3)
1320 U=0
1330 FOR I=2 TO N-1
1340 T=W*(-s(I)-B(I)*s(I-1)-(.5-B(I))*s(I+1)+G(I))
1350 H=ABS (T)
1360 IF H>U THEN U=H
1370 s(I)=s(I)+T
1380 NEXT I
1390 IF U>= E THEN 1320
1400 AREA=0
```

```
1410 FOR I=1 TO N-1
1420 H=XB(I+1)-XB(I)
1430 AREA=AREA+(.5*H*(V(K,I)+V(K,I+1))-1/24*H^3*(s(I)+s(I+1)))
1440 NEXT I
1450 RETURN
```

88-GT-256

THE AMERICAN SOCIETY OF MECHANICAL ENGINEERS
345 E. 47 St., New York, N.Y. 10017

The Effects of Relative Motion, Blade Edge Radius and Gap Size on the Blade Tip Pressure Distribution in an Annular Turbine Cascade With Clearance

G. MORPHIS
Graduate Assistant

J. P. BINDON
Associate Professor

University of Natal, Durban
South Africa

ABSTRACT

Flow visualisation and microscopic static pressure measurements were done in the tip clearance region of an annular turbine cascade with a rotating outer casing to simulate the relative motion at the tip of an axial rotor. The effect of relative motion did not have a significant effect on the blade gap pressure distributions. As in previous studies the narrow deep pressure depression on a sharp pressure edge was seen. It was confirmed that the width of the gap separation bubble depends on clearance and a correlation with flow visualisation showed that at the reattachment line there is the expected slight pressure peak. The separation bubble, which is thought to contribute a major part of the leakage loss, was shown to disappear when the pressure surface tip is give a radius of 2.5 gap widths.

NOMENCLATURE

C_{p2}	Static pressure coeff = $2\,(p-p_1)\,/\,\rho\,V_2^2$
p	Static pressure
V	Absolute velocity
ρ	Density
1	Refers to cascade inlet, tip
2	Refers to cascade outlet, tip
Y	Distances from pressure face tip edge measured normal to chord along clearance gap face
Y'	distance down pressure face measured from tip edge

1. INTRODUCTION

The degradation of turbomachine performance with increasing tip clearance is well known for both turbines (see for example Booth et al 1982a, and Ewen et al 1973) and compressors (Ruden 1937 and Rains 1954). The efforts at reducing this loss are dominated by mechanical control of gap size and by aerodynamic methods of limiting the gap leakage mass flow for a given gap size. The leakage related quantities of loss, gap mass flow and tip sealing efficiency are often conveniently described by the gap discharge coefficient. Much of the previous work has sought to predict and measure this quantity or to use it as a basis for evaluating tip performance (Rains 1954, Wadia and Booth 1982, Moore and Tilton 1987). All of these models are related in some way to the driving pressure difference across the profile and are based on a single physical clearance flow model applicable at all axial stations between the leading and trailing edges. These models all acknowledge the separation bubble near the pressure surface and the subsequent reattachment or mixing.

In order to extend the understanding of the flow physics inside the clearance gap Bindon (1986a,b and 1987a,b,c), using miniaturised probes and tappings in a linear turbine cascade with clearance, measured both the complete static pressure field and the boundary layers inside the gap and on the endwall and also visualised the minute flow structures with smoke.

In a companion paper offered, Bindon (1988) analysed the data to obtain the variation with axial distance of the tip clearance losses due separately to internal gap friction, mixing of the leakage flow and normal secondary flow and attempted to relate some of the findings to the observed flow

Presented at the Gas Turbine and Aeroengine Congress
Amsterdam, The Netherlands—June 6-9, 1988

phenomena. It is suggested that the separation bubble plays a dominant part in loss formation inside and outside of the gap. Due to the accelerating gap pressure field over the forward half of the blade, a strong chordwise flow is established within the separation bubble. This flow accumulates near mid chord and near the pressure edge where the gap pressure is the lowest. The only way that this flow can leave the gap is by mixing with the leakage jet at inlet thus forming a very intense loss zone due the high inlet jet velocity. On the endwall, mixing losses are insignificant over the forward half of the blade despite the entry of leakage flow there. Mixing losses only appear to emerge and grow very rapidly when the high loss wake containing the mixed out bubble enters at 70% chord. The exceptionally rapid growth of the endwall mixing loss was tentatively attributed to the possibility of the bubble wake having insufficient energy to negotiate the diffusion in the suction corner. The result would then be a "separation" or flow reversal with accompanying mixing loss. Finally it was suggested that since so much entropy is generated within the gap in reducing the discharge coefficient, fewer losses may result from a relatively loss free flow in which the combination of tip deflection and entropy production is optimised. Such a loss free flow may also reduce the mixing loss.

This paper therefore in the first instance begins to address the question of eliminating the clearance gap separation since it appears to play such an important part in loss formation. The sharp edged pressure corner at gap inlet is progressively radiused and the effect of this on the separation bubble as refected by pressure distribution and in surface flow visualisation is investigated. The radiused edge studies also extend the very limited radius studies originally performed by Bindon (1986b, 1987a).

Since much of the understanding of tip clearance flow was obtained in experimental rigs which do not model the relative motion in the tip region, this paper also studies this effect by rotating the casing of an annular test cascade. There is conflicting evidence in the literature regarding the influence of relative motion. Mayle and Metzger (1982) argued that the gap path length was not long enough for the two boundary layers to meet and interact viscously. A spinning disc rectangular surface experiment proved the thesis by showing that the heat transfer coefficient was virtually independant of simulated turbine wall motion. Graham (1985) for a turbine cascade configuration found that wall motion had the effect of significantly reducing the leakage flow, of moving the leakage vortex in towards the suction surface and of virtually eliminating the suction surface depression caused by the vortex. He also provided gap exit velocity traverses which showed that the bubble wake boundary layer almost filled the gap which is in agreemnent with the traverses of Bindon (1987c) in the same general region. Dean (1954) found that the vortex core was moved further away from the suction surface of a compressor rig in which relative motion enhances tip leakage flow. Gearhart (1964), also for a comprssor rig, reported that endwall motion increased the gap static pressure depression. The 2D numerical model of Wadia and Booth (1982) allows for wall motion and a drop in discharge coefficient was calculated with the wall in motion as for a turbine.

Finally this paper responds to Moore (1987) who has suggested that the width of the separation bubble increases with the clearance gap and the width is measured for various gap sizes.

2. ROTATING CASING CASCADE AND INSTRUMENTATION

An existing one and a half stage low speed research turbine was converted to model the relative motion between a rotor blade and casing. As shown in Figure 1, the stator row becomes the stationary annular test cascade while the rotor row is attached to a segment of the outer annulus. This segment extends forward over the stator and rotates with the rotor to create the required relative motion at the tip.

To provide adequately sized blade profiles for the microscopic pressure measurements needed, relatively low aspect ratio untwisted cascade was chosen. A NACA A_3K_7 profile with a slightly thickened trailing edge to model a cooled turbine was used. The profile and test data are summarised in Table 1.

The profiles were cast in epoxy resin using a mould created from a hand-made wooden master blade. As described in Bindon 1987a,

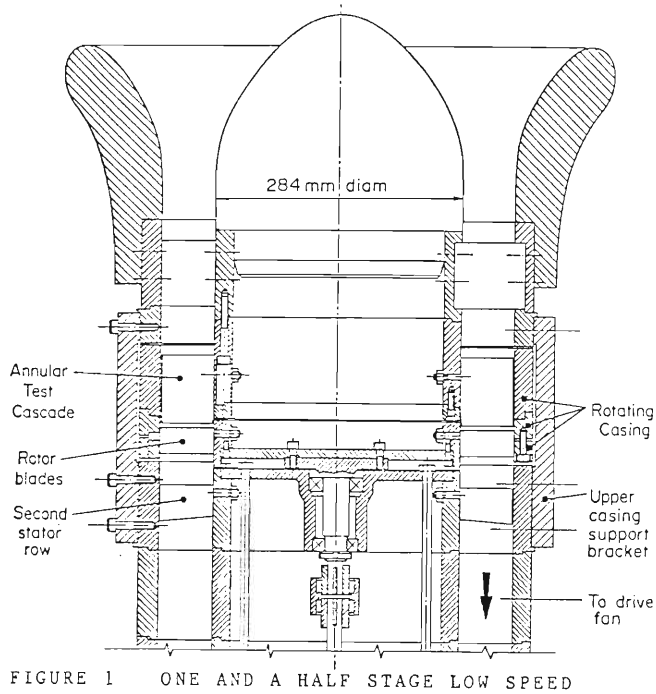

FIGURE 1 ONE AND A HALF STAGE LOW SPEED RESEARCH TURBINE ADAPTED FOR ROTATING CASING STUDY.

the blades were slotted at the tip, the slots taped over and micropunctured for high resolution static pressure measurements of up to 5 tappings per millimeter. After puncturing the position of a tapping was measured using a hand held magnifier with 0.1mm engraved graduations. Each slot was accessed by a spanwise hole drilled through into the hub region and connected to a multitube manometer by a tube bunch exiting through the nose cone.

TABLE 1 : CASCADE AND TEST DATA

Chord	115mm
Span	61mm
Annulus Tip diameter	406mm
Solidity (tip)	1.35
Maximum thickness	20% chord
Trailing edge thickness	5% chord
Cx / Ucasing	0.7
Camber angle	60 deg
Number of blades	15
Reynolds number (exit)	3×10^5
Gas inlet angle	0 deg
Clearance gaps :	4% chord (4.6mm)
	2% chord (2.3mm)
	1% chord (1.2mm)
Tape thickness	0.06mm

3. THE CLEARANCE GAP PRESSURE DISTRIBUTIONS AND THE EFFECT OF RELATIVE MOTION

In a turbine the relative motion of the casing is in the opposite direction to the leakage flow. The viscous shear on the gap endwall is therefore much more intense than in a compressor. Although gap sizes are small, the flow path even at maximum blade thickness is also short and the internal boundary layers would not normally be fully developed at gap exit. A relatively loss free core layer was seen in Bindon (1987c) over most of the gap length except at mid chord where the mixed out bubble flow is thought to emerge. Thus the casing boundary layer is unlikely to have a marked effect on the blade boundary layer and hence on the pressure distribution.

By allowing the casing to either rotate or remain stationary, the pressure distribution on the blade within the clearance gap was measured along lines roughly normal to the blade chord and hence the direction of the leakage flow. In Figure 2 results are shown at 30%, 40%, 50% and 60% chord and for the stationary wall, are similar to those obtained from the linear cascade of Bindon (1987a). A low pressure region exists right on the pressure corner which is thought to be due to an attached flow around the small blade edge radius. This diffuses sharply before separating to form the bubble. With relative motion, this pressure trough is less evident and edge pressures are higher. No explanation is advanced for this since very little is known about the microstructure of the corner flow. These new results for the corner are however significant because in Bindon (1987a) only a single measurement had been available to define the phenomena. An improvement in the micro tapping technique has added 3 more holes close enough to the corner to record the pattern. It can therefore be stated with more confidence that these narrow regions of low pressure do exist on sharp edged pressure surfaces.

The pressure level in the bubble zone is little affected by wall motion as is the apparent width of the bubble. The pressures reached in the fully attached area behind the bubble are significantly higher (about 14%) with rotation. Since wall motion would increase the viscous shear action within the clearance gap, both the leakage flow quantity and the size of the resulting vortex, could be slightly reduced. This could increase the suction surface (i.e. gap exit) pressure which

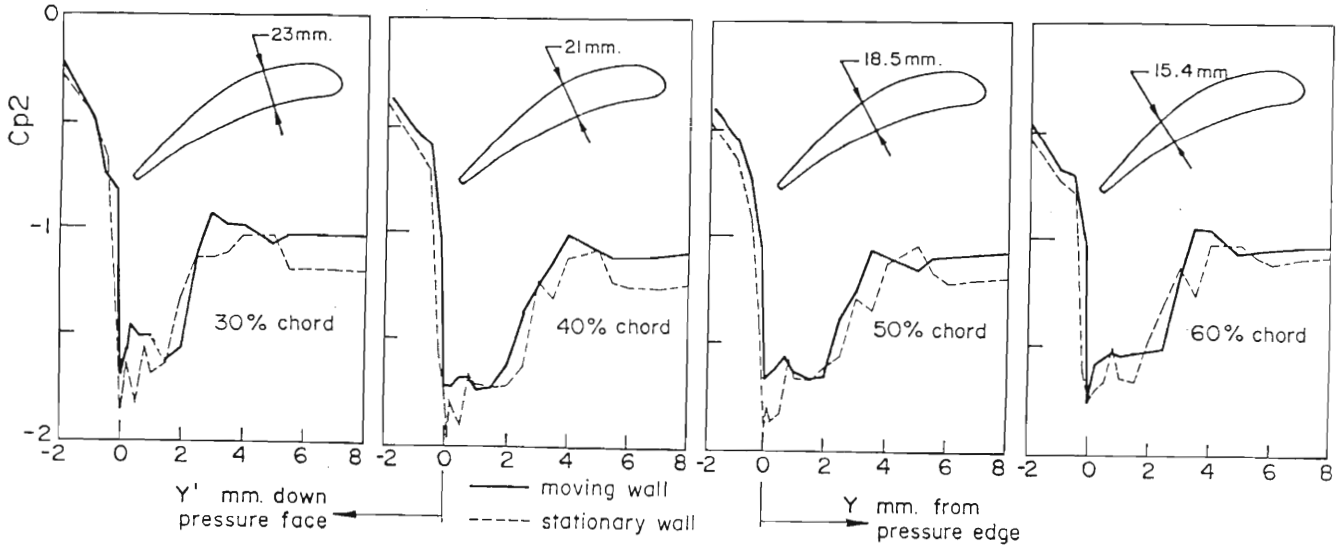

FIGURE 2 EFFECT OF RELATIVE MOTION ON THE BLADE PRESSURE DISTRIBUTIONS IN THE TIP CLEARANCE GAP

has been found to be radically affected by the leakage vortex blockage (Graham 1985, Bindon 1987a).

The remainder of the study was done with the outer annulus rotating.

In order to highlight the low pressure levels encountered in the separation bubble and therefore the kinetic energy that needs to be imparted to the separation bubble flow, Figure 3 shows the mean of the lowest part of the pressure trough related to the bubble in comparison to the suction surface distribution. It should be noted that this bubble pressure is perhaps the quantity most representative of the pressure side distribution. The gradient on the pressure face at the tip is too intense to realistically define a tip pressure and the actual edge pressure is too narrow a zone for it to be regarded as defining the tip loading. It is also difficult to use the pressure surface loading some distance away from the tip, before the gap acceleration starts, because in an annular cascade, radial effects are present. The clearance gap was therefore sealed with felt and, with a stationary casing, a zero clearance distribution recorded and presented in Figure 3 as the "2D" or zero clearance reference loading.

Figure 3 shows that the suction surface pressure is much lower than the "sealed" or semi 2D value and corresponds to the linear cascade measurements of Bindon (1987a) and Graham (1985). While the suction surface pressure is reduced by clearance, there is no evidence of the significant distortions seen by Bindon (1987a) and Graham (1985) and attributed to the influence of the leakage vortex in the suction corner. Since endwall motion is present this could due to the reduced strength and penetration of the leakage flow as found by Graham (1985) and by Sjolander and Amrud (1987). The bubble pressure is lower than that measured on the suction surface, or clearance gap exit value, from 30% chord onwards. The nature of the pressure distribution indicates that the loading is weighted towards the leading edge, a factor which may have a significant influence on the flows inside the gap. Sjolander and Amrud (1987) found, for a different profile, that the suction surface had two depressions which were associated with two leakage vortices emerging from the gap. Thus very different flows could occur inside the gap depending on the profile, the important factors being perhaps camber and thickness.

The actual bubble pressures and the remainder of the blade gap surface pressure distributions are given in Figures 4 and 5. The first figure shows 3 distributions over the forward half of the blade in the zone where it can clearly be seen that the flow within the bubble undergoes a strong acceleration towards the trailing edge. A new result seen in these curves is that the pressure towards the suction side begins to fall well within the parallel walls of the clearance gap. This effect reduces with chord and, as Figure 5 shows, the distributions are virtually flat from mid chord onwards.

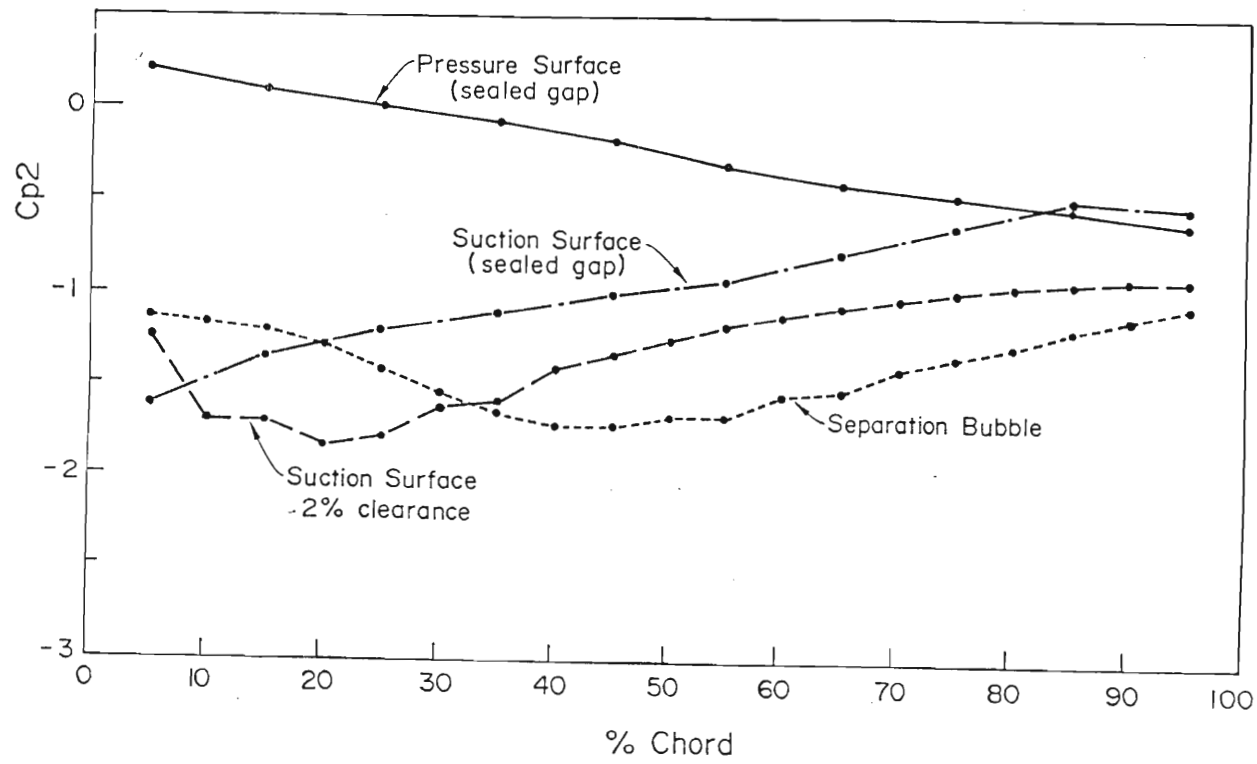

FIGURE 3 BLADE PROFILE PRESSURE DISTRIBUTIONS COMPARED TO THE SEPARATION BUBBLE PRESSURE

Figure 5 shows the pressures over the rear half of the blade and the steep pressure rise required of the flow inside the bubble can be seen. It is this gradient which is thought to separate the internal bubble flow that is established over the forward half of the blade and to force the accumulated fluid to mix with the gap inlet jet in order to move towards the reltively high pressure at gap exit. This mixing process may form the major part of the internal gap loss and appears to be a significant factor in reducing the gap discharge coefficient (Bindon 1988).

This pressure gradient raises the interesting question of whether the flow within the bubble is not in actual fact towards the leading edge. A careful study was made using oil flow visualisation and at a clearance gap of 4% chord, oil could clearly be seen moving sluggishly from the trailing edge towards mid chord. Unfortunately, the turbine rig was vertical and the oil was moving against gravity. Since oil therefore could be moving towards mid chord from both directions, it explains why oil is seen in Figure 6 to collect near mid chord and break away towards

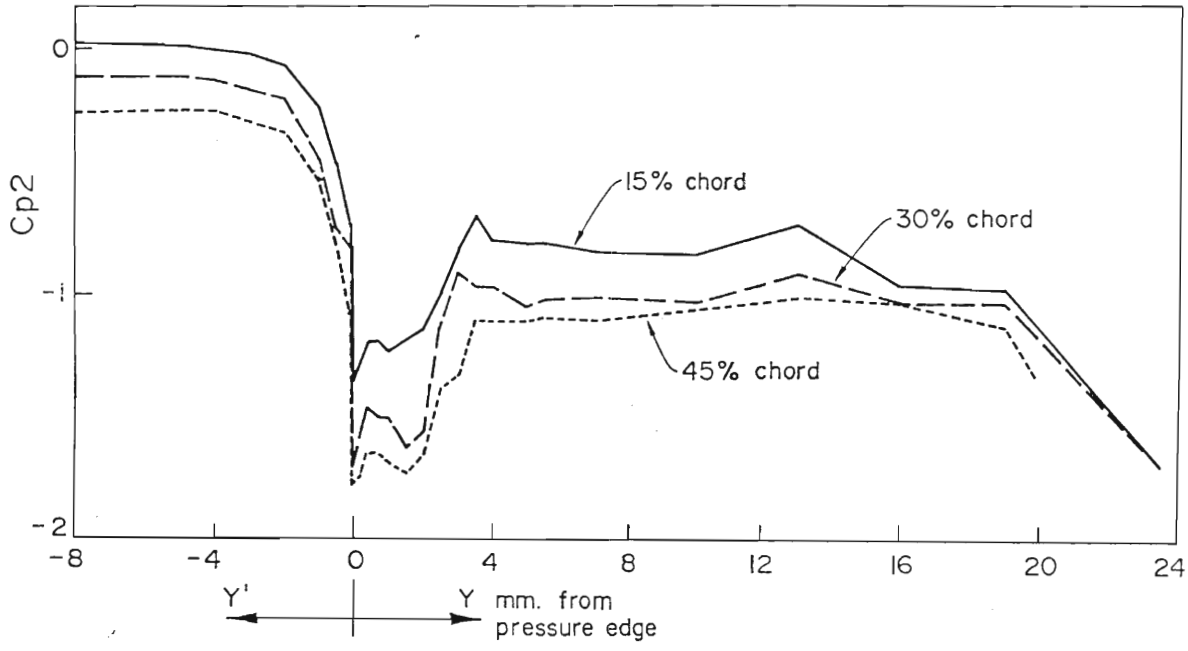

FIGURE 4 BLADE PRESSURE DISTRIBUTIONS IN THE CLEARANCE GAP OVER THE FORWARD REGION OF PROFILE WHERE PRESSURES ARE FALLING

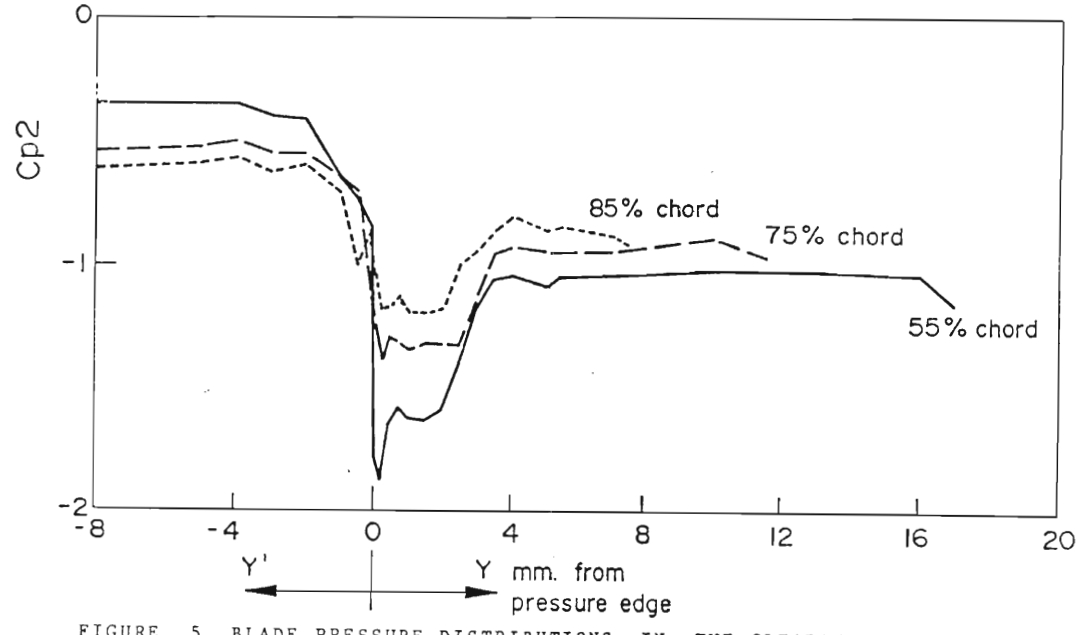

FIGURE 5 BLADE PRESSURE DISTRIBUTIONS IN THE CLEARANCE GAP OVER THE REAR OF THE PROFILE WHERE PRESSURES ARE INCREASING.

the gap exit. The oil movement over the forward half of the blade, although aided by gravity, is not solely due to gravity as can be demonstrated by the strong chordwise corkscrew motion clearly seen in the smoke flow visualisation of Bindon (1986a, 1987b).

The possible counter flow of separation bubble fluid is thought to be important since more fluid would be convected towards mid chord and would add to the internal gap loss generation and to the reduction in gap discharge coefficient.

4. THE EFFECT OF GAP SIZE ON CLEARANCE FLOW

The smoke flow visualisation of Bindon (1986a, 1987b) showed that the width of a separation bubble became wider with increased clearance gap. However, the pressure distributions seemed to indicate that the bubble width was independent of gap size. In an oil surface flow study, Moore (1987), also claimed that the bubble increased with clearance.

In the annular cascade, the gap size was set at 1%, 2% and 4% chord and the pressure distribution recorded and the oil surface flow visualisation photographed through a transparent rotating outer casing. Figure 6 shows the pressures at 40% chord and the complete flow visualisation except for the trailing edge, which was hidden by the metal casing.

It is quite obvious that the width of the bubble increases with clearance gap. It also tends to become wider with axial distance and, in the case of the largest clearance, almost breaks away near mid chord, probably due to the accumulation of oil which is fed there from both directions. The bubble width at 40% chord was measured and the positions indicated on the pressure distributions. The edge of the visible bubble coincides almost exactly with termination of the pressure rise which has been associated with the reattaching flow behind the bubble. When this interpretation of the pressure distribution is applied to the results of Bindon (1987a), then the bubble width in that study can also be said to vary with clearance gap size. Since at the edge of the separation bubble (ie where the flow reattaches) there is a flow of considerable strength towards the blade surface, a slight pressure peak can be seen which immediately falls away in the direction of the leakage flow.

The minimum pressure within the bubble is also strongly dependent on gap size but is not monotonic and the 2% clearance shows a very much lower pressure than the values at lower and higher clearances. A somewhat similar result can be seen in the pressure distributions of Bindon (1986b, 1987a)

5. THE EFFECT OF BLADE EDGE RADIUS ON GAP FLOW

In Bindon (1987a), a brief study was made of the effect of pressure edge radius and it was seen that the sharp pressure dip on the edge was reduced as the radius was increased. Since the pattern of tip leakage loss development inside the clearance gap and on the endwall is thought to be strongly connected to the gap separation bubble, the effect of increasing edge radius on the formation of the bubble was investigated. If the formation of the separation bubble could be prevented there could be a significant reduction overall loss.

The inlet to the clearance gap is equivalent to a sudden contraction and the corner radius dimension which will keep the flow attached and avoid a separation bubble will most likely depend on the gap size. Tests were therefore done at a fixed gap width of 2% chord and once the critical radius was found, a single experiment at a smaller gap was made for confirmation. By monitoring the bubble using surface flow visualisation and the gap

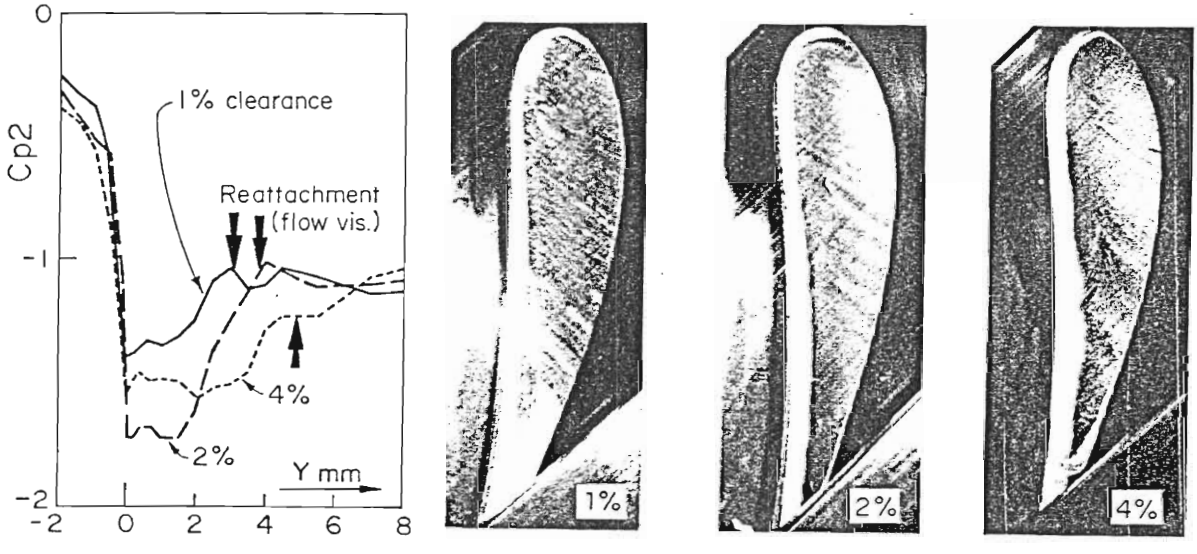

FIGURE 6 EFFECT OF GAP SIZE ON PRESSURE DISTRIBUTION AND SEPARATION BUBBLE

pressure distribution, the edge radius was progressively increased from the original "sharp" value of 1/4 gap width (0.5% chord) until the signs of separation vanished.

Figure 7 shows the surface flow visualisation for pressure edge radii of 0.25, 1, 1.5 and 2.5 gap widths (0.5%, 2%, 3% and 5% chord). For the smallest radius the bubble is very wide and starts right at the edge of the blade and runs unbroken from leading to trailing edge. At a radius of 1 gap width the pattern is quite different. The oil indicates that the bubble starts part way around the radius and the attached flow off the pressure surface can be distinctly seen. The bubble appears to be very narrow. Near mid chord the bubble itself separates and thereafter the flow does not appear to reattach. At a radius of 1.5 gap widths, the flow has remained attached even further around the edge before forming a narrow bubble. At 2.5 gap widths the flow is clearly attached around the edge and right across the gap surface.

In Figure 8 the pressure distributions for various edge radii are presented for 30%, 40% and 50% chord. The characteristic depression attributed to the bubble can be clearly seen at the sharp edge radius of 0.25 gap widths and also at 0.5 gap widths. At the next radius of 1.5 gap widths, the edge pressure is as much as 35% higher and there is a distinct rise slightly before the termination of the radiused section. This coincides exactly with the position of the thin separation line seen in the flow visualisation.

At an edge radius of 2.5 gap widths where the flow visualisation indicated attached flow, the minimum pressure occurs at the termination of the radius. There is a slight pressure rise which could indicate either a small separation but a boundary layer traverse would be needed to ascertain the nature of the flow. The pressure level within the clearance gap is the lowest for the apparently completely attached flow and this low pressure persists right through to gap exit (not shown in Figure 8). This would indicate that the suction surface pressure is actually decreased by the more energetic nature of the leakage flow as also found by Graham (1985).

The clearance gap was finally set at 0.8% chord and a blade with an edge radius of 2% chord (2.5 gap widths) was tested using flow visualisation. No signs of separation were seen thus confirming that separation can be avoided by using edge radii of 2.5 gap widths.

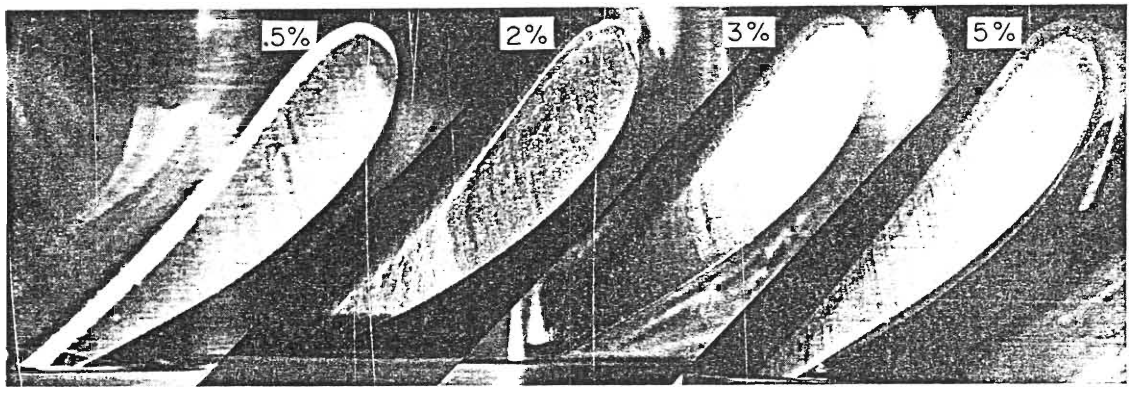

FIGURE 7 SURFACE OIL FLOW VISUALISATION SEEN THROUGH MOVING CASING SHOWING GAP SEPARATION BUBBLE FOR INCREASING PRESSURE EDGE RADIUS AND FOR A CLEARANCE GAP OF 2% CHORD

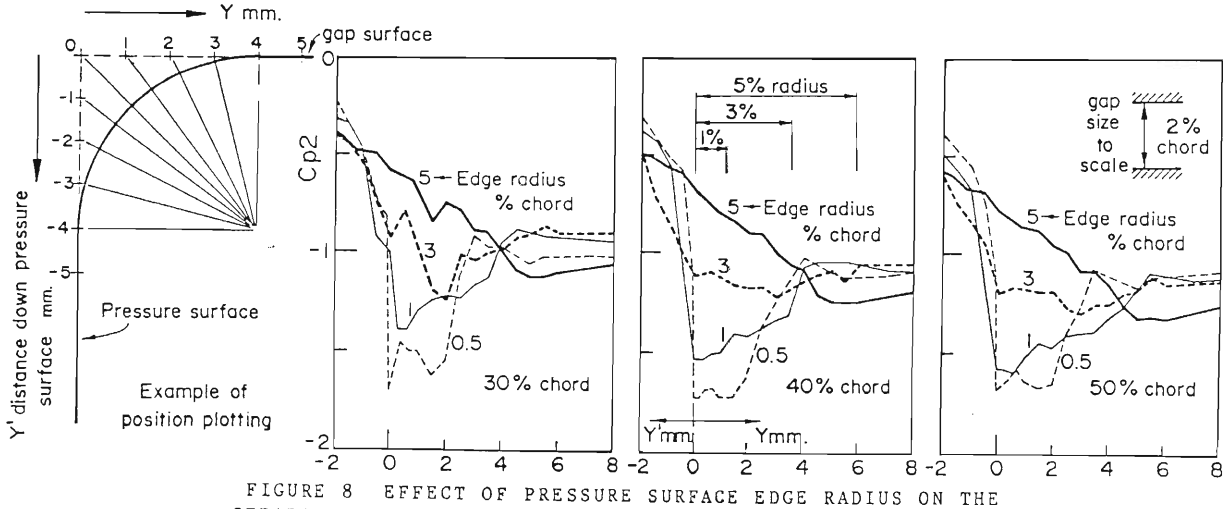

FIGURE 8 EFFECT OF PRESSURE SURFACE EDGE RADIUS ON THE SEPARATION BUBBLE AND THE BLADE GAP PRESSURE DISTRIBUTION

6. CONCLUSIONS

The annular rotating casing rig has provided a relatively simple vehicle for creating a relative motion in the tip clearance region of a cascade. Due to the layer of virtually loss free flow between the casing boundary layer and the blade gap surface boundary layer, the effect of relative motion was found to have little influence over the general shape of the pressure distributions measured in the tip clearance region and hence over the basic flow mechanisms in the gap. The low pressure associated with the separation bubble was little influenced by relative motion but in the reattached regime behind the bubble, the pressures were higher, probably as a result of a reduced leakage flow and reduced distortion of the suction surface pressure. This reduction in leakage flow means that relative motion is more important with respect to loss formation and gap discharge coefficient than in determining the basic nature of the gap flow.

The existence of what is thought to be a flow attachment around the pressure edge leading to very low pressures and high heat transfer, was confirmed by a higher resolution pressure tapping procedure which provided additional data in the microscopic zone of interest.

It was confirmed that the width of the separation bubble depends on gap size and the reattachment line was seen to coincide with a slight pressure peak. A pressure gradient which would accelerate flow within the bubble was again seen over the forward half of the blade. Since a separation bubble clearly also exists over the latter half of the blade where the pressure gradient is such as to move flow from trailing edge towards mid chord, it is suggested that both bubble flows meet at mid chord to mix out with the incoming leakage jet and greatly enhance the internal gap loss and reduce the gap discharge coefficient.

Increasing the radius of the pressure edge of the profile to 2.5 times the clearance gap width prevented the formation of the separation bubble and its associated deep pressure depression within the gap. This also had the effect of apparently strengthening the leakage flow and therefore reducing the suction side pressure and hence the pressure inside the gap.

The next part of the investigation will deal with the effect of eliminating the separation bubble on internal gap and endwall loss generation, on tip region flow deflection and on a deduced rotor output when the stationary cascade results are converted into the rotational frame.

BIBLIOGRAPHY

Bindon J P, 1986a "Visualisation of axial turbine tip clearance flow using a linear cascade" Cambridge University, Whittle Laboratory Report CUED/A-Turbo TR122

Bindon J P, 1986b "Pressure and flow field measurements of axial turbine tip clearance flow using a linear cascade" Cambridge University, Whittle Laboratory Report CUED/A-Turbo TR123

Bindon J P, 1987a "Pressure distributions in the tip clearance region of an unshrouded axial turbine as affecting the problem of tip burnout", ASME Paper 87-GT-230.

Bindon J P, 1987b "Visualisation of tip clearance flow in a linear turbine cascade", AIAA 8th International Symposium on Air Breathing Engines, Cincinatti, June 1987, page 436-444, Paper No. ISABE 87-7032.

Bindon J P, 1987c "Measurements of tip clearance flow structure on the endwall and within the clearance gap of an axial turbine cascade". Proceedings of the I Mech E, International Conference on Turbomachinery - Efficiency Prediction and Improvement, Cambridge, September 1987, page 43 - 52, Paper No C273/87.

Booth T C, Dodge P R, Hepworth H K, 1982 "Rotor tip leakage: Part 1-Basic methodology" ASME Transactions, J of Engineering for Power, V 104, Jan 1982, p 154

Dean R C, 1954 "The influence of tip clearance on boundary layer flow in a linear cascade" MIT Gas Turbine Laboratory Report No 63

Gearhart W S, 1964 "Tip clearance flows in turbomachines" The Pennsylvania State University Science and Engineering Ordnance Research Laboratory TM 506.2491-04

Graham J A H, 1985 "Investigation of a tip clearance cascade in a water analog rig", ASME Paper Number 85-IGT-65.

Mayle R E, Metzger D E, 1982 "Heat transfer at the tip of an unshrouded turbine blade" The 7th International Heat Transfer Conference, Munich, V3, p87

Moore J, Tilton J G, 1987 "Tip leakage flow in a linear turbine cascade", ASME Paper No 87-GT-222

Moore J, 1987, Virginia Polytechnic Institute and State University, Private communication.

Rains D A, 1954 "Tip clearance flows in in axial flow compressors and pumps" California Institute of Technology, Hydrodynamics Laboratory Report No 5 1954

Sjolander S A, Amrud K K, 1987 "Effects of tip clearance on blade loading in a planar cascade of turbine blades" ASME Journal of Turbomachinery, V104, p237 (ASME Paper No 86-GT-245)

Wadia A R, Booth T C, 1982 "Rotor tip leakage: Part II - Design optimization through viscous analysis and experiment" ASME Transactions, Journal of Engineering for Power, V 104, Jan 1982, p 162